ISSN (print) 2686-7397
ISSN (online) 3034-5065

Российская Академия Наук

Volume 520, No. 1

January 2025

# ДОКЛАДЫ РОССИЙСКОЙ АКАДЕМИИ НАУК.

## НАУКИ О ЗЕМЛЕ

# DOKLADY EARTH SCIENCES

NAUKA
1727

# CONTENTS

## Vol. 520, No. 1, 2025

## GEOLOGY

## OIL AND GAS GEOLOGY

## PETROLOGY

## MINERALOGY

## PALEOGEOGRAPHY

## GEOPHYSICS

## OCEANOLOGY

## PHYSICS OF THE EARTH

## SOIL SCIENCE

*DOKLADY EARTH SCIENCES, 2025, Vol. 520, No. 1, pp. 3–7*

# EVIDENCE OF THE EARLY PRECAMBRIAN AGE OF METAMORPHIC ROCKS OF THE UFALEY BLOCK (MIDDLE URALS): RESULTS OF U-Th-Pb (LA-ICP-MS) DATING OF DETRITAL ZIRCON FROM QUATERNARY DEPOSITS

**© 2025 G. Yu. Shardakova**[a, *], **E. V. Pushkarev**[a],
**Corresponding Member of RAS A. B. Kotov**[b], **and A. O. Simankova**[a]

Received August 21, 2024
Revised August 29, 2024
Accepted September 02, 2024

**Abstract.** U-Th-Pb (LA-ICP-MS) geochronological studies of detrital zircon from the Quaternary deposits of the western part of the Ufaley block in the Middle Urals, in a tectonic fragment composed of amphibolite-gneiss complex and associated bodies the Precambrian clinopyroxenites, were performed. The main statistical age maximum corresponds to the range of 2100-2000 Ma. Several small peaks correspond to the range of 3200-2500 Ma. So there is the real reason to believe that rocks of the Early Precambrian age are present within the Ufaley block. They were not previously identified here.

**Keywords :** *detrital zircon, U–Th–Pb isotope studies, quaternary deposits, age of the substrate*

**DOI**: 10.31857/S26867397250101e8

The modern appearance of the Uralian Orogen was formed as a result of time-varying geodynamic regimes, from the destruction of an ancient platform, through the development of an oceanic basin, to subduction and subsequent collisional and post-collisional events. As a result of these processes, an accretion zone consisting of blocks of different ages and origin was formed in the area of the junction of the Uralian Orogen with the East European Platform (EEP) [1]. In particular, there are blocks in the structure of which rocks of Early Precambrian age are involved. In the Southern Urals, these are the Taratashsky and Alexandrovsky blocks (the rock types composing these blocks are often described in the literature as complexes of the same name), which are considered fragments of the EEP integrated into the structure of the Uralian Orogen ([2, 3, 4], etc.). These blocks are composed mainly of granulites, gneisses, and amphibolites, which contain zircon with a U–Th–Pb age of 2800-2500 Ma, and the model Nd age of the rocks reaches 3.5 billion years [4, 5]. Structural metamorphic transformations of the rocks of these blocks occurred in the intervals of 2460–1800, 1350–1200 Ma and further up to 300 Ma [3-5].

In the post-collisional structure of the Paleo-Uralian Hercynian orogen, the Ufaley block (UB) is located at the same latitude as the Taratashsky and Alexandrovsky blocks, but somewhat to the east, which is the southern part of the anticlinorium of the same name. The UB is bounded on the north by the Kukazar fault, which separates it from the northern part of the Ufaleysky anticlinorium, on the east by the Main Uralian Fault zone (MUF), and on the west by the Ufa fault.

The eastern part of the UB, adjacent to the MUF, is composed of schists, amphibolites, quartzites, and eclogite-like rocks of the Kurtinskaya Formation, while the western and central parts consist of amphibolites and gneisses of the Yegustinskaya and Slyudyanogorskaya Formations (Fig. 1). The age of metamorphism of the latter two formations is estimated to be in the range of 550–480 Ma [6–8], although on the geological map they are assigned to the Proterozoic, and the Kurtinskaya Formation to the Middle Riphean [9]. Reliable geochronological data confirming the Precambrian age of the UB rocks and a consensus on their nature do not yet exist [1, 6–8].

---

[a] *Institute of Geology and Geochemistry, Ural Branch of the Russian Academy of Sciences, Yekaterinburg, Russia*
[b] *Institute of Precambrian Geology and Geochronology, Russian Academy of Sciences, St. Petersburg, Russia*
**e-mail: shardakovagalina@mail.ru*

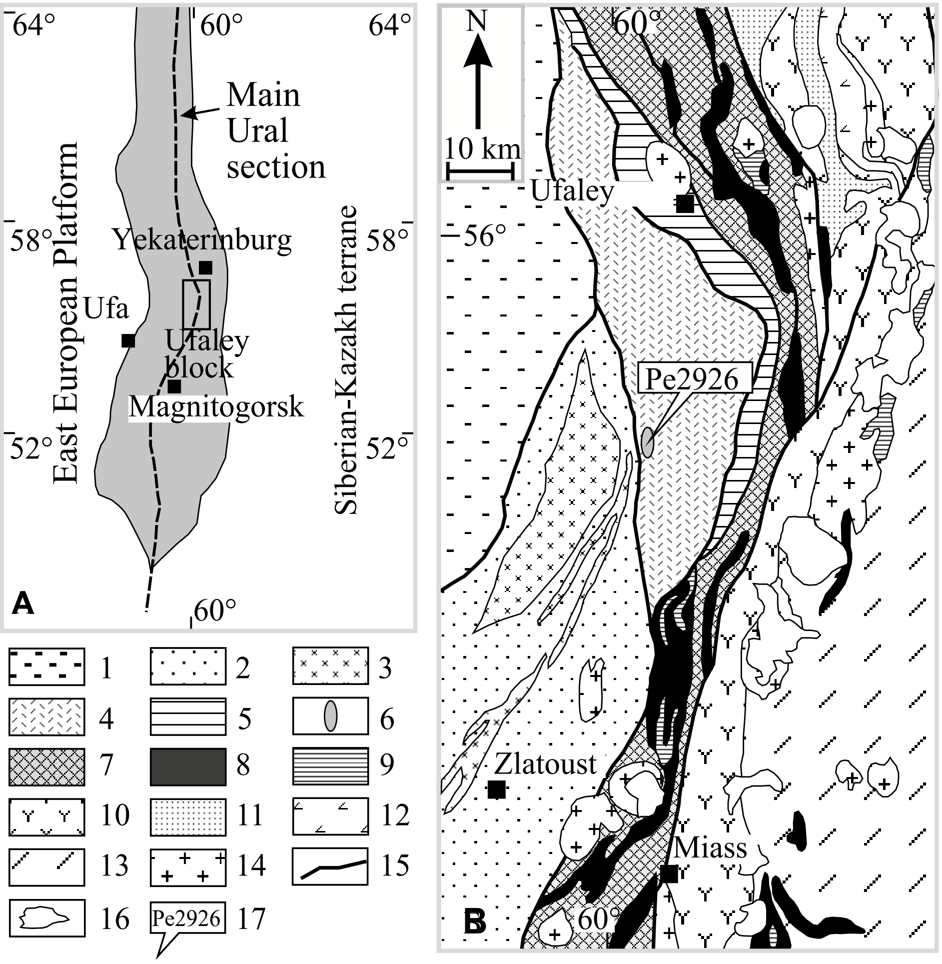

**Fig.** 1. Geotectonic position (A) and simplified geological structure scheme (B) of the Ufaley Block [1, 2]. 1 – Paleozoic sedimentary cover complexes of the East European Platform; 2 – Proterozoic sedimentary complexes, 3 – Taratash and Alexandrovsky blocks (AR-PR), 4–5 – Ufaley Block: 4 – amphibolites and gneisses of the Egustinskaya and Slyudyanogorskaya Formations, undivided; 5 – eclogite-schist Kurtinskaya Formation; 6 – pyroxenites of Shigir Hills; 7–9 – zone of the Main Uralian Fault with fragments of Magnitogorsk and Tagil island arc complexes (7), serpentinized ophiolites (8) and gabbroids (9); 10–12 – complexes of the Sysert-Ilmenogorsk anticlinorium: 10 – metamorphic and alkaline rocks, 11 – metasedimentary rocks, 12 – metavolcanic rocks; 13 – Middle-Upper Paleozoic sedimentary-volcanogenic rocks with ultrabasic bodies (also sign (8)); 14 – diorites and granodiorites; 15 – tectonic faults; 16 – lakes; 17 – number and position of detrital zircon sample.

In the western part of UB, along the right bank of the Ufa River, in a fragment bounded on all sides by faults, among gneisses and amphibolites of the Yegustinskaya Formation, there is a submeridional body (4 x 0.5 km) of orthopyroxene-plagioclase-olivine clinopyroxenites, expressed in the relief as the northern and southern Shigir Hills (SH), separated by a sublatitudinal valley of a temporary watercourse. The geological relationships of pyroxenites with surrounding rocks have not been established. Pyroxenites have petrogeochemical similarities with the same-named rocks from dunite-clinopyroxenite-gabbro complexes of the Ural-Alaskan type. It is assumed that the original melt for them had ankaramite characteristics: a high $CaO/Al_2O_3>1$ ratio, indicating a wehrlitic composition of the mantle source [10]. According to data from A.A. Krasnobaev et al., the U–Pb age of the oldest zircons from the SH pyroxenites corresponds to 1651±47 and 1444±46 Ma [11], based on which the Paleoproterozoic age of the rocks was accepted, as recorded on the geological map [9]. However, these works do not discuss the probability that ancient zircons could have been captured during the intrusion of the SH pyroxenites. It is significant that in rocks of similar composition

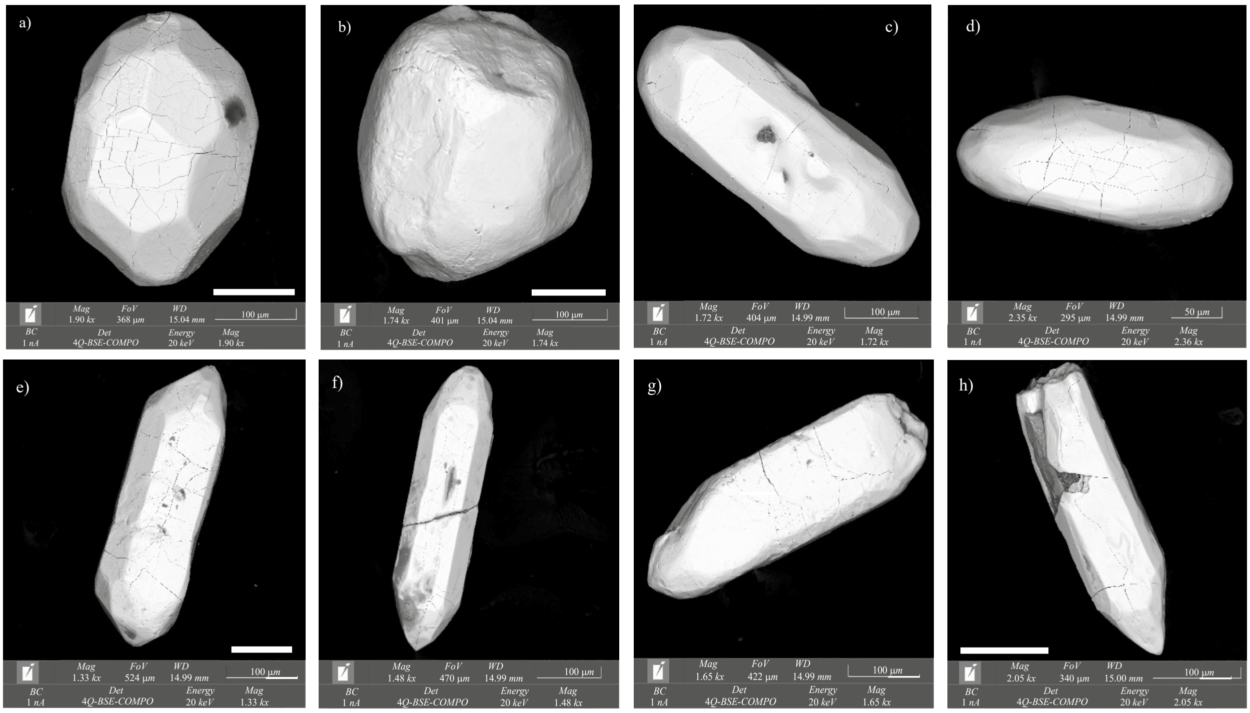

**Fig.** 2. Morphology of detrital zircon grains from Quaternary gravel-clay deposits surrounding the pyroxenites of Shigir Hills. Scanning electron microscope Mira Tescan, backscattered electron mode.

in the Alexandrovsky block [12], an older U–Pb zircon age of 2022±15 Ma was determined, and an Archean age of the protolith is assumed [5, 13]. Even if we assume the xenogenic nature of zircon in the SH pyroxenites, we can suggest the presence of Early Precambrian metamorphic rocks in their frame, which had not been previously established.

To verify this assumption, a U-Th-Pb (LA-ICP-MS) age determination of detrital zircon was performed from Quaternary clay-gravel deposits of the dry bed of a temporary watercourse in a sublatitudinal valley about 1 km long, separating the pyroxenites of the Northern and Southern Shigir Hills. The drainage area of the watercourse captures both the ultramafic rocks themselves and the directly enclosing gneisses and amphibolites of the Yegustinskaya Formation. The introduction of material from distant sources is not excluded but unlikely.

Research was conducted at the "Geoanalytik" Shared Research Facility, IMG UB RAS, Yekaterinburg. The morphology and internal structure of zircon were studied using a TESCAN MIRA scanning electron microscope in backscattered electron and cathodoluminescence modes. U–Th–Pb isotope studies were performed on a NexION 300S quadrupole ICP-MS with a NWR 213 laser ablation attachment (LA-ICP-MS). The crater diameter was 25 μm, pulse repetition rate 10 Hz, energy density 10–11 J/cm². Calibration was performed using the standard zircon GJ-1 [14]. Standard zircon crystals 91500 and Plešovice were used to control the quality of analytical data. During the studies, weighted average age estimates were obtained for the ratio $^{206}$Pb/$^{238}$U– $^{207}$Pb/$^{235}$U: for standard 91500, 1065±5.8 Ma (1σ, $n$=8, MSWD=0.00079, probability=0.98), for standard Plešovice, 337.9±1.6 Ma (1σ, $n$=9, MSWD=0.078, probability=0.38). The age values obtained for zircon standards are consistent with the recommended data [15]. U–Th–Pb isotope ratios were calculated using GLITTER 4.0 GEMOC software [16]. Corrections for common lead were made using the ComPb program [17]. Calculation of concordant ages (Concordia Ages) was performed using IsoplotR software. When constructing histograms, relative probability distribution curves of ages, and calculating peak ages (Peak Ages) [18], only concordant age estimates (D</5/) were taken into account (Analysts V. S. Chervyakovsky, M. V. Chervyakovskaya). The results of isotopic studies are presented in the supplementary materials to the article (Suppl. Table 1).

Detrital zircon is represented predominantly by large (600–200 μm) slightly rounded grains and unrounded crystals, with short- and long-prismatic habits ($K_{el}$ = 0.5–2 and 3–5, respectively) (Fig. 2).

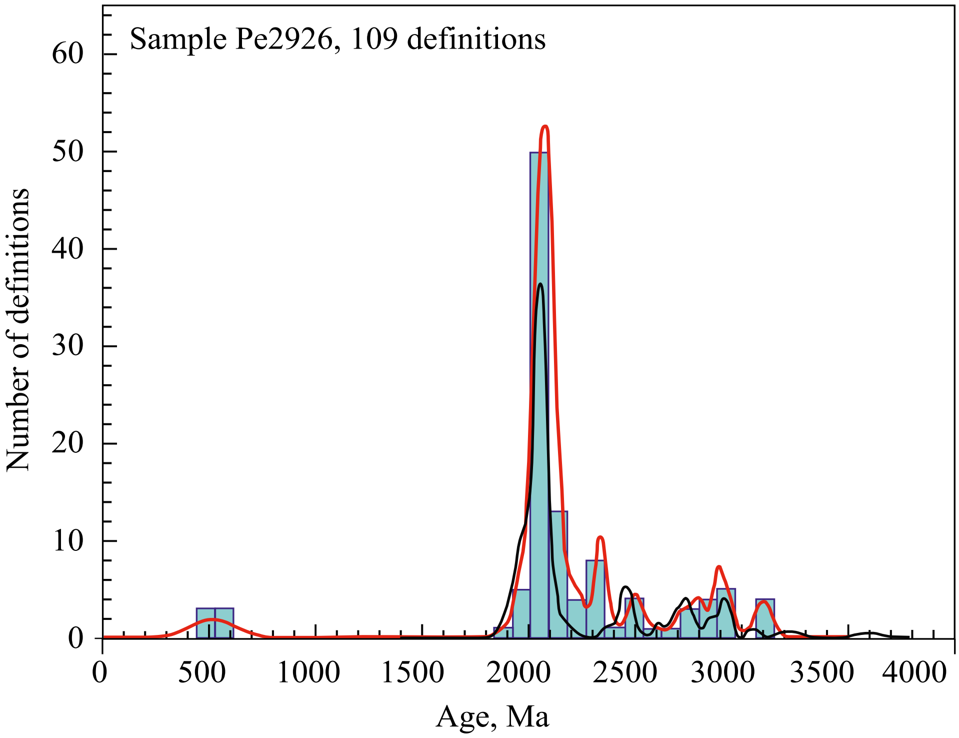

**Fig.** 3. Histogram of distribution and relative probability curve (red line) of detrital zircon ages from Quaternary deposits of the Ufaley block ( n =109). Black line is the relative probability curve of detrital zircon age distribution from sandstones of the Ai Formation of the Riphean [19].

Reddish-brown and dark tea-colored grains strongly predominate; pink and pale yellow individuals are also found. Prism faces {100}, {110} and dipyramid {111} are developed. The internal structure of most grains is characterized by cores surrounded by zonal shells. Inclusions of quartz, potassium feldspar, apatite, phlogopite, monazite, and rutile are found in the zircon.

176 zircon grains were used for isotope-geochronological studies, from which 253 age estimates were obtained from cores and shells. 109 of them are concordant (D</5/), and 22 are sub-concordant (5%<D<10%). The relative probability curve of age distribution shows a main peak at 2100–2000 Ma, which includes about 30% of all determinations, and several weakly expressed peaks in the range of 3200–2500 Ma (Fig. 3). Individual zircon grains have ages of 570–485 million years, corresponding to the time of metamorphism in the UB, synchronous with the Timanian orogeny in the Urals [1, 7]. It should be noted that among the studied zircon grains, there are no samples with ages of 1650–1400 Ma, previously established in pyroxenites of SH [11]. This may be due to low zircon content in ultramafic rocks and the flotation size (less than 50–60 μm) of its grains, which prevents accumulation in sedimentary rocks.

Thus, in the Quaternary deposits from the tectonic fragment in the western part of the UB, where clinopyroxenites of Precambrian age occur among the amphibolite-gneiss strata, detrital zircon with an age of 2100–2000 Ma predominates. This interval corresponds to the time of granulite metamorphism and migmatization in the Taratash and Alexandrovsky blocks, the rocks of which served as a source of detrital zircon for sandstones at the base of the Ai Formation of the Riphean [4, 5, 19]. In our case, the transport distance was insignificant, and the source of clastic material is predominantly the rocks of the UB directly surrounding the clinopyroxenites of the Shigir Hills. The obtained results suggest that the structure of the UB contains metamorphic rocks of Early Precambrian age, which had not been previously established. The presence of Proterozoic clinopyroxenites here enhances the similarity in geological structure and evolution of the Ufaley block with the Taratash and Alexandrovsky fragments of the East European Platform, exposed in the structures of the folded Urals.

## ACKNOWLEDGEMENTS

The authors are grateful to the reviewer, Corresponding Member of the Russian Academy of Sciences N.B. Kuznetsov, for comments that helped improve the manuscript.

## FUNDING

The research was carried out using funds from the Russian Science Foundation, grant No. 23-17-00224. https://rscf.ru/project/23-17-00224.

## REFERENCES

1. *Puchkov V.N.* Geology of the Urals and Cis-Urals (current issues of stratigraphy, tectonics, geodynamics and metallogeny). Ufa: DesignPoligrafService, 2010. 280 p.
2. *Echtler H.P., Ivanov K.S., Ronkin Y.L., Karsten L.A., Hetzel R., Noskov A.G.* The tectono-metamorphic evolution of gneiss complexes in the Middle Urals, Russia: a reapprisal // Tectonophysics. 1997. V. 276. No. 1–4. Pp. 229–251.
3. *Sindern S., Ronkin Yu.L., Hetzel R., Schulte B.A., Kramm U., Maslov A.V., Lepikhina O.P., Popova O.Yu.* Taratash and Alexandrovsky metamorphic complexes (Southern Urals): P-T constraints // Yearbook-2005. Yekaterinburg: IGG UB RAS, 2006. Pp. 322–330.
4. *Tevelev Al.V., Kosheleva I.A., Tevelev Ark.V., Khotylev A.O., Moseychuk V.M., Petrov V.I.* New data on the isotopic age of the Taratash and Alexandrovsky metamorphic complexes // Moscow University Bulletin. 2015. Series 4. Geology. No. 1. Pp. 27–42.
5. *Ronkin Yu.L., Sindern S., Lepikhina O.P.* Isotope geology of the oldest formations of the Southern Urals // Lithosphere. 2012. No. 5. Pp. 50–76.
6. *Krasnobaev A.A., Rusin A.I., Busharina S.V., Cherednichenko N.V., Davydov V.A.* Composition, zircons and zircon geochronology of metamorphites of the Ufaley complex // Yekaterinburg: IGG UB RAS, 2010. Proc. IGG UB RAS. Issue 157. Pp. 273–279.
7. *Shardakova G.Yu.* Granitoids of the Ufaley block: geodynamic settings, age, sources, problems // Lithosphere, 2016. No. 4. Pp. 133–137.
8. *Belkovsky A.I.* Geology and mineralogy of quartz veins of the Kyshtym deposit (Middle Urals). Miass: IMIN UB RAS, 2011. 234 p.
9. State Geological Map of the Russian Federation, scale 1:200,000. Second edition. South Ural Series. Sheet N-41-I (Kyshtym). Explanatory note/ N.S. Kuznetsov, B.A. Puzhakov, V.D. Shokh et al.; Ministry of Natural Resources of Russia, Rosnedra, Chelyabinsknedra, JSC “Chelyabinsgeosyomka”. M.: Moscow Branch of FSBI “VSEGEI”, 2021. 181 p.
10. *Pushkarev E.V., Ryazantsev A.V., Gottman I.A. Degtyarev K.E., Kamenetsky V. S.* Ankaramites – a new type of magnesian, high-calcium primitive melts in the Magnitogorsk island-arc zone in the Southern Urals. // DAN. 2018. Vol. 479. No. 4. Pp. 433–437.
11. *Krasnobaev A.A., Pushkarev E.V., Busharina S.V., Gottman I.A.* Zirconology of clinopyroxenites of Shigir hills (Ufaley complex, Southern Urals) // DAN, 2013. Vol. 450. No. 5. Pp. 586–591.
12. *Pystin A.M., Pystina S.N., Lennykh V.I.* Changes in the chemical and mineral composition of gabbroids during metamorphism (western slope of the Southern Urals) // Alkaline, basic and ultrabasic complexes of the Urals. Sverdlovsk: USC AS USSR, 1976. Pp. 41–54.
13. *Krasnobaev A.A., Puchkov V.N., Busharina S.V., Kozlov V.I., Presnyakov S.L.* Zirconology of izrandites (Southern Urals) // DAN. 2011. Vol. 439. No. 3. Pp. 394–398.
14. *Jackson S.E., Pearson N.J., Griffin W.L., Belousova E.A.* The application of laser ablation-inductively coupled plasma-mass spectrometry to in situ U–Pb zircon geochronology // Chemical Geology. 2004. V. 211(1–2). Pp. 47–69.
15. *Horstwood M.S.A., Košler J., Gehrels G. et al.* Community-Derived Standards for LA-ICP-MS U-(Th-)Pb Geochronology Uncertainty Propagation, Age Interpretation and Data Reporting // Geostandards and Geoanalytical Research. 2016. V. 40. No. 3. Pp. 311–332.
16. *Van AchterberghE., Ryan C.G., Jackson S.E., Griffin W.L.* LA-ICP-MS in the Earth Science – Appendix 3, data reduction software for LA-ICP-MS / Ed. P.J. Sylvester) // Mineral. Assoc. Canada. Short Course. 2001. V. 29. Pp. 239–243.
17. *Andersen T.* Correction of common lead in U-Pb analyses that do not report 204Pb // Chemical Geology. 2002. V.192. No. 1–2. Pp. 59–79.
18. *Gehrels G . E .* / In: Tectonics of Sedimentary Basins: Recent Advances. Chichester: Wiley/Blackwell, 2012. Pp. 47–62.
19. *Kuznetsov N.B., Maslov A.V., Belousova E.A., Romanyuk T.V., Krupenin M.T., Gorozhanin V.M., Gorozhanina E.M., Seregina E.S., Tselmovich V.A.* First results of U-Pb LA-ICP-MS isotope dating of detrital zircons from the basal levels of the Riphean stratotype // Doklady Earth Sciences. 2013. Vol. 451. No. 3. Pp. 308–313.

*DOKLADY EARTH SCIENCES, 2025, Vol. 520, No. 1, pp. 8–13*

## GEOLOGY

# FIRST DATA ON THE AGE OF ZIRCON GRAINS FROM THE UPPER MESOZOIC LESKOVO UNIT OF THE UNDO-DAYA DEPRESSION OF EASTERN TRANSBAIKALIA

© 2025 **I. N. Kosenko**[a, *], **V. D. Efremenko**[a], **E. K. Metelkin**[a], **O. S. Dzyuba**[a],
**Corresponding Member of RAS B. N. Shurygin**[a], **P. D. Kotler**[b, c], **A. V. Kulikova**[b, c],
**and A. E. Igolnikov**[a]

Received July 05, 2024
Revised September 01, 2024
Accepted September 09, 2024

**Abstract.** The results of the determination of the age of zircon grains from tuffites of the Leskovo Unit of the Unda-Daya Basin, Eastern Transbaikalia, are presented for the first time. The age of the youngest population of zircon grains is 145.8±3.8 Ma, approximately corresponding to the Jurassic–Cretaceous boundary and indicating the Early Cretaceous age of most of the Leskovo Unit. Given that the similar taxonomic composition of ostracods from the middle part of the Leskovo Unit and the Valanginian–Lower Hauterivian Dabeigou Formation of northeastern China, our U–Pb age from the lower part of the Leskovo Unit allows confident correlations of these lithostratons.

**Keywords :** *Lower Cretaceous, Transbaikalia, U–Pb age of zircon grains, Jehol Biota*

**DOI**: 10.31857/S26867397250102e6

Continental Upper Mesozoic deposits are widely distributed throughout Transbaikalia. They are confined to numerous depressions and are characterized by diverse facies composition and genesis. Despite a long history of study, the age of many strata remains a subject of discussion.

The new wave of interest in the continental Mesozoic of Transbaikalia is associated with the discovery of uniquely preserved vertebrate remains, including pterosaurs, feathered dinosaurs, birds, and mammals, in the deposits of the Jehol Group in northeastern China (Jehol biota) [1]. The core of this biota consists of an assemblage of organisms including the conchostracans *Eosestheria*, insects *Ephemeropsis* and bony fishes *Lycoptera*, widely distributed in the Lower Cretaceous deposits beyond northeastern China, including Transbaikalia [2-4]. Three evolutionary phases have been established in the development of the Jehol biota, successively replacing each other [5, 6]. To date, the age of strata containing the remains of organisms belonging to all three evolutionary phases of the Jehol biota has been established with high precision, thanks to numerous isotopic dating, which allows the continental Lower Cretaceous sections of northeastern China to be used as references for clarifying the age and correlation of the continental Lower Cretaceous of eastern Asia.

The area of localities with assemblages of organism remains characterizing the early phase of the Jehol biota evolution is the most limited compared to the middle and late phases, and covers a narrow region extending northward from the northern part of China's Hebei Province to Eastern Transbaikalia. Questions concerning the origin, paleogeographic distribution, and migration routes of organisms belonging to this evolutionary phase remain the least studied.

In Transbaikalia, several localities with fauna identified with the early phase of the Jehol biota evolution are known. Conchostracans *Keratestheria* are known from the Utan locality in the Olov Depression, *Nestoria* from the Ust-Kara Formation in the Ust-Kara Depression, where they occur together with conchostracans *Defretinia* [7, 8]. In southeastern Transbaikalia, between the Upper Jurassic Undino-Daya series and the overlying

---

[a] *Trofimuk Institute of Petroleum Geology and Geophysics, Siberian Branch of the Russian Academy of Sciences, Novosibirsk, Russia*
[b] *Sobolev Institute of Geology and Mineralogy, Siberian Branch of the Russian Academy of Sciences, Novosibirsk, Russia*
[c] *Kazan Federal University, Kazan, Russia*
**e-mail: KosenkoIN@ipgg.sbras.ru*

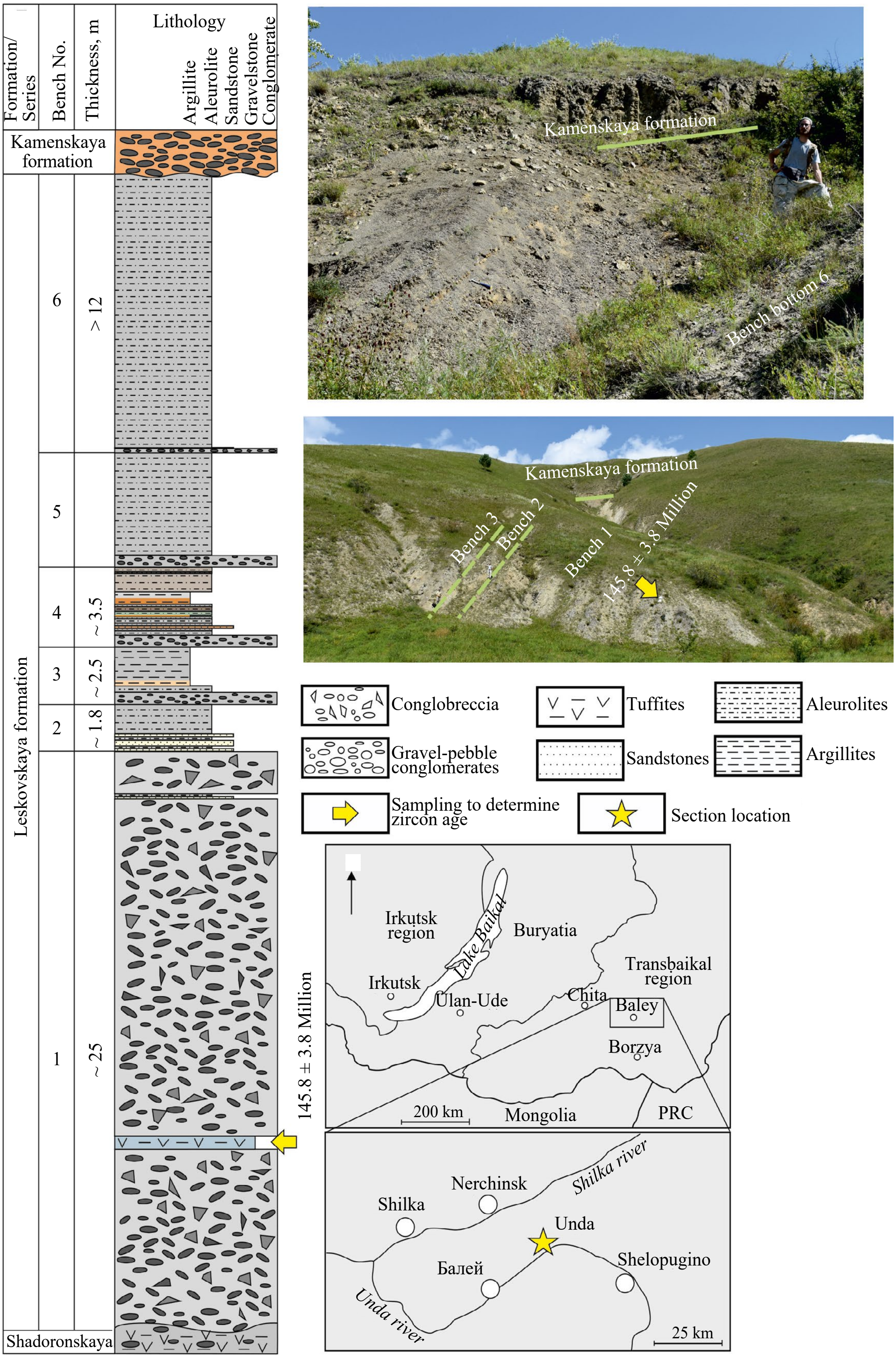

**Fig. 1.** Location, general view, and lithological column of the Leskovo sequence section near the village of Unda.

Lower Cretaceous Turga Formation, a so-called transitional Ust-Kara (Defretinian) horizon (characterized by conchostracans *Defretinia*) is recognized [8]. One of the few sections in which this horizon can be traced is the well-accessible and fauna-characterized section of the Leskovskaya strata near the village of Unda.

The "Unda" section is located on the right bank of the Unda River, 500 m upstream from the village of Unda, in a narrow steep ravine and on its western side on the southern slope of Mount Malaya Berezovaya [7, 9] (Fig. 1). Tectonically, the section is confined to the Leskovo graben, superimposed on the Unda-Daya depression. The Leskovo sequence, about 50 m thick, lies with angular unconformity on the volcanogenic-sedimentary rocks of the Middle-Upper Jurassic Shadoron series [9]. The basal member of the Leskovskaya sequence is represented by conglobreccias with rare thin interlayers of sandstones and siltstones, with a thickness of about 25 m. At 8 m from the base of the member, we discovered a tuffite layer about 0.5 m thick, from which a sample was taken to determine the absolute age of zircon grains. The middle and upper parts of the section (members 2–6) are composed predominantly of siltstones and mudstones. At the base of each member lie conglomerates or sandstones (Fig. 1). The Leskovo sequence is overlain with angular unconformity by conglomerates of the Lower Cretaceous Kamenskaya sequence.

## VIEWS ON THE AGE OF THE LESKOVO SEQUENCE

The Leskovo sequence is most completely represented in the "Unda" section. There are different perspectives on its age. G.G. Martinson [10] attributed the Leskovo sequence to the Unda-Baley Formation, which he considered younger than the Turga Formation. A.N. Oleynikov [7] attributed the Leskovo sequence to the Baley Formation, which, according to his stratigraphic scheme of Transbaikalia, is also younger than the Turga Formation and corresponds to the upper part of the Lower Cretaceous. In the regional stratigraphic scheme of the Cretaceous deposits of Transbaikalia, the Leskovo sequence is considered as part of the Dain Formation, which belongs to the upper part of the Turga Horizon [11]. On modern geological maps, this sequence is attributed to the Turga Formation, the age of which is accepted as Berriasian-Barremian [12].

The most complete list of paleontological remains found in the "Unda" section is provided by S.M. Sinitsa [9]. From the basal horizon (corresponding to packages 1–4 in Fig. 1), the ostracods *Daurina* and " *Torinina"*, gastropods *Radix* and conchostracans *Defretinia* are indicated. In the overlying siltstones, insect remains are numerous, and among the stratigraphically important fossils are taxa characteristic of the Turga Formation: conchostracans *Eosestheria* (= *Bairdestheria*) *middendorfii* (Jones, 1862), fish *Lycoptera middendorfii* Müller, 1847, insects *Ephemeropsis trisetalis* Eichwald, 1864, plants *Pseudolarix*. It is concluded that the upper part of the section corresponds to the Turga Formation, while the lower part of the section, based on the presence of conchostracans *Defretinia*, belongs to the Ust-Kara transitional horizon [8, 9]. The authors of this article, during the investigation of the "Unda" section, did not find conchostracans *Eosestheria* , insects *Ephemeropsis* , and fish *Lycoptera* , which are characteristic of the Turga Formation fossil assemblages.

Data on ostracods from the Lower Cretaceous of northeastern China show that the species *Ocrocypris obesa* (Pang et al., 1984) from the Dabeigou Formation is very similar to the Transbaikalian species *Ocrocypris* (= *Torinina* ) *tersa* (Sinitsa, 1992) [13]. In the fossil assemblage from the Dabeigou Formation, which characterizes the early phase of the Jehol biota evolution [6], ostracods of the genus *Daurina* are characteristic, also described from the Leskovo sequence [8]. In the "Unda" section, according to S.M. Sinitsa [8, 9], conchostracans *Defretinia* were found, which occur together with conchostracans *Nestoria* in the section of the Ust-Kara Formation in the Ust-Kara depression [8].

It can be concluded that at least the middle part of the Leskovo sequence, which lies on basal conglomeratic breccia and is characterized by ostracods *Daurina* and *Ocrocypris*, can be correlated with the Dabeigou Formation in northeastern China, the age of which is dated within the Valanginian-early Hauterivian range [13]. Evidence supporting this correlation is the results of the first study of the absolute age of zircon grains from tuffites confined to the lower part of this sequence, which are discussed in this paper.

## METHODOLOGY FOR DETERMINING THE ABSOLUTE AGE OF ZIRCON GRAINS FROM TUFFITES OF THE LESKOVO SEQUENCE

For U-Pb dating of zircon grains, a laser ablation system based on an excimer laser (wavelength 193 nm) Analyte Excite ("Teledyne

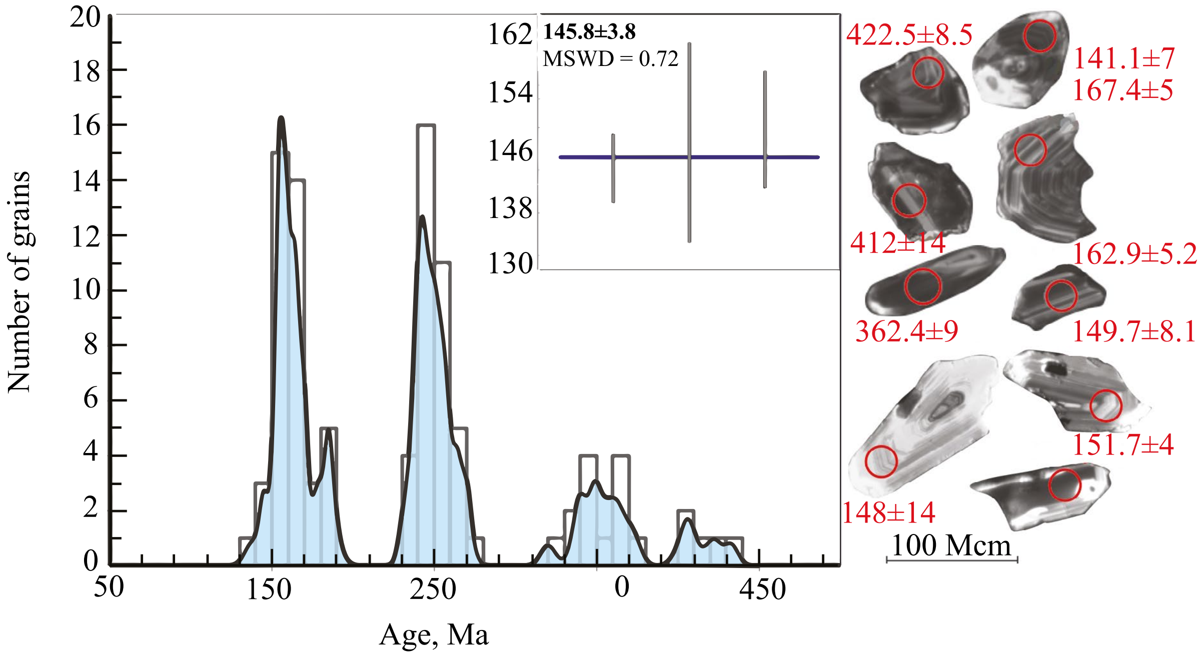

**Fig. 2.** Results of U-Pb dating of zircon grains from tuffites in the lower part of the Leskovo sequence section near the village of Unda.

Cetac Technologies") connected to a quadrupole mass spectrometer with inductively coupled plasma ionization "ThermoScientific" iCAP Q at the Geothermochronology Center of Kazan Federal University (KFU) was used. The diameter of the laser beam was 35 μm, the pulse repetition frequency was 5 Hz, and the laser energy density was 3.0 J/cm$^2$. Reference samples of zircon grains were used for analysis: 91500 as a control sample (1065 Ma) and Plešovice as an external standard (337 Ma). At the beginning, middle, and end of the measurement session, standard synthetic glass NIST SRM 612 was additionally measured to account for the mass spectrometer sensitivity. Processing of mass spectrometric data, accounting for corrections, selection of the optimal signal segment, calculation of isotopic ratios and corresponding ages were carried out using Iolite 3.65 software integrated into Igor Pro 7. Calculation of weighted average age values based on isotopic ratios, plotting concordia diagrams were performed in Microsoft Excel with the integrated Isoplot 4.15 package. For discordance calculation, the formulas $D = 100^*(\mathrm{Age}(^{207}\mathrm{Pb}/^{235}\mathrm{U})/\mathrm{Age}(^{206}\mathrm{Pb}/^{238}\mathrm{U}) - 1)$ were used. Measurements where discordance < –5% or >5% were excluded from the sample.

## RESEARCH RESULTS

In the Unda-1 sample, 131 zircon grains were analyzed, of which 96 zircon grain ages fell within the discordance interval from –5% to 5%. The sample is dominated by zircon grains with oscillatory zoning, less frequently with banded zoning (Fig. 2). Some grains show secondary, younger crystal growth zones and recrystallization. The Th/U ratio in all analyzed zircon grains is greater than 0.1, which is characteristic of zircon grains from igneous rocks.

For constructing the relative probability histogram, the ratio $^{206}\mathrm{Pb}/^{238}\mathrm{U}$ was used. Within the studied sample, four populations of zircon grains are distinguished, with a characteristic feature being an increase in the proportion of zircon grains from older to younger ones. The oldest population of zircon grains is represented by five grains with Silurian-Early Devonian age (433–403 Ma) (here and below according to [14]). The next population of 12 grains has an age range of 373–339 Ma, suggesting the involvement of Late Devonian-Early Carboniferous source areas. The Middle Permian-Middle Triassic population contains 37 grains with an age range of 271–237 Ma. The largest and youngest population of 41 grains has an age range of 187–144 Ma (Early-Late Jurassic up to the boundary with the Cretaceous). The age of the youngest population, determined by the weighted average age of the three youngest zircon grains, has a value of 145.8±3.8 Ma (MSWD = 0.72), which approximately corresponds to the Jurassic-Cretaceous boundary.

## DISCUSSION OF RESULTS

Potential sources of detrital zircon grains for the oldest cluster of Early Paleozoic age may be rocks of the Olyokma granodiorite-granite complex, which are exposed in the Unda and Urulga river basins in close proximity to the location of the "Unda" section. The age of the Olyokma complex granitoids was determined by the Rb-Sr method as 438±39 Ma [12], which, within the margin of error, corresponds to the age of the oldest population of zircon grains in the dated sample. It should also be considered that zircon grains of this age may be present in the rocks of the Aginsk-Borshchovochny dynamometamorphic complex of the Middle Paleozoic, for which the older rocks of the Olyokma complex likely served as a protolith.

The probable source material for the Late Devonian-Early Carboniferous cluster of zircon grains could be rocks of the Alenui granodiorite-rhyolite complex, which formed volcanic cover structures in the eastern part (Gazimur block) of the Argun terrane. The age of the Alenui complex rocks is accepted as Early-Middle Carboniferous [12].

The source of detritus for the large cluster of Permian-Triassic zircon grains is most likely the rocks of the Unda granodiorite-granite complex, which is widely distributed within the study area. The age of the Unda complex granitoids, according to Rb-Sr isochron dating, is 275-250 Ma [15], and according to U-Pb dating – 254-249 Ma [16]. The geodynamic nature of the Unda complex rocks is currently under discussion.

The youngest cluster of zircon grains in the studied tuffite has a Mesozoic age. Within the Argun terrane, granitoid complexes of Jurassic-Cretaceous age are widely developed: Borshchovochny, Shakhtaminsky, Amudzhikano-Sretensky (163–142 Ma) [17, 18], associated with the intraplate stage of the region's development. Also, most likely, a significant portion of the Mesozoic zircon grains in the dated sample are the indigenous zircon grains of the volcanic rocks of the Leskovo strata. The obtained age of the youngest population in the sample (145.8±3.8 Ma) implies that the formation of the dated volcanogenic-sedimentary rocks occurred no earlier than the Tithonian age of the Late Jurassic.

The new data obtained on the age of zircon grains from tuffites in the lower part of the Leskovo strata section allow us to conclude that most of the section is of Early Cretaceous age, although a Late Jurassic age for the basal conglomeratic breccias cannot be excluded. The presence of ostracods *Daurina* and *Ocrocypris*, typical taxa of the Luangpingella–Ocrocypris–Eoparacypris ostracod zone identified in the Dabeigou Formation in northeastern China, suggests a Valanginian-Early Hauterivian age for the middle part of the Leskovo strata and allows correlation with the Dabeigou Formation. The presence of ostracods *Daurina* and *Ocrocypris*, conchostracans *Nesthoria* and *Keratestheria* in the sections of strata united in the Ust-Kara horizon is evidence that the range of organisms belonging to the early phase of the Jehol biota evolution extended northward as far as Eastern Transbaikalia. This allows us to consider the territory of Eastern Transbaikalia together with northeastern China as the center of origin of the Jehol biota, from where its subsequent dispersal occurred.

## FUNDING

The study was supported by the Russian Science Foundation grant No. 22-17-00228, https://rscf.ru/project/22-17-00228/, based on the A.A. Trofimuk Institute of Petroleum Geology and Geophysics, SB RAS with scientific and methodological support of FSR FWZZ-2022-0004.

## REFERENCES

1. The Jehol Fossils: The emergence of feathered dinosaurs, beaked birds and flowering plants. Chang M.-M., Chen P.-J., Wang Y., Wang Y.-Q. (eds.). Beijing: Academic Press, 2008. 208 p.
2. *Sinitsa S.M., Reshetova S.A., Vilmova E.S.* Classical sections of the Turga Formation of Transbaikalia as a possible analogue of the Yixian dinosaur formation in Liaoning Province, China // Bulletin of ZabGU. 2016. Vol. 22. No. 11. Pp. 24-41.
3. *Kosenko I.N., Peshchevitskaya E.B., Efremenko V.D. et al.* Turga Lagerstätte (Middendorf outcrop, Eastern Transbaikalia, Barremian-Aptian): stratigraphic position and paleoenvironments // Geology and Geophysics. Vol. 64. No. 11. Pp. 1628-1653.
4. *Bugdaeva E.V., Golovneva L.B.* Siberian Jehol Biota / Cretaceous Project 200. Hart M.B., Batenburg S.J., Huber B.T., et al. (eds.). Volume 2: Regional Studies. Geol. Soc. London Spec. Publ. 2024. V. 545.
5. *Zhou Z., Meng Q., Zhu R., Wang M.* Spatiotemporal evolution of the Jehol Biota: Responses to the North

China craton destruction in the Early Cretaceous // PNAS. 2021. V. 118. No. 34. e2107859118.

6. *Qin Z., Xi D., Wagreich M. et al.* Living environment of the early Jehol Biota: A case study from the Lower Cretaceous Dabeigou Formation, Luanping Basin (North China) // Cretaceous Res. 2021. V. 124. 104833.
7. *Oleynikov A.N.* Stratigraphy and phyllopods of Jurassic and Cretaceous of Eastern Transbaikalia. Moscow: Nedra, 1975. 171 p.
8. *Sinitsa S.M.* Transitional horizons in the stratigraphy of the Upper Mesozoic of Transbaikalia // Bulletin of Chita State University. 2011. No. 3 (70). Pp. 98–103.
9. *Sinitsa S.M., Vilmova E.S., Yurgenson G.A. et al.* Geological monuments of Transbaikalia: cadastre of stratigraphic and paleontological geological natural monuments. Novosibirsk: Nauka, 2014. 312 p.
10. *Martinson G.G.* Mesozoic and Cenozoic mollusks of continental deposits of the Siberian Platform, Transbaikalia and Mongolia. Moscow-Leningrad: Publishing House of the USSR Academy of Sciences, 1961. 358 p.
11. Decisions of the 4th Interdepartmental Regional Stratigraphic Meeting on the Precambrian and Phanerozoic of the South of the Far East and Eastern Transbaikalia (Khabarovsk, 1990). Turbin M.T., Bazhanov V.A., Belyaeva G.V. et al. (eds.). Khabarovsk: KHGGGP, 1994. 124 p., 38 schemes.
12. State Geological Map of the Russian Federation. Scale 1:1000000 (third generation). Sheet M-50 — Borzya. Explanatory note. St. Petersburg: Cartographic Factory VSEGEI, 2010. 553 p.
13. *Qin Z., Xi D., Shi Z., Wan X.* Ostracod biostratigraphy of Lower Cretaceous lacustrine sequences in northern Hebei, North China: A revision // Cretaceous Res. 2023. V. 141. 105340.
14. *Cohen K.M., Finney S.C., Gibbard P.L., Fan J.-X.* The ICS International Chronostratigraphic Chart // Episodes. 2013 (updated, v2023/09). V. 36. Pp. 199-204.
15. *Kozlov V.D., Efremov S.V., Dril S.I., Sandimirova G.P.* Geochemistry, isotopic geochronology, and genesis of the Verkhnyaya Unda granitoid batolith // Geochemistry International. 2003. V. 41. No. 4. Pp. 364—378.
16. *Dril S.I., Noskova Yu.V., Wang K.-L. et al.* Geochronology and Sr-Nd isotope geochemistry of Late Paleozoic collisional granitoids of Undinsky complex (Eastern Transbaikal region) // Geodynamics & Tectonophysics. 2017. V. 8 (3). Pp. 455—459.
17. *Nevolko P.A., Svetlitskaya T.V., Savichev A.A. et al.* Uranium-Pb zircon ages, whole-rock and zircon mineral geochemistry as indicators for magmatic fertility and porphyry Cu-Mo-Au mineralization at the Bystrinsky and Shakhtama deposits, Eastern Transbaikalia, Russia // Ore Geol. Rev. 2021. V. 139. Pt B. 104532.
18. *Naryzhnova A.V., Khromykh S.V., Kruk N.N., Kotler P.D.* New geochronological and isotopic data on Mesozoic granitoids of Eastern Transbaikalia // RAN Reports. Earth Sciences. 2023. V. 510. No.2. Pp. 181–188.

*DOKLADY EARTH SCIENCES, 2025, Vol. 520, No. 1, pp. 14–28*

## GEOLOGY

# ISOTOPIC U-Pb-SHRIMP DATING OF MUGODZHARI ECLOGITES (KAZAKHSTAN)

**© 2025 K. S. Ivanov[a], V. S. Ponomarev[a], *,**
**Corresponding Member of RAS V. N. Puchkov[a], and D. A. Khanin[b]**

Received August 19, 2024
Revised September 10, 2024
Accepted September 16, 2024

**Abstract.** In the extreme south of the Urals, zircons from eclogites and amphibolite were dated in metamorphites of the East Mugodzhar zone. Of the 4 eclogite samples, close (and the most "ancient" – 520±4 Ma) concordant age values were obtained in 3 samples, which probably corresponds to the age of the protolith. Concordant dates of 472±3 Ma and 379±3 Ma reflect the time of the main stages of metamorphism of the East Mugodzhari, the more ancient relate to high-pressure, and the latter to amphibolite facies metamorphism. The presence of ancient and at the same time different-aged zircons, probably with traces of rounding, indicates the primary sedimentary nature of the studied amphibolites. The youngest zircons from the Mugodzhar eclogites have an age of 282±2 Ma, corresponding to the collision stage. The obtained data show that the Mugodzhar metamorphic complexes are not Early Proterozoic or Riphean formations (as was previously believed), but represent Lower-Middle Paleozoic complexes of the middle part of the earth's crust. That is, these metamorphites by their nature are fragments of the deep part of the island-arc system of the eastern sector of the Urals, which were later brought to a near-surface level during the rise and erosion of individual regions of the Urals.

**Keywords :** *eclogite, amphibolite, zircon, U–Pb age, Mugodzhary, Urals, Kazakhstan*

**DOI**: 10.31857/S26867397250103e1

The eclogites of the Eastern Mugodzhary are located in the southernmost part of the Ural fold belt, in Kazakhstan. Here, in the western part of the East Mugodzhari zone, the Taldyk sialic block is located (Fig. 1), which contacts along faults with the basic volcanics of the West Mugodzhari zone of the Magnitogorsk megazone to the west, and with the Balkymbai near-strike graben to the east. The Taldyk block is composed of metamorphic rocks predominantly of amphibolite facies, which host massifs of granites, granodiorites, and others. Among the metamorphites, the Taldyk and South Mugodzhari series are usually distinguished, subdivided into several strata [2, 10, 13], which include mainly mica gneisses, crystalline schists with kyanite and garnet, interlayers of quartzites, amphibolites, amphibole gneisses, often migmatized, and others. The metamorphism of these strata at the progressive stage corresponded to the high-temperature ($T$ =680–720°C; $P$ =7–8.5 kbar), and at the regressive stage to the low-temperature ($T$ =580–630°C; $P$ =5.5–6.5 kbar) zones of amphibolite facies [4, 14]. The age of the metamorphic strata of the Taldyk block has been the subject of lengthy discussion. They were usually considered Early Proterozoic ([13] et al.), opinions about their Riphean [2, 4] or Early-Middle Paleozoic age [5] were also expressed. However, there have been practically no modern geochronological studies here, and the data [8, 9], unfortunately, were not linked to the geology of the region. Within the Taldyk block, high-pressure rocks such as two-mica kyanite-garnet schists (among which there are kyanite deposits), eclogites and eclogite-like rocks have been described [1, 13, 15]. The Mugodzhari eclogites are usually divided into two complexes – Tulepsay and Kitarsay [4, 13, 14, 16]. The Kitarsay complex (eclogite-peridotite ophiolite association) consists of numerous small bodies confined to a linear zone of northeast strike

---

[a] *Zavaritsky Institute of Geology and Geochemistry, Ural Branch of the Russian Academy of Sciences, Ekaterinburg, Russian Federation*
[b] *Korzhinskii Institute of Experimental Mineralogy, Russian Academy of Sciences, Chernogolovka, Russian Federation*
**e-mail: p123v@yandex.ru*

(Bugetysay fault), traced for 25 km. This zone has a thickness of up to 1 km and is composed mainly of quartz-feldspar blastomylonites of staurolite facies. The bodies (boudins, lenses) of the Kitarsay eclogite-peridotite association are located on the left bank of the Uly-Taldyk River (Fig.1), they range in size from several meters to the first hundreds of meters. Usually they are composed of serpentinites, which contain inclusions of garnet serpentinites, websterites, eclogites, eclogite-like rocks, garnetites, and garnet amphibolites. Temperatures calculated for metabasic parageneses are 600–850°C and higher, and pressures are estimated as 7–14 kbar [13]. Eclogite and eclogite-symplectite bodies of the Tulepsai complex are located (Fig. 1) among amphibolites on the right bank of the Tulepsai River [4, 13]. Recently, A.V. Ryazantsev and colleagues obtained a U-Pb age (SHRIMP II) from zircons of 374–372 Ma and a U-Pb age from rutile of 360 Ma from eclogites of the Tulepsai complex. The date of 374 Ma is estimated [15] as the age of eclogite facies metamorphism (with maximum parameters $P = 15$ kbar, $T = 700–750^0$ C). These authors associate the date of 360 Ma with a later transformation of eclogites under decreasing pressure.

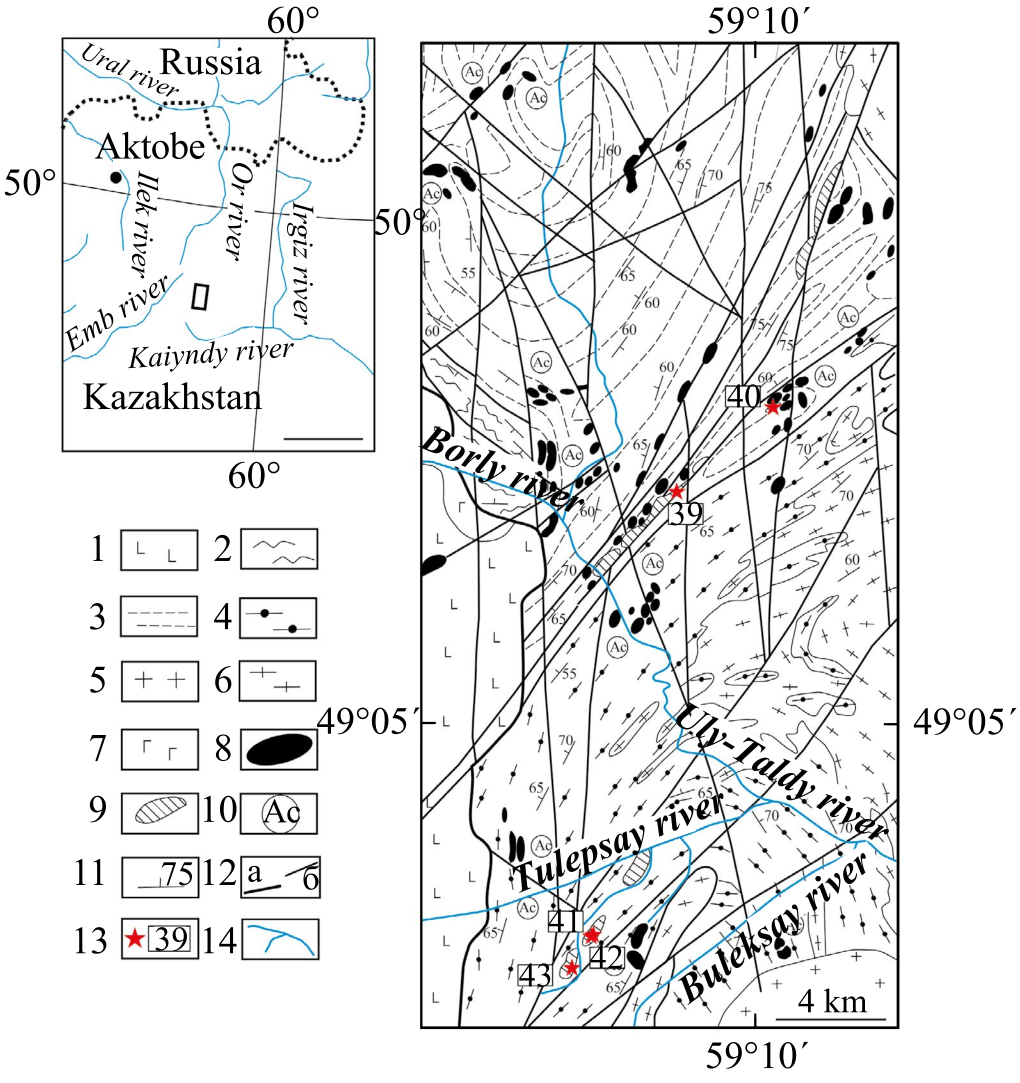

**Fig. 1.** Scheme of high-pressure and ultrabasic complexes distribution in the central part of the Taldyk sialic block of Mugodzhari (based on data from [1, 13, 16], with authors' modifications). 1 – basalts (D$_2$); 2–4 – metamorphites: quartz-phyllite series; 3 – gneiss-shale series; 4 – gneiss-amphibolite series; 5 – granites (C$_2$-P$_1$); 6 – plagiogneiss-granites (D); 7 – gabbro, gabbro-norites (D$_2$); 8 – ultrabasic rocks; 9 – eclogites and eclogite-like rocks; 10 – locations of asbestized ultrabasic rock bodies; 11 – elements of schistosity occurrence; 12 – faults: main (a), secondary (b); 13 – sampling locations for dating and their numbers; 14 – rivers and streams.

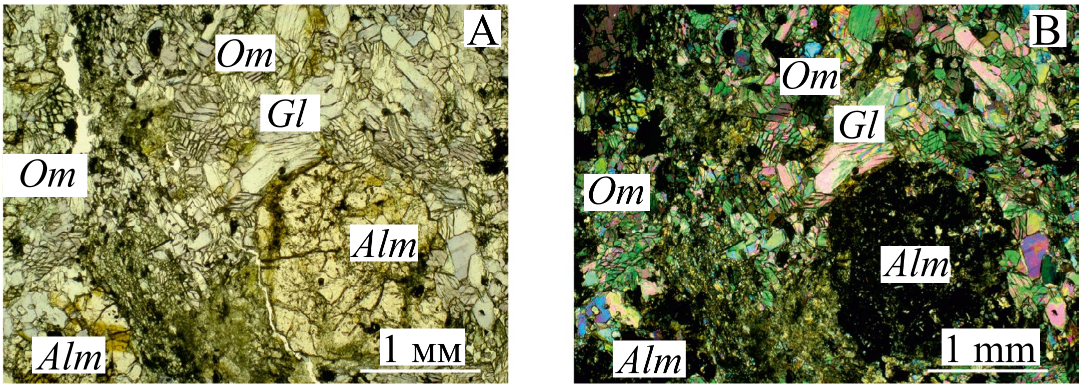

**Fig. 2.** Eclogite of the Tulepsay complex of the Eastern Mugodzhari (sample 41). In transmitted light (A), in polarized light (B). Alm – almandine, Om – omphacite, Gl – glaucophane.

For isotope-geochronological studies, 4 samples of eclogites and 1 sample of amphibolites were collected (see Fig. 1), each weighing more than 30 kg. The samples were taken from the central, least altered parts of boudin-shaped eclogite bodies exposed by trenches dug by the Priuralskaya team of PGO "Zapkazgeologiya" (team chief B.F. Ivanshin). Zircon separation was carried out according to standard methodology, including crushing the sample to a fraction < 0.4 mm, washing the crushed material in water to gray concentrate, magnetic separation, separation in heavy liquids, and manual selection of zircon grains under a binocular microscope. The size of the isolated zircons ranged from 100 to 350 μm. U-Th-Pb geochronological studies of zircons from eclogites were performed by A.N. Larionov on a SHRIMP-II secondary ion microprobe at the VSEGEI Research Center using the methodology described in [20]. The intensity of the primary beam of molecular negatively charged oxygen ions was ~2.5–4 nA, with a spot (crater) diameter of ~15 · 10 μm. Individual errors are given for the 1σ (%) interval, calculated ages – 2σ (Ma). The obtained data were processed using SQUID and ISOPLOT software [19].

## MATERIAL COMPOSITION OF ECLOGITES

The studied eclogites are represented by fine-grained to very fine-grained aggregate of glaucophane, omphacite, and almandine porphyroblasts (Fig. 2 A, B, sample 41). The rocks contain veins filled with omphacite, epidote, zoisite, clinozoisite, second-generation glaucophane, and albite. The rock structure varies from fine-grained to very fine-grained, porphyroblastic, granonematoblastic, with a massive texture. The main rock-forming minerals are omphacite, almandine, and glaucophane. Secondary minerals include: actinolite, zoisite, clinozoisite, calcite, paragonite, ferropargasite, ferro-edenite, clinochlore, chamosite, muscovite (phengite), quartz, rutile, titanite, fluorapatite, ilmenite, albite, pyrite, zircon, and allanite-(Ce). The chemical composition of minerals and their crystal-chemical recalculations are given in Appendix 1.

*Garnet* in eclogites forms metacrystals (up to 1 cm) with inclusions of omphacite, actinolite, ferropargasite, ferroedenite, glaucophane, ilmenite, titanite, rutile, and fluorapatite. In terms of chemical composition, the garnet corresponds to almandine

$Alm_{59.8-72.9}\,Prp_{9.28-17.8}\,Grs_{12.3-26.7}\,Sps_{0.4-2.0}\,And_{0-1.5}$. In almandine, a slight increase in MgO content and decrease in CaO from the center to the periphery of the crystals is observed. *Glaucophane* (up to 50% of the rock volume) is the main mineral of eclogites. Relict grains of omphacite, partially replaced by clinozoisite, titanite, and paragonite, are found in the glaucophane aggregate. The magnesium content of glaucophane ($Mg^{\#}$) is 0.64–0.73. *Omphacite* (20–30% of the rock volume) is represented by a fine-grained aggregate around almandine porphyroblasts. The jadeite minal content in omphacite ranges from 39 to 47%. In the omphacite-glaucophane aggregate, symplectites are found, the matrix of which is represented by albite ($Ab_{99}$) with actinolite inclusions. A fine-grained albite-clinochlore-chamosite aggregate with phengite is noted around large almandine porphyroblasts in the rocks. Zoisite in the rocks overgrows small elongated individuals of glaucophane. Some zoisite grains in the glaucophane-omphacite aggregate are replaced by clinozoisite at the periphery. Also, clinozoisite individuals are noted in the rocks,

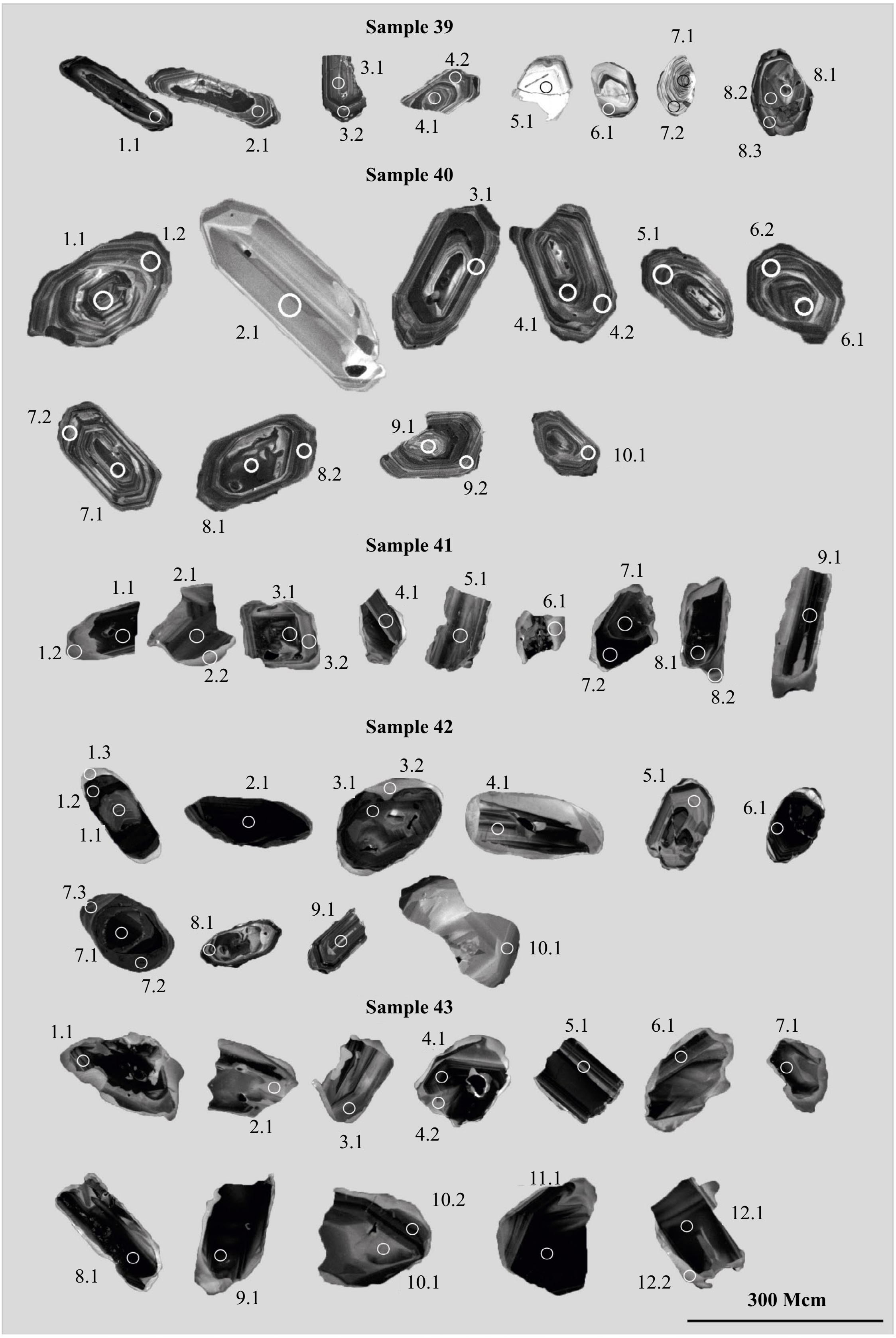

**Fig. 3.** Cathodoluminescence images of zircons from Eastern Mugodzhar eclogites, studied using SHRIMP II. (sample 42 – amphibolite). Circles show the location of measurement points, numbers correspond to analysis numbers in Table 1.

**Table 1**. U–Pb (SHRIMP II) isotopic data for zircons from Mugodzhari eclogites

| Analysis No. | $^{206}Pb_c$, % | U, ppm | Th, ppm | $^{206}Pb^*$, ppm | $^{232}Th/^{238}U$ | $^{207}Pb/^{235}U$, ±% | $^{206}Pb/^{238}U$, ±% | Rho | Age $^{206}Pb/^{238}U$, Ma |
|---|---|---|---|---|---|---|---|---|---|
| Sample 39 | | | | | | | | | |
| 1.1 | 0 | 262 | 215 | 17 | 0.85 | 0.618±2.3 | 0.07549±0.75 | 0.3 | 469.1± 3.4 |
| 2.1 | 0.15 | 456 | 221 | 29.9 | 0.5 | 0.621±1.9 | 0.07622±0.58 | 0.3 | 473.5± 2.6 |
| 3.1 | 0.19 | 324 | 122 | 21.4 | 0.39 | 0.585±2.5 | 0.07658±0.68 | 0.3 | 475.7± 3.1 |
| 3.2 | 0.49 | 973 | 372 | 63.4 | 0.39 | 0.591± 2 | 0.07544±0.44 | 0.2 | 468.9± 2 |
| 4.1 | 0.74 | 422 | 229 | 27.5 | 0.56 | 0.584±3.8 | 0.07526±0.75 | 0.2 | 467.7± 3.4 |
| 4.2 | 0 | 487 | 220 | 31.8 | 0.47 | 0.613±1.8 | 0.07596±0.56 | 0.3 | 472± 2.6 |
| 5.1 | 0.28 | 70 | 31 | 4.98 | 0.45 | 0.674±5.2 | 0.0826±1.4 | 0.3 | 511.5±6.7 |
| 6.1 | 0 | 223 | 82 | 16.1 | 0.38 | 0.684±2.7 | 0.08405±0.8 | 0.3 | 520.3±4 |
| 7.1 | 0 | 314 | 181 | 22.4 | 0.6 | 0.659±2.3 | 0.08318±0.69 | 0.3 | 515.1±3.4 |
| 7.2 | 0.2 | 105 | 54 | 7.51 | 0.53 | 0.671±4.3 | 0.08333±1.2 | 0.3 | 516±5.8 |
| 8.1 | 4.52 | 271 | 151 | 21.6 | 0.58 | 0.705±9.8 | 0.08815± 1 | 0.1 | 544.6± 5.3 |
| 8.2 | 0.15 | 353 | 222 | 23.3 | 0.65 | 0.584± 3 | 0.07678±0.68 | 0.2 | 476.9±3.1 |
| 8.3 | 0 | 453 | 61 | 24.8 | 0.14 | 0.528±2.3 | 0.06372±1.2 | 0.5 | 398.2± 4.7 |
| Sample 40 | | | | | | | | | |
| 1.1 | 5.99 | 740 | 987 | 29.8 | 1.38 | 0.315±9.1 | 0.04403±1.7 | 0.2 | 277.7±4.6 |
| 1.2 | 1.24 | 854 | 428 | 33.8 | 0.52 | 0.339±3.7 | 0.04551±1.1 | 0.3 | 286.9±3.1 |
| 2.1 | 0 | 144 | 197 | 5.68 | 1.41 | 0.323±4.1 | 0.04596±1.5 | 0.4 | 289.6±4.3 |
| 3.1 | 0.26 | 818 | 354 | 30.7 | 0.45 | 0.3142±2.6 | 0.04356±1.1 | 0.4 | 274.9±3 |
| 4.1 | 0.1 | 1079 | 465 | 41.7 | 0.45 | 0.3175±2.1 | 0.04497±1.1 | 0.5 | 283.6±3 |
| 4.2 | 0.06 | 1021 | 446 | 39.4 | 0.45 | 0.3251±2 | 0.04488±1.1 | 0.6 | 283±3.1 |
| 5.1 | 0.14 | 797 | 607 | 30.2 | 0.79 | 0.3085±2.4 | 0.04404±1.1 | 0.5 | 277.8±3 |
| 6.1 | 0 | 816 | 409 | 31.9 | 0.52 | 0.3265±2 | 0.04554±1.1 | 0.6 | 287.1±3.2 |
| 6.2 | 0.42 | 1098 | 815 | 42.2 | 0.77 | 0.3226±2.5 | 0.04452±1.1 | 0.4 | 280.8±2.9 |
| 7.1 | 3.39 | 1121 | 694 | 43.5 | 0.64 | 0.314±9.9 | 0.0436±1.2 | 0.1 | 275.1±3.2 |
| 7.2 | 7.55 | 979 | 1133 | 34.7 | 1.2 | 0.252±30 | 0.03817±1.6 | 0.1 | 241.5±3.8 |
| 8.1 | 0 | 2151 | 4080 | 83.8 | 1.96 | 0.3269±1.4 | 0.04532±1 | 0.7 | 285.7±2.9 |
| 8.2 | 0.73 | 675 | 344 | 25.5 | 0.53 | 0.318±3.8 | 0.04367±1.1 | 0.3 | 275.5±3.1 |
| 9.1 | 0.32 | 315 | 196 | 12.3 | 0.64 | 0.333±4.1 | 0.0453±1.3 | 0.3 | 285.6±3.6 |
| 9.2 | 0.27 | 415 | 239 | 15.7 | 0.6 | 0.314±3.4 | 0.04397±1.2 | 0.4 | 277.4±3.3 |
| 10.1 | 0 | 621 | 389 | 24.3 | 0.65 | 0.3219±2.2 | 0.04545±1.2 | 0.5 | 286.5±3.3 |
| Sample 41 | | | | | | | | | |
| 1.1 | 0 | 367 | 348 | 26.4 | 0.98 | 0.667±2.3 | 0.08391±0.72 | 0.3 | 519.4±3.6 |
| 1.2 | 0.72 | 46 | 9 | 3.44 | 0.2 | 0.687±9.2 | 0.0857±1.9 | 0.2 | 530.1±9.9 |
| 2.1 | 0.15 | 212 | 85 | 15.5 | 0.42 | 0.683±3.2 | 0.08519±0.91 | 0.3 | 527±4.6 |
| 2.2 | 0 | 10 | 3 | 0.598 | 0.28 | 0.538±15 | 0.0687±4.9 | 0.3 | 429±20 |
| 3.1 | 0 | 271 | 176 | 19.5 | 0.67 | 0.655±2.8 | 0.08394±0.96 | 0.3 | 519.6±4.8 |
| 3.2 | 0 | 123 | 46 | 8.86 | 0.39 | 0.659±4.2 | 0.0839±1.2 | 0.3 | 519.6±6.1 |
| 4.1 | 0 | 270 | 228 | 19.3 | 0.87 | 0.656±2.8 | 0.08351±0.95 | 0.3 | 517±4.7 |

*Ending*

| Analysis No. | $^{206}Pb_c$, % | U, ppm | Th, ppm | $^{206}Pb^*$, ppm | $^{232}Th/^{238}U$ | $^{207}Pb/^{235}U$, ±% | $^{206}Pb/^{238}U$, ±% | Rho | Age $^{206}Pb/^{238}U$, Ma |
|---|---|---|---|---|---|---|---|---|---|
| 5.1 | 0 | 99 | 46 | 7.16 | 0.48 | 0.674±4.5 | 0.0842±1.3 | 0.3 | 521.4±6.7 |
| 6.1 | 0 | 2 | 1 | 0.0858 | 0.34 | 1.31±27 | 0.0589±12 | 0.5 | 369±44 |
| 7.1 | 0.04 | 1183 | 521 | 87 | 0.46 | 0.6675±1.4 | 0.08555±0.52 | 0.4 | 529.2±2.7 |
| 7.2 | 0 | 542 | 293 | 39 | 0.56 | 0.67±1.9 | 0.08359±0.61 | 0.3 | 517.5±3 |
| 8.1 | 0.58 | 64 | 16 | 4.76 | 0.27 | 0.674±7.6 | 0.0865±1.7 | 0.2 | 535.1±8.7 |
| 8.2 | 0.21 | 443 | 315 | 30.4 | 0.73 | 0.599±3 | 0.07965±0.7 | 0.2 | 494±3.3 |
| 9.1 | 0 | 469 | 393 | 31.8 | 0.87 | 0.611±2.2 | 0.07882±0.77 | 0.3 | 489.1±3.6 |
| Sample 42 | | | | | | | | | |
| 1.1 | 0.2 | 161 | 45 | 27.2 | 0.29 | 2.085±2.5 | 0.1963±0.91 | 0.4 | 1155.5±9.6 |
| 1.2 | 5.06 | 11 | 0 | 0.594 | 0 | 0.34±75 | 0.0619±5.6 | 0.1 | 387±21 |
| 1.3 | 0.34 | 395 | 3 | 20.7 | 0.01 | 0.478±3.5 | 0.0609±0.78 | 0.2 | 381.1±2.9 |
| 2.1 | 0 | 701 | 350 | 51.5 | 0.52 | 0.675±1.6 | 0.08553±0.52 | 0.3 | 529±2.7 |
| 3.1 | 0 | 180 | 55 | 12 | 0.32 | 0.604±3.5 | 0.07783±1.2 | 0.3 | 483.2±5.5 |
| 3.2 | 0 | 11 | 0 | 0.587 | 0.02 | 0.538±15 | 0.0625±4.3 | 0.3 | 391±16 |
| 4.1 | 0.11 | 219 | 243 | 16.5 | 1.14 | 0.688±3.3 | 0.0875±1.4 | 0.4 | 540.6±7.2 |
| 5.1 | 0.39 | 84 | 51 | 7.65 | 0.63 | 0.887±5.3 | 0.1062±1.4 | 0.3 | 650.5±8.5 |
| 6.1 | 0.83 | 594 | 301 | 25.4 | 0.52 | 0.37±5.7 | 0.04937±0.73 | 0.1 | 310.7±2.2 |
| 7.1 | 0.08 | 494 | 633 | 48.8 | 1.33 | 0.99±1.8 | 0.11504±0.59 | 0.3 | 701.9±3.9 |
| 7.2 | 0.13 | 288 | 4 | 14.8 | 0.01 | 0.474±3.3 | 0.05981±0.88 | 0.3 | 374.5±3.2 |
| 7.3 | 0 | 206 | 2 | 10.9 | 0.01 | 0.483±3.6 | 0.06169±1 | 0.3 | 385.9±3.8 |
| 8.1 | 0.15 | 346 | 135 | 22.6 | 0.4 | 0.6±3.5 | 0.07617±0.87 | 0.2 | 473.3±4 |
| 9.1 | 0.19 | 214 | 130 | 14.1 | 0.63 | 0.595±3.7 | 0.07688±1.1 | 0.3 | 477.5±5 |
| 10.1 | 0.18 | 207 | 87 | 10.6 | 0.44 | 0.433±4.1 | 0.05939±1 | 0.3 | 371.9±3.7 |
| Sample 43 | | | | | | | | | |
| 1.1 | 0.13 | 176 | 64 | 13.1 | 0.37 | 0.664±3.3 | 0.08644±0.93 | 0.3 | 534.5±4.7 |
| 2.1 | 0.72 | 32 | 7 | 2.3 | 0.24 | 0.637±9.7 | 0.0836±2.2 | 0.2 | 517±11 |
| 3.1 | 0 | 91 | 28 | 6.47 | 0.31 | 0.68±4.4 | 0.0826±1.3 | 0.3 | 511.8±6.4 |
| 4.1 | 0 | 1044 | 734 | 75 | 0.73 | 0.6643±1.3 | 0.08361±0.43 | 0.3 | 517.6±2.2 |
| 4.2 | 0.47 | 47 | 13 | 3.41 | 0.28 | 0.65±7.4 | 0.084±1.8 | 0.2 | 520.2± 9 |
| 5.1 | 0.82 | 237 | 88 | 17.7 | 0.38 | 0.655±4.9 | 0.08626±0.84 | 0.2 | 533.4±4.3 |
| 6.1 | 0.21 | 193 | 81 | 14.3 | 0.43 | 0.678±3.5 | 0.08577±1 | 0.3 | 530.5±5.3 |
| 7.1 | 0 | 114 | 31 | 8.26 | 0.28 | 0.646±4 | 0.08454±1.2 | 0.3 | 523.2±5.9 |
| 8.1 | 0.5 | 145 | 40 | 10.5 | 0.28 | 0.639±5.7 | 0.08381±1.1 | 0.2 | 518.8±5.4 |
| 9.1 | 0.19 | 104 | 24 | 7.77 | 0.24 | 0.688±5.1 | 0.0871±1.4 | 0.3 | 538.5±7.4 |
| 10.1 | 0.62 | 173 | 60 | 12.6 | 0.36 | 0.638±5.7 | 0.08421±1 | 0.2 | 521.2±5 |
| 10.2 | 0 | 14 | 5 | 1 | 0.38 | 0.812±9.8 | 0.0836±3.5 | 0.4 | 517±17 |
| 11.1 | 0.8 | 100 | 27 | 7.26 | 0.27 | 0.627±7.6 | 0.0835±1.3 | 0.2 | 516.7±6.6 |
| 12.1 | 1.09 | 653 | 253 | 46.9 | 0.4 | 0.631±3.3 | 0.08269±0.56 | 0.2 | 512.1± 2.8 |
| 12.2 | 0 | 39 | 9 | 2.51 | 0.23 | 0.554±7.7 | 0.0746±2.1 | 0.3 | 463.8±9.5 |

with epidote growing on their edges. Inclusions of allanite-(Ce) are found in glaucophane. *Titanite* in the rock occurs as inclusions together with rutile in almandine, omphacite, glaucophane, and in the aggregate of minerals of the epidote group. *Rutile* is found throughout the rocks both as separate grains of elongated or irregular shape and with titanite rims. Iron-enriched rutile (FeO up to 12.51 wt.%) occurs in the rocks. *Paragonite* forms small clusters of grains, partially replacing omphacite. In eclogites, cobalt-bearing *pyrite* (Co up to 2.46 wt.%) is noted as single grains in the almandine-amphibole aggregate. *Ilmenite* with high manganese content (MnO up to 4.71 wt.%) is found as an inclusion in almandine in eclogite together with rutile and titanite. *Albite* in rocks forms elongated grains in chamoisite-clinochlore aggregate together with phengite, muscovite, and calcite, as well as veinlets and accumulations with large glaucophane grains. *Quartz* in eclogites is present in small amounts as inclusions in garnet and calcite grains. *Fluorapatite* is noted as inclusions in almandine, omphacite, and calcite together with quartz. *Zircon* occurs as idiomorphic elongated grains up to 350 μm in size within rock-forming minerals.

## U-PB SHRIMP DATING OF ECLOGITE ZIRCONS

*Sample 39* (Kitarsay complex). Eclogites (amphibolized, sometimes with plagioclase) in serpentinites. The thickness of eclogite bodies does not exceed 5 m. Their shape is elongated, boudin-like, up to 100 m in length. Zircons have a pink color, prismatic and elongated-prismatic habit (Fig. 3). The faces of crystals are shiny, the edges of some crystals are slightly rounded. The internal structure of the crystals is rhythmically zoned. In some crystals, an inner core is distinguished. Practically all obtained dates (Table 1) fall on the concordia (Fig. 4 A). Two clusters with concordant ages are distinguished on the concordia: 517±5 Ma (MSWD = 0.43), which corresponds to the Cambrian (Series 2, Stage 3, ≈ 521-514 Ma, according to [17]) and 472±3 Ma (MSWD = 5.9) – corresponding to the Early Ordovician, Floian Stage. One analysis from the zircon core (Table 1, an. 8.1) showed an older date of 544.6±5.3 Ma.

*Sample 40* (Kitarsay complex). Eclogite body among melanged serpentinites. The eclogites are amphibolized, especially at contacts with serpentinites. Serpentinites contain layers of intensely lightened (silicified) rocks, sometimes containing fuchsite. Among the eclogites, there are granite veinlets, and banded albitized varieties of eclogites are also noted, in which leucocratic bands make up ≈ 5%. Zircons in the rock form transparent pink prismatic and elongated-prismatic crystals with shiny faces (Fig. 3). The internal structure of the crystals is rhythmically zoned. In some crystals, a core part is observed. The obtained results gave a concordant age (Fig. 4 B, Table 1) of 282±2 Ma (MSWD = 0.2), which corresponds to the Early Permian time. One analysis of the edge part of the zircon showed a rejuvenated result of 241.5±3.8 million years (Table 1, sample 40, an. 7.2).

*Sample 41* (Tulepsai complex) was collected from the right side of a small tributary of Tulepsai, in a drop-shaped eclogite boudin located among amphibolites with outcrop widths of more than 5 m. The eclogites are massive, medium-grained, and partially amphibolitized. The eclogites are conformably embedded in amphibolites. The amphibolites are platy, composed of muscovite-amphibole-garnet-feldspar; among accessory minerals, rutile strongly predominates, leucocratic interlayers constitute up to 35% of the rock volume. *Sample 42* was collected from the most massive and fresh amphibolites 3 m from the eclogite boudin. *Sample 43* from eclogites also located among amphibolites was taken 1.45 km southwest of sample 41.

Zircons from sample 41 eclogite are mainly represented by crystal fragments and short-prismatic crystals. The zircons are colorless and lightly pinkish with rounded edges and complex internal structure. Almost all zircons have a central core and zones with sectoriality and rhythmic zonation at the periphery (Fig. 3). Analyses were performed on the central and peripheral parts of the zircons (Table 1). Almost all the results obtained plot on the concordia (Fig. 4 B). The concordant age obtained for the zircons is 523±3 Ma (MSWD = 1.8), corresponds to the upper part of the Lower Cambrian (Stage 2). Analyses were made in the core, intermediate, and peripheral parts of the mineral grains. Four analyses gave younger ages: dates of 494, 489, and 429 Ma were obtained from the zone of later overgrowth of zircon crystals (Fig. 3, sample 41, an. 8.2, 9.1, 2.2). The point with analysis in the peripheral part of the zircon (Fig. 3, sample 41, an. 6.1) (≈ 369 Ma) deviated from the concordia.

Zircons from amphibolite sample 42. Different morphological types of zircon grains are observed in the sample. There are crystals of short-prismatic, elongated-prismatic dipyramidal habitus, and their fragments. Almost all grains have distinct shiny faces and are colorless. The sample also contains elongated grains with smoothed edges (Fig. 3).

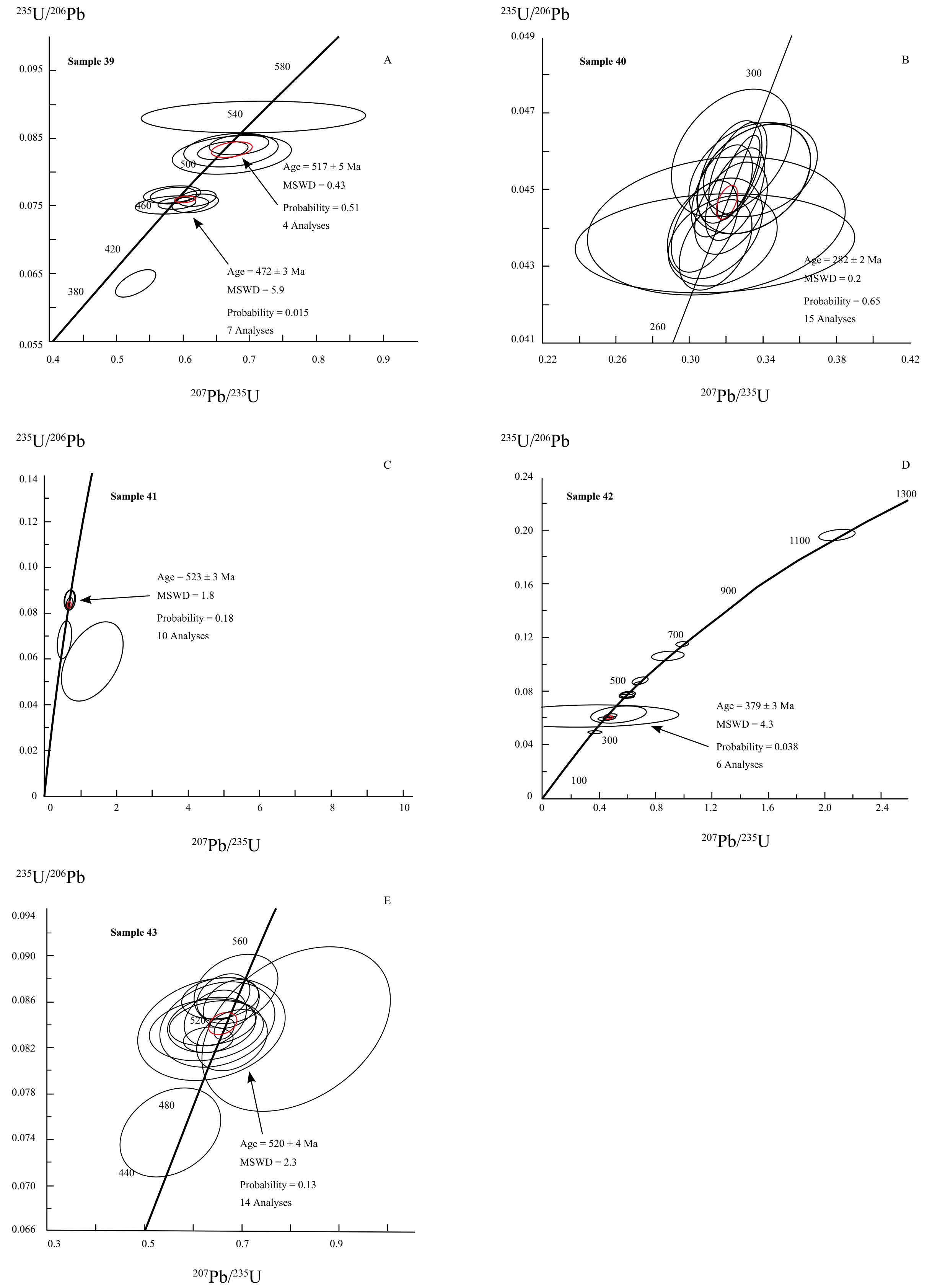

**Fig. 4.** Isotopic U-Pb concordia diagrams constructed from mass spectrometric study of zircon grains from Mugodzhari eclogites. A – sample 39; B – sample 40; C – sample 41; D – sample 42 (amphibolite); E – sample 43.

Crystals exhibit sectoriality and zonality. Zircons with a central, core part and subsequent overgrowth are observed. In the peripheral zones of four zircon grains, the concordant age (Fig. 4 G, Table 1) is 379±3 Ma (MSWD = 4.3), corresponding to the Frasnian stage.

Zircons from eclogite sample 43 are represented by elongated crystals and their fragments (Fig. 3). The crystals have rounded edges, dissolution traces, and are colorless. Within the crystals, a core part and a peripheral part are noted. Rhythmic zonality is observed in the peripheral zone of the grains. The obtained results (Table 1, Fig. 4 D) gave a concordant age of 520±4 Ma (MSWD = 2.3). A younger age of 464 Ma was obtained from the edge of one zircon fragment.

## DISCUSSION OF RESULTS AND CONCLUSIONS

The metamorphic rocks we studied, represented predominantly by omphacite with up to 47% of jadeite minal, glaucophane and almandine containing up to 18% of pyrope minal, as well as paragonite, clinozoisite, a large amount of accessory rutile, judging by the association, are fairly typical eclogites that underwent retrograde metamorphism with the formation of a large amount of Na-amphibole and albite-actinolite symplectites.

The results of isotopic U-Pb dating of zircons from the eclogites of the Eastern Mugodzhari showed a very complex history of their formation and transformation, the detailed decoding of which will apparently be possible only in the future, with the use of other isotope-geochronometric systems (Rb-Sr, Sm-Nd, etc.). However, the data presented in the article already prove the main point that the metamorphic complexes of the Mugodzhars are not Early Proterozoic or Riphean formations (as previously thought), but represent Lower-Middle Paleozoic complexes of the middle part of the Earth's crust. That is, these metamorphites are not the once-assumed Madagascar-type microcontinent [7], nor part of the foundation of the Russian platform [14], but are fragments of the deep part of the island arc system of the eastern sector of the Urals, which later (in the Middle-Late Triassic) were brought to a near-surface level during the uplift and erosion of certain areas of the Urals (for more details, see [6]). It should be noted that in the rocks of the eastern (paleo-island arc) sector of the Urals (i.e., east of the Main Uralian Fault), not a single reliable pre-Paleozoic dating is known today [5].

Of the 4 eclogite samples, samples 39, 41, and 43 have similar (and the "oldest") concordant age values with dates of 517±5 Ma, 523±3 Ma, and 520±4 Ma, respectively. The obtained age (average 520±4 Ma) approximately corresponds to the upper boundary of the Early Cambrian (Terreneuvian Series) [17] and probably *corresponds to the age of the protolith.* And although Cambrian formations in the Urals are poorly preserved, Cambrian basalts are known, for example, in the Sakmara zone of the Southern Urals, near the city of Mednogorsk [12].

The youngest zircons from the eclogites of Mugodzhari have a clearly manifested age of 282±2 Ma (Early Permian, sample 40), apparently corresponding to the stage of collision and associated granite massifs [2, 3]. In this case, this is also the age of formation of the Bugetysai fault.

The other two concordant dates: 472±3 Ma (Lower-Middle Ordovician, sample 39) and 379±3 Ma (Frasnian age, sample 42), obviously reflect the time of the main stages of metamorphism. As noted in [15], the "Frasnian" age of the Mugodzhari metamorphites coincided with the age of the main phase of high-pressure metamorphism in the zone of the Main Ural deep fault in the Southern Urals (Maksyutov complex, see [18]), as well as with the age of high-grade metamorphites in the northeast of the Middle Urals (Salda complex, see [11]). The Salda complex, although located 1100 km to the north, is in the same zone as the considered metamorphites of the Eastern Mugodzhari. The data presented above force us to consider the Frasnian age of the amphibolite facies metamorphism of the Eastern Mugodzhari. This also corresponds to the information [8] that the age of newly formed (i.e., not clastic) zircons in biotite-bearing quartz-feldspar gneisses of the South Mugodzhari series was also 373±4 Ma. The concordant dating of 472±3 Ma (sample 39), according to our data, corresponds to the age of high-pressure metamorphism of Mugodzhari.

We note that in sample 42 (amphibolites), the core parts of 4 crystals gave ancient dates of 1155, 702, and 483 Ma. The central zones of zircons with smoothed edges have ages of 650, 541, and 529 Ma. Two zircons of prismatic habit showed similar ages of 471 and 478 Ma. The presence of ancient and diverse-aged zircons, apparently with traces of rounding, indicates the primary sedimentary nature of the amphibolite in this sample.

## ACKNOWLEDGEMENTS

For their help and support, the authors express their sincere gratitude to colleagues Yu.V. Erokhin, L.A. Karsten, and I.A. Pelevin (IGG RAS), as well as to A.N. Larionov from the VSEGEI IRC (St. Petersburg) for conducting zircon analyses, and to the anonymous reviewer for comments that helped improve the article.

## FUNDING

The work was carried out within the framework of the topic No. 123011800014-3 of the state assignment of the IGG UB RAS.

## REFERENCES

1. *Biryukov V.M.* High-pressure complexes of mobile belts. Moscow: Nauka, 1988. 208 p.
2. Geological map of the Kazakh SSR. Scale 1:500,000. Turgai-Mugodzhari Series. Alma-Ata. 1981. 228 p.
3. *Golionko B.G., Ryazantsev A.V.* Deformations and structural evolution of metamorphic complexes of the Taldyk antiform of the East Mugodzhari zone of the Urals (Western Kazakhstan) // Geodynamics and Tectonophysics. 2021. Vol. 12. No. 1. P. 48–59.
4. *Efimov I.A., Burd G.I.* Regional metamorphism, age and formation conditions of some deep Precambrian rocks of Mugodzhari // Soviet Geology. 1970. No. 11. P. 36–56.
5. *Ivanov K.S., Panov V.F., Likhanov I.I., Kozlov P.S., Ponomarev V.S., Hiller V.V.* Precambrian of the Urals // Mining Bulletin. 2016. Vol. 148. No. 9. P. 4–21.
6. *Ivanov K.S., Puchkov V.N.* Structural-formational zones of the Ural folded belt: review of data and development of new ideas // Geotectonics. 2022. No. 6. P. 78–113.
7. *Ivanov S.N., Puchkov V.N., Ivanov K.S., Samarkin G.I., Semenov I.V., Pumpyansky A.I., Dymkin A.M., Poltavets Yu.A., Rusin A.I., Krasnobaev A.A.* Formation of the Earth’s crust in the Urals. Moscow: Nauka. 1986. 246 p.
8. *Krasnobaev A.A., Bayanova T.B.* New data on zircon geochronology of the Taldyk block of Mugodzhary // Yearbook-2005. Yekaterinburg: IGG UB RAS. 2006. P. 297–300.
9. *Krasnobaev A.A., Davydov V.A.* Zircon geochronology of the Taldyk block of Mugodzhary // Reports of the Academy of Sciences. 1999. Vol. 366. No. 1. P. 95–99.
10. *Milovsky A.V., Getling R.V., Zverev A.T., Roshkovan G.R., Svalnova V.I.* Precambrian and Lower Paleozoic of Western Kazakhstan. Moscow: MSU. 1977. 268 p.
11. *Petrov G. A., Ronkin Yu.L. Maslov A.V., Svyazhina I.A., Rybalka A.V., Lepikhina O.P.* The timing of the beginning of collision in the Middle and Northern Urals. // DAN. 2008. Vol. 422. No. 3. P. 365–370.
12. *Puchkov V.N.* Paleogeodynamics of the Southern and Middle Urals. Ufa: Gilem, 2000. 146 p.
13. *Rusin A.M.* Kitarsai Eclogite-Peridotite Association of Mugodzhar // Yearbook-1995. Yekaterinburg: IGG UB RAS. 1996. P. 99–103.
14. *Rusin A.I.* Metamorphic Complexes of the Urals and the Problem of Metamorphism Evolution in the Complete Cycle of Lithosphere Development in Mobile Belts. Abstract of dissertation for the degree of Doctor of Geological and Mineralogical Sciences. Yekaterinburg: IGG UB RAS. 2004. 46 p.
15. *Ryazantsev A.V., Golionko B.G., Kotov A.B., Skoblenko A.V., Stifeeva M.V., Plotkina Yu.V., Salnikova E.B., Koreshkova M.Yu., Machev F.* Age and Thermal History of Eclogites from the Tulepsai Complex of the Eastern Mugodzhar (Western Kazakhstan) // Doklady RAS. Earth Sciences. 2022. Vol. 506. No. 1. P. 5–13.
16. *Yurish V.V., Ulukpanov K.T.* Geodynamics of the Paleozoic of the Kazakh Urals. Aktobe: AKTYUBNIGRI LLP. 2020. 365 p.
17. *Cohen K.M., Harper D.A.T., Gibbard P.L., Car N.* The ICS International Chronostratigraphic Chart, February 2022. Available from: http://www.stratigraphy.org/ ICSchart/ ChronostratChart2022-02.pdf .
18. *Glodny J., Bingen B., Austrheim H., Molina J.F., Rusin A.* Precise Eclogitization Ages Deduced from Rb/Sr Mineral Systematics: The Maksyutov Complex, Southern Urals, Russia // Geoch. Acta. 2002. V. 66 (7). P. 1221–1235.
19. *Ludwig K.R.* ISOPLOT 3.00. A User’s Manual // Berkeley Geochronology Center Special Publication. 2003. № 4. 2455 RidgeRoad, Berkeley. CA 94709. USA. 70 p.
20. *Williams I.S.* U–Th–Pb geochronology by ion microprobe. Applications of microanalytical techniques to understanding mineralizing processes // Rev. Econ. Geol. 1998. V. 7. P. 1–35.

## APPENDIX 1. CHEMICAL COMPOSITION OF MINERALS FROM MUGODZHAR ECLOGITES (KAZAKHSTAN)

The chemical composition of minerals was determined using a Camebax SX50 X-ray microanalyzer (Department of Mineralogy, Faculty of Geology, Moscow State University, analyst D. A. Khanin) at an accelerating voltage of 15 kV and a probe current of 30 nA. The corresponding phosphates were used as standards for REE, for Na, Si – chkalovite, Mg, Ca, Fe – hornblende, Al – albite, K – orthoclase, Ti – $KTiPO_5$ synth., Cr – magnesiochromite, V – vanadium, $MnTiO_5$, Co – cobaltin, Ni – NiO, Sr – celestine, Ba – barite. Water content was not carried out by direct method.

**Table 1.** Chemical composition (in wt.%) of minerals from eclogites

| No. | $SiO_2$ | $TiO_2$ | $Al_2O_3$ | $V_2O_5$ | MgO | FeO | MnO | SrO | CaO | $Na_2O$ | $K_2O$ | Amount |
|---|---|---|---|---|---|---|---|---|---|---|---|---|
| Almandine | | | | | | | | | | | | |
| 1 | 37.86 | – | 21.83 | – | 4.50 | 31.15 | 0.34 | – | 4.33 | – | – | 100.01 |
| 2 | 37.69 | – | 21.60 | – | 3.04 | 32.38 | 0.56 | – | 4.73 | – | – | 100.00 |
| 3 | 37.81 | – | 21.56 | – | 3.51 | 29.00 | 0.19 | – | 7.56 | – | – | 99.63 |
| 4 | 38.07 | 0.15 | 21.66 | – | 2.32 | 28.22 | 0.28 | – | 9.30 | – | – | 100.00 |
| 5 | 38.04 | 0.23 | 21.87 | – | 3.16 | 27.30 | 0.24 | – | 9.16 | – | – | 100.00 |
| 6 | 38.16 | – | 21.88 | – | 4.43 | 28.86 | 0.20 | – | 6.47 | – | – | 100.00 |
| 7 | 37.75 | – | 21.72 | – | 4.32 | 31.06 | 0.45 | – | 4.71 | – | – | 100.01 |
| 8 | 38.03 | 0.16 | 21.65 | – | 3.24 | 27.65 | 0.20 | – | 9.06 | – | – | 99.99 |
| 9 | 37.98 | – | 21.75 | – | 3.59 | 28.74 | 0.22 | – | 7.72 | – | – | 100.00 |
| 10 | 37.54 | 0.39 | 21.03 | – | 3.13 | 27.78 | 0.84 | – | 9.18 | – | – | 99.89 |
| 11 | 37.14 | 0.20 | 20.96 | – | 2.91 | 28.62 | 0.87 | – | 9.08 | – | – | 99.78 |
| 12 | 38.12 | 0.39 | 21.23 | – | 3.84 | 28.30 | 0.62 | – | 8.87 | – | – | 101.37 |
| 13 | 37.57 | – | 21.06 | – | 3.12 | 29.63 | 1.11 | – | 7.84 | – | – | 100.33 |
| 14 | 37.90 | – | 21.17 | – | 4.35 | 31.08 | 0.67 | – | 5.12 | – | – | 100.29 |
| Glaucophane | | | | | | | | | | | | |
| 15 | 58.16 | – | 11.71 | – | 10.69 | 8.92 | 0.05 | – | 0.32 | 7.77 | – | 97.62 |
| 16 | 57.92 | – | 11.36 | – | 10.62 | 9.44 | – | – | 0.74 | 7.72 | – | 97.80 |
| 17 | 57.85 | – | 11.50 | – | 9.58 | 10.72 | – | – | 0.19 | 7.88 | – | 97.72 |
| 18 | 56.59 | – | 10.89 | – | 11.17 | 9.59 | – | – | 1.58 | 7.31 | – | 97.13 |
| 19 | 56.10 | 0.11 | 11.37 | – | 10.14 | 10.63 | – | – | 1.56 | 7.25 | – | 97.16 |
| Omphacite | | | | | | | | | | | | |
| 20 | 56.88 | – | 10.04 | 0.10 | 8.37 | 5.05 | – | – | 13.22 | 6.64 | – | 100.30 |
| 21 | 56.83 | – | 10.52 | – | 8.86 | 4.44 | – | – | 13.62 | 7.21 | – | 101.48 |
| 22 | 57.00 | 0.11 | 10.05 | – | 7.91 | 5.40 | – | – | 12.57 | 6.63 | – | 99.67 |
| 23 | 56.19 | 0.07 | 11.02 | 0.10 | 8.32 | 5.53 | 0.06 | – | 12.76 | 7.16 | – | 101.21 |
| 24 | 55.85 | – | 10.11 | 0.10 | 8.54 | 4.99 | – | – | 13.22 | 7.25 | – | 100.06 |
| 25 | 55.58 | 0.10 | 10.98 | 0.09 | 7.20 | 5.63 | 0.07 | – | 12.09 | 7.96 | – | 99.70 |
| 26 | 54.96 | 0.23 | 11.95 | 0.15 | 6.44 | 6.41 | 0.05 | – | 10.24 | 8.58 | – | 99.01 |
| 27 | 55.99 | 0.16 | 11.49 | – | 7.40 | 6.08 | – | – | 10.48 | 8.33 | – | 99.93 |
| 28 | 56.48 | 0.18 | 11.23 | 0.11 | 7.04 | 6.03 | 0.09 | – | 11.31 | 8.42 | – | 100.89 |
| 29 | 56.72 | 0.25 | 11.94 | 0.08 | 7.00 | 5.48 | – | – | 10.93 | 8.63 | – | 101.03 |

*Ending*

| No. | $SiO_2$ | $TiO_2$ | $Al_2O_3$ | $V_2O_5$ | MgO | FeO | MnO | SrO | CaO | $Na_2O$ | $K_2O$ | Amount |
|---|---|---|---|---|---|---|---|---|---|---|---|---|
| Actinolite | | | | | | | | | | | | |
| 30 | 51.81 | 0.09 | 4.39 | 0.11 | 11.46 | 18.13 | 0.28 | – | 10.71 | 1.63 | 0.14 | 98.75 |
| 31 | 50.73 | 0.07 | 4.24 | 0.24 | 12.10 | 17.86 | 0.29 | 0.09 | 11.58 | 1.21 | 0.11 | 98.28 |
| Amphiboles of a number of ferropargasite–ferroedenite | | | | | | | | | | | | |
| 32 | 41.45 | 0.25 | 12.29 | 0.19 | 4.64 | 26.09 | 0.25 | – | 10.56 | 2.94 | 0.35 | 99.01 |
| 33 | 41.03 | 0.14 | 11.7 | 0.09 | 4.54 | 25.97 | 0.21 | | 10.29 | 2.87 | 0.35 | 97.19 |
| 34 | 42.69 | 0.05 | 9.96 | 0.00 | 5.56 | 25.82 | 0.26 | – | 10.83 | 2.52 | 0.36 | 98.05 |
| Chlorite | | | | | | | | | | | | |
| 35 | 24.66 | 0.79 | 19.25 | – | 10.80 | 29.72 | 0.23 | – | 0.81 | 0.18 | – | 86.44 |
| 36 | 26.06 | 0.26 | 16.16 | – | 11.12 | 31.27 | 0.38 | 0.29 | 0.54 | 0.22 | – | 86.30 |
| 37 | 28.27 | – | 19.25 | 0.12 | 23.95 | 13.79 | 0.09 | – | 0.10 | 0.08 | – | 85.65 |
| 38 | 28.99 | – | 19.49 | – | 23.58 | 14.50 | – | – | 0.24 | 0.14 | – | 86.94 |
| Muscovite | | | | | | | | | | | | |
| 39 | 50.50 | 0.30 | 27.00 | 0.16 | 3.32 | 2.57 | – | – | 0.11 | 0.71 | 11.05 | 95.72 |
| 40 | 50.62 | 0.25 | 27.10 | 0.12 | 3.31 | 2.63 | – | – | – | 0.68 | 10.89 | 95.60 |
| Zoisite | | | | | | | | | | | | |
| 41 | 39.56 | – | 32.40 | 0.10 | 0.06 | 1.08* | – | 0.16 | 24.58 | – | – | 97.94 |
| 42 | 39.22 | 0.05 | 31.69 | 0.22 | – | 2.81* | – | 0.42 | 24.04 | 0.07 | – | 98.52 |
| Clinozoisite–epidote | | | | | | | | | | | | |
| 43 | 37.73 | 0.11 | 26.63 | 0.12 | – | 7.90* | 0.11 | 0.00 | 23.21 | 0.06 | – | 95.87 |
| 44 | 38.20 | 0.00 | 25.93 | 0.41 | – | 9.49* | 0.10 | 0.16 | 23.56 | 0.00 | – | 97.85 |
| Paragonite | | | | | | | | | | | | |
| 45 | 47.46 | 0.00 | 37.00 | 0.11 | 0.89 | 0.56 | – | – | 0.16 | 7.66 | 0.94 | 94.78 |
| 46 | 46.68 | 0.11 | 37.48 | 0.33 | 0.50 | 0.64 | – | – | 0.10 | 7.25 | 1.22 | 94.31 |
| Titanite | | | | | | | | | | | | |
| 47 | 30.44 | 37.48 | 1.48 | 0.77 | – | 0.27 | – | 0.06 | 28.59 | 0.08 | – | 99.17 |
| 48 | 30.59 | 38.13 | 1.61 | 0.50 | – | 0.24 | 0.08 | 0.14 | 28.67 | 0.05 | – | 100.01 |
| Rutile | | | | | | | | | | | | |
| 49 | 0.16 | 97.63 | 0.07 | 0.97 | – | 1.03 | – | – | – | – | – | 99.86 |
| 50 | | 98.11 | 0.07 | 2.07 | – | 0.25 | – | – | – | – | – | 100.50 |
| 51 | – | 86.42 | – | 0.81 | – | 12.51 | 1.27 | – | – | – | – | 101.01 |
| Ilmenite | | | | | | | | | | | | |
| 52 | 0.26 | 53.89 | 0.12 | 0.34 | – | 39.80 | 4.71 | – | 0.25 | – | – | 99.37 |
| Albite | | | | | | | | | | | | |
| 53 | 67.32 | – | 19.10 | – | – | 0.68 | – | – | 0.15 | 12.21.21 | – | 99.46.46 |
| 54 | 69.13.13 | – | 19.12.12 | – | – | 0.54.54 | – | – | 0.27.27 | 11.67.67 | – | 100.73.73 |
| Calcite | | | | | | | | | | | | |
| 55 | 0.34.34 | – | – | – | – | 1.55.55 | 0.46.46 | 0.14.14 | 50.50.50 | – | – | 52.99.99 |
| 56 | – | – | – | – | – | 0.74.74 | 0.41.41 | 0.08.08 | 51.48.48 | – | – | 52.71.71 |

Note: here and in Table 2 – analyses: 32, 33 – ferropargasite; 34 – ferroedenite; 35, 36 – chamosite; analyses 37, 38 – clinochlore. BAn. 3 – additionally determined $Cr_2O_3$ 0.37.37 wt.% (0.02 f.u.).

* – the content of $Fe_2O_3$ in the mineral.

**Table 2.** Crystal chemical recalculations (in f.u.) of minerals from eclogites

| No | Si | Ti | Al | V | Mg | $Fe^{2+}$ | $Fe^{3+}$ | Mn | Sr | Ca | Na | K |
|---|---|---|---|---|---|---|---|---|---|---|---|---|
| Almandine | | | | | | | | | | | | |
| 1 | 2.99 | – | 2.03 | – | 0.53 | 2.06 | | 0.02 | – | 0.37 | – | – |
| 2 | 3.01 | – | 2.03 | – | 0.36 | 2.16 | – | 0.04 | – | 0.40 | – | – |
| 3 | 2.99 | – | 2.01 | – | 0.41 | 1.92 | – | 0.01 | – | 0.64 | – | – |
| 4 | 3.02 | 0.01 | 2.02 | – | 0.27 | 1.87 | – | 0.02 | – | 0.79 | – | – |
| 5 | 3.00 | 0.01 | 2.03 | – | 0.37 | 1.80 | – | 0.02 | – | 0.77 | – | – |
| 6 | 3.00 | – | 2.03 | – | 0.52 | 1.90 | – | 0.01 | – | 0.55 | – | – |
| 7 | 2.98 | – | 2.02 | – | 0.51 | 2.05 | 0.01 | 0.03 | – | 0.40 | – | – |
| 8 | 3.00 | 0.01 | 2.01 | – | 0.38 | 1.82 | – | 0.01 | – | 0.77 | – | – |
| 9 | 3.00 | – | 2.02 | – | 0.42 | 1.90 | – | 0.02 | – | 0.65 | – | – |
| 10 | 2.97 | 0.02 | 1.96 | – | 0.37 | 1.79 | 0.05 | 0.06 | – | 0.78 | – | – |
| 11 | 2.95 | 0.01 | 1.96 | – | 0.35 | 1.79 | 0.12 | 0.06 | – | 0.77 | – | – |
| 12 | 2.97 | 0.02 | 1.95 | – | 0.45 | 1.76 | 0.08 | 0.04 | – | 0.74 | – | – |
| 13 | 2.97 | – | 1.96 | – | 0.37 | 1.87 | 0.10 | 0.07 | – | 0.66 | – | – |
| 14 | 2.99 | – | 1.97 | – | 0.51 | 2.00 | 0.05 | 0.05 | – | 0.43 | – | – |
| Glaucophane | | | | | | | | | | | | |
| 15 | 7.93 | – | 1.88 | – | 2.17 | 0.91 | 0.11 | 0.01 | – | 0.05 | 2.05 | – |
| 16 | 7.91 | – | 1.83 | – | 2.16 | 0.93 | 0.15 | – | – | 0.11 | 2.04 | – |
| 17 | 7.94 | – | 1.86 | – | 1.96 | 1.12 | 0.11 | – | – | 0.03 | 2.10 | – |
| 18 | 7.81 | – | 1.77 | – | 2.30 | 0.87 | 0.24 | – | – | 0.23 | 1.96 | – |
| 19 | 7.78 | 0.01 | 1.86 | – | 2.10 | 1.03 | 0.20 | – | | 0.23 | 1.95 | |
| Omphacite | | | | | | | | | | | | |
| 20 | 2.02 | – | 0.42 | – | 0.44 | 0.15 | – | – | – | 0.50 | 0.46 | – |
| 21 | 1.98 | – | 0.43 | – | 0.46 | 0.04 | 0.09 | – | – | 0.51 | 0.49 | – |
| 22 | 2.04 | – | 0.43 | – | 0.42 | 0.16 | – | – | – | 0.48 | 0.46 | – |
| 23 | 1.97 | – | 0.46 | – | 0.44 | 0.08 | 0.08 | – | – | 0.48 | 0.49 | – |
| 24 | 1.98 | – | 0.42 | – | 0.45 | 0.03 | 0.12 | – | – | 0.50 | 0.50 | – |
| 25 | 1.98 | – | 0.46 | – | 0.38 | 0.04 | 0.13 | – | – | 0.46 | 0.55 | – |
| 26 | 1.97 | 0.01 | 0.50 | – | 0.34 | 0.05 | 0.15 | – | – | 0.39 | 0.60 | – |
| 27 | 1.98 | – | 0.48 | – | 0.39 | 0.00 | 0.13 | 0.18 | – | 0.40 | 0.57 | – |
| 28 | 1.98 | 0.01 | 0.47 | – | 0.37 | 0.05 | 0.13 | – | – | 0.43 | 0.57 | – |
| 29 | 1.98 | 0.01 | 0.49 | – | 0.37 | 0.05 | 0.12 | – | – | 0.41 | 0.59 | – |
| Actinolite | | | | | | | | | | | | |
| 30 | 7.51 | 0.01 | 0.75 | 0.01 | 2.48 | 1.80 | 0.40 | 0.03 | – | 1.66 | 0.46 | 0.03 |
| 31 | 7.43 | 0.01 | 0.73 | – | 2.64 | 1.89 | 0.30 | 0.04 | 0.01 | 1.82 | 0.34 | 0.02 |

*Ending*

| No | Si | Ti | Al | V | Mg | $Fe^{2+}$ | $Fe^{3+}$ | Mn | Sr | Ca | Na | K |
|---|---|---|---|---|---|---|---|---|---|---|---|---|
| Amphiboles of a number of ferropargasite–ferroedenite | | | | | | | | | | | | |
| 32 | 6.36 | 0.03 | 2.22 | 0.02 | 1.06 | 2.92 | 0.43 | 0.03 | – | 1.74 | 0.87 | 0.07 |
| 33 | 6.41 | 0.02 | 2.16 | 0.01 | 1.06 | 2.94 | 0.45 | 0.03 | – | 1.72 | 0.87 | 0.07 |
| 34 | 6.61 | 0.01 | 1.82 | – | 1.28 | 3.01 | 0.34 | 0.03 | – | 1.80 | 0.76 | 0.07 |
| Chlorite | | | | | | | | | | | | |
| 35 | 2.73 | 0.07 | 2.51 | – | 1.78 | 2.75 | – | 0.02 | – | 0.10 | 0.04 | – |
| 36 | 3.00 | 0.02 | 2.19 | – | 1.91 | 2.71 | – | 0.04 | – | 0.07 | 0.05 | – |
| 37 | 2.87 | – | 2.30 | 0.01 | 3.62 | 1.17 | – | 0.01 | – | 0.01 | 0.02 | – |
| 38 | 2.94 | – | 2.33 | – | 3.57 | 1.11 | – | – | – | 0.03 | 0.03 | – |
| Muscovite | | | | | | | | | | | | |
| 39 | 3.38 | 0.02 | 2.13 | 0.01 | 0.33 | 0.14 | – | – | – | 0.01 | 0.09 | 0.94 |
| 40 | 3.39 | 0.01 | 2.14 | 0.01 | 0.33 | 0.15 | – | – | – | – | 0.09 | 0.93 |
| Zoisite | | | | | | | | | | | | |
| 41 | 3.01 | – | 2.91 | 0.01 | 0.01 | – | 0.06 | – | 0.01 | 2.00 | – | – |
| 42 | 2.99 | – | 2.85 | 0.01 | – | – | 0.16 | – | 0.02 | 1.96 | – | – |
| Clinozoisite–epidote | | | | | | | | | | | | |
| 43 | 3.01 | 0.01 | 2.50 | 0.01 | – | – | 0.47 | 0.01 | – | 1.98 | 0.01 | – |
| 44 | 3.01 | – | 2.41 | 0.02 | – | – | 0.56 | 0.01 | 0.01 | 1.99 | – | – |
| Paragonite | | | | | | | | | | | | |
| 45 | 3.04 | – | 2.80 | 0.01 | 0.09 | 0.03 | – | – | – | 0.01 | 0.95 | 0.08 |
| 46 | 3.02 | 0.01 | 2.86 | 0.01 | 0.05 | 0.04 | – | – | – | 0.01 | 0.91 | 0.10 |
| Titanite | | | | | | | | | | | | |
| 47 | 0.99 | 0.92 | 0.06 | 0.02 | – | – | – | – | – | 1.00 | 0.01 | – |
| 48 | 0.99 | 0.93 | 0.06 | 0.01 | – | – | – | – | – | 1.00 | – | – |
| Rutile | | | | | | | | | | | | |
| 49 | – | 0.98 | – | 0.01 | – | 0.01 | – | – | – | – | – | – |
| 50 | – | 0.97 | – | 0.02 | – | – | – | – | – | – | – | – |
| 51 | – | 0.84 | – | 0.01 | – | 0.14 | 0.01 | – | – | – | – | – |
| Ilmenite | | | | | | | | | | | | |
| 52 | 0.01 | 1.03 | – | 0.01 | – | 0.85 | 0.10 | – | – | 0.01 | – | – |
| Albite | | | | | | | | | | | | |
| 53 | 2.95 | – | 0.99 | – | – | 0.03 | – | – | – | 0.01 | 1.04 | – |
| 54 | 3.01 | – | 0.98 | – | – | 0.02 | – | – | – | 0.01 | 0.98 | – |
| Calcite | | | | | | | | | | | | |
| 55 | 0.01 | – | – | – | – | 0.02 | 0.01 | – | – | 0.96 | – | – |
| 56 | – | – | – | – | – | 0.01 | 0.01 | – | – | 0.98 | – | – |

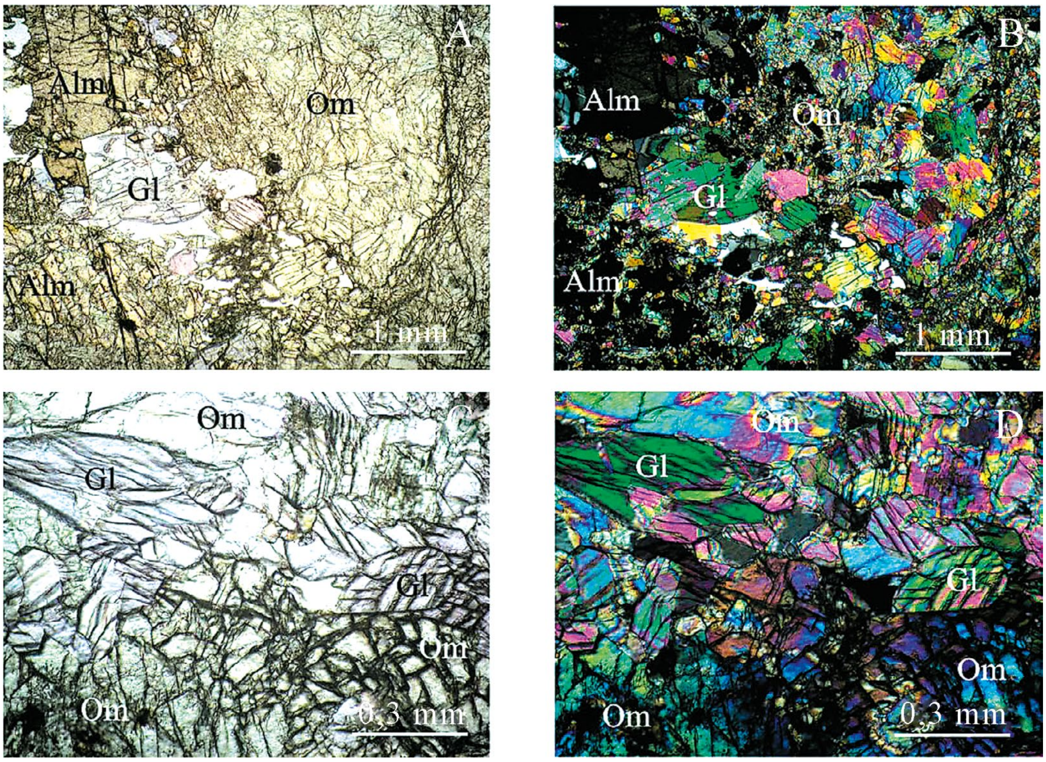

**Fig.** Eclogite of the Tulepsay complex of Eastern Mugodzhary (sample 43). In transmitted light (A), in polarized light (B). Omphacite and glaucophane from eclogite (sample 43); in transmitted light (B), in polarized light (G). Alm – almandine, Om – omphacite, Gl – glaucophane.

DOKLADY EARTH SCIENCES, 2025, Vol. 520, No. 1, pp. 29–42

# FINDING OF NEOARCHEAN (2.71 Ga) CONGLOMERATES IN THE KOSTOMUKSHA IRON ORE PROVINCE: ON THE YOUNGEST ARCHEAN STRATOTECTONIC ASSOCIATION IN THE KARELIAN CRATON

© 2025 **A. I. Slabunov**[a, *], **N. S. Nesterova**[a], **S. V. Mudruk**[a, b], **O. A. Maksimov**[a], **and A. V. Kervinen**[a]

Presented by Academician of the RAS Y. A. Kostitsyn July 15, 2024
Received July 15, 2024
Revised September 13, 2024
Accepted September 16, 2024

**Abstract.** A lens of earlier unknown polymict conglomerates was found in the axis of the Kostomuksha greenstone belt (KGB), Karelian Craton. Their clastic portion consists of poorly graded, largely angular pebbles. They are comparable in composition to rocks from the surrounding greenstone complex, such as: 1) amphibolites similar to KGB's Mesoarchean gabbroic rocks and basalts; 2) magnetite-amphibole quartzites similar to Mesoarchean magnetite-biotite-amphibole quartzites associated with banded iron formation; 3) Neoarchean (2.75 Ga) quartz metagraywacke. The conglomerates are highly deformed ($\gamma > 10$) under conditions of a sinistral shear. The conglomerates were deposited about 2.71 Ga ago, as indicated by analysis of zircons from the matrix. Thus, a new Neoarchean stratotectonic association, the youngest in the greenstone complex, was found in the KGB. It seems to have been formed in a pull-apart basin at the final stage of KGB formation, in which shearing played an important part. Volcanogenic and sedimentary associations of similar age are known in the Khedozero-Bolshozero, Kuhmo and Takanen greenstone belts of the Karelian Craton.

**Keywords :** *conglomerate, zircons, U-Th-Pb age, Archean, Kostomuksha greenstone belt, Karelian Craton*

**DOI**: 10.31857/S26867397250104e9

Conglomerates are among the sedimentary rocks that have significant importance for paleotectonic and paleogeographic reconstructions, as they make it possible to judge the composition of rocks in the area of destruction and indicate an active environment in the area of sedimentation. These can be river systems, basins with rapidly eroding shores, including those under the influence of active tectonics. Deformed conglomerates are a classic object for studying the conditions and nature of deformations and their quantitative assessment [1].

Conglomerates are widely developed in the Archean and are known in the sections of many greenstone belts, for example, in the Moodies Group of the classic Barberton belt of the Kaapvaal Craton [2], in the Timiskaming Group of the Abitibi belt in the Superior Province [3], as well as in the greenstone belts of the Karelian Craton of the Fennoscandian Shield [4–7] , including in the Kostomuksha Greenstone Belt (KGB) [8].

The KGB (Fig. 1 a) is located in the central part of the Karelian Craton of the Fennoscandian Shield [9] and hosts the largest iron deposit in NW Russia [10]. The main ore-bearing sequence of the KGB (Gimoly Group) contains at its base the well-known conglomerates of the Sukkozero Formation. However, during the field work of 2022 in this important mining region of the country, previously unknown conglomerates were discovered, to which this article is devoted for their first description.

The stratotectonic section of the KGB includes two stratotectonic associations (STA): Kontokki and Gimoly 10]. The thickness of the greenstone complex section is estimated up to 5.5 km [8]. The Kontokki STA traditionally includes three formations (Fig. 1 a): Niemijarvi (thickness 200–1300 m), composed of metamorphosed tholeiitic

---

[a] *Karelian Research Centre of the Russian Academy of Sciences, Karelia, Petrozavodsk, Russian Federation*
[b] *Geological Institute of the Kola Science Centre of the Russian Academy of Sciences, Apatity, Russian Federation*
**e-mail: slabunov@krc.karelia.ru*

**Table 1**. Results of age determination for rocks of the Kostomuksha greenstone belt of the Karelian Craton.

| No. | Age, Ma | Interpretation | Rock | Position | Dating method | Reference |
|---|---|---|---|---|---|---|
| Kontokki series | | | | | | |
| 1 | 2874±35 | magmatic event | komatiites | Ruvinvaara Formation, Kontokki Group | Sm-Nd isochron | Vrevskii, 2022 [11] |
| 2 | 2843±39 | magmatic event | komatiites and basalts | Kontokki Group | Sm-Nd isochron | Puchtel et al., 1998 [11] |
| 3 | 2813±78 | magmatic event | komatiites and basalts | Kontokki Group | Pb-Pb isochron | Puchtel et al., 1998 [11] |
| 4 | 2808±95 | magmatic event | komatiites and basalts | Niemijarvi and Ruvinvaara Formations, Kontokki Group | Sm-Nd isochron | Lobach-Zhuchenko et al., 2000a[11] |
| 5 | 2795±40 | magmatic event | komatiites | Kontokki Group | Re-Os isochron | Puchtel et al., 2001 [11] |
| 6 | 2837±4.6 | detrital magmatic zircon | BIF-1 | Ruvinvaara Formation, Kontokki Group | Zr, U-Pb (LA-ICP-MS ) | Slabunov et al., 2023[11] |
| | 2748 ±7 | metamorphic event | | | | |
| | 1890–1830 | metamorphic event | | | | |
| 7 | 2800±10 | magmatic event | rhyolite | Shurlavaara Formation, Kontokki Group | Zr, U-Pb (SHRIMP-II) | [12] |
| 8 | 2795±10 | magmatic event | rhyolite | Shurlavaara Formation, Kontokki Group | Zr, U-Pb (TIMS) | Lobach-Zhuchenko et al., 2000a [11] |
| 9 | 2792±6 | magmatic event | dacitic tuff | Kontokki Group | Zr, U-Pb (SHRIMP-II) | Kozhevnikov et al., 2006[11] |
| 10 | 2791±23 | magmatic event | dacite | Shurlavaara Formation, Kontokki Group | Zr, U-Pb (NORDSIM) | Bibikova et al., 2005a[11] |
| 11 | 2790 ±21 | magmatic event | rhyolitic tuff | Shurlavaara Formation, Kontokki Group | Zr, U-Pb (TIMS) | Bibikova et al., 2005a[11] |
| 12 | 2757±113 | metamorphic event | rhyolite | Shurlavaara Formation, Kontokki Group | Sm-Nd isochron | Puchtel et al., 1998 [11] |
| 13 | 2810–2790 | detrital zircon | BIF-2 | Shurlavaara Formation, Kontokki Group | Zr, U-Pb (LA-ICP-MS ) | Slabunov et al., 2023[11] |
| | 2725±6 | metamorphic event | | | | |
| | 2412±17 | metamorphic event | | | | |
| 14 | 2734 ±3.5 | metamorphic event | BIF-2 | Shurlavaara Formation, Kontokki Group | Zr, U-Pb (SHRIMP-II) | Slabunov et al. 2023 [11] |
| 15 | 2729±62 | metamorphic event | komatiites and basalts | Kontokki Group | Pb-Pb isochron | Puchtel et al., 1998 [11] |
| 16 | 2691±5.3 | metamorphic event | rhyolite | Shurlavaara Formation, Kontokki Group | Titanite, U-Pb (TIMS) | Bibikova et al., 2001 [11] |
| 17 | 2688±6.3 | metamorphic event | andesite | Kontokki Group | Titanite, U-Pb (TIMS) | Bibikova et al., 2001 [11] |

*Continuation*

| No. | Age, Ma | Interpretation | Rock | Position | Dating method | Reference |
|---|---|---|---|---|---|---|
| 18 | 2674±13 | metamorphic event | amphibolite | Kontokki Group | Zr, U-Pb (SHRIMP-II) | Levskii et al., 2009 [11] |
| Gimoly Group | | | | | | |
| 19 | 2759±8.9 | magmatic event | rhyolite | Kostomuksha Formation, Gimoly Group | Zr, U-Pb (SHRIMP-II) | [13] |
| 20 | 3146–2770 | detrital zircon | graywacke | Kostomuksha Formation, Gimoly Group | Zr, U-Pb (SHRIMP-II) | [13] |
| | 2753±15 | detrital zircon | graywacke | Kostomuksha Formation, Gimoly Group | Zr, U-Pb (SHRIMP-II) | [13] |
| 21 | 2743 ±15 | magmatic event | rhyolite | Kostomuksha Formation, Gimoly Group | Zr, U-Pb (SHRIMP-II) | [13] |
| 22 | 2910±12 | detrital zircon | BIF-3 | Kostomuksha Formation, Gimoly Group | Zr, U-Pb (LA-ICP-MS ) | [11] |
| | 2753±4 | detrital zircon | | | | |
| | 2720±2.9 | metamorphic event | | | | |
| | 2652±5 | metamorphic event | | | | |
| | 2560 | metamorphic event | | | | |
| | 2452±12 | metamorphic event | | | | |
| 23 | 2978±24 | detrital zircon | BIF-3 | Kostomuksha Formation, Gimoly Group | Zr, U-Pb (SHRIMP-II) | Slabunov et al., 2023 [11] |
| | 2914±7 | detrital zircon | | | | |
| | 2786±55 | detrital zircon | | | | |
| | 2732±5 | metamorphic event | | | | |
| | 2639±7 | metamorphic event | | | | |
| | 1855±8 | metamorphic event | | | | |
| Neoarchean conglomerates | | | | | | |
| 24 | **2749±3** | detrital zircon | clast in conglomerate | | Zr, Pb-Pb (LA-ICP-MS ) | present study |
| 25 | **2716±15** | detrital zircon (MDA) | Conglomerate matrix | | Zr, U-Pb (LA-ICP-MS ) | present study |
| | **2668±21** | metamorphic event | | | | |
| Intrusions | | | | | | |
| 26 | 2797±5 | magmatic event | TTG | intrusion | Zr, U-Pb (NORDSIM) | Bibikova et al., 2005a [11] |

*Ending*

| No. | Age, Ma | Interpretation | Rock | Position | Dating method | Reference |
|---|---|---|---|---|---|---|
| 27 | 2788±13 | magmatic event | TTG | intrusion | Zr, U-Pb (NORDSIM) | Bibikova et al., 2005a[11] |
| 28 | 2782±5 | magmatic event | TTG | intrusion | Zr, U-Pb | Samsonov, 2004[11] |
| 29 | 2747±17 | magmatic event | TTG | intrusion | Zr, U-Pb (TIMS) | Bibikova et al., 2005a [11] |
| 30 | 2719±6 | magmatic event | granodiorite | sanukitoid intrusion | Zr, U-Pb (NORDSIM) | Bibikova et al. 2005b [11] |
| 31 | 2712 ± 9 | magmatic event | granodiorite | sanukitoid intrusion | Zr, U-Pb (NORDSIM) | Bibikova et al., 2005b [11] |
| 32 | 2707 ± 9 | magmatic event | diorite | sanukitoid intrusion | Zr, U-Pb (NORDSIM) | Bibikova et al., 2005b [11] |
| 33 | 2707 ± 31 | magmatic event | granite-porphyry | intrusion | Zr, U-Pb (TIMS) | Lobach-Zhuchenko et al., 2000a [11] |
| 34 | 2679±8 | magmatic event | microcline granite | intrusion | Zr, U-Pb (TIMS) | Lobach-Zhuchenko et al., 2000a [11] |
| 35 | 2635±11 | metamorphic event | granite-porphyry | intrusion | Titanite, U-Pb (TIMS) | Nesterova et al., 2011 [11] |
| 36 | 2404±5 | magmatic event | dolerite | dyke | baddeleyite, U-Pb (TIMS) | Stepanova et al., 2017 [11] |
| 37 | 2132±33 | magmatic event | dolerite | dyke | Sm-Nd isochron | Stepanova et al., 2014 [11] |
| 38 | 1200 | magmatic event | kimberlites and lamprophyres | dyke | Rb-Sr isochron | Nikitina et al., 1999 [11] |

basalts with rare interlayers of komatiites and magnetite quartzites; Shurlovaara (thickness up to 600 m), represented by felsic volcanics with interlayers of banded iron formations ( banded iron formation – BIF); Ruvinvaara (thickness up to 1300 m ), composed of metabasalts and komatiites with felsic differentiates, as well as with interlayers of schists and BIF. The age of the (rhyolite)-basalt-komatiite sequence of the Kontokki STA is estimated at 2.87–2.84 Ga, while the age of felsic volcanics with interlayers of BIF (Shurlovaara Formation) is 2.81–2.78 Ga (Table 1).

The Gimoly STA, with widely varying thickness (180-2300 m), is composed of metasediments and volcanics. At its base, conglomerates (Sukkozersk Formation) up to several meters thick are identified. The clastic portion of these conglomerates consists of granitoids, and also contains felsic volcanics comparable in composition to the rocks of the Shurlavaara Formation. Metasediments of this sequence are represented by flyschoid-type graywackes [14] with thick interlayers of BIF-3, whose proportion decreases eastward. An integral part of the section includes Neoarchean (2.76–2.74 Ga) felsic volcanics – helleflintas (Table 1), analogues of which are the main source material for graywackes ([13] and references therein). The close relationship between felsic volcanics and metagraywackes has been established based on rock geochemistry studies [14], but is also emphasized by zircon data. Zircons from graywacke predominantly (70% of the sample) consist of crystals whose morphology, structure, geochemistry, and age are analogous to those from helleflinta [13].

The greenstone belt is surrounded by Neoarchean (2.78–2.75 Ga) granitoids of the tonalite-trondhjemite-granodiorite (TTG) association (Fig. 1a), and it is also intersected by several generations of Neoarchean granites and granodiorites (sanukitoids), Paleoproterozoic gabbroid dykes and Mesoproterozoic bodies of lamproites and kimberlites (Table 1).

The evolution of the KGB structure [16] suggests that the greenstone complex underwent multiple

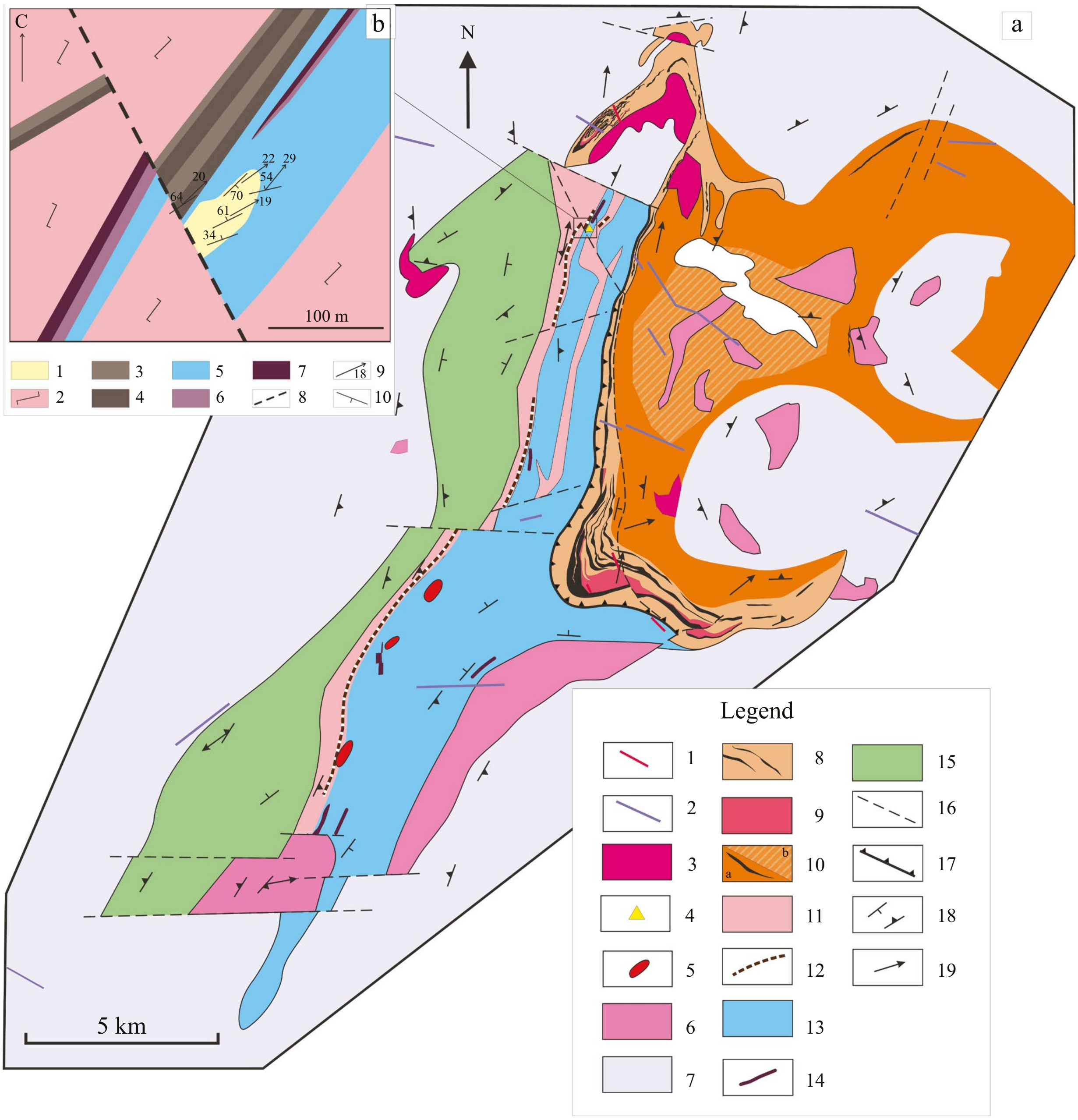

**Fig. 1.** Geological structure scheme (a) of the Kostomuksha greenstone belt ([11, 15], with the authors' additions) and (b) detailed area with a lens of Neoarchean (2.71 Ga) conglomerates. (a): *1* – Neoproterozoic (1.2 Ga) lamproites and kimberlites (Table 1), *2* – Paleoproterozoic (2.40 and 2.14 Ga) dolerites (Table 1); *3–9* Neoarchean (Table 1): *3* – 2.68 Ga granites; *4* – 2.71 Ga polymictic conglomerates; 5 – 2.71 Ga sanukitoids; 6 – 2.72 Ga granites; *7* – 2.78 Ga granitoids of TTG association; *8–10* – rocks of the Gimoly STA (Table 1): *8* – 2.76-2.74 Ga metagreywackes with BIF-3 interlayers; *9* – 2.76–2.74 Ga sills and dykes of metarhyolites (helleflintas); *10* – metasediments of the Surlampi Formation with BIF interlayers: a – weakly and b – strongly migmatized; *11–14* – Mesoarchean (2.87-2.78 Ga) (Table 1): *11* – tuffs, rhyolite tuffites (Shurlovaara Formation); *12* – BIF-2 interlayers; *13* – komatiite-basalt complex with dacites (Ruvinvaara Formation); *14* – BIF-1 interlayers; *15* – basalts and komatiites (Niemijarvi Formation); *16* – faults; *17* – thrust; *18* – *19* – bedding elements: *18* – banding and gneissosity, *19* – mineral lineation. (b): *1* – 2.71 Ga polymictic conglomerates; *2–4* – Mesoarchean (2.80–2.78 Ga) rocks of Shurlovaara Formation: *2* – felsic volcanics, *3* – BIF-2 interlayers; *4* – schist interlayers; *5–7* – Mesoarchean (2.87–2.81 Ga): *5* – komatiite-basalt complex with dacites (Ruvinvaara Formation), *6* – BIF-1 interlayers, *7* – interlayers of barren quartzites and schists; *8* – faults; *9–10* – bedding elements: *9* – mineral lineation, *10* – banding and gneissosity.

deformation events (D1-5): the early stage (D1) was accompanied by the formation of isoclinal folds with horizontal hinges and lineation; the second stage (D2) involved multi-phase NE-trending folding, associated with sinistral shear, while D2 stage folds are characterized by schistosity and mineral lineation parallel to their axial surfaces and hinges respectively; later stages D3-5 manifested as faults: D3 – in the northern part of the belt as NW-trending faults and dextral shears, D4 – meridional faults and tectonic breccia zones, D5 – system of sublatitudinal faults with a strike–slip component.

The greenstone complex KGB underwent metamorphic transformations under epidote-amphibolite to amphibolite facies conditions [8] at 2.72, 2.69 Ga (Table 1) (the latter being most significant), as well as in certain zones under lower parameters at 2.42 and 1.89 Ga (Table 1) ([10, 11] and references therein). The early deformation stage D1 corresponded to amphibolite facies conditions, D2 – to epidote-amphibolite to amphibolite facies conditions, while albite-chlorite metasomatites formed during the later stages [16].

A previously unknown conglomerate body (Fig. 1b) was discovered among basalts with BIF lenses of the Kontokki STA (Ruvinvaara Formation), with felsic volcanics containing BIF interlayers of the Shurlovaara Formation located in their immediate vicinity. The conglomerate body can be traced along strike for approximately 80 m, with a width of about 50 m (Fig. 1b). The direct contact between conglomerates and underlying metabasalts is exposed in a very small area, which prevents detailed study, however, the relationship between banding orientations in conglomerates and schistosity in surrounding rocks indicates that this contact is tectonized. Squeezing and significant stretching of pebbles parallel to fold hinges and lineation, as will be discussed below, support this conclusion.

*Structural features of conglomerates*. The studied conglomerates display layering (Fig. 2a), expressed in alternating layers with cement of different colors, as well as variations in pebble composition and orientation. Bedding is deformed into compressed with mean orientation of hinge line is NE (55°/19°) [17].

The wings of the fold are complicated by additional minor folds, whose average hinge orientation is also close to the orientation of the main fold hinge. Mineral lineation along amphibole is parallel to the hinges of both large and small folds.

The size of the clastic component of conglomerates varies from 1–2 cm to 40 cm, i.e., from pebbles to boulders (Fig. 2a–d), with all fragments significantly elongated parallel to lineation (Fig. 2a, d). In the plane perpendicular to lineation, it is clearly visible that fragments of mafic composition typically have an elliptical shape with smoothed contours, while quartzite fragments are often angular (Fig. 2 c, d). These observations indicate that elongated pebbles form classical stretching lineation. Analysis of pebble morphology suggests significant planar deformation ($K \approx 1$; $\gamma > 10$) under simple shear conditions with sinistral movement along the trajectory NE 55°/23° along steep NE-trending shear planes [17].

The orientation of folds and sinistral simple shear deformation of conglomerates correspond to NE-trending folds and sinistral shear zones of stage D2 of the structural-age scale constructed by V.N. Kozhevnikov for the KGB [16].

*Petrographic features of conglomerates*. The studied conglomerates belong to the polymictic type: their fragments consist of amphibolites (metagabbroids and metabasites) with various structures and textures and a wide range of quartzites (Fig. 2b).

Amphibolites from conglomerate fragments vary from leucocratic to melanocratic, characterized by spotted texture, porphyroblastic and granonematoblastic structure. Porphyroblasts are represented by amphibole. The groundmass consists of plagioclase and amphibole. Mineral composition of the rock: plagioclase (10–55%), amphibole (30–90%), epidote (up to 6%), titanite (up to 4%), magnetite (up to 1%), quartz (less than 1%). *Plagioclase* is represented by hypidiomorphic grains with concentric zoning, less commonly by unzoned grains with polysynthetic twins. Compositionally, plagioclase corresponds to andesine. In zoned grains, the anorthite component content changes from 45 to 30% from core to rim. Among plagioclase grains, probably relicts of magmatic origin have been preserved. Its metamorphic transformation is manifested in epidote replacement and desilication (to oligoclase). *Amphibole* occurs both as large porphyritic segregations (up to 2mm) and as small individual grains (up to 0.3 mm) or their aggregates in the rock matrix. Large porphyroblasts contain titanite inclusions. All studied amphiboles compositionally correspond to magnesian hornblende. *Epidote* develops after primary plagioclase. Individual xenomorphic grains or intergrowths of several grains are observed, which often contain quartz inclusions. Grain boundaries are often rimmed by amphibole. *Titanite* forms lenticular intergrowths of several grains or can form

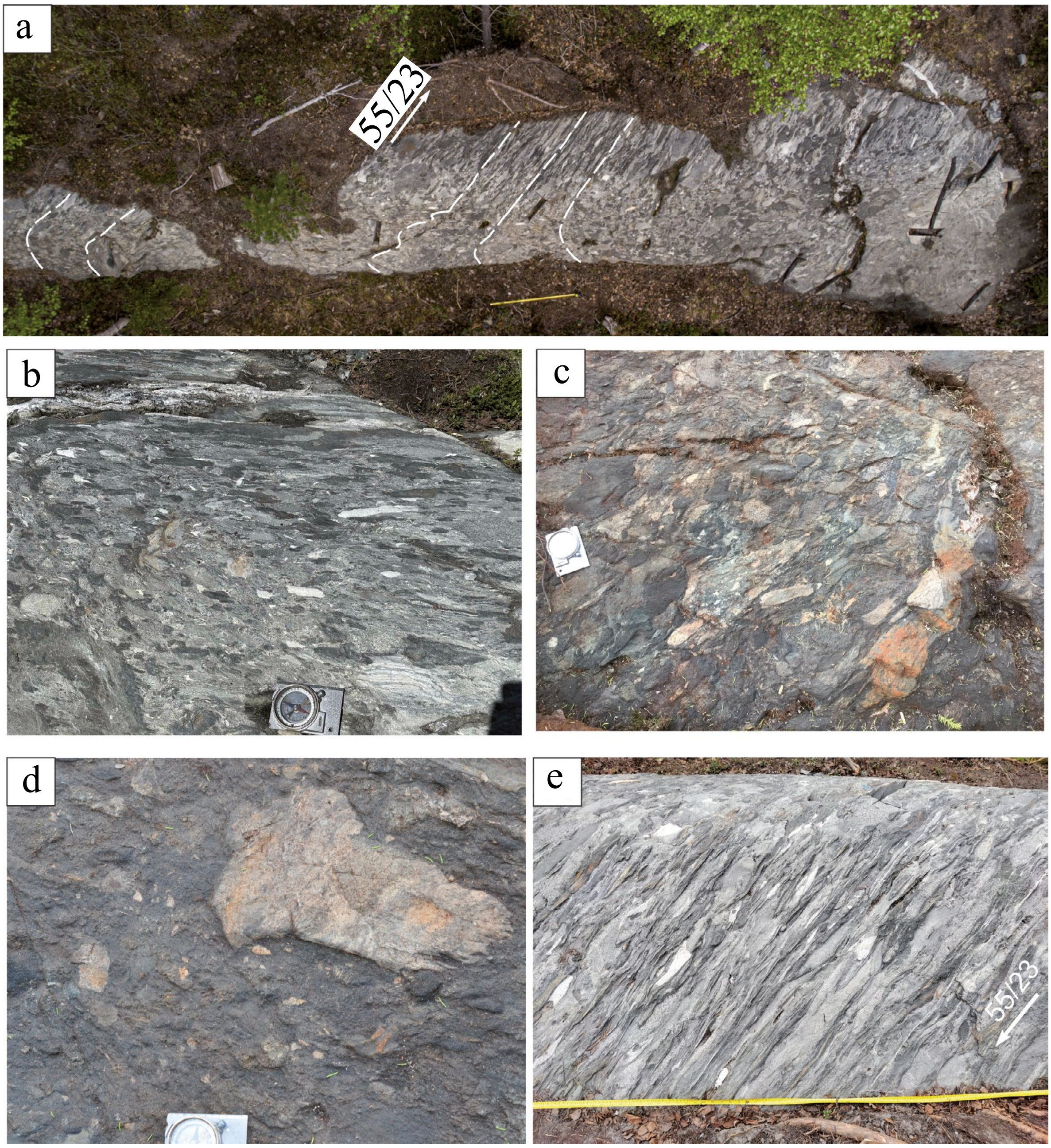

**Fig. 2.** Neoarchean (2.71 Ga) conglomerates of the Kostomuksha greenstone belt in outcrop: (a) general view of the outcrop (scale – yellow measuring tape 1 m), dotted line – structural lines, arrow – average orientation of lineation plunge (NE 55° at angle 23°); (b) conglomerates with ellipsoidal fragments of metabasites, banded quartzites – quartz graywacke, banding is visible in the rocks, photo plane is suborthogonal to the schistosity surface (scale – compass 10 cm); (c) conglomerates with angular and ellipsoidal fragments of amphibolites (metabasalts), metabasalts with plagioclase porphyries, quartz metagraywacke (scale – compass 10 cm); (d) large fragment of deformed quartz metagraywacke (scale – compass 10 cm); (e) conglomerates in a plane orthogonal to the schistosity surface and parallel to lineation, arrow – orientation of lineation plunge (NE 55° at angle 23°).

thin layers in the rock matrix. Titanite overgrowth around magnetite is observed.

Light-colored conglomerate fragments are represented by various quartzites and quartz metagreywackes. A typical rock of such fragments is a banded magnetite-amphibole quartzite with grano-nematoblastic texture. The rock consists of closely adjacent isometric quartz grains, among which amphibole and magnetite grains are evenly distributed. Additionally, thin (about 1 mm) magnetite-amphibole layers are observed in the rock.

*Quartz* makes up the bulk of the rock (up to 75–80%). In leucocratic layers, quartz is distinguished by larger grain size up to 1 mm. In amphibole-magnetite bands, grain size does not exceed 0.3 mm. *Amphibole* (comprises about 15% of the rock) is represented by elongated prismatic grains with pleochroism from light green to dark green. Together with magnetite, it forms darker layers in quartzites, where amphibole overgrowth around magnetite can be traced. *Magnetite* comprises about 10% of the rock volume, forms rounded grains 0.1-0.2 mm in size and is evenly distributed in the rock.

Among the fragments of quartzites in conglomerates, varieties are also noted where plagioclase plays a significant role, and they can be classified as quartz greywackes. The mineral composition of such rocks (for example, sample E-KS22-34-5a): quartz – 62%, amphibole – 25%, plagioclase – 8%, magnetite – 4%, pyrite – 1%. *Plagioclase* is observed as small xenomorphic grains of andesine-oligoclase composition. They are not zonal and do not have polysynthetic twins.

In terms of petrographic characteristics, these rocks are similar to low-ore quartzites associated with Mesoarchean BIF [15].

The cement of conglomerates constitutes 30–40% of the rock volume and is represented by gray and light-gray fine-grained rock with schistose texture and grano-nematoblastic structure. These schists show wide variations in dark-colored minerals content. In melanocratic varieties, amphibole content reaches 50%, quartz – 20%, plagioclase – 20%, chlorite – 5%, biotite – 5%. *Amphibole* is represented by elongated grains of magnesian and ferrous hornblende. Large grains contain inclusions of carbonate and quartz. *Chlorite and biotite* often occur in intergrowths with amphibole.

In more leucocratic variety of cement, plagioclase predominates – 33% and quartz – 40%, dark-colored minerals are mainly represented by hornblende – 17%, chlorite – 6%, and biotite – 4%. Accessory minerals include grains of zircon, titanite, calcite, and ore mineral.

*Petrogeochemical characteristics of conglomerate clasts.* By chemical composition (Table 2), basic rock clasts from conglomerates correlate well with basalts of the Kontokki STA (Fig. 3a), which is particularly evident in spider diagrams of normalized REE content (Fig. 3b). A slight enrichment of amphibolite fragments relative to the basic rocks sample of the Kontokki STA in light REEs and wider variations in the composition of petrogenic oxides may be associated with both the predominance of basalts in the control sample and more differentiated gabbroids in the fragments, as well as with the influence of superimposed processes. Fragments of quartzites and quartz graywackes are distinguished by high silica content and low – $K_2O+Na_2O$, which distinguishes them from felsic volcanics of KGB but relates them to quartzites associated with BIF. Geochemical characteristics of quartzites from conglomerate fragments (Fig. 3c, d) make it possible to more confidently correlate this group with the latter [15]. Among them, two subgroups are distinguished by the degree of REE differentiation (Fig. 3d): the first is differentiated ($La_N/Yb_N = 9 - 19$), the second is weakly differentiated ($La_N/Yb_N = 1 - 2$). The rocks of the first subgroup correlate well with Mesoarchean low-ore quartzites [15], while compositions with such weakly differentiated REEs are noted among metagraywackes of the Gimoly STA.

Based on the presented geological data, the studied conglomerates formed later than the Mesoarchean (2.87–2.84 Ga) basic rocks and possibly the Neoarchean (2.75–2.74 Ga) rocks of the Gimoly STA, since rocks similar in composition to the latter were found in fragments, but preceded intense deformations that were probably associated with accretionary processes dated at 2.72 and 2.69 Ga [11].

*U – Th – Pb geochronology of zircons from conglomerates.* For a more reliable age assessment of the discovered conglomerates, zircons extracted from the cement and from one of the fragments were studied. U – Th – Pb dating of zircon from the cement (120 analytical points) and from the fragment (60 points) was performed by LA-ICP-MS at the Laboratory of Chemical-Analytical Research of the the Geological Institute, Russian Academy of Sciences (GIN RAS, Moscow, Russia), using the approved methodology ([11] and references therein). For quality control of the analyses, zircon standards 91500 and Plesovice with standardized ages of 1062.4±0.4 and 337.1±0.4 Ma, respectively, were used. During the study of samples E-K22-34-2 and E-KS22-34-5a, the weighted mean $^{206}Pb/^{238}U$ age estimates (±2σ) obtained for the control standards were 1067±14.8 ($n$ =12) and 1069±7.4 ($n$ =6) Ma and 335.2±5.8 ($n$ =12) and 337.7±5.8 ($n$ =12) Ma, respectively, which agrees well with the reference values. The Isoplot 4.15 program [18] was used for graphical illustration of the obtained results.

From sample E-K22-34-2 (conglomerate cement), collected at point 64°46’10’’ N, 30°40’09’’ E, weighing about 700 g, more than

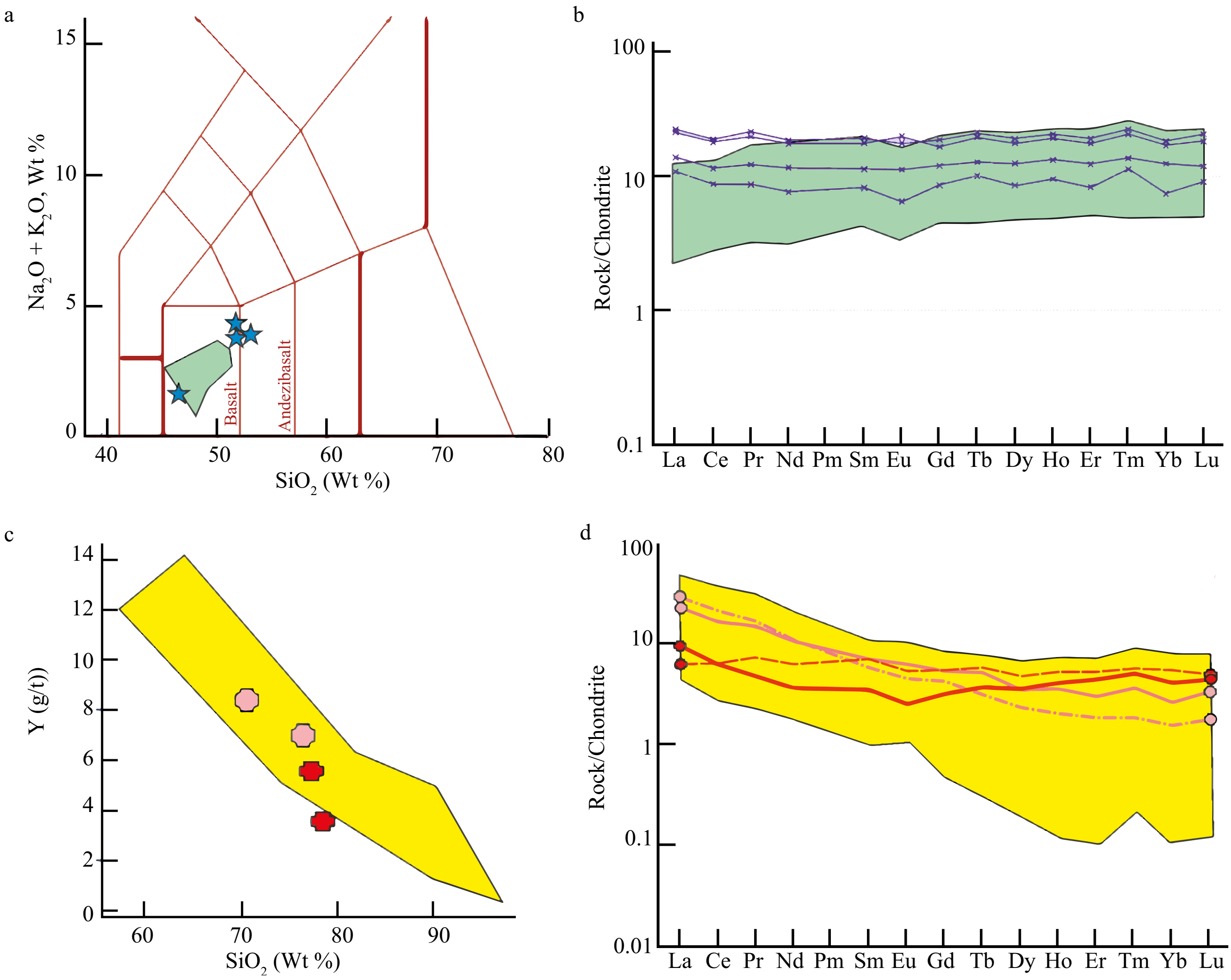

**Fig. 3.** Figurative points of amphibolite compositions (blue asterisks) (a, b), quartzites (pink symbols) – quartz graywacke (red symbols) (c, d) from conglomerate clasts on diagrams $SiO_2$-$Na_2$+$K_2O$ (a), $SiO_2$-Y (c) and chondrite-normalized REE patterns (b, d), green fields – composition of Mesoarchean basalts of KGB, yellow fields – compositions of Mesoarchean quartzites associated with BIF [15].

**Table 2**. Chemical composition (oxides in wt.%, elements in ppm) of fragments in Neoarchean (2.71 Ga) conglomerates of the Kostomuksha greenstone belt

| | 1 | 2 | 3 | 4 | 5 | 6 |
|---|---|---|---|---|---|---|
| $SiO_2$ | 70.52 | 78.69 | 76.36 | 52.22 | 50.72 | 45.08 |
| $TiO_2$ | 0.28 | 0.19 | 0.14 | 1.15 | 1.35 | 0.72 |
| $Al_2O_3$ | 7.8 | 9.98 | 2.79 | 16.8 | 17.19 | 11.59 |
| $Fe_2O_3$ | 1.21 | 0.47 | 3.16 | 1.05 | 1.02 | 1.9 |
| FeO | 7.39 | 2.15 | 6.75 | 8.48 | 7.39 | 13.06 |
| MnO | 0.164 | 0.076 | 0.125 | 0.223 | 0.187 | 0.436 |

*Ending*

| | 1 | 2 | 3 | 4 | 5 | 6 |
|---|---|---|---|---|---|---|
| MgO | 4.34 | 0.37 | 2.42 | 4.85 | 5.23 | 11.23 |
| CaO | 5.36 | 4.32 | 2.74 | 9.82 | 11.1 | 12.04 |
| $Na_2O$ | 1.09 | 2.35 | 0.22 | 3.56 | 4.03 | 1.02 |
| $K_2O$ | 0.16 | 0.11 | 0.11 | 0.28 | 0.21 | 0.46 |
| $P_2O_5$ | 0.015 | 0.02 | 0.02 | 0.07 | 0.1 | 0.05 |
| $H_2O$ | 0.26 | 0.04 | 0.72 | 0.11 | 0.05 | 0.13 |
| LOI | 0.96 | 0.98 | 4.25 | 1.26 | 1.31 | 2.06 |
| Li | 5.89 | 2.83 | 5.79 | 9.40 | 7.10 | 18.55 |
| Sc | 9.34 | 3.52 | 3.66 | 58.89 | 46.62 | 37.49 |
| V | 80.52 | 34.12 | 34.88 | 395.74 | 375.63 | 266.60 |
| Cr | 223.26 | 79.48 | 146.84 | 144.61 | 331.51 | 1513.63 |
| Co | 54.42 | 4.81 | 37.10 | 47.27 | 36.79 | 75.21 |
| Ni | 66.50 | 12.70 | 42.83 | 100.28 | 96.88 | 533.36 |
| Cu | 802.37 | 21.61 | 1281.09 | 13.22 | 22.41 | 22.57 |
| Zn | 59.92 | 36.45 | 40.24 | 100.68 | 75.94 | 160.12 |
| Rb | 1.67 | 3.48 | 2.76 | 3.50 | 5.89 | 4.78 |
| Sr | 50.64 | 117.23 | 5.92 | 211.93 | 246.74 | 18.17 |
| Y | 8.36 | 3.57 | 6.90 | 19.33 | 27.80 | 13.82 |
| Zr | 50.60 | 93.03 | 21.95 | 55.10 | 81.76 | 34.59 |
| Nb | 1.97 | 2.58 | 1.03 | 2.96 | 4.44 | 1.72 |
| Ba | 55.19 | 205.06 | 19.57 | 191.36 | 216.56 | 78.99 |
| La | 1.99 | 9.31 | 3.04 | 4.56 | 7.03 | 3.57 |
| Ce | 5.31 | 17.78 | 5.27 | 9.93 | 15.54 | 7.56 |
| Pr | 0.79 | 1.83 | 0.52 | 1.37 | 2.21 | 0.97 |
| Nd | 3.81 | 6.67 | 2.23 | 7.30 | 11.03 | 4.80 |
| Sm | 1.39 | 1.14 | 0.69 | 2.30 | 3.59 | 1.67 |
| Eu | 0.40 | 0.34 | 0.19 | 0.86 | 1.53 | 0.50 |
| Gd | 1.47 | 1.13 | 0.84 | 3.32 | 4.57 | 2.37 |
| Tb | 0.26 | 0.14 | 0.17 | 0.60 | 0.92 | 0.47 |
| Dy | 1.60 | 0.77 | 1.20 | 4.27 | 6.05 | 2.92 |
| Ho | 0.35 | 0.14 | 0.28 | 0.93 | 1.34 | 0.67 |
| Er | 1.15 | 0.40 | 0.96 | 2.78 | 3.95 | 1.87 |
| Tm | 0.17 | 0.05 | 0.15 | 0.41 | 0.62 | 0.34 |
| Yb | 1.17 | 0.33 | 0.87 | 2.73 | 3.74 | 1.63 |
| Lu | 0.16 | 0.06 | 0.15 | 0.40 | 0.62 | 0.31 |
| Hf | 1.46 | 2.24 | 0.75 | 2.20 | 3.00 | 1.39 |
| Ta | 0.17 | 0.22 | 0.24 | 0.33 | 0.39 | 0.17 |
| Pb | 1.91 | 3.29 | 1.09 | 6.18 | 8.20 | 1.86 |
| Th | 1.99 | 2.51 | 1.40 | 0.40 | 0.71 | 0.45 |
| U | 0.40 | 0.46 | 0.22 | 0.12 | 0.22 | 0.21 |

Note. 1 – E-K22-34/5a, plagioclase-magnetite-amphibole quartz graywacke (with predominant zircons aged 2749 Ma); 2 – E-K22-34/4, amphibole-biotite quartzite; 3 – E-K22-34/1, quartzite with sulfides; 4 – E-K22-34/3B, amphibolite (metagabbro); 5 – E-K22-34/6A, amphibolite (metagabbro); 6 – E-K22-34/8B, amphibolite. Major elements were determined by classical chemical silicate analysis method, and trace elements – by ICP MS method (X Series II, ThermoScientific) with dissolution in autoclaves at the Analytical Laboratory of the Institute of Geology, resource sharing center, Karelian Research Center RAS (Petrozavodsk).

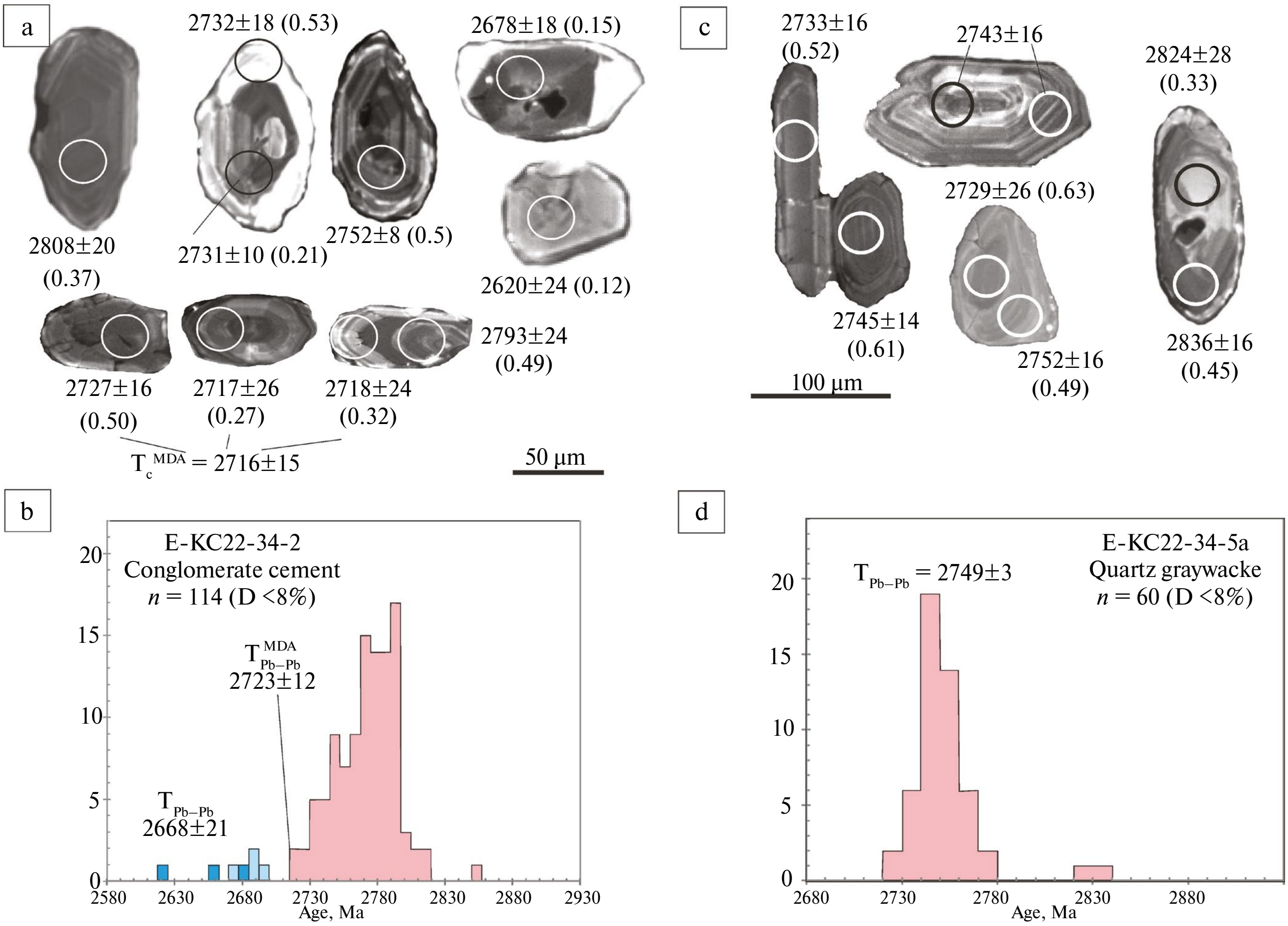

**Fig. 4.** Grain structure (a, c) and isotopic age (determined by LA-ICP-MS, *n* – number of analytical points, D* – discordance in %) of zircon from conglomerate cement (b) and quartz greywacke fragment (d) : (a, c) cathodoluminescent image of zircons from cement (a) and fragment (c) of conglomerate, circles – location of analytical dating points and their values $T_{\text{Pb-Pb}}$ in Ma (1σ), in brackets – Th/U ratio; (b, d) histograms of $^{207}$Pb – $^{206}$Pb ages ( $T_{\text{Pb-Pb}}$ ) of zircon from cement, $T^{\text{MDA}}_{\text{Pb-Pb}}$ – $^{207}$Pb – $^{206}$Pb age of three youngest grains (MDA – maximum depositional age). * D=100×( $T$ ($^{206}$Pb/ $^{238}$U)/ $T$ ($^{207}$Pb/ $^{206}$Pb)-1)

300 zircon grains were extracted. They are represented by yellowish-brown colored crystals of prismatic habit: from short- to long-prismatic with Ke – 1:2, 1:3, ranging in size from 40 to 150 μm (Fig. 4a). Based on internal structure, two morphological types can be distinguished among zircons in this sample. Grains of the first type, which strongly predominate, are characterized by distinct fine oscillatory zoning and Th/U ratio significantly greater than 0.2 (Fig. 4a), which is characteristic of magmatic zircon. Grains of the second type show signs of patchy zoning (Fig. 4a) and Th/U ratios for most of them are less than 0.2, which is typical for metamorphogenic zircon. Moreover, in zircons of both morphotypes, there are grains with light rims (Fig. 4a), which may indicate the presence of late metamorphogenic processes that cannot be dated in this sample.

$^{207}$Pb – $^{206}$Pb age ($T_{\text{Pb-Pb}}$) of zircons of the first morphological type varies from 2.86 to 2.717 Ga with a complex polymodal distribution of values (Fig. 4 c). $T_{\text{Pb/Pb}}$ of the three youngest zircon grains from this sample (2717±26 (discordance in % (D) = 0.01); 2718±24 (D = –0.01); 2727±16 (D = –2.5), Fig. 4a bottom row) is estimated at 2723±12 Ma (Fig. 4b). Similar estimates are obtained when calculating U – Pb concordant age ($T_{\text{c}}$) from these three points – 2716±15 (MSWD = 1.9) Ma. This figure is most accurate for estimating the maximum age of conglomerate sedimentation. $T_{\text{Pb-Pb}}$ of metamorphogenic zircons of the second morphological type, with discordance less than 5%, falls within the interval of 2.62–2.70 Ga and is estimated at 2668±21 Ma based on 7 points. Meanwhile, $T_c$ for the 5 most concordant points from this sample is 2672±12 (MSWD = 0.023) Ma.

Thus, the age of conglomerate sedimentation falls within the interval of 2716±15 – 2672±12 Ma. Its most probable estimate corresponds to the area of minimum density of analytical points between the two main peaks on the age distribution histogram (Fig. 4b) and is estimated at approximately 2.71 Ga.

The second sample for geochronological studies of conglomerates was taken from a quartz metagreywacke fragment (sample E-KS22-34-5a). From this 800 g sample, 250 zircon grains were separated. Their study showed that they are represented by transparent brown-colored idiomorphic crystals of elongated prismatic habit with elongation coefficient 1:2, 1:3, rarely 1:4 (Fig. 4c). These crystals are characterized by relatively high idiomorphism and diversity of morphological forms. Among them are prismatic, short-prismatic and isometric crystals of relatively large size (70—180 μm). The internal structure of all studied zircons is very similar and characterized by fine oscillatory zoning (Fig. 4c), their Th/U ratio varies from 0.2—1.1 (average 0.7), suggesting their original magmatic nature.

The distribution pattern of $T_{\text{Pb-Pb}}$ zircon in the histogram (it falls within a narrow range of 2.73—2.77 Ga) (Fig. 4 d), as well as the uniformity of its structural features, indicates the homogeneity of the sample. $T_{\text{Pb-Pb}}$ zircon population, comprising 97% of the total sample, is estimated at 2749±3 Ma (Fig. 4d), which within error margins coincides with its U – Pb-age at the upper intersection of discordia with concordia – 2748±3.5 (MSWD = 0.62) Ma. Additionally, among the studied zircons, a grain was identified with $T_{\text{Pb/Pb}}$ values of 2836±16 and 2824±28 Ma (D = –0.11 and –0.35) in two analytical points, respectively (Fig. 4b). Thus, the main source of material detritus (including zircon) during the formation of quartz metagreywacke from the conglomerate fragment is felsic igneous rocks aged 2749±3 Ma. Comparable age (2759 – 2743 Ma, [13]) is characteristic of rhyolites from the Gimoly STA (Table 1), which probably constitute the main source of detritus for sediments of this sequence. Additionally, Mesoarchean felsic igneous rocks contributed a small portion to the quartz metagreywacke composition. Thus, the quartz metagreywacke fragment shows similarities with greywackes of the Gimoly STA in terms of morphology and detrital zircon age, which formed nearly synchronously with Neoarchean (2.75– 2.74 Ga) dacites and BIF of this STA (Table 1) [11, 13].

## FORMATION CONDITIONS

Thus, the Neoarchean (2.71 Ga) polymictic conglomerates found in the KGB consist of fragments of surrounding metabasalts, Kontokki STA quartzites, and Gimoly STA quartz greywacke. Importantly, no zircons older than 2.85 Ga (with discordance less than 10%) were found in the cement. The fragments are poorly sorted, and angular fragments are common alongside rounded ones (Fig. 2). All these facts indicate that the conglomerate sequence formed in a basin that received local poorly sorted detrital material. The morphology of the fragments indicates that they were deformed under sinistral simple shear conditions. Considering the composition characteristics, structure, and subsequent deformation conditions, it can be suggested that the conglomerates mark a pull-apart type basin.

## MAIN CONCLUSIONS

1. In the axial part of the KGB among metabasalts of the Kontokki STA, a lens of previously unknown polymictic conglomerates was identified, whose clastic component consists of 1) metamorphosed basic rocks comparable in composition to Mesoarchean gabbroids and basalts of the KGB; 2) magnetite-amphibole quartzites comparable to Mesoarchean quartzites associated with BIF; 3) quartz metagreywacke comparable in composition and zirconology to sediments of the Neoarchean Gimoly STA.

2. The age of sedimentation of the discovered conglomerates based on the study of zircon from the cement is definitely younger than 2716±15 Ma and older than 2672±12 Ma, estimated at approximately 2.71 Ga. These data show that a new youngest among Archean STA has been established in the KGB. It is comparable in age to volcanics (2712–2703 Ma) of Khedozero-Bolshezero [12], Takanen (2706 Ma) [19] and sediments (<2.70 – 2.73 Ga) of Kuhmo [20] greenstone belts of the Karelian craton.

3. The studied conglomerates are intensely deformed under conditions of sinistral simple shear along the steep NE-trending planes.

4. The formation of late Neoarchean conglomerates of the KGB probably occurred in a pull-apart basin at the final stage of belt formation under shear deformation conditions. Under such

conditions, the well-known Timiskaming-type conglomerates of the Abitibi greenstone belt of the Superior Province were formed, which are associated with large gold deposits [3 ] .

## ACKNOWLEDGEMENTS

The authors express their gratitude to GIN RAS (Moscow) staff K.G. Erofeeva and A.S. Dubensky for conducting zircon dating work and consultations on using the results. The authors are grateful to Academician N.S. Bortnikov and the second reviewer of the manuscript for valuable comments and remarks that helped improve the article.

## FUNDING

This work was financially supported by the RSF (grant No. 22-17-00026)

## REFERENCES

1. *Ramsay J.G.* Folding and fracturing of rocks. McGraw-Hill, New York. 1967. 580 p.
2. *Brandl G., Cloete M., Anhaeusser C.R.* Archaean Greenstone Belt. In: The Geology of South Africa. Johnson M.R, Anhaeusser C.R., Thomas R.J. (Eds). The Geologly of South Africa. Geologica Society of South Africa, Johannesburg/Council for Geoscience, Pretoria. 2006. Pp. 9–56.
3. *Jackson S.L., Fyon J.A.* The Western Abitibi Subprovince in Ontarion. In: Geology of Ontario. Thurston P.C., Williams H.S., Sutcliffe R.H., Stott G.M. (Eds). Special Vol. 4, Part 1. Ontario Ministry of Northern Development and Mines, 1991. Pp. 405–484.
4. *Chernov V.M* . Stratigraphy and Sedimentation Conditions of Volcanogenic (Leptitic) Iron-Siliceous Formations of Karelia. Moscow-Leningrad: Nauka. 1964. 104 p.
5. *Svetov S.A., Svetova A.I. et al.* Neoarchean Pull-Apart Basins of the Central Karelian Terrane: Rock Sequences and Lithogeochemical Characteristics // Geology and Mineral Resources of Karelia. Issue 8. Petrozavodsk: KarRC RAS. 2005. Pp. 5–17.
6. *Piirainen T* . The geology of the Archaean greenstone-granitoid terrain in Kuhmo, eastern Finland // Archaean geology of the Fennoscandian Shield. Geol. Surv. Finland Spec. Pap.1988. No. 4. Pp. 39–51.
7. *Sorjonen Ward P.* An overview of structural evolution and lithic units within and intruding the late Archean Hattu schist belt, Ilomantsi, eastern Finland. In: Nurmi, P. A. & Sorjonen-Ward, P. (eds.) / Geological development, gold mineralization and exploration methods in the late Archean Hattu schist Belt, Ilomantsi, Eastern Finland. Geol. Surv. of Finland. Spec. Paper. 17. 1993. Pp. 9–102.
8. *Gorkovets V.Ya., Raevskaya M.B., Volodichev O.I. et al.* Geology and Metamorphism of Iron-Siliceous Formations in Karelia. Leningrad: Nauka; 1991. 176 p.
9. *Kulikov V.S., Svetov S.A., Slabunov A.I. et al.* Geological Map of Southeastern Fennoscandia Scale 1:750,000: New Approaches to Compilation // Proceedings of Karelian Research Centre RAS. Precambrian Geology Series. 2017. No.2. Pp. 3–41. DOI: 10.17076/geo444
10. Kostomuksha Ore District (Geology, Deep Structure and Minerageny). Gorkovets V.Ya., Sharov N.V. (eds.). Petrozavodsk: KarRC RAS. 2015. 322 p.
11. *Slabunov A.I., Kervinen A.V., Nesterova N.S.* Zircon from banded iron formation as a sensitive indicator of its polychronous background: a case study on the Kostomuksha greenstone belt, Karelian Craton. Fennoscandian Shield // International Geology Review. 2024. V. 66. No. 6. Pp. 1321–1333. DOI:10.1080/00206814.2023.2248501
12. *Myskova T.A., Milkevich R.I., Lvov P.A. et al.* Neoarchean Volcanics of the Khedozero-Bolshozero Greenstone Structure in Central Karelia: Composition, Age and Tectonic Setting // Stratigraphy and Geological Correlation. 2020. V. 28. No. 2. Pp. 3–32. DOI: 10.31857/S0869592X20020040
13. *Slabunov A.I., Nesterova N.S., Egorov A.V. et al.* Geochemistry, Zircon Geochronology and Age of the Archean Iron Formation of the Kostomuksha Greenstone Belt, Karelian Craton, Fennoscandian Shield // Geochemistry International. 2021. V. 66. No. 4. Pp. 291–307. DOI: 10.31857/S0016752521040063
14. *Milkevich R.I., Myskova T.A.* Late Archean Metaterrigenous Rocks of Western Karelia (Lithology, Geochemistry, Source Areas) // Lithology and Mineral Resources. 1998. No. 2. Pp. 177–194.
15. *Slabunov A.I., Nesterova N.S., Maksimov O.A.* .Geochemistry and Formation Conditions of Mesoarchean Banded Iron Formation (BIF-1) of the Kostomuksha Greenstone Belt, Karelian Craton // Geochemistry International. 2024. V. 69. No. 3. Pp. 28–50. DOI: 10.1134/S0016702924030054

16. *Kozhevnikov V.N.* Archean Greenstone Belts of the Karelian Craton as Accretionary Orogens. Petrozavodsk. 2000. 223 p.

17. *Mudruk S.V., Nesterova N.S., Maksimov O.A.* Structural Analysis of Archean Conglomerates of the Kostomuksha Greenstone Belt (Fennoscandian Shield): First Results // Proceedings of the Fersman Scientific Session of the GI KSC RAS. 2024. 21. Pp. 181–189. DOI: 10.31241/FNS.2024.21.022

18. *Ludwig K.R.* Isoplot v.4.15: A geochronological Toolkit for Microsoft Excel. Special Publication No.4. Berkeley Geochronology Center. 2008.

19. *Järvinen V., Karampelas N., Rämö O.T* . Secular change of tectonic setting in the Archean Takanen greenstone belt, northeastern Karelia Province, Fennoscandian Shield // Bulletin of the Geological Society of Finland. 2023. V. 95. No.2. Pp. 107–134. https://doi.org/10.17741/bgsf/95.2.002

20. *Lehtonen E., Heilimo E., Halkoaho T., Kapyaho A. Holtta P.* U-Pb geochronology of Archaean volcanic-sedimentary sequences in the Kuhmo greenstone belt, Karelia Province – Multiphase volcanism from Meso- to Neoarchaean and a Neoarchaean depositional basin? // Precambrian Research. 2016. V. 275. Pp. 48–69. DOI:10.1016/j.precamres.2015.12.002

DOKLADY EARTH SCIENCES, 2025, Vol. 520, No. 1, pp. 43–57

# THE AGE, COMPOSITION AND METALLOGENY OF THE PYRKATAGHIN GRANITOID MASSIF, CHUKOTKA ARCTIC COAST, NORTH-EAST RUSSIA

© 2025 **M. V. Luchitskaya**[a, *], **E. V. Vatrushkina**[a], **K. N. Mazurkevich**[b],
**and** Corresponding Member of RAS **S. D. Sokolov**[a]

Received August 20, 2024
Revised September 25, 2024
Accepted September 30, 2024

**Abstract.** The first U–Th–Pb zircon data for Pyrkataghin massif granitoids, located in the central part of Kuul Rise of Anyui-Chukotka fold system on the coast of East Siberian Sea are provided. They indicate the intrusion of granitoids in Albian time (106–104 Ma), which corresponds to Albian granitoid magmatism of Chaun province of Chukotka (110–100 Ma [1]) and coincides with Aptian-Albian postcollisional extension after termination of collision between Chukotka-Arctic Alaska microcontinent and Siberian continent with earlier accreted Kolyma-Omolon microcontinent. Increased alkalinity and geochemical features of Pyrkataghin massif granitoids, as enrichment of LIL and LREE, depletion in Ta, Nb, Ba, Sr make them similar to other postcollisional granitoids of Chauna province. The comparison of granitoids of the massif and granitoids with different types of mineralization is carried out.

**Keywords:** *granitoids, Pyrkataghin massif, zircon, Chukotka, postcollisional extension, Albian Chaun granitoid province, mineralization*

**DOI**: 10.31857/S26867397250105e6

## INTRODUCTION

The Chukotka region is characterized by widespread Early Cretaceous (Aptian-Albian) granitoid magmatism [2, 3]. It is related to post-collisional extension, accompanied by the formation of granite-metamorphic dome structures, superimposed basins in the continental part, and rift basins on the shelf of the Arctic seas [4, 5]. The collision itself of the Chukotka-Arctic Alaska microcontinent with the Siberian continent ended in the late Early Cretaceous (Hauterivian-Barremian) with the closure of the Late Jurassic residual South Anyui turbidite basin and the formation of a nappe-fold structure [4].

A number of authors divide the Chukotka belt of granitoid plutons into two provinces: Albian (Chaun) and Aptian (Bilibino or Tytelveem) based on the predominance of granitoids of one age or another, although the boundaries of these provinces are drawn differently [1, 2, 6].

The Upper Cretaceous Chaun metallogenic belt is directly associated with the Chaun granitoid province of the same name [7]. The main types of mineralization in this belt are cassiterite-silicate-sulfide, Sn–W-greisen, Sn-porphyry, and gold associated with granitoids [7]. Foreign researchers combine belts with such types of mineralization into Au–Bi–Sn–W provinces associated with granitoids, the most famous of which is the Middle-Late Cretaceous Tintina in Alaska (for example, [8]).

Large granitoid massifs of the Chukotka belt have a two-phase structure: the early phase is represented by porphyritic monzonitoids or granodiorites, biotite-amphibole granites, and the late phase – by subalkaline granites or leucogranites [9].

The granitoids of the Pyrkataghin massif discussed in the article, located in the central part of the Kuul uplift on the Arctic coast of the East Siberian Sea (Fig. 1) and having a two-phase structure, belong to the group of Early Cretaceous intrusive formations according to the materials of the Anyui-Chaun serial

---

[a] *Geological Institute Russian Academy of Sciences, Moscow, Russian Federation*
[b] *A.P.Karpinsky Russian Geological Research Institute, Saint-Petersburg, Russian Federation*
[*] *e-mail: luchitskaya@ginras.ru*

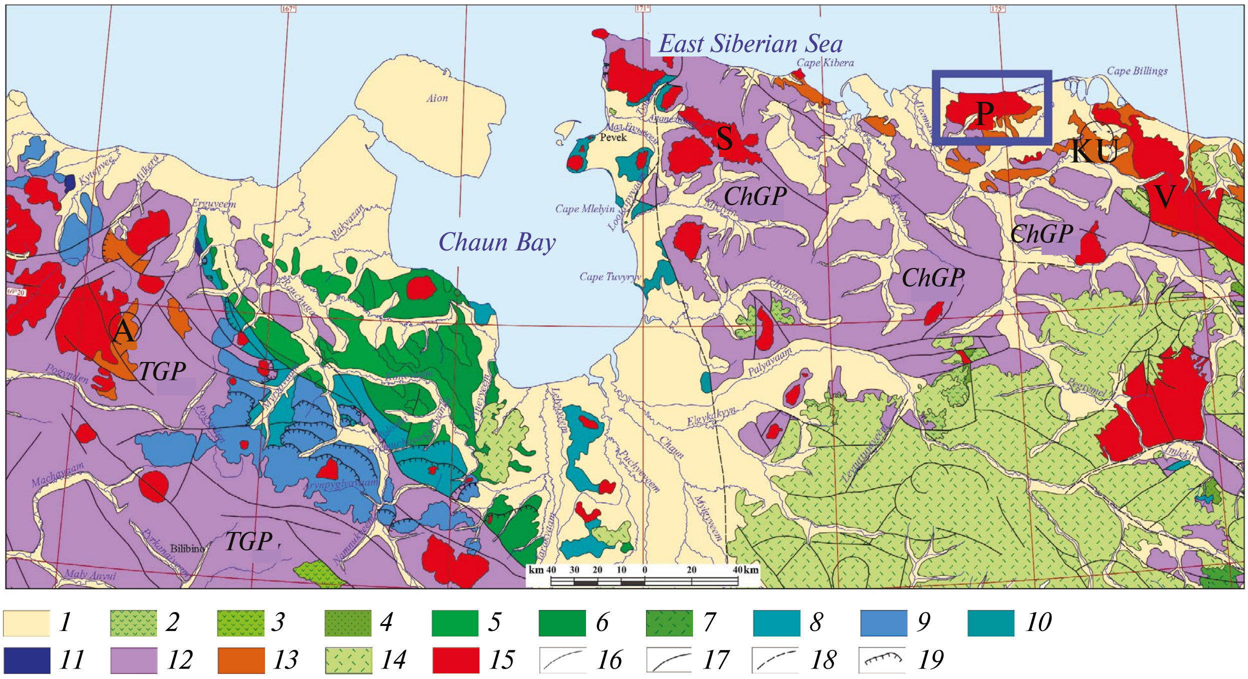

**Fig. 1.** Geological map of the Anyui-Chukotka fold system (after [9] with modifications). *1* – Cenozoic sedimentary cover; *2* – Etchikun Albian volcanic complex; *3* – Tytelveem Aptian volcanic complex; *4* – Aptian-Albian continental coal-bearing deposits; *5* – Valanginian terrigenous deposits; *6* – Berriasian terrigenous deposits; *7* – Berriasian volcanic deposits; *8* – Volgian volcanic-terrigenous deposits; *9* – Oxford-Kimmeridgian terrigenous deposits; *10* – undifferentiated Upper Jurassic-Lower Cretaceous deposits; *11* – Lower Jurassic terrigenous deposits; *12* – Triassic terrigenous deposits; *13* – Paleozoic terrigenous-carbonate deposits; *14* – Okhotsk-Chukotka volcanic belt; *15* – Cretaceous intrusive complex; *16* – geological boundaries; *17*–*19* – tectonic faults: *17* – established, *18* – hidden, *19* – thrusts . Letters in circles – tectonic uplifts: KU – Kuul, A – Alyarmaut. ChGP – Albian Chaun granitoid province; TGP – Aptian Tytelveemsky granitoid province [1]. Massifs: P – Pyrkataghin, V – Velitkenay, S – Severny. Blue rectangle shows the study area.

legend GK-200; precise geochronological data, as well as data on the rare element composition for the massif granitoids are absent.

In this article, we present the first U-Pb SIMS data on the age of granitoids from two intrusive phases of the Pyrkataginsky massif and the petrogeochemical characteristics of the granitoids, which allowed us to conduct their geochemical typification and attribute them to the Aptian-Albian postcollisional stage of development of the Chukotka Mesozoids. A comparison of the granitoids of the Pyrkataghin massif was carried out according to a number of geochemical criteria and granitoids with various types of mineralization.

## GEOLOGICAL AND PETROGRAPHIC CHARACTERISTICS

Kuul Uplift is located in the northern part of the Anyui-Chukotka fold system and extends west-northwest along the Arctic coast of the East Chukchi Sea east of Cape Kibera for approximately 200 km with a width ranging from 10 to 50 km (Fig. 1). In the central part of the uplift, predominantly terrigenous Devonian and terrigenous-carbonate Lower-Middle Carboniferous strata are exposed, which are unconformably overlain by terrigenous deposits of the Upper Permian – Triassic.

The Pyrkataghin massif is located in the central part of the Kuul Uplift, has an area of about 400 km$^2$ and represents an intrusive body elongated in the latitudinal direction with gentle contacts, discordant to the strike of the folded structures of the host Paleozoic and Triassic deposits (Fig. 2). The northern part of the massif is hidden under the waters of the East Siberian Sea. According to the gravimetric data of M.B. Rybakov (1964), the Pyrkataginsky massif is a laccolith-like body with a thickness of about 4 km.

Granitoids of the Pyrkataghin massif intrude the terrigenous-carbonate strata of the Devonian, Carboniferous terrigenous-carbonate strata, and terrigenous strata of the Permian and Lower-Middle Triassic (Fig. 2). In the southern part of the massif, granitoids contain xenoliths of host rocks [10]. Granitoids form numerous residual outliers (kekurs) of various shapes among eluvial talus on the surface

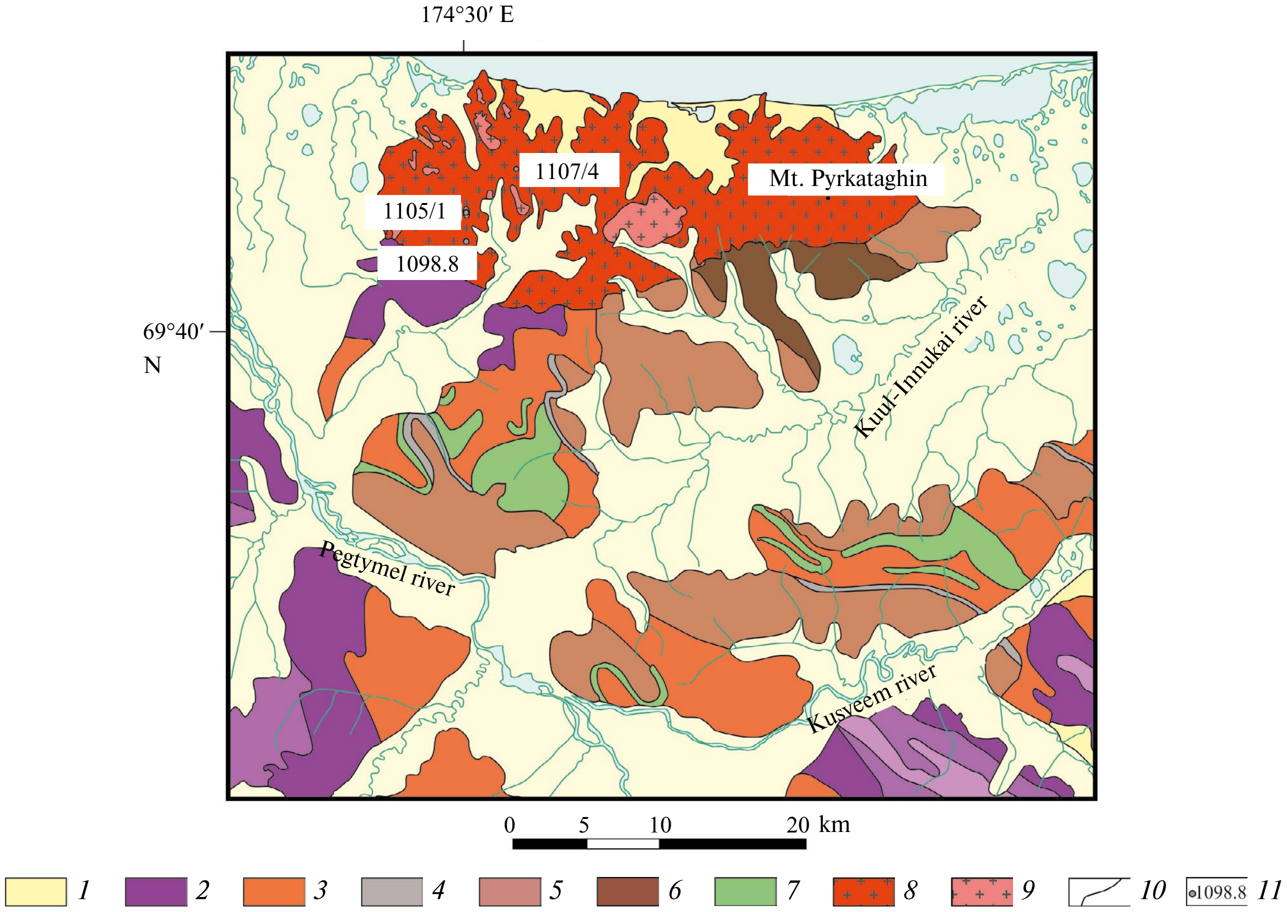

**Fig. 2.** Geological map of the Pyrkataghin massif and its framing (according to [10]). *1* – Quaternary deposits; *2* – Lower-Middle Triassic sandstones, siltstones, clay shales, lenticular interlayers of gravelites and conglomerates; *3* – Permian-Triassic carbonaceous-clay shales, siltstones and calcareous sandstones; *4* – Carboniferous limestones, conglomerates, gravelites, sandstones; *5* – Upper Devonian calcareous sandstones, clay-calcareous and siliceous-sericitic shales, siltstones, limestones; *6* – Lower-Middle Devonian quartz and calcareous sandstones, siltstones, clay and carbonaceous-clay shales, limestone lenses; *7* – Anyui gabbro-doleritic hypabyssal complex: sills and isometric bodies of gabbroids; *8* – porphyritic granodiorites and granites of the early phase; *9* – leucocratic fine-grained granites of the late phase; *10* – geological boundaries; *11* – sampling locations and numbers of geochronological samples.

of the massif (Fig. 3 a–c). Sedimentary rocks near the massif are transformed into cordierite-plagioclase-quartz-biotite and biotite-quartz hornfels; the width of hornfels outcrops ranges from 600 to 1100 m [10].

The Pyrkataghin massif consists of granitoids from two intrusion phases. The early phase is represented by porphyritic amphibole-biotite medium-coarse-grained granites forming the central part of the massif and porphyritic medium-coarse-grained granodiorites (Fig. 3e) in the peripheral parts of the massif, with gradual transitions between them; in places, schlieren texture is present in the granitoids (Fig. 3d). Porphyritic phenocrysts of pinkish potassium feldspar in granitoids make up 20–25%, their size ranges from 1 to 6 cm. Among the rocks of the early phase, quartz syenites are also described, forming small linearly elongated clusters and veins with diffuse outlines, not shown on the scale of the map [10]. They differ from porphyritic granodiorites by a higher content of potassium feldspar phenocrysts.

The granitoids of the early phase contain rare rounded inclusions of finer-grained and melanocratic rocks, 10–15 cm in size, often with porphyritic phenocrysts of potassium feldspar (Fig. 3h), corresponding to monzonites in composition.

The late phase includes fine-grained leucocratic subalkaline granites (Fig. 3g), forming local outcrops in the central and western parts of the massif and having cross-cutting contacts with granitoids of the early phase. Granitoids of both phases are cut by dikes of granite-porphyries, granodiorite-porphyries, granite-aplites (Fig. 3e), and monzodiorite-porphyrites.

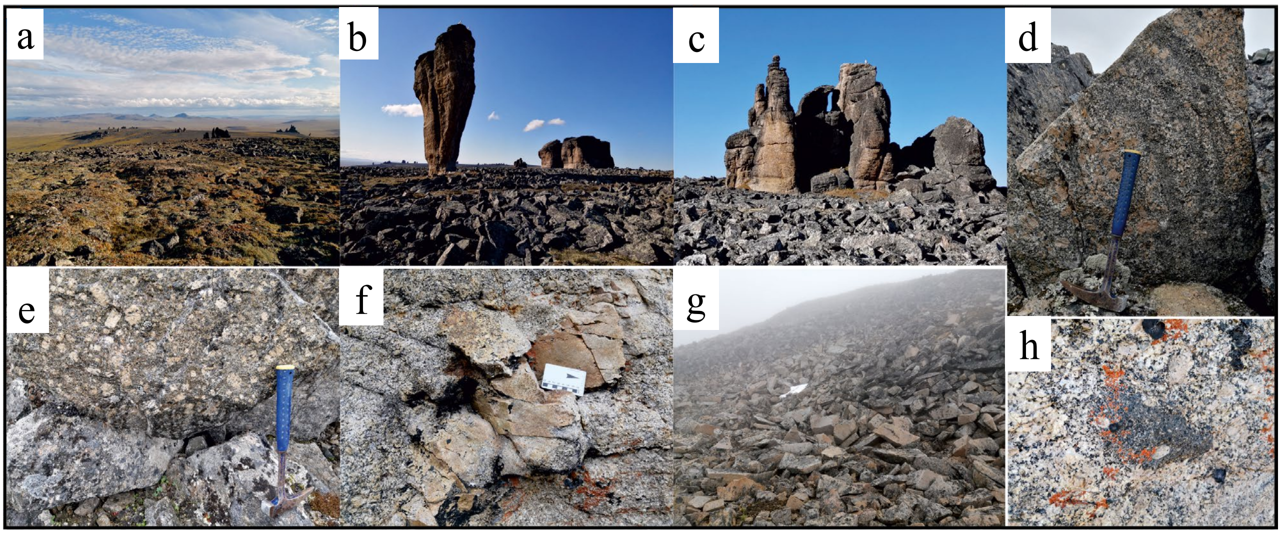

**Fig. 3.** Photos of the Pyrkataghin massif and its constituent granitoids. a–c – view of the massif with granitoid outliers; d – banded texture in early phase granitoids; e – porphyritic granodiorite of the early phase; f – granite-aplite dike in porphyritic granites of the early phase; g – eluvial talus of fine-grained leucocratic granites of the late phase; h – monzonite enclaves in granodiorites of the early phase.

Granodiorites have a porphyritic hypidiomorphic structure. Porphyritic phenocrysts are represented by potassium feldspar, and to a lesser extent, plagioclase. The groundmass is composed of plagioclase (35–45%), potassium feldspar (20–25%), quartz (20–25%), olive-green amphibole + brown biotite (10–12%). Accessory minerals are represented by apatite, sphene, zircon, epidote, orthite, and ore mineral (pyrite).

Among the minerals of the heavy fraction, hematite, almandine, magnetite, monazite, rutile, tourmaline, fluorite, anatase, molybdenite, and cassiterite have been identified. Less represented are arsenopyrite, barite, cinnabar, galena, chalcopyrite, scheelite, and cerussite [10].

Granites have a porphyritic hypidiomorphic structure and consist of the same minerals as granodiorites, but they have increased contents of quartz (30–35%) and potassium feldspar (35–40%) and a decreased amount of mafic minerals (5–7%).

Subalkaline leucocratic granites have a hypidiomorphic-granular texture with areas of graphic texture and are composed of plagioclase (30–35%), potassium feldspar (35–40%), quartz (25–30%), biotite (<5%). Accessory minerals are represented by apatite, sphene, and zircon.

Heavy fraction minerals in granites are represented by ilmenite, magnetite, orthite, tourmaline, fluorite, anatase, molybdenite, galena, pyrite, basaltic hornblende, epidote [10].

Monzonites from melanocratic enclaves in granodiorites of the early phase have a hypidiomorphic texture with areas of monzonitic texture and are composed of olive-green hornblende (20–25%), potassium feldspar (30–40%), plagioclase (30–35%), quartz (<5%). Accessory minerals are represented by sphene, apatite, epidote.

Granite-porphyries from dikes have a porphyritic texture with phenocrysts of potassium feldspar, quartz, and singular biotite. The groundmass is fine-grained and composed of quartz, plagioclase, and potassium feldspar in equal amounts and rare small laths of chloritized biotite. Accessories are represented by sphene, zircon, orthite.

Monzodiorite-porphyrites from dikes have a porphyritic texture with phenocrysts of plagioclase, amphibole, biotite, and singular quartz. The groundmass has a microlitic-granular texture and is composed of pyroxene, epidote, feldspars, and rare quartz.

## RESULTS OF GEOCHRONOLOGICAL STUDIES

Zircon separation was carried out at GIN RAS using standard methodology with heavy liquids. Geochronological studies by local U-Th-Pb method (SIMS, SHRIMP-II) were performed at the Center for Isotopic Research of the A.P. Karpinsky Russian Geological Research Institute according to the methodology described in [11].

Zircons were extracted from 3 samples: porphyritic granodiorites and granites of the early phase of the Pyrkataghin massif and subalkaline leucocratic granites of the late phase.

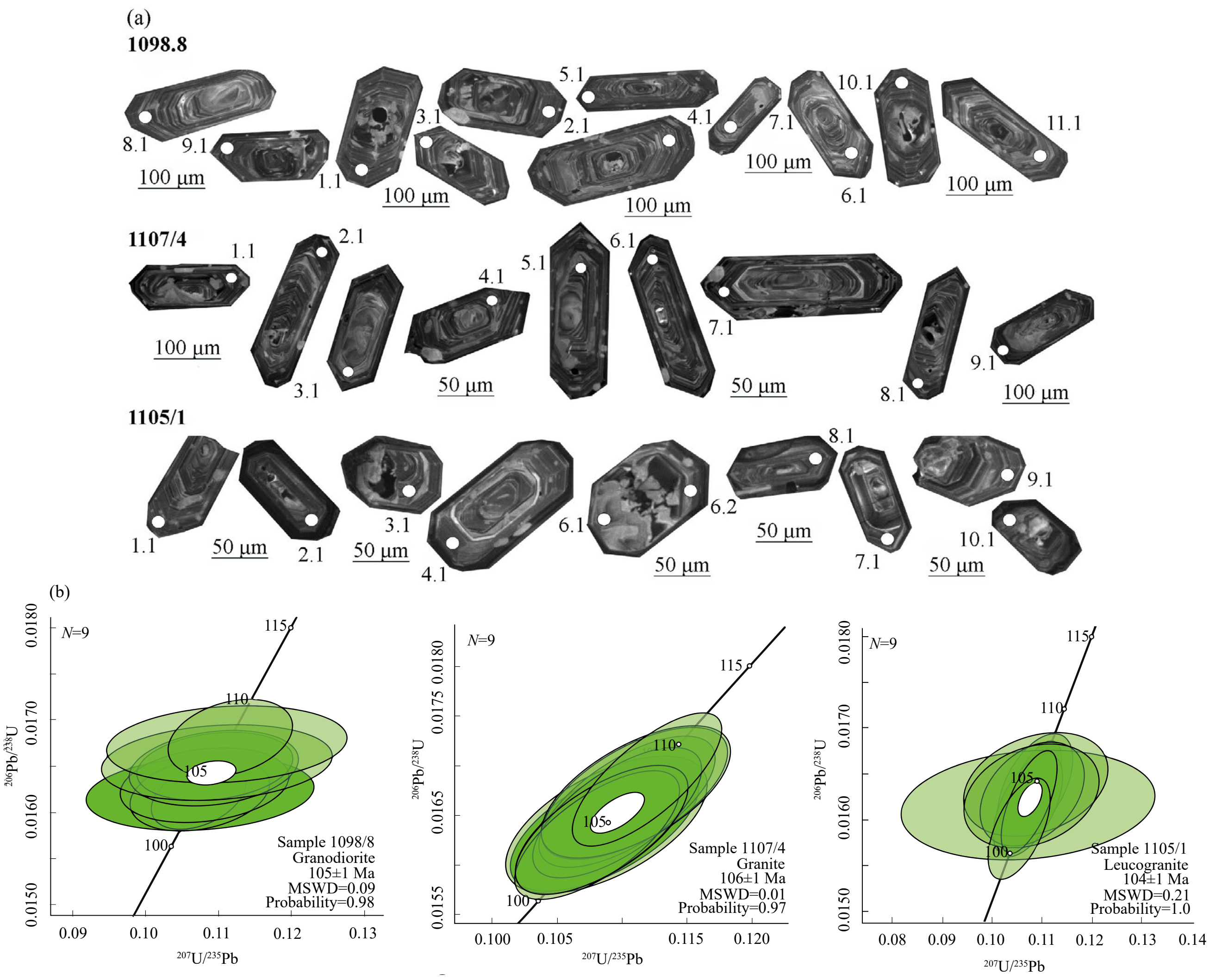

**Fig. 4.** Microphotographs of zircon crystals in cathodoluminescence mode (a) and concordia diagrams for zircon from granodiorite (sample 1098.8), granite (sample 1107/4) of the early phase and leucogranite (sample 1105/1) of the late phase (b). Point numbers correspond to the numbers in table 1.

Zircon crystals from granitoids of both phases in cathodoluminescence microphotographs show short and long prismatic habits, with crystal sizes varying from 150 to 370 µm (1.5–3.5) (Fig. 4a). Zircon is characterized by well-defined oscillatory magmatic zoning, and core parts in some cases have complex heterogeneous structure (Fig. 4 a). Only zircon areas with oscillatory zoning were analyzed. The Th/U ratio in the analyzed zircon varies from 0.31 to 0.73 (Table 1).

Concordant zircon ages from porphyritic granodiorites and granites of the early phase of the Pyrkataghin massif are 105±1 and 106±1 Ma; subalkaline leucocratic granites of the late phase 104±1 Ma (Table 1). The obtained age estimates coincide within error limits for granitoids of both phases, reflect the crystallization age of magmatic zircon, and correspond to the Early Cretaceous (Albian).

## PETRO-GEOCHEMICAL COMPOSITION OF GRANITOIDS

Analysis of rock-forming major elements was carried out in the accredited laboratory of chemical-analytical research at the Geological Institute, RAS (Moscow, Russia) using X-ray fluorescence method with a sequential spectrometer S4 Pioneer (Bruker, Germany) and Spectra-Plus software.

Trace element analysis was conducted at the Analytical Certification Testing Center of the Institute of Microelectronics Technology and High Purity Materials RAS (Chernogolovka, Moscow Region, Russia) using inductively coupled plasma atomic emission spectrometry (ICAP-61, Thermo Jarrell Ash , USA) and inductively coupled plasma

**Table 1**. Results of U-Th-Pb SIMS dating of zircon from granitoids of the Pyrkataghin massif.

| Analysis spot | $Pb_c$, % | U, ppm | Th, ppm | Pb*, ppm | $^{232}Th/^{238}U$ | Age, Ma | | Isotope ratios | | | | | | error corr. |
|---|---|---|---|---|---|---|---|---|---|---|---|---|---|---|
| | | | | | | $^{206}Pb/^{238}U$ (2) | ±% | $^{207}Pb^*/^{206}Pb^*$ (1) | ±% | $^{207}Pb^*/^{235}U$ (1) | ±% | $^{206}Pb^*/^{238}U$ (1) | ±% | |
| 1098.8 – early phase granodiorite; 105±1 Ma, 69°44'13.9", 174°28'13.6" | | | | | | | | | | | | | | |
| 1098-8_7.1 | 0.20 | 1122 | 795 | 15.3 | 0.73 | 102 | 1 | 0.048 | 2.7 | 0.105 | 3.0 | 0.016 | 1.3 | .420 |
| 1098-8_5.1 | 0.55 | 854 | 448 | 11.9 | 0.54 | 103 | 1 | 0.048 | 5.8 | 0.107 | 5.9 | 0.016 | 1.0 | .173 |
| 1098-8_10.1 | 0.13 | 1686 | 771 | 23.5 | 0.47 | 103 | 1 | 0.049 | 2.2 | 0.110 | 2.4 | 0.016 | 0.9 | .388 |
| 1098-8_6.1 | 0.27 | 778 | 376 | 10.9 | 0.50 | 104 | 1 | 0.048 | 3.4 | 0.107 | 3.6 | 0.016 | 1.0 | .278 |
| 1098-8_8.1 | 0.40 | 1172 | 481 | 16.4 | 0.42 | 104 | 1 | 0.048 | 4.2 | 0.108 | 4.3 | 0.016 | 1.0 | .226 |
| 1098-8_4.1 | 0.41 | 1715 | 595 | 24.3 | 0.36 | 106 | 1 | 0.045 | 4.1 | 0.102 | 4.2 | 0.016 | 0.9 | .224 |
| 1098-8_11.1 | 0.59 | 742 | 297 | 10.6 | 0.41 | 106 | 1 | 0.046 | 6.6 | 0.105 | 6.7 | 0.016 | 1.1 | .161 |
| 1098-8_3.1 | 0.38 | 1165 | 501 | 16.6 | 0.44 | 106 | 1 | 0.049 | 4.1 | 0.112 | 4.2 | 0.017 | 1.0 | .231 |
| 1098-8_9.1 | 0.57 | 1632 | 719 | 23.3 | 0.46 | 106 | 1 | 0.051 | 5.4 | 0.116 | 5.5 | 0.017 | 1.0 | .177 |
| 1098-8_2.1 | 0.55 | 1338 | 600 | 19.3 | 0.46 | 107 | 1 | 0.047 | 6.0 | 0.109 | 6.1 | 0.017 | 1.0 | .165 |
| 1098-8_1.1 | 0.16 | 1534 | 728 | 22.1 | 0.49 | 107 | 1 | 0.047 | 3.0 | 0.111 | 3.1 | 0.017 | 1.0 | .307 |
| 1107/4 – early phase granite; 106±1 Ma; 69°47'21.8", 174°35'19.1" | | | | | | | | | | | | | | |
| 1107-4-1.1 | 0.00 | 1018 | 491 | 14.3 | 0.50 | 105 | 2 | 0.049 | 2.1 | 0.110 | 2.7 | 0.016 | 1.6 | .615 |
| 1107-4-2.1 | 0.00 | 1354 | 818 | 19 | 0.62 | 105 | 2 | 0.048 | 1.9 | 0.109 | 2.5 | 0.016 | 1.6 | .650 |
| 1107-4-3.1 | 0.00 | 798 | 356 | 11.2 | 0.46 | 105 | 2 | 0.048 | 2.4 | 0.109 | 2.9 | 0.016 | 1.7 | .580 |
| 1107-4-4.1 | 0.00 | 1256 | 811 | 17.9 | 0.67 | 106 | 2 | 0.048 | 1.8 | 0.110 | 2.5 | 0.017 | 1.6 | .664 |
| 1107-4-5.1 | 0.07 | 1130 | 776 | 16.2 | 0.71 | 107 | 2 | 0.049 | 1.9 | 0.113 | 2.6 | 0.017 | 1.6 | .622 |
| 1107-4-6.1 | 0.00 | 1314 | 743 | 18.7 | 0.58 | 106 | 2 | 0.049 | 1.8 | 0.111 | 2.4 | 0.017 | 1.6 | .671 |
| 1107-4-7.1 | 0.00 | 1349 | 793 | 19.3 | 0.61 | 107 | 2 | 0.047 | 2.1 | 0.109 | 2.7 | 0.017 | 1.6 | .612 |
| 1107-4-8.1 | 0.00 | 1549 | 669 | 21.7 | 0.45 | 104 | 2 | 0.048 | 1.7 | 0.107 | 2.4 | 0.016 | 1.6 | .688 |
| 1107-4-9.1 | 0.00 | 1244 | 843 | 17.5 | 0.70 | 105 | 2 | 0.048 | 1.9 | 0.108 | 2.5 | 0.016 | 1.6 | .659 |
| 1107-4-10.1 | 0.00 | 2189 | 771 | 31.7 | 0.36 | 108 | 2 | 0.047 | 1.4 | 0.110 | 2.1 | 0.017 | 1.6 | .751 |
| 1105/1 – late phase leucogranite; 104±1 Ma; 69°46'8.13", 174°29'23.3" | | | | | | | | | | | | | | |
| 1105-1_1.1 | 0.09 | 1973 | 891 | 28.9 | 0.47 | 109 | 1 | 0.049 | 1.5 | 0.114 | 2.1 | 0.017 | 1.4 | .676 |
| 1105-1_2.1 | 0.11 | 1683 | 710 | 23.5 | 0.44 | 104 | 1 | 0.047 | 1.7 | 0.106 | 2.2 | 0.016 | 1.4 | .635 |
| 1105-1_3.1 | 0.10 | 1425 | 606 | 20.1 | 0.44 | 105 | 1 | 0.048 | 2.4 | 0.109 | 2.8 | 0.016 | 1.4 | .513 |
| 1105-1_4.1 | 0.09 | 1087 | 425 | 15.1 | 0.40 | 103 | 1 | 0.049 | 2.1 | 0.109 | 2.6 | 0.016 | 1.4 | .557 |
| 1105-1_5.1 | 3.93 | 1634 | 491 | 23.7 | 0.31 | 103 | 1 | 0.052 | 8.8 | 0.116 | 8.9 | 0.016 | 1.5 | .168 |
| 1105-1_6.1 | 1.77 | 1418 | 441 | 20.4 | 0.32 | 105 | 1 | 0.052 | 4.7 | 0.119 | 5 | 0.016 | 1.4 | .292 |
| 1105-1_6.2 | 0.41 | 1085 | 205 | 15.2 | 0.19 | 104 | 1 | 0.047 | 3.7 | 0.105 | 4 | 0.016 | 1.4 | .361 |
| 1105-1_7.1 | 0.47 | 1358 | 812 | 19.0 | 0.62 | 104 | 1 | 0.047 | 5.0 | 0.105 | 5.2 | 0.016 | 1.4 | .277 |
| 1105-1_8.1 | 0.04 | 1586 | 744 | 22.1 | 0.48 | 104 | 1 | 0.048 | 1.6 | 0.108 | 2.1 | 0.016 | 1.4 | .662 |
| 1105-1_9.1 | 0.13 | 1535 | 642 | 21.0 | 0.43 | 102 | 1 | 0.048 | 2.0 | 0.104 | 2.4 | 0.016 | 1.4 | .580 |

Note. Error at 1-sigma level; $Pb_c$ and $Pb^*$ – common and radiogenic lead respectively. (1) – corrected for $^{204}$Pb, (2) – corrected for $^{207}$Pb, error corr. – error correlation coefficient.

mass spectrometry (X-7, Thermo Elemental, USA).

All examined rocks of the Pyrkataghin massif, according to the ratio of total alkalis to silica, belong to moderately alkaline rocks: granodiorites and granites of the early phase ($SiO_2$ 64.7–73.2%, $Na_2O+K_2O$ 7.13–8.84%) belong to granosyenites and moderately alkaline granites, subalkaline leucocratic granites of the late phase and granite-porphyries from dikes ($SiO_2$ 74.5–76.74%, $Na_2O+K_2O$ 8.05–9.51%) belong to moderately alkaline leucogranites, monzonites from enclaves and monzodiorite-porphyrites from dikes ($SiO_2$ 58.54–59.3%, $Na_2O+K_2O$ 7.62–9.15%) belong to monzonites (Fig. 5 a; Table 2). The composition points of granitoids are located in the field of granitoids of the Chaun province [1], where Albian age granitoids predominate (Fig. 1, 5). In terms of $K_2O/SiO_2$, granitoids of both phases of the Pyrkataghin massif belong to high-potassium and partially to shoshonitic series.

In the diagrams of B.R. Frost et al. [12], granitoids of both phases are predominantly magnesian (Fe*=0.59–0.80), calc-alkalic and alkali-calcic formations (MALI=3.71–8.93), characterized by low and

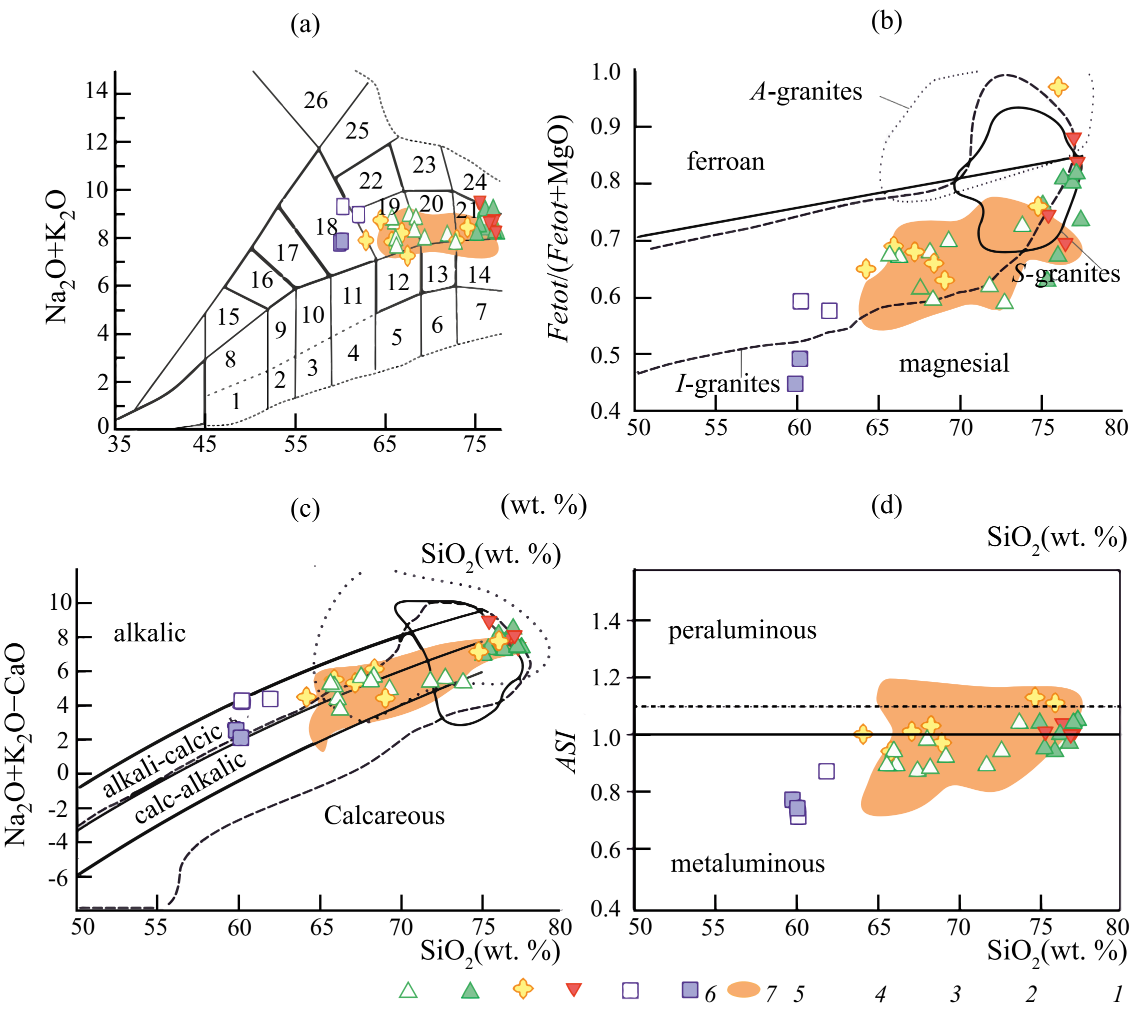
(a)
(b)
(c)
(d)

**Fig. 5.** Diagrams of $Na_2O+K_2O-SiO_2$ (a), $Fe_{tot}/(Fe_{tot}+MgO)-SiO_2$ (b), $Na_2O+K_2O-CaO-SiO_2$ (c), ASI-$SiO_2$ (d) for granitoids of the Pyrkataghin massif. 1 – low-alkaline gabbro, 2 – low-alkaline gabbro-diorites, 3 – low-alkaline diorites, 4 – low-alkaline quartz diorites, 5 – low-alkaline granodiorites, 6 – low-alkaline granites, 7 – low-alkaline leucogranites, 8 – gabbro, 9 – gabbro-diorites, 10 – diorites, 11 – quartz diorites, granodiorites, 12 – granodiorites, 13 – granites; 14 – leucogranites, 15 – monzogabbro, 16 – monzogabbro-diorites, 17 – monzodiorites, 18 – monzonites, 19 – granosyenites, 20 – moderately alkaline granites, 21 – moderately alkaline leucogranites, 22 – syenites, 23 – alkaline granites, 24 – alkaline leucogranites, 25 – alkaline syenites, 26 – foid syenites. *1* – granosyenites, moderately alkaline granites of early phase; *2* – moderately alkaline leucogranites of late phase; *3* – massif granitoids according to [6]; *4* – granite-aplites from dikes; *5* – monzonites from inclusions in early phase granitoids; *6* - monzonite-porphyrites from dikes; *7* – field of granitoids of the Chaun province according to [1].

moderate alumina saturation (ASI=0.89–1.06) (Fig. 5 b–d).

Variations of major elements in granitoids of both phases depending on $SiO_2$ content demonstrate well-defined trends of decreasing $Al_2O_3$, CaO, $FeO_{tot}$ + $TiO_2$ + MgO, $P_2O_5$ contents (Fig. 6). The behavior of $Na_2O$, $K_2O$ relative to $SiO_2$ is less regular: their contents in the early phase granitoids remain approximately at the same level, while in the late phase granitoids they are somewhat higher. Monzonites from enclaves and dikes form separate fields (Fig. 6).

The contents of Zr, La, Sc, Sr also decrease with increasing $SiO_2$. Simultaneous decrease in Sr contents and increase in Rb contents correspond to the fractional crystallization trend [13]. Covariations of $FeO_{tot}$ + $TiO_2$ + MgO and $SiO_2$ in granitoids indicate fractionation of amphibole and biotite, while covariations of Ba and Sr indicate fractionation of plagioclase and potassium feldspar (Fig. 6).

Granosyenites and moderately alkaline granites of the early phase are distinguished by higher total concentrations of trace elements in general, have higher total REE concentrations (304–403 ppm) and Th, elevated concentrations of Co, Ni, V, Cr compared to moderately alkaline leucogranites of the late phase and granite-aplites from dikes (ΣREE 52–307 ppm) (Table 2).

Granosyenites and moderately alkaline granites of the early phase have fractionated REE distributions with LREE enrichment ($La_N$ /$Lu_N$ = 21.61–29.72; $La_N$ /$Sm_N$ =4.69–6.92; $Gd_N$ / $Lu_N$ = 2.18–2.73) and negative Eu anomaly (Eu/Eu*=0.38–0.59) (Fig. 7a). The REE distribution for early phase rocks generally fits within the field of granitoids and orthogneisses of the Chukotka Belt [2] and differs from the Chaun province granitoids by more fractionated character and less pronounced negative Eu anomaly (Fig. 7a).

Monzonites from enclaves in early phase granosyenites and from dikes have REE patterns similar to early phase granitoids: $La_N$ /$Lu_N$ =10.68–30.74; $La_N$ /$Sm_N$ =2.90–5.09; $Gd_N$ /$Lu_N$ =2.41–3.53; Eu/Eu* = 0.44–0.64) (Fig. 7c).

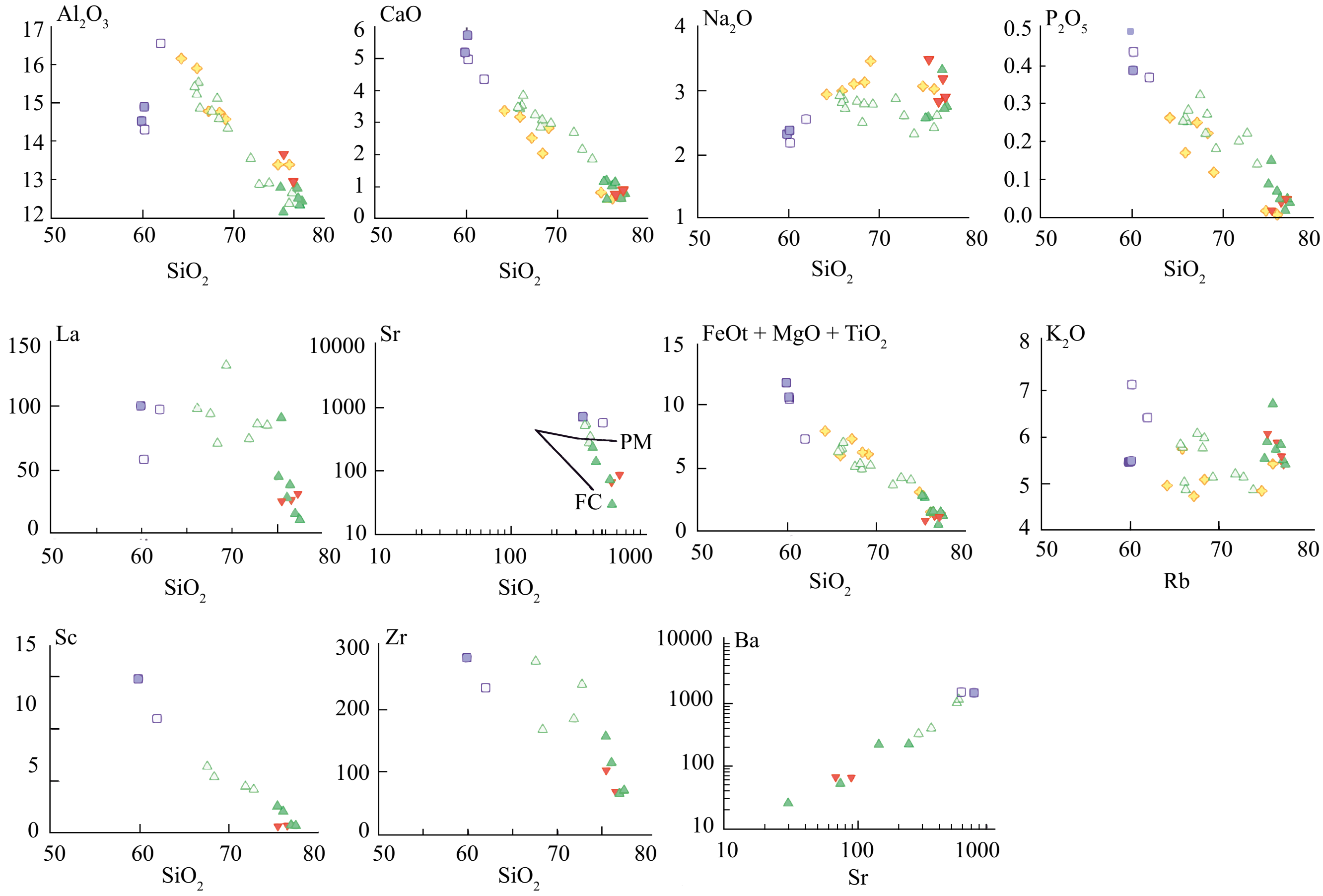

**Fig. 6.** Variations of major and trace elements in granitoids of the Pyrkataghin massif. Trends: PM – partial melting, FC – fractional crystallization. For other symbols see Fig. 5.

**Table 2**. Chemical composition of granitoids from the Pyrkataghin massif

| Sample | 1107/2 | 1102/2 | 1098/9 | 1104/2 | 1104/1 | 1110/2 | 1110/1 | 1100/6 | 1100/4 | 1098/1 | 1098/2 | 1100/2 | 1099/1 |
|---|---|---|---|---|---|---|---|---|---|---|---|---|---|
| No. | 1 | 2 | 3 | 4 | 5 | 6 | 7 | 8 | 9 | 10 | 11 | 12 | 13 |
| $SiO_2$ | 64.7 | 64.9 | 65.5 | 65.5 | 67.00 | 67.6 | 67.75 | 68.6 | 71.24 | 72.03 | 73.2 | 74.5 | 75.70 |
| $TiO_2$ | 0.61 | 0.62 | 0.63 | 0.69 | 0.56 | 0.52 | 0.49 | 0.47 | 0.40 | 0.45 | 0.44 | 0.30 | 0.19 |
| $Al_2O_3$ | 15.20 | 15.00 | 15.40 | 14.70 | 14.67 | 15.00 | 14.47 | 14.20 | 13.45 | 12.75 | 12.80 | 12.70 | 12.33 |
| $Fe_2O_3$ | 1.15 | 1 | 0.85 | 1.18 | 0.89 | 0.89 | 0.68 | 0.83 | 0.95 | 1.10 | 0.73 | 0.73 | 0.47 |
| FeO | 2.8 | 3.09 | 3.27 | 3.22 | 2.00 | 2.47 | 2.01 | 2.56 | 1.15 | 1.23 | 1.95 | 1.23 | 0.41 |
| MnO | 0.07 | 0.08 | 0.10 | 0.08 | 0.07 | 0.06 | 0.06 | 0.07 | 0.05 | 0.06 | 0.05 | 0.02 | 0.00 |
| MgO | 1.86 | 1.85 | 1.91 | 2.08 | 1.76 | 1.55 | 1.79 | 1.43 | 1.23 | 1.55 | 0.99 | 0.59 | 0.41 |
| CaO | 3.42 | 3.37 | 3.5 | 3.8 | 3.21 | 2.83 | 3.05 | 2.94 | 2.66 | 2.13 | 1.83 | 1.13 | 1.00 |
| $Na_2O$ | 2.88 | 2.77 | 2.84 | 2.69 | 2.81 | 2.48 | 2.77 | 2.76 | 2.85 | 2.58 | 2.3 | 2.55 | 2.41 |
| $K_2O$ | 5.76 | 5.69 | 4.99 | 4.82 | 6.03 | 5.72 | 5.93 | 5.09 | 5.17 | 5.09 | 4.83 | 5.5 | 6.68 |
| $P_2O_5$ | 0.25 | 0.26 | 0.25 | 0.28 | 0.32 | 0.22 | 0.27 | 0.18 | 0.20 | 0.22 | 0.14 | 0.088 | 0.07 |
| LOI | 0.55 | 0.5 | 0.39 | 0.42 | 0.46 | 0.45 | 0.49 | 0.4 | 0.53 | 0.67 | 0.6 | 0.45 | 0.25 |
| Sum | 99.25 | 99.13 | 99.63 | 99.46 | 99.78 | 99.79 | 99.77 | 99.53 | 99.88 | 99.86 | 99.86 | 99.79 | 99.92 |
| Li | – | – | – | – | 67.6 | – | 76.8 | – | 70.8 | 63.8 | – | – | 61.5 |
| Be | – | – | – | – | 6.8 | – | 7.0 | – | 9.4 | 7.3 | – | – | 7.5 |
| Sc | – | – | – | – | 6.4 | – | 5.4 | – | 4.5 | 4.2 | – | – | 2.1 |
| V | – | – | – | – | 57.6 | – | 51.2 | – | 33.2 | 30.6 | – | – | 10.6 |
| Cr | – | – | – | – | 19.6 | – | 22.7 | – | 19.4 | 9.4 | – | – | 5.3 |
| Co | – | – | – | – | 9.1 | – | 8.3 | – | 6.2 | 5.8 | – | – | 1.8 |
| Ni | – | – | – | – | 10.7 | – | 10.5 | – | 8.9 | 5.9 | – | – | 1.9 |
| Zn | – | – | – | – | 42.6 | – | 48.2 | – | 39.2 | 37.8 | – | – | 12.6 |
| Ga | – | – | – | – | 16.9 | – | 16.9 | – | 16.2 | 14.9 | – | – | 13.3 |
| Rb | – | – | – | – | 352 | – | 348 | – | 379 | 371 | – | – | 417 |
| Sr | – | – | – | – | 556 | – | 538 | – | 347 | 279 | – | – | 141 |
| Y | – | – | – | – | 28.0 | – | 24.2 | – | 18.4 | 29.3 | – | – | 25.3 |
| Zr | – | – | – | – | 277 | – | 168 | – | 185 | 240 | – | – | 115 |
| Nb | – | – | – | – | 19.9 | – | 16.8 | – | 18.0 | 23.1 | – | – | 23.8 |
| Mo | – | – | – | – | 1.5 | – | 1.0 | – | 2.7 | 1.9 | – | – | 1.1 |
| Sn | – | – | – | – | 6.6 | – | 5.6 | – | 4.5 | 10.1 | – | – | 5.9 |
| Sb | – | – | – | – | 0.25 | – | 0.23 | – | 0.32 | 0.19 | – | – | 0.24 |
| Cs | – | – | – | – | 29.0 | – | 20.8 | – | 31.1 | 19.2 | – | – | 28.3 |
| Ba | – | – | – | – | 1163 | – | 1022 | – | 403 | 328 | – | – | 221 |
| La | – | – | 98.8 | – | 94.7 | – | 71.3 | 133 | 74.9 | 86.6 | 85.6 | 45.1 | 28.4 |
| Ce | – | – | 196 | – | 188 | – | 135 | 240 | 124 | 146 | 157 | 73.2 | 63.3 |
| Pr | – | – | 21.5 | – | 19.2 | – | 14.9 | 25.4 | 12.3 | 15.4 | 16.1 | 6.28 | 7.5 |
| Nd | – | – | 75.2 | – | 66.6 | – | 53.6 | 88.2 | 40.7 | 53 | 57 | 20.5 | 28.9 |
| Sm | – | – | 11.4 | – | 11.4 | – | 9.8 | 12.4 | 7.1 | 10.1 | 9.87 | 2.8 | 6.5 |
| Eu | – | – | 1.88 | – | 1.8 | – | 1.5 | 1.45 | 1.1 | 1.1 | 0.97 | 0.45 | 0.69 |
| Gd | – | – | 10.2 | – | 7.9 | – | 6.6 | 10.7 | 4.8 | 7.1 | 8.66 | 2.51 | 4.7 |
| No. | 1 | 2 | 3 | 4 | 5 | 6 | 7 | 8 | 9 | 10 | 11 | 12 | 13 |
| Tb | – | – | 1.17 | – | 1.1 | – | 0.90 | 1.28 | 0.65 | 1.0 | 1.04 | 0.33 | 0.71 |
| Dy | – | – | 6.39 | – | 5.2 | – | 4.6 | 6.7 | 3.2 | 5.4 | 5.87 | 1.53 | 4.1 |
| Ho | – | – | 1.06 | – | 0.95 | – | 0.85 | 1.15 | 0.59 | 0.96 | 0.91 | 0.27 | 0.78 |

*Continued*

| Sample | 1107/2 | 1102/2 | 1098/9 | 1104/2 | 1104/1 | 1110/2 | 1110/1 | 1100/6 | 1100/4 | 1098/1 | 1098/2 | 1100/2 | 1099/1 |
|---|---|---|---|---|---|---|---|---|---|---|---|---|---|
| Er | – | – | 2.89 | – | 2.5 | – | 2.2 | 2.95 | 1.7 | 2.6 | 2.66 | 0.83 | 2.3 |
| Tm | – | – | 0.37 | – | 0.35 | – | 0.32 | 0.42 | 0.24 | 0.39 | 0.37 | 0.11 | 0.35 |
| Yb | – | – | 2.57 | – | 2.5 | – | 2.1 | 2.96 | 1.8 | 2.6 | 2.75 | 1.04 | 2.5 |
| Lu | – | – | 0.49 | – | 0.36 | – | 0.30 | 0.55 | 0.27 | 0.38 | 0.42 | 0.23 | 0.38 |
| Hf | – | – | – | – | 7.1 | – | 4.3 | – | 4.9 | 6.9 | – | – | 3.8 |
| Ta | – | – | – | – | 1.9 | – | 1.5 | – | 1.8 | 2.5 | – | – | 2.9 |
| W | – | – | – | – | 9.4 | – | 9.4 | – | 10.8 | 7.0 | – | – | 2.7 |
| Pb | – | – | – | – | 62.2 | – | 64.9 | – | 65.4 | 56.9 | – | – | 79.0 |
| Bi | – | – | – | – | 0.23 | – | 0.28 | – | 0.16 | 0.22 | – | – | 0.36 |
| Th | – | – | – | – | 55.8 | – | 55.7 | – | 53.7 | 59.6 | – | – | 59.0 |
| U | – | – | – | – | 7.3 | – | 10.9 | – | 12.2 | 9.4 | – | – | 7.5 |
| $SiO_2$ | 74.88 | 76 | 76.67 | 76.74 | 76.3 | 75.10 | 75.83 | 76.3 | 76.4 | 58.67 | 59.3 | 58.54 | 58.9 |
| $TiO_2$ | 0.33 | 0.16 | 0.06 | 0.17 | 0.15 | 0.09 | 0.14 | 0.08 | 0.10 | 0.63 | 0.78 | 0.89 | 0.75 |
| $Al_2O_3$ | 12.07 | 12.60 | 12.74 | 12.33 | 12.20 | 13.60 | 12.81 | 12.40 | 12.20 | 15.69 | 14.10 | 14.22 | 14.60 |
| $Fe_2O_3$ | 0.70 | 0.53 | 0.18 | 0.35 | 0.55 | 0.28 | 0.40 | 0.5 | 0.45 | 1.30 | 1.74 | 1.62 | 1.36 |
| FeO | 0.82 | 0.62 | 0.17 | 0.43 | 0.58 | 0.27 | 0.35 | 0.44 | 0.58 | 2.69 | 4.21 | 3.44 | 3.67 |
| MnO | 0.03 | 0 | 0.00 | 0.00 | 0.02 | 0.00 | 0.03 | 0.00 | 0.03 | 0.09 | 0.14 | 0.09 | 0.09 |
| MgO | 0.86 | 0.26 | 0.08 | 0.27 | 0.24 | 0.18 | 0.31 | 0.12 | 0.19 | 2.84 | 3.96 | 6.04 | 5.05 |
| CaO | 1.17 | 1.11 | 0.68 | 0.75 | 0.75 | 0.58 | 0.70 | 0.6 | 0.81 | 4.13 | 4.91 | 5.09 | 5.62 |
| $Na_2O$ | 2.57 | 2.6 | 3.32 | 2.73 | 2.69 | 3.46 | 2.78 | 3.15 | 2.85 | 2.42 | 2.15 | 2.27 | 2.33 |
| $K_2O$ | 5.86 | 5.71 | 5.82 | 5.37 | 5.45 | 6.05 | 5.84 | 5.54 | 5.36 | 6.08 | 7.02 | 5.35 | 5.38 |
| $P_2O_5$ | 0.15 | 0.05 | 0.02 | 0.04 | 0.05 | 0.02 | 0.04 | 0.05 | 0.05 | 0.35 | 0.43 | 0.48 | 0.38 |
| LOI | 0.47 | 0.27 | 0.24 | 0.76 | 0.57 | 0.33 | 0.73 | 0.34 | 0.46 | 4.81 | 0.52 | 1.58 | 1.29 |
| Sum | 99.91 | 99.86 | 99.98 | 99.93 | 99.50 | 99.95 | 99.96 | 99.47 | 99.43 | 99.70 | 99.26 | 99.61 | 99.42 |
| Li | 51.2 | 24.5 | 24.5 | 30.2 | 25.5 | 25.5 | 49.0 | – | – | 68.8 | – | 104.7 | – |
| Be | 6.5 | 19.7 | 19.7 | 7.8 | 10.4 | 10.4 | 8.8 | – | – | 7.4 | – | 6.7 | – |
| Sc | 2.6 | 0.80 | 0.80 | 0.74 | 0.68 | 0.68 | 0.76 | – | – | 11.0 | – | 14.8 | – |
| V | 26.1 | 2.4 | 2.4 | 7.6 | 3.5 | 3.5 | 6.2 | – | – | 59.1 | – | 96.4 | – |
| Cr | 15.4 | 9.0 | 9.0 | 11.3 | 9.9 | 9.9 | 10.5 | – | – | 123 | – | 240 | – |
| Co | 4.0 | 0.57 | 0.57 | 1.0 | 1.2 | 1.2 | 1.4 | – | – | 14.1 | – | 22.8 | – |
| Ni | 6.9 | 3.2 | 3.2 | 4.1 | 3.5 | 3.5 | 3.8 | – | – | 43.3 | – | 112 | – |
| Zn | 26.2 | 2.2 | 2.2 | 14.1 | 9.3 | 9.3 | 13.6 | – | – | 53.9 | – | 60.7 | – |
| Ga | 13.7 | 17.8 | 17.8 | 14.0 | 14.4 | 14.4 | 13.7 | – | – | 18.0 | – | 15.8 | – |
| Rb | 394 | 547 | 547 | 528 | 621 | 621 | 543 | – | – | 469 | – | 333 | – |
| Sr | 236 | 29.8 | 29.8 | 73.0 | 88.0 | 88.0 | 67.3 | – | – | 580 | – | 721 | – |
| Y | 15.5 | 5.4 | 5.4 | 3.9 | 5.3 | 5.3 | 6.7 | – | – | 29.1 | – | 30.8 | – |
| Zr | 157 | 65.6 | 65.6 | 70.9 | 103 | 103 | 68.9 | – | – | 235 | – | 283 | – |
| Nb | 15.9 | 56.5 | 56.5 | 12.0 | 18.0 | 18.0 | 13.8 | – | – | 18.9 | – | 19.4 | – |

*Ending*

| Sample | 1100/1 | 1099/2 | 1101/1 | 1105/1 | 1105/2 | 1110/4 | 1098/4 | 1110/5 | 1098/5 | 1104/3 | 1100/8 | 1108/1 | 1108/2 |
|---|---|---|---|---|---|---|---|---|---|---|---|---|---|
| No. | 14 | 15 | 16 | 17 | 18 | 19 | 20 | 21 | 22 | 23 | 24 | 25 | 26 |
| Mo | 3.5 | 1.7 | 1.7 | 2.3 | 0.10 | 0.10 | 0.78 | – | – | 1.9 | – | 1.2 | – |
| Sn | 4.8 | 1.7 | 1.7 | 5.0 | 1.8 | 1.8 | 3.8 | – | – | 5.7 | – | 5.4 | – |
| Sb | 0.24 | 0.22 | 0.22 | 0.22 | 0.27 | 0.27 | 0.26 | – | – | 0.74 | – | 0.53 | – |
| Cs | 25.4 | 26.1 | 26.1 | 36.1 | 49.2 | 49.2 | 39.0 | – | – | 38.8 | – | 40.2 | – |
| Ba | 224 | 25.5 | 25.5 | 52.4 | 66.1 | 66.1 | 67.1 | – | – | 1526 | – | 1491 | – |
| La | 91.5 | 38.5 | 15.8 | 11.0 | 25.6 | 25.6 | 26.8 | 31.6 | 31,6 | 98.2 | 58.8 | 101 | – |
| Ce | 144 | 76.2 | 25.1 | 36.8 | 47.9 | 47.9 | 48.3 | 56.3 | 56,3 | 176 | 143 | 199 | – |
| Pr | 12.8 | 7.78 | 2.1 | 1.8 | 3.7 | 3.7 | 4.0 | 4.54 | 4,54 | 19.8 | 17.5 | 23 | – |
| Nd | 40.5 | 26.3 | 5.6 | 5.8 | 10.0 | 10.0 | 12.1 | 14.7 | 14,7 | 70.6 | 70.8 | 85.6 | – |
| Sm | 6.1 | 4.37 | 0.83 | 1.0 | 1.3 | 1.3 | 2.0 | 2.12 | 2,12 | 12.4 | 13.1 | 15.3 | – |
| Eu | 0.67 | 0.61 | 0.073 | 0.19 | 0.18 | 0.18 | 0.22 | 0.25 | 0,25 | 2.2 | 1.78 | 2.5 | – |
| Gd | 3.8 | 3.74 | 0.56 | 0.73 | 0.80 | 0.80 | 1.2 | 1.65 | 1,65 | 8.5 | 11.5 | 10.1 | – |
| Tb | 0.52 | 0.5 | 0.094 | 0.11 | 0.13 | 0.13 | 0.18 | 0.22 | 0,22 | 1.1 | 1.31 | 1.3 | – |
| Dy | 2.7 | 2.83 | 0.56 | 0.59 | 0.73 | 0.73 | 1.0 | 1.23 | 1,23 | 5.4 | 7.86 | 6.2 | – |
| Ho | 0.48 | 0.52 | 0.13 | 0.11 | 0.15 | 0.15 | 0.19 | 0.24 | 0,24 | 0.96 | 1.22 | 1.1 | – |
| Er | 1.4 | 1.7 | 0.45 | 0.37 | 0.52 | 0.52 | 0.61 | 0.61 | 0,61 | 2.5 | 3.85 | 2.8 | – |
| Tm | 0.21 | 0.26 | 0.093 | 0.063 | 0.10 | 0.10 | 0.10 | 0.094 | 0,094 | 0.35 | 0.49 | 0.37 | – |
| Yb | 1.5 | 2.06 | 0.90 | 0.52 | 0.96 | 0.96 | 0.91 | 1.15 | 1,15 | 2.4 | 3.94 | 2.5 | – |
| Lu | 0.24 | 0.37 | 0.18 | 0.097 | 0.18 | 0.18 | 0.15 | 0.22 | 0,22 | 0.35 | 0.59 | 0.35 | – |
| Hf | 4.3 | 4.5 | 4.5 | 2.3 | 4.3 | 4.3 | 2.7 | – | – | 6.0 | – | 7.3 | – |
| Ta | 1.7 | 5.0 | 5.0 | 1.4 | 2.2 | 2.2 | 1.5 | – | – | 1.6 | – | 1.6 | – |
| W | 3.5 | 7.3 | 7.3 | 18.0 | 3.8 | 3.8 | 9.8 | – | – | 7.5 | – | 2.6 | – |
| Pb | 69.7 | 101.7 | 101.7 | 81.4 | 109 | 109 | 96.5 | – | – | 52.3 | – | 58.0 | – |
| Bi | 0.17 | 8.8 | 8.8 | 0.66 | 0.40 | 0.40 | 0.28 | – | – | 0.38 | – | 0.62 | – |
| Th | 77.9 | 21.3 | 21.3 | 35.2 | 46.1 | 46.1 | 45.5 | – | – | 55.7 | – | 50.5 | – |
| U | 13.4 | 57.8 | 57.8 | 8.9 | 15.0 | 15.0 | 11.1 | – | – | 15.5 | – | 11.0 | – |

Note. 1–11 – granosyenites, moderately alkaline granites of early phase; 12–18 – moderately alkaline leucogranites of late phase; 19–22 – granite-porphyries, granite-aplites from dikes; 23, 24 – monzonites from inclusions in early phase granitoids; 25, 26 – monzonite-porphyrites from dikes.

Late phase moderately alkaline leucogranites and granite-aplites from dikes are also characterized by fractionated REE patterns ($La_N/Lu_N = 8.10–40.10$; $La_N/Sm_N = 2.82–12.23$; $Gd_N/Lu_N = 0.38–1.93$) and negative Eu anomaly (Eu/Eu*=0.33–0.67), but differ by wider spread of REE spectra (Fig. 7b).

Spider diagrams for granosyenites, moderately alkaline granites of early phase, monzonites from inclusions and dikes are characterized by Ba, Ta, Nb, Sr, P, Ti minima and Cs, Th, Pb, LREE maxima (Fig. 7d, e). Spider diagrams of late phase granitoids and granite-aplites from dikes differ by deeper Ba, Sr, P, Ti minima (Fig. 7f).

The classification of granitoids related to different mineralization varieties is based on geochemical criteria, such as the ratio of ferrous and ferric iron (belonging to magnetite or ilmenite series) and Rb/Sr ratio [8, 14]. The composition points of the Pyrkataghin massif granitoids fall into fields characteristic of granitoids associated with W- and W–Mo-, partially Au–(Bi) mineralization (Fig. 8).

The presence of magnetite and ilmenite in the heavy fraction of early and late phase granitoids, respectively, suggests that granosyenites and granites of the early phase can be attributed to the magnetite series, while moderately alkaline leucogranites of the

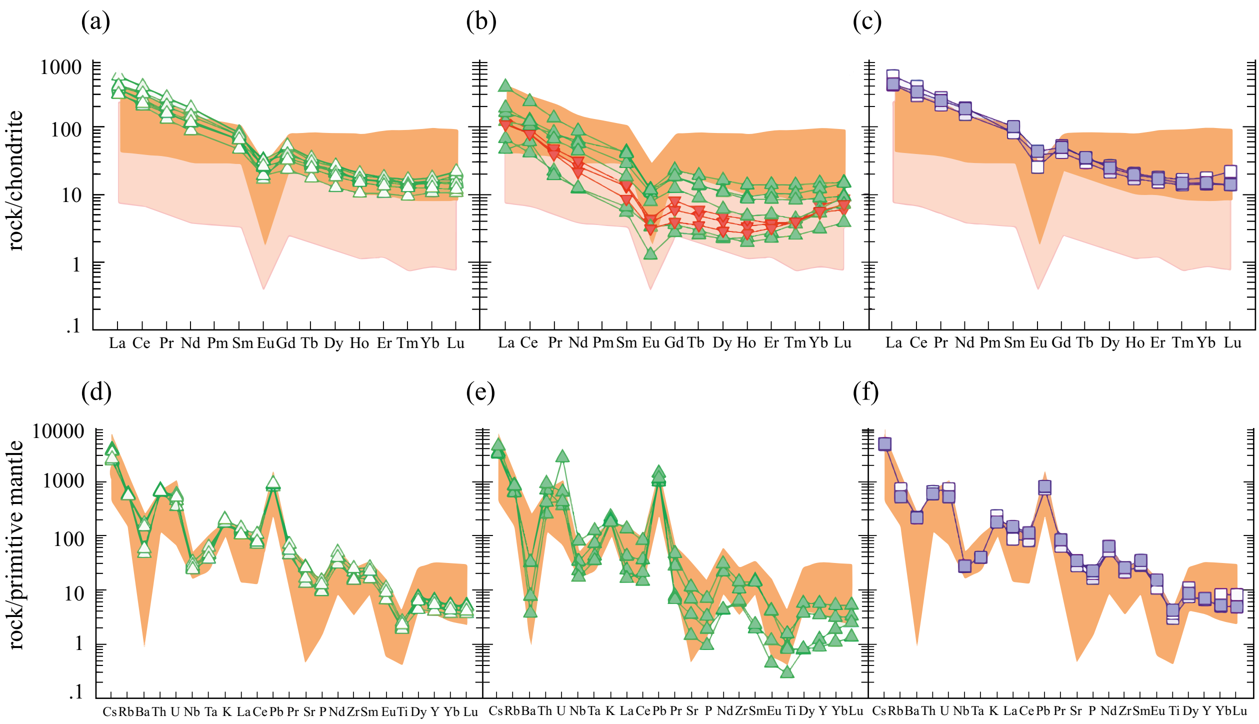

**Fig. 7.** Chondrite-normalized REE patterns (a-c) and primitive mantle-normalized spider diagrams (d-f) for granitoids of the Pyrkataginsky massif. Pink field shows granitoids and orthogneisses of the Chukotka Peninsula after [2, 6]. For other symbols see Fig. 5.

late phase belong to the ilmenite series. According to the ratio of $Fe_2O_3/FeO$ and $SiO_2$ [8], granitoids of both phases ($Fe_2O_3/FeO = 0.26–1.15$) are located along the division line between magnetite and ilmenite series granitoids (Fig. 8 a), and according to the iron oxidation coefficient ($f = 0.28–0.54$ [15]), the granitoids belong predominantly to the magnetite series. The $Fe_2O_3/FeO$ ratio increases with increasing $SiO_2$. The Chaun province granitoids shown for comparison also belong to both magnetite and ilmenite series, but the latter predominates.

## DISCUSSION AND CONCLUSIONS

New U–Pb zircon age estimates for granitoids of both phases of the Pyrkataghin massif indicate their emplacement during the Albian time (106–104 Ma), which corresponds to the interval of Albian granitoid magmatism in the Chaun province of Chukotka (110–100 Ma [1]). The Aptian-Albian stage of granitoid magmatism coincides with post-collisional extension after the termination of collision between the Chukotka-Arctic Alaska microcontinent and the Siberian continent with the previously accreted Kolyma-Omolon microcontinent [2–4]. The extension was accompanied by the formation of granite-metamorphic core complexes within structures previously described as uplift structures, where the crystalline basement and Paleozoic cover of the Chukotka microcontinent are exposed, as well as the formation of superimposed orogenic basins [4]. The Aptian-Albian extension stage is also widely manifested within the Laptev, East Siberian, and Chukchi sea shelves adjacent to the Arctic margin of Chukotka [5].

The age of the Pyrkataginsky massif granitoids also overlaps with the age of volcanics from the Etchikun Formation (Fig. 1) of shoshonite and latite series (110–106 Ma [16]; 107±2 Ma [17]), which correspond to a separate magmatic stage preceding the formation of the Okhotsk-Chukotka volcanic belt and also characterize the post-collisional extension stage [17].

On the Rb-Y+Nb diagram, used to distinguish intermediate-felsic magmatic rocks by geodynamic settings of formation, the Pyrkataghin massif granitoids occupy a boundary area between syn- and post-collisional granites, due to relatively high Rb contents, although the Chaun province granitoids generally fall within the post-collisional granitoid field (Fig. 9a).

Comparison of the Pyrkataghin massif granitoids with petrogeochemical granite types

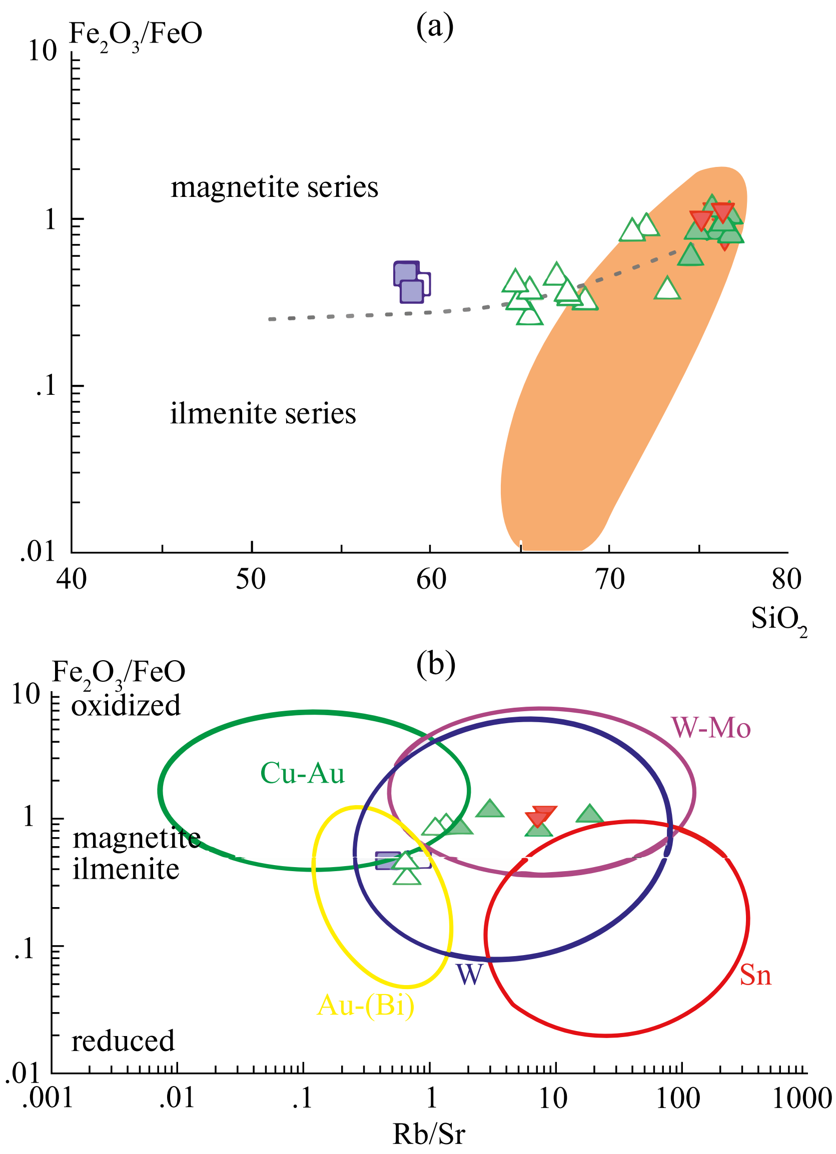

**Fig. 8.** $Fe_2O_3/FeO-SiO_2$ (b) [8] and $Fe_2O_3/FeO-Rb/Sr$ (a) [14] diagrams for granitoids of the Pyrkataghin massif. For symbols see Fig. 5.

on FeO*/MgO-Zr+Nb+Ce+Y and $Fe_2O_3$ *x5-$Na_2O+K_2O-(CaO+MgO)x5$ diagrams (Fig. 9b, c) shows that granitoids of both phases are localized in I- and S-type granite fields, as are the Chaun province granitoids in general, but some of the latter show similarity to A-type granites based on rare element content. The late-phase leucogranites of other Chaun province massifs also show similarity to A-granites: based on zircon geochemistry for the Velitkenay massif [6] and biotite compositions for the Severny massif [18].

The authors of [1] note the similarity of Albian granitoids of the Chaun province with orogenic high-K series [19] depleted in Ta, Nb and enriched in large-ion lithophile elements and LREE. The formation of orogenic high-potassium magmas is associated with the melting of lithospheric mantle previously enriched by earlier magmatic and metasomatic processes [20]. According to [1], in the case of the Chaun granitoid province, source enrichment may occur due to fluid influx from the previously subducting lithosphere of the South Anyui Ocean. For granitoids of this province, mixing of magmas from protoliths of coeval shoshonitic series volcanics and continental crust rocks is also assumed based on Nd−Sr isotope data [1].

The increased alkalinity and geochemical characteristics of the Pyrkataghin massif granitoids, such as enrichment in large-ion lithophile elements and LREE, depletion in Ta, Nb, Ba, Sr, make

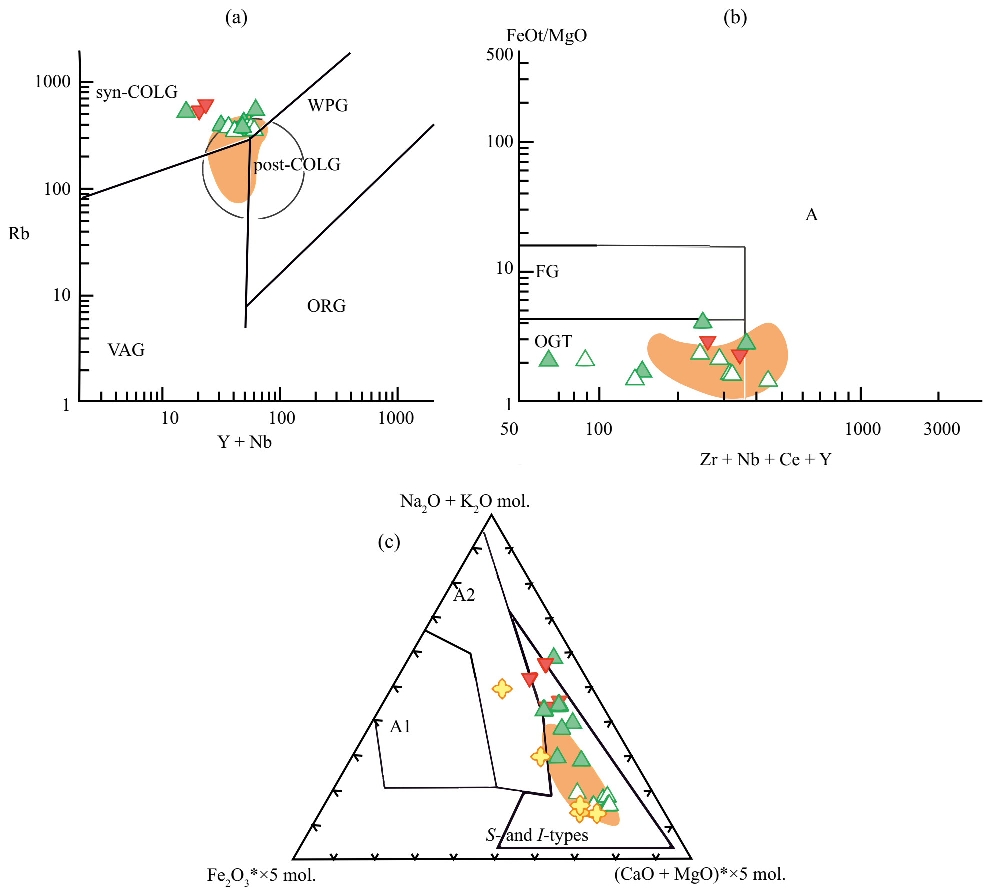

**Fig. 9.** Rb-Y+Nb (a), FeOt/MgO-Zr+Nb+Ce+Y (b), $Fe_2O_3$ *x5-$Na_2O$+$K_2O$-(CaO+MgO)x5 (mol. prop.) diagrams for the Pyrkataghin massif granitoids.

them similar to other granitoids of the Chaun province and suggest similar magma sources. The presence of monzonite inclusions with K-feldspar phenocrysts in early-phase granosyenites indicates a process of mechanical and chemical interaction between magma formed by lower crustal material melting due to magmatic underplating and acidic magma. According to Harker diagrams and Sr and Rb, $TiO_2$ and Zr, Ba and Sr covariations, fractional crystallization subsequently took place with fractionation of amphibole, biotite, apatite, plagioclase, and K-feldspar. Late-phase leucogranites are likely products of silicic melt differentiation. However, judging by data from late-phase leucogranites of other Chaun province massifs, they may also have an independent source, which is proven based on isotopic data for both rocks and zircons [2, 6, 18].

The classification of granitoids from the Pyrkataghin massif as both magnetite and ilmenite series based on the $Fe_2O_3$/FeO ratio and the presence of corresponding heavy fraction minerals suggests the possibility of both Cu-Au and Sn-W mineralization. However, comparison of granitoids from both phases of the massif and granitoids with Cu-Au, W-Mo, W, Sn, and Au-(Bi) mineralization based on $Fe_2O_3$/FeO and Rb/Sr parameters shows that the granitoids may be potentially ore-bearing in relation to W-Mo, W, and partially Au-(Bi) (Fig 8). The obtained results are in good agreement with the data from geological prospecting works conducted earlier [10]. A large W halo with an area of about 550 sq km was identified here, located in the upper reaches of rivers draining the granitoids of the Pyrkataghin massif. The scheelite content in the alluvium of these watercourses reaches 75 g/$m^3$. Within the massif, 4 molybdenum occurrences were also noted, represented by molybdenite flakes in thin pegmatite veinlets of aplites and quartz-fluorite veins [10].

## ACKNOWLEDGEMENTS

Field work was carried out with funding from the A.P. Karpinsky Russian Geological Research Institute; analytical data were obtained through state assignment No. FMMG-2024-0001, with basic funding for GIN RAS staff provided through subsidies. The authors express gratitude to anonymous reviewers for constructive comments and recommendations that helped improve the article.

## REFERENCES

1. *Tikhomirov P.L., Luchitskaya M.V., Prokof'ev V.Yu., Akinin V.V., Miller E.L., Isaeva E.P., Palechek T.N., Starikova E.V., Boldyreva A.I., Wiegand B.* Evolution of Aptian and Albian magmatism of Western and Northern Chukotka (Northeast Russia) based on zircon U-Pb geochronology and rock geochemistry // International Geology Review. 2023.
2. *Akinin V.V., Polzunenkov G.O., Gottlieb E.S., Miller E.L.* Cretaceous monolith-granite-pegmatite Velitkenai complex: petrology, geochemistry of rocks and zircon (U-Pb, Hf, and O) as applied to the reconstruction of the evolution of magmatism and continental crust in the Arctic Alaska-Chukotka block // Petrology. 2022. Vol. 30. No. 3. Pp. 227–259.
3. *Luchitskaya M.V., Sokolov S.D.* Stages of granitoid magmatism and formation of the continental crust of the Eastern Arctic // Geotectonics. 2021. No. 5. Pp. 1–25.
4. *Sokolov S.D., Tuchkova M.And. Ganelin A.V., Bondarenko G.E., Leyer P.* Tectonics of the South Anyui suture (Northeast Asia) // Geotectonics. 2015. No. 1. Pp. 5–30.
5. *Nikishin A.M., Petrov E.I., Malyshev N.A, Ershova V.P.* Rift systems of the Russian Eastern Arctic shelf and Arctic deep-water basins: link between geological history and geodynamics // Geodynamics and Tectonophysics. 2017. V. 8. No. 1. Pp. 11–43.
6. *Polzunenkov G.O.* Petrology and isotopic geochronology of the Velitkenai monzonite-granite-migmatite complex (Arctic Alaska). Novosibirsk, 2023. 20 p.
7. Geodynamics, magmatism and metallogeny of the East of Russia / Edited by Academician of the Russian Academy of Sciences A.I. Khanchuk. Book 2. Vladivostok: Dalnauka, 2006. Pp. 573–981.
8. *Hart C.J.R., Goldfarb R.J., Lewis L.L., Mair J.L.* The Northern Cordilleran Mid-Cretaceous plutonic province: ilmenite-magnetite-series granitoids an intrusion-related mineralization // Resource geology. 2004. V. 54. No. 3. Pp. 253–280.
9. *Varlamova V.A., Malysheva G.M., Vyatkin B.V. et al.* Information report on the unfinished works on the object "Creation of a digital set of maps of geological content on a scale of 1:500,000 of the territory of the Chukotka Autonomous District". Anadyr, FGUGP "Georegion", 2004.
10. 1:200,000 scale geological map of the USSR. Anyuysko-Chaunskaya series. Sheet R-60-XIX, XX. A.Ya. Pyankov, T.P.Hyppenen. Edited by V.T. Matveenko. An explanatory note. Moscow, 1980. Pp. 1–75.
11. *Larionov A.N., Andreichev V.A., Gee D.G.* The Vendian alkaline igneous suite of northern Timan: ion microprobe U–Pb zircon ages of gabbros and syenite / In: The Neoproterozoic Timanide Orogen of Eastern Baltica. Ed. by D.G. Gee, V.L. Pease. Geol. Soc. London. Mem. 2004. V. 30. Pp. 69–74.
12. *Frost B.R., Barnes C.G., Collins W.J. et al.* A geochemical classification for granitic rocks // J. Petrology. 2001. V. 42. No. 11. Pp. 2033–2048.
13. *Cocherie A.* Systematic use of trace element distribution patterns in log-log diagrams for plutonic suites // Geochimica et Cosmochimica Acta. 1986. V. 50. P. 2517–2522.
14. *Baker T., Pollard P.J., Mustard R., Mark G., Graham J.L.* A comparison of granite-related tin, tungstein, and gold-bismuth deposits: implications for exploration // SEG NEWSLETTER. 2005. No. 61. Pp. 6–17.
15. *Mishin L.F., Konovalova E.A., Taltykin Yu.V.*. Influence of oxidative conditions on geochemical and metallogenic zonation using the example of Mesozoic magmatic belts of Eastern Yakutia // Petrology. 2022. Vol. 30. No. 3. Pp. 260–280.
16. *Ganelin A.V., Vatrushkina E.V., Luchitskaya M.V.*. Geochemistry and geochronology of Cretaceous volcanism in the Chaunsky district of Central Chukotka // Geochemistry. 2019. Vol. 64. No. 1. Pp. 20–42.
17. *Tikhomirov P.L.* Cretaceous marginal-continental magmatism of Northeast Asia and the genesis of the largest Phanerozoic provinces of silicic acid volcanism. Moscow: GEOS, 2020. 176 p.
18. *Alexeyev V.I.* Lithium-fluoride granites of the Far East. Saint Petersburg: National University of Mineral Resources "Gorny", 2014. 244 p.
19. *Foley S.F., Venturelli G., Green D.H., Toscani L.* Ultrapotassic rocks: characteristics, classification, and constraints for petrogenetic models // Earth-Science Reviews. 1987. V. 24. Pp. 81–134.
20. *Wang Q., Wyman D.A., Xu J.-F., Zhao Z.-H., Jian P., Xiong X.-L., Bao Z.-W., Li C.-F., Bai Z.-H.* Petrogenesis of Cretaceous adakitic and shoshonitic igneous rocks in the Luzong area, Anhui Province (eastern China): implications for geodynamics and Cu–Au mineralization // Lithos. 2006. V. 89. Pp. 424–446.

*DOKLADY EARTH SCIENCES, 2025, Vol. 520, No. 1, pp. 58–67*

## OIL AND GAS GEOLOGY

# THE SEARCH FOR NATURAL HYDROGEN IN RUSSIA: THE STATE OF THE PROBLEM AND POSSIBLE STARTING SOLUTIONS

**© 2025 L. A. Abukova[a], *, Yu. A. Volozh[b], D. S. Filippova[a] and E. A. Safarova[a]**

Presented by Academician of the Russian Academy of Sciences M. A. Fedonkin on August 19, 2024

Received August 19, 2024
Revised September 08, 2024
Accepted September 09, 2024

**Abstract.** By the time the decision was made (Rosstandart Order 07.07.2023 No. 490-st) on the inclusion of hydrogen in the all-Russian classifier of minerals in Russia, research on the geological and economic analysis of the possibilities of industrial development of hydrogen resources had not been conducted. Moreover, fossil hydrogen has been studied extremely poorly. The current situation requires the accelerated development of a hydrogen search concept based on the scientific justification of the most promising regional areas of work. In the article, the authors present their vision of this problem and propose possible solutions. In particular, the necessity of organizing scientific and technological hydrogen polygons is argued, the tasks of which will include: (i) the development of theoretical ideas about the role of hydrogen in the evolution of the Earth; (ii) detailing the mechanisms of hydrogen localization in the geological environment; (iii) the development of criteria and methods for geological and economic assessment of hydrogen prospecting, exploration and production; (iv) conducting geological and commercial research at the most promising sites for the development and testing of methods for searching for deposits of hydrogen and related minerals.

**Keywords:** *natural hydrogen, ancient platforms, great depths, serpentinization, radiolysis, microbiological processes of hydrogen generation, mineral and energy resources of the bowels of the Earth*

**DOI**: 10.31857/S26867397250106e5

## INTRODUCTION

Hydrogen energy is a key direction of the modern economy, based on ecological imperatives. To date, significant progress has been made in the production and storage of technical hydrogen. In the last decade, there has been a steadily growing interest in natural hydrogen ($H_2$) as an energy resource not associated with greenhouse gas emissions.

Hydrogen produced in the Earth's interior has been extremely poorly studied. Meanwhile, the "hydrogen boom" is growing. Many countries (Australia, the USA, China, Spain, France, Mali, Oman, etc.) and dozens of companies are already working on the search for natural hydrogen, most often focusing on previously accidentally discovered outflows of this gas.

In Russia, hydrogen has been included in the national classifier of mineral resources (order of Rosstandart dated July 07, 2023, No. 490-st). This decision requires accelerated scientific justification for selecting the most promising objects within which it is advisable to prioritize geological, geophysical, geochemical, and hydrogeological studies necessary to substantiate a comprehensive methodology for conducting exploration works for hydrogen.

The purpose of this article is to substantiate proposals for forming the scientific basis of the concept of natural hydrogen exploration in Russia.

## DATA AND RESEARCH METHODS

The source materials for solving the target problem have been collected from numerous literary and archival sources reflecting the results of studying the geological structure of the Earth's interior, mechanisms of hydrogen generation and accumulation.

---

[a] *Oil and Gas Research Institute, Russian Academy of Sciences. Moscow, Russian Federation*
[b] *Geological Institute, Russian Academy of Sciences. Moscow, Russian Federation*
**e-mail: abukova@ipng.ru*

For generalizing the source materials, general scientific methods were used, as well as special methodological approaches focused on the analysis of geological and geophysical information. Thus, bibliometric analysis tools revealed the dynamics of publication activity on issues of natural hydrogen generation and accumulation, showing the interest of various countries, scientific centers, and resource-extracting companies in conducting exploration work to detect industrial accumulations of $H_2$ (Fig. 1).

It is worth noting that the number of publications devoted to natural hydrogen has been increasing in recent years with growing rapidity; many works have a high five-year citation level (over 1000).

### *Previous research level*

To date, hundreds of hydrogen degassing manifestations are known, most of them gravitate toward lithospheric plate boundaries, fault zones, regions with increased seismicity [4, 17, 20], however only one industrially significant free hydrogen deposit is reliably known; its discovery in Mali [18] served as the “starting point” in the history of this gas as a mineral resource. Currently, global $H_2$ resources are estimated at 5 trillion tons. It is assumed that the cost of natural hydrogen production will be multiple times lower than that of “green hydrogen” [16].

The trend of searching for deeply submerged hydrogen accumulations is intensifying. For example, in France, $H_2$ of low concentration was found at a depth of 200 m, but as the sampling objects deepened, the hydrogen concentration increased to 14% at a depth of 1100 m and 20% at a depth of 1250 m [20]. Such examples are not isolated. Strong arguments have been presented in favor of the existence of favorable conditions for hydrogen generation and accumulation at great depths of ancient platforms [16].

The experience of Australia is interesting: state licenses are issued for natural hydrogen exploration there. Here, the search for $H_2$ is combined with the production of technical hydrogen from coal seams using the energy of solar panels, wind, and tides. Simultaneously, issues of underground hydrogen

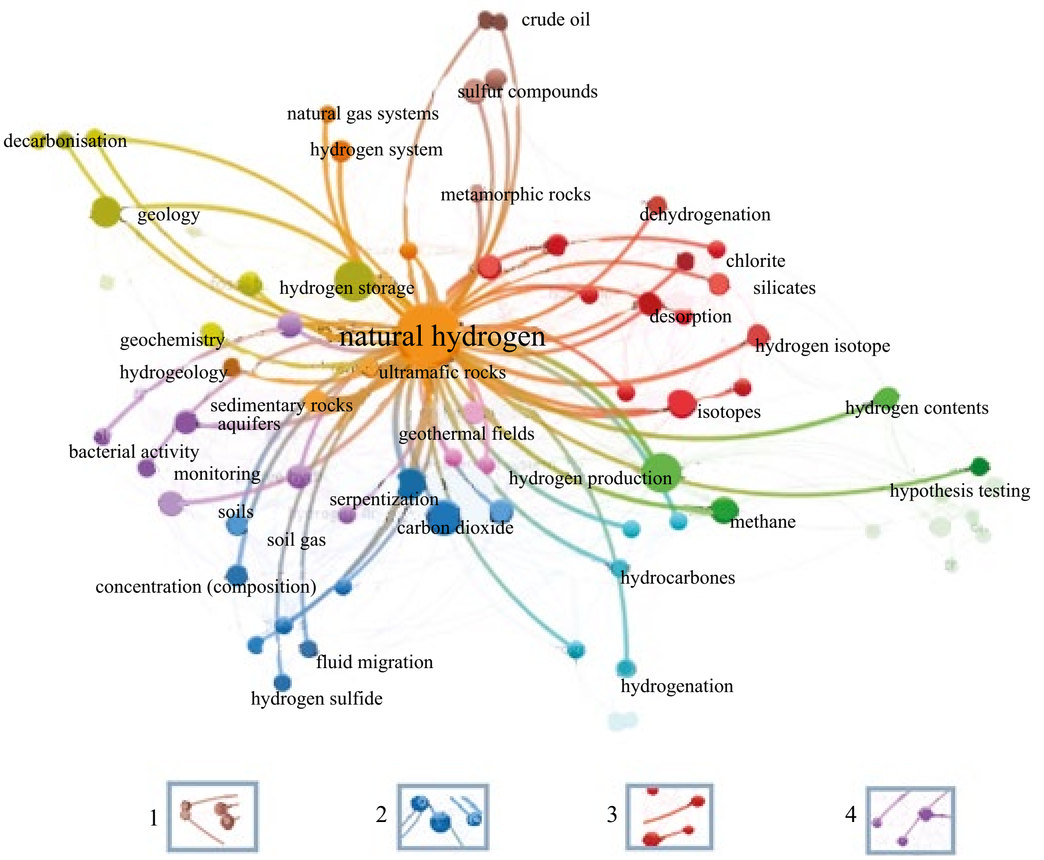

**Fig. 1.** Thematic landscape of the subject area “natural hydrogen” (native/natural/geological/white/gold/hydrogen) based on the Scopus database for a 20-year period (VOSviewer software). Legend: 1 – biogenic sources; 2 – abiogenic sources; 3 – interaction with rocks; 4 – microbiological processes.

storage are being addressed regardless of the method of its production [15].

In Russian scientific literature until recently, $H_2$ as a mineral resource was mentioned only in rare cases [5, 12, 14]; such function of $H_2$ is not reflected in state policy documents, including the Roadmap for the development of hydrogen energy in the Russian Federation until 2024 (Government Decree of October 12, 2020 No. 2634-r). There are no methodological developments for assessing its reserves and resources, economic criteria for profitability have not been justified, and there is no regulatory framework for conducting prospecting and exploration work for hydrogen.

There is much controversy regarding the genesis and localization conditions of natural hydrogen. However, thanks to the work of scientists from several countries (G. Etiope, I. Moretti, R. Nandi, A. Prinzhofer, L. Truche, V. Zgonnik, et al.) and Russia (E.M. Galimov, V.N. Larin, S.P. Levshunova, V.A. Nivin, V.A. Sokolov, M.A. Fedonkin, V.P. Yakutseni, et al.), certain issues regarding the generation and accumulation of hydrogen do not cause disagreements. Thus, today, magmatogenic, metamorphogenic, radiogenic, and microbiological sources of hydrogen in the geological environment are well known [6, 7, 8, 20]. In particular, there is no doubt about the global geological role of serpentinization and water radiolysis in hydrogen generation [13, 15, 17]. The absence of correlation between hydrogen and methane content for gases of metamorphic origin has been noted [8], but the presence of an inverse correlation (Fig. 2) for methane and hydrogen of biochemical genesis has been revealed [3, 14]. These issues are discussed in more detail in works [4, 14, 20].

Ideas about hydrogen accumulation processes are less definite. As a rule, they are judged by surface manifestations of hydrogen degassing, indicating the directions (and partly the scale) of unhindered hydrogen degassing. But the physical essence of degassing processes is not the concentration but the dispersion of hydrogen in the geological environment, therefore, external manifestations of hydrogen degassing (for example, bleached circles) are not always reliable diagnostic criteria for the localization of natural hydrogen.

A large volume of research has been conducted on modeling geochemical and geomechanical processes accompanying the joint storage of hydrogen and methane at natural gas storage facilities (UGS). Our results from several UGS facilities located in aquifers (Fig. 3) demonstrate the activity of methanogenic archaea and bacteria capable of using hydrogen as an energy source [9].

Studies aimed at identifying the nature of the interaction of this gas with the rocks of their host reservoirs are also of interest for the industrial development of hydrogen resources. As a particular example of such studies, we can note the identification, based on experimental models,

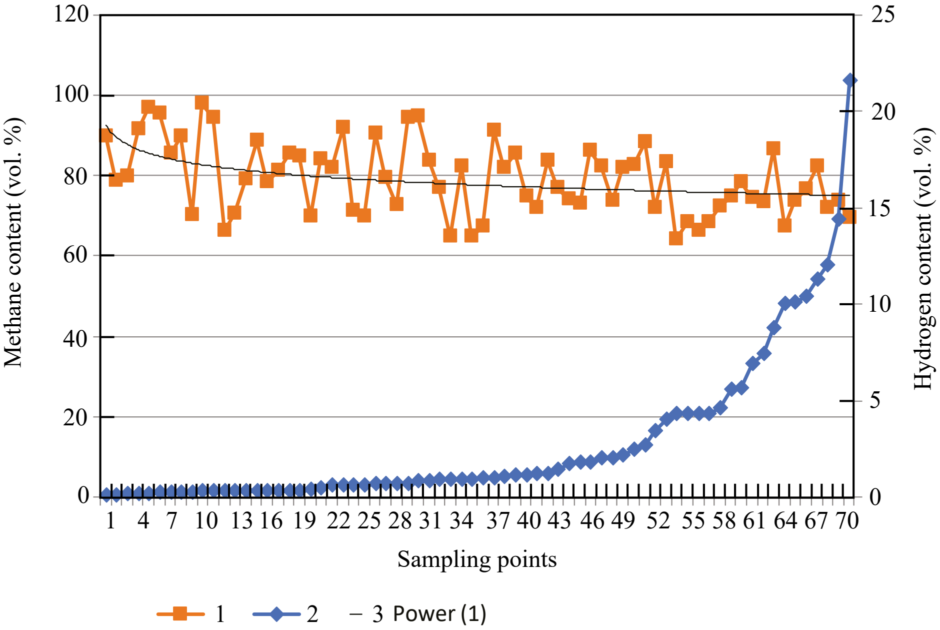

**Fig. 2.** Character of hydrogen and methane accumulation in the waters of the supra-salt floor of the Caspian oil and gas province. 1 – methane content (% volume); 2 – hydrogen content (% volume); 3 – power averaging of methane content.

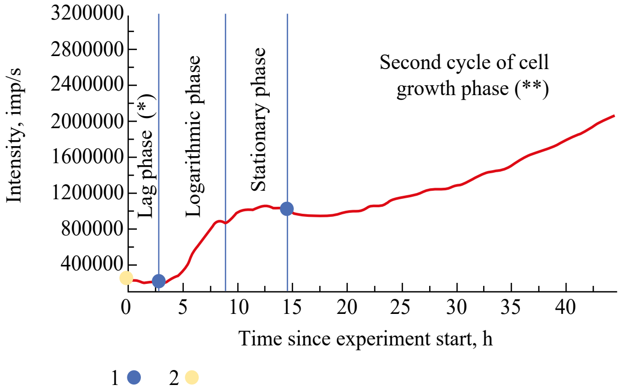

**Fig. 3.** Results of sequencing formation water samples from Shchelkovo UGS and growth of microbiological populations in these waters with additional hydrogen feeding according to the authors' experimental data. 1 – addition of hydrogen during the experiment; 2 – sampling for determination of microbiological composition; (*) initial microbiological composition of the studied groups of microorganisms: methanotrophs (Marinobacter) – 92% (**) final microbiological composition of the studied groups of microorganisms: methanotrophs (Marinobacter) – 9%, methanogens (Methylophaga) – 8%, sulfate-reducing microorganisms (Desulfopila) – 9%, sulfur-oxidizing (Thiohalobacter, Thioalkalispiraceae) – 30%.

of significant changes in the capacity-filtration and strength properties of terrigenous rocks induced by their geochemical interaction with hydrogen in case of their moistening and the absence of significant effects during contact of hydrogen with dry samples of terrigenous rocks, both under cyclic loading and under stationary conditions (Fig. 4) [2].

The information provided above about previously conducted research, without claiming to be a comprehensive review of accumulated knowledge in the field of natural hydrogen, demonstrates only various aspects of studying the interaction of hydrogen with the geological environment. Nevertheless, it makes it possible to express some judgments about regional directions of hydrogen exploration in Russia.

## RESEARCH RESULTS: POSSIBLE DIRECTIONS OF SCIENTIFIC JUSTIFICATION FOR SEARCHING HYDROGEN ACCUMULATION ZONES IN RUSSIA

Based on the current level of our knowledge about the patterns of distribution of natural hydrogen outflows to the surface and into the near-surface layers of the Earth's crust, as well as taking into account existing hypotheses of hydrogen formation, it is possible to formulate the following basic provisions of the hydrogen exploration concept (Table 1):

Abiogenic hydrogen synthesis supplies the largest volume of hydrogen to the lithosphere. It is implemented in various ways, but the most common are serpentinization of ultrabasic rocks and water radiolysis.

1. The compositions of gas mixtures from abiogenic generation sources do not show correlation between hydrogen and methane content; methane is present in low, sometimes trace concentrations, which excludes the possibility of forming industrially significant accumulations. Hydrogen of abiogenic origin, due to its high volatility, can be detected in a wide range of depths.

2. The compositions of gas mixtures from biogenic generation sources are characterized by an inverse correlation between hydrogen and methane (Isaev's antagonism), the hydrogen content is significantly lower than the methane content. Hydrogen of biogenic origin is concentrated in the sedimentary cover, predominantly under salt-bearing and doleritic caprocks.

3. The mechanisms of hydrogen accumulation are fundamentally different for oil and gas bearing and oil and gas prospective continental territories, on the one hand, and shields and orogenic (folded and block) structures of the mobile belt, on the other (Table 1). Within oil and gas bearing territories, dominant and regional fluid seals play a key role. The role of dominant fluid seals (DFS) is especially significant, as they divide the sedimentary cover sections of oil and gas provinces in plate structures of young and ancient platforms into two stories with different types of water pressure regimes (the upper with free and the lower with (quasi)stagnant). In lithological terms, the DFS most often consist of salt-bearing and/or doleritic gigantic strata. The fluid isolation properties of the DFS can be enhanced by the presence of gas hydrate layers in the upper parts of the section, as well as by the development of hydrodynamically screened autoclave-type hydrocarbon systems below the salt (or doleritic) covers [1]. Thus, the presence of DFS, the placement of hydrogen accumulation zones in the lower geofluid dynamic story, and the spatial proximity of $H_2$ generation sources and hydrogen accumulation zones collectively provide the most favorable conditions for the formation of large hydrogen deposits at great depths in oil and gas provinces/basins.

Within the shields of ancient platforms and plates of young and ancient platforms, vertical migration of hydrogen predominates, which has been repeatedly recorded in the form of hydrogen (methane-hydrogen) emanations. Nevertheless, the stability of flow rates and the geochemical composition of gas mixtures are the most important objects of study.

Let us emphasize the important point: the path from orienting hydrogen searches based on individual direct and indirect indicators to creating a comprehensive methodology for forecasting industrially significant hydrogen deposits lies through conducting a large volume of fundamental research and experimental work. This, in turn, actualizes the task of organizing integrated scientific and technological test sites for detailing the scientific and methodological foundations for $H_2$ forecasting and developing technologies for its prospecting, exploration, and development. The question of the

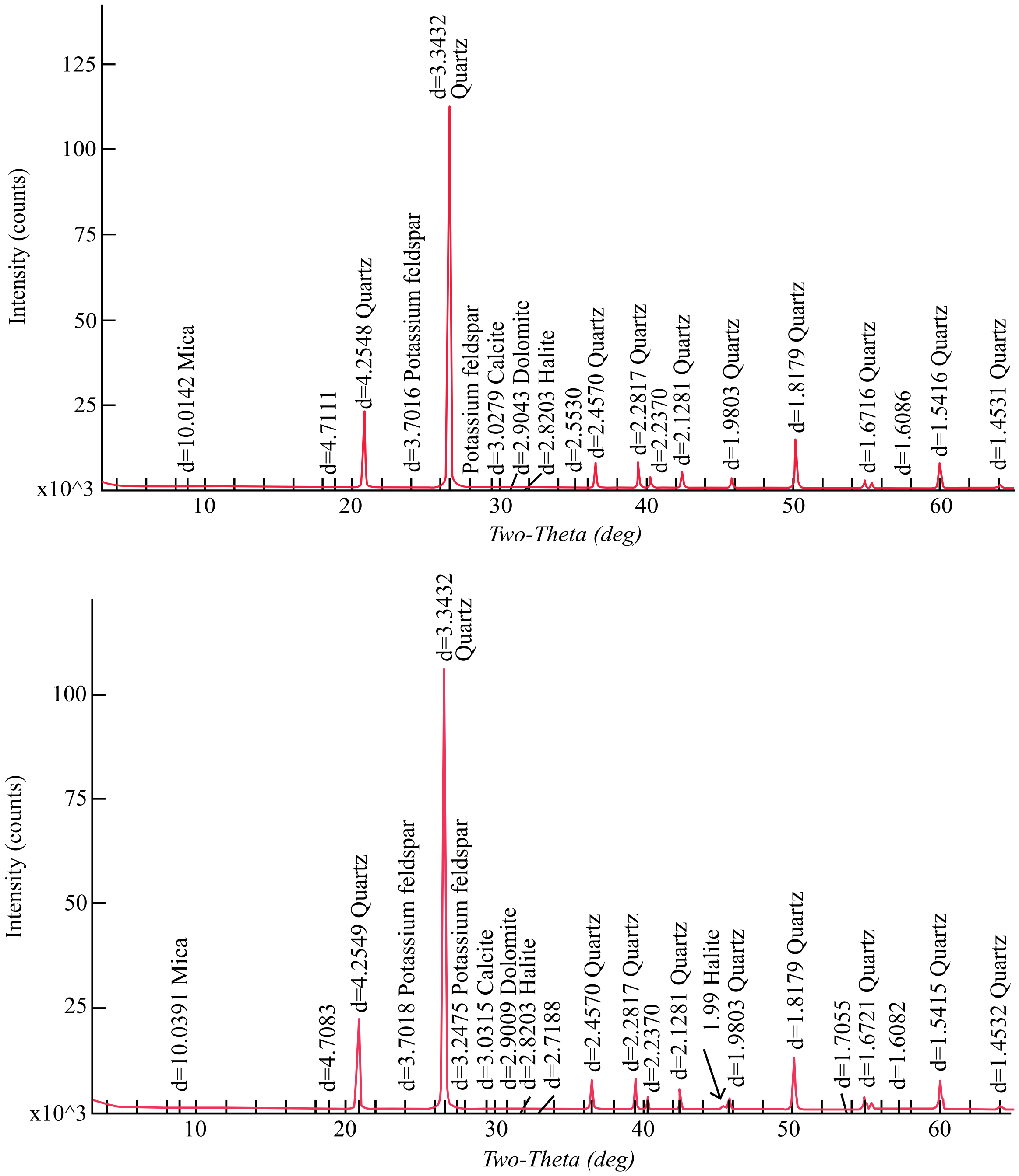

**Fig. 4.** Comparative evaluation of the X-ray diffraction pattern of a sandstone sample before (a) and after (b) exposure to hydrogen (mineral composition of sandstone: quartz – 94%, mica – 2%, dolomite – 1.1%, potassium feldspar – 2%, calcite – 0.6%, halite – 0.3%)

**Table 1**. Forecast objects and directions of scientific research on substantiation of search criteria for natural hydrogen as a mineral resource

| Forecast of the nature of hydrogen generation and accumulation processes | Differences between regions by presence (absence) of regional and dominant fluid seals in the Earth's crust | | | | | | | | | | |
|---|---|---|---|---|---|---|---|---|---|---|---|
| | Regions where regional and dominant fluid seals are absent | | | Regions where Regional and dominant fluid seals are present | | | | | | | |
| | Shields of ancient and young platforms | Block orogenic structures | Folded orogenic structures | Provinces* oil and gas bearing and prospective (tectonic-sedimentary provinces) of plate structures of ancient and young platforms | | | | | Oil and gas bearing and prospective basins* (sedimentary-rock basins) | | |
| | | | | located in the internal parts of plates | | located at plate edges | | | | | |
| | | | | of ancient platforms | of young platforms | at boundaries with folded structures | at junction of ancient and young platforms | on passive continental margins | marginal-continental seas | mediterranean seas | intracontinental rifts |
| Examples of territories* | Aldan, Baltic shields | Kuril-Kamchatka volcano-plutonic arc | Altai-Sayan folded structure | Lena-Tunguska, Volga-Ural OGP | West Siberian Siberian OGP | Timan-Pechora, Lena-Pechorskaya, Leno-Vilyui OGP | Caspian, Barents-Kara OGP | East Arctic prospective OGPP | Sea of Okhotsk OGB | Black Sea OGB | Baikal OGPB |
| Generation sources of $H_2$: | | | | | | | | | | | |
| a) serpentinization | * | * | * | * | ? | ? | * | ? | ? | ? | ? |
| b) radiolysis | * | * | * | * | ? | ? | * | ? | ? | ? | ? |

*Ending*

| | | | | | | | | | | | |
|---|---|---|---|---|---|---|---|---|---|---|---|
| c) microbiological processes | ? | ? | ? | ? | * | ? | ? | ? | | * | |
| Predominant transit direction:<br>a) vertical<br>b) lateral | *<br>* | *<br>* | *<br>? | ? | ? | ? | *<br>* | ? | ? | ? | ? |
| Predicted accumulation features:<br>a) $H_2$ focal type accumulations, small in size, frequently occurring<br>b) $H_2$ reservoir type accumulations, large, rarely occurring | * | * | * | ? | ? | ? | ? | ? | ? | ? | ? |
| | – | – | ? | ? | ? | ? | * | ? | ? | ? | ? |
| Most promising regional objects | Baltic Shield | | | | | | Caspian OGP | | | | |
| Priority objects for placement of scientific and technological test sites | Onega trough | | | | | | Astrakhan arch | | | | |

Note: provinces and basins are distinguished considering the geodynamic regime of the Earth's crust development: provinces – platform regime, basins – block-orogenic and fold-orogenic. The selection of regional search objects was performed using the following materials:

(1) structural map of the basement surface of the USSR platform territories at scale 1:5,000,000 (1982) edited by V.V. Semenovich, L.I. Rovnin, N.V. Nevolin et al.

(2) geodynamic map of Russia, scale 1:10,000,000 (1995) edited by N.V. Mezhelovsky, A.I. Burde.

(3) scheme of thicknesses of the unexplored deep part of the sedimentary cover section of oil and gas provinces of Russia and adjacent countries (Yu.A. Volozh, M.A. Fedonkin, *V.M. Tolkachev*. On new approaches to exploration in traditional production provinces //: Oil and Gas Vertical. 2020. No. 7. P. 74.

(1) the following notations are used to indicate the significance of characteristics: * – significant manifestation; – absence of manifestation; ? – nature of manifestation not identified.

(2) -OGP – oil and gas province; OGPP – oil and gas prospective province; OGB – oil and gas basin; OGPB – oil and gas prospective basin

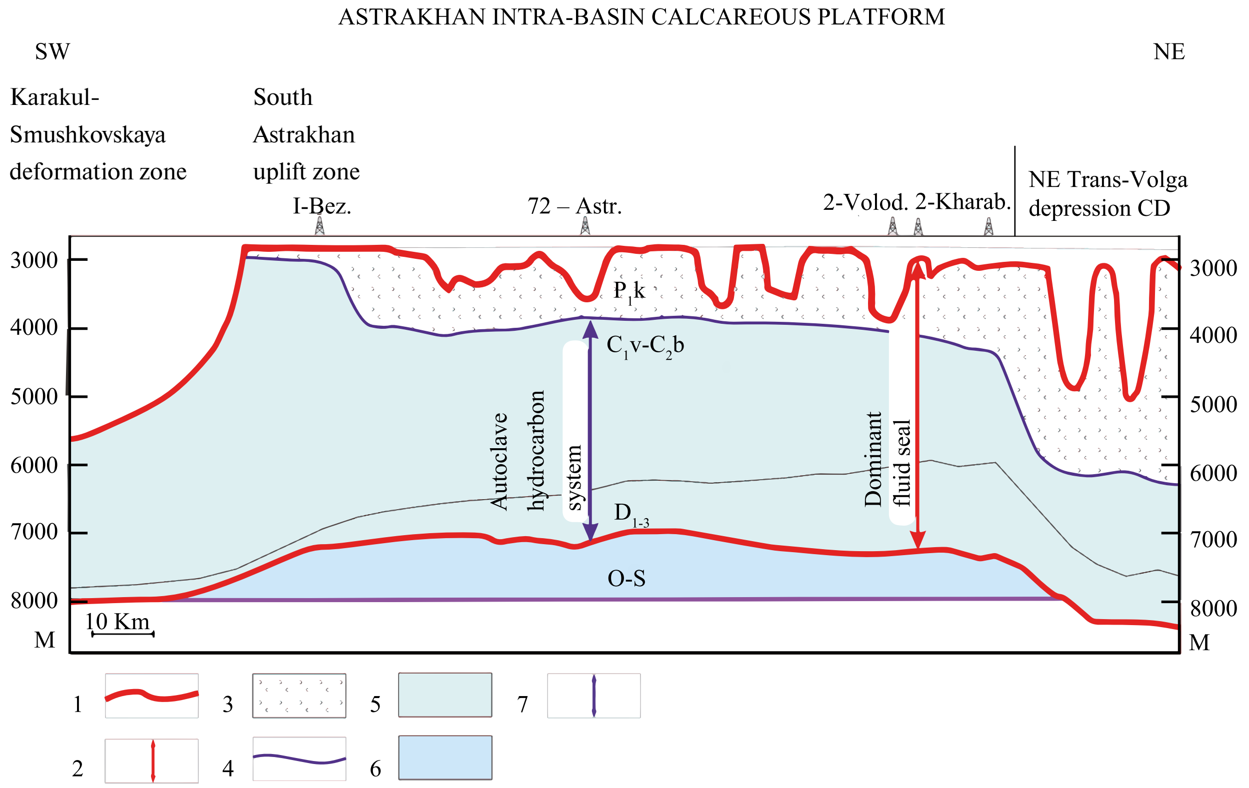

**Fig. 5.** Geofluid dynamic model of the Astrakhan platform, within which a scientific and technological testing site can be located. Dominant fluid seal: 1 – boundaries, 2 – distribution area (thickness 4–8 km); 3 – salt-bearing stratum with a thickness of 3–6 km; 4 – sulfate-carbonate-clay horizon at the base of the salt-bearing stratum; autoclave hydrocarbon system: 5 – distribution area, 6 – thickness 4-8 km; 7 – area of potential hydrogen accumulation.

need to create scientific and technological test sites for studying hydrogen as a mineral resource was previously raised in a work by one of the authors of this article; the latter also formulated the main tasks that are advisable to study at these test sites [14]. With some additions, they are reduced to the following: (1) development of a terminological glossary of hydrogen geology; (2) creation of a classification of planetary gases based on hydrogen content; (3) formation of a program for geophysical, geochemical, and hydrogeological studies of test wells; (4) transition from indicators (prerequisites) to criteria of hydrogen prospectivity for various geological and tectonic settings; (5) substantiation of reliable methods for delineating natural hydrogen accumulations, estimating hydrogen reserves (resources); (6) testing various criteria for ranking $H_2$ deposits by their reserve size and depth of placement; (7) investigating the possibilities and feasibility of accounting for volumes of sorbed and water-dissolved hydrogen when assessing resources; (8) evaluating the significance of differences in hydrogen accumulation mechanisms under conditions of closed and open hydrodynamic systems.

In terms of geology and field development, it is important to: (1) clarify the conditions for hydrogen embrittlement of reservoir rock cement and the geomechanical consequences of active hydrogen degassing; analyze the possibilities of inhibiting undesirable consequences of these processes; (2) monitor the stability of natural hydrogen emanation flow rates; (3) analyze the activity of hydrogenation of organic matter and hydrocarbon compounds under mass exposure to transit hydrogen flows; (4) account for hydrogen-induced processes of methane and carbon dioxide generation under reservoir conditions; (5) select criteria for assessing hydrogen purity, qualitative and quantitative composition of impurities.

When selecting locations for scientific and technological testing sites, preference should be given to objects located within oil and gas provinces/basins with a sedimentary cover thickness of at least 5–7 km. These may include depressions at the boundaries of ancient and young platforms, as well as depressions of intracontinental rifts. Additionally, platform shields, tectonic-sedimentary provinces of mobile belts: intermontane depressions, mediterranean and marginal-continental seas, and depressions of intercontinental rifts can be added as potential testing sites.

Given the absence of any specially conducted studies on natural hydrogen, the authors propose selecting one object each from the presumed most promising and less promising areas as priority objects. According to the authors, two testing sites within the East European platform, provisionally named “Onega” and “Astrakhan,” can be selected for this purpose.

The “Onega” testing site can be located in the area of the Onega parametric well (depth 3537 m), which penetrated the dominant fluid seal at a depth of 2944 m, represented mainly by halite [10]. The Onega structure shows an analogy with the geological structure of the industrial hydrogen development site (Bourakebougou, Mali), but has more favorable conditions for preserving this gas.

The “Astrakhan” testing site can be located on the Astrakhan arch in the area of the Astrakhan 2-D well, which penetrated a thick deposit layer (6–9 km) at a depth of more than 6 km, serving as a dominant fluid seal (Fig. 5). The predicted hydrogen accumulation zone may be located below the base of the Domanic shale sequence, which simultaneously serves as the base of the predicted autoclave hydrocarbon system [1].

It is predicted that the combination of lithological type of isolation (through salt and shale strata) with geofluid dynamic screening (due to the formation of a giant hydrocarbon system with extremely high reservoir pressures) creates unique conditions for the preservation of hydrogen (as well as helium) under the bottom of the autoclave hydrocarbon system. Such a geological situation should be considered as a very favorable environment for the formation of an industrially significant hydrogen (and helium) deposit.

## CONCLUSION

1. Due to high geological risks caused by poor geological understanding of the processes of generation and accumulation of natural hydrogen, currently only preliminary studies are available at scientific and technological test sites, clarifying the conditions for the localization of hydrogen in various geological and tectonic settings. Any plans to initiate hydrogen exploration should be considered premature at present.

2. Large and unique $H_2$ deposits within oil and gas provinces/basins are most likely to be encountered at great depths and under autoclave hydrocarbon systems.

3. The most optimal solution (from scientific and practical perspectives) is the development of methods for extracting hydrogen of geological origin together with traditional energy carriers, helium, industrially valuable components of associated underground waters and, more broadly, hydrothermal resources and heat from the Earth’s interior. This approach will reduce geological, technical and economic risks of exploration activities, best meets the requirements of ecologization of the geological industry, and will provide a scientific and practical basis for the comprehensive development of energy and mineral resources of deep horizons of the lithosphere, which can be considered a task of the national level. In this regard, it is necessary to develop a modern concept for the search and development of resources of liquid and gaseous minerals within the deep horizons of the sedimentary cover of oil and gas provinces and megabasins, as well as the consolidated continental crust in zones where it outcrops within the shields of ancient platforms.

## FUNDING

The work is based on the results of work carried out under the state assignment of OGRI, RAS No. 122022800276-2 (FMME-2022-0007) “Scientific substantiation of the influence of hydrochemical and microbiological processes on the development of corrosion phenomena in the co-occurrence of hydrogen and methane in a wide range of concentrations in geological objects of various types”, as well as through state budget funding of research work at the Geological Institute, RAS.

## REFERENCES

4. *Abukova L.A., Volozh Yu.A.* Fluid dynamics of deeply submerged oil and gas accumulation zones in sedimentary basins // Geology and Geophysics. 2021. Vol. 62. No. 8. Pp. 1069–1080. https://doi.org/10.15372/GiG2021132

5. *Abukova L.A., Safarova E.A., Filippova D.S., Podnek V.E., Kiyachenko Yu.F., Yudin I.K., Isaeva G.Yu., Melnik A.D., Bevzo M.O.* Hydrochemical and microbiological processes accompanying hybrid storage of hydrogen and methane in aquifers // Current Problems of Oil and Gas. 2023. No. 3. https://doi.org/10.29222/ipng.2078-5712.2023-42.art14

6. *Isaev V.P.* Thermodynamic aspects of natural gas geochemistry. Part 2 // Irkutsk University Publishing House. Irkutsk. 1991. 192 p.

7. *Larin V.N.* Hypothesis of the initially hydride Earth. Moscow: Nedra. 1975. 100 p.

8. *Levshunova S.P.* Hydrogen and its biogeochemical role in the formation of hydrocarbon gases in sedimentary rocks of the Earth's crust. Abstract of doctoral thesis in geological and mineralogical sciences. Moscow. MSU. 1994. 40 p.
9. *Lein A.Yu., Bogdanov Yu.A., Sagalevich A.M. et al.* New type of hydrothermal field on the Mid-Atlantic Ridge (Lost City field, 30°N) // Reports of RAS. Earth Sciences. 2004. Vol. 394. No. 3. Pp. 380–383.
10. *Trofimuk A.A., Molchanov V.I., Paraev V.V.* Features of geodynamic settings in the formation of giant oil and gas deposits // Geology and Geophysics. 1998. Vol. 39(5). No. 5. Pp. 673–682.
11. *Pukha V.V., Nivin V.A., Mokrushina O.D.* Variations in molecular hydrogen concentrations in loose deposits of the Khibiny and Lovozero massifs and their exocontact zones // Proceedings of the Fersman Scientific Session of the GI KSC RAS. 2022. No. 19. Pp. 312–317. https://doi.org/10.31241/FNS.2022.19.057
12. *Nazina T.N. Abukova L.A.; Tourova T.P. Babich T.L. Bidzhieva S.K. Loiko N.G. Filippova D.S.; Safarova E.A.* Biodiversity and Potential Activity of Microorganisms in Underground Gas Storage Horizons // Sustainability. 2023. No. 15. 9945. https://doi.org/10.3390/su15139945
13. Onega Paleoproterozoic structure (geology, tectonics, deep structure and minerageny) / Ed. L.V. Glushanin, N.V. Sharov, V.V. Shchiptsov. Petrozavodsk: Karelian Scientific Center RAS. 2011. 431 p.
14. *Sokolov V.A.* Geochemistry of natural gases. Moscow: Nedra. 1971. 337 p.
15. Russian Federation Patent No. 2316028C2. Method for prospecting accumulations of gaseous hydrogen and helium in the earth's interior // Kudrin I.V., LLC "Vettos", IPC G01V 11/00 (2006.01)
16. *Fedonkin M.A.* The role of hydrogen and metals in the formation and evolution of metabolic systems // Problems of biosphere origin and evolution (ed. E.M. Galimov). Moscow: Book House "Librokom". 2008. Pp. 417–437.
17. *Filippova D.S.* Hydrogen in the geological environment: features of generation and accumulation // SOCAR Proceedings. 2023. Special Issue no. 2. Pp. 079–013. http://doi.org/10.5510/OGP2023SI200885
18. *Aimikhe V., Eyankware O.E.* Recent Advances in White Hydrogen Exploration and Production: A Mini Review // J. Energy Res. Rev. 2023. V. 13. No. 4. Pp. 64–79. http://doi.org/10.9734/jenrr/2023/v13i4272
19. *Lapi T., Chatzimpiros P., Raineau A., Prinzhofer A.* System approach to natural versus manufactured hydrogen: An interdisciplinary perspective on a new primary energy source // International Journal of Hydrogen Energy. 2022. No. 47(2). http://doi.org/10.1016/j.ijhydene.2022.05.039
20. *Parnell J., Blamey N* . Global hydrogen reservoirs in basement and basins // Geochemical Transactions. 2017. Issue 18. No. 2. https://doi.org/10.1186/s12932-017-0041-4
21. *Prinzhofer A., Cissé C.S.T., Diallo A.B.* Discovery of a large accumulation of natural hydrogen in Bourakebougou (Mali) // International Journal of Hydrogen Energy. 2018. 43(42). Pp. 19315–19326. http://doi.org/10.1016/j.ijhydene.2018.08.193
22. *Truche L., Jodin-Caumon M.C., Lerouge C., et al.* Sulphide mineral reactions in clay-rich rock induced by high hydrogen pressure. Application to disturbed or natural settings up to 250°C and 30 bar. // Chem. Geol. 2013. No. 351. Pp. 217–228. http://doi.org/10.1016/j.chemgeo.2013.05.025
23. *Zgonnik V.* The occurrence and geoscience of natural hydrogen: A comprehensive review // Earth-Science Reviews. 2020. No. 203. Pp. 103–140. http://doi.org/10.1016/j.earscirev.2020.103140

DOKLADY EARTH SCIENCES, 2025, Vol. 520, No. 1, pp. 68–75

OIL AND GAS GEOLOGY

# GAS SHOWS WITHIN THE SOUTHEASTERN SHELF OF THE CRIMEA ACCORDING TO CONTINUOUS SEISMOACOUSTIC PROFILING DATA

**© 2025 A. V. Khortov*, A. A. Pronin, N. A. Rimsky-Korsakov, and A. D. Mutovkin**

Presented by Academician of the Russian Academy of Sciences M. A. Fedonkin on July 08, 2024

Received July 08, 2024
Revised September 12, 2024
Accepted September 16, 2024

**Abstract.** The research was carried out by a team from the Institute of Oceanology of the Russian Academy of Sciences during the expeditions of the research vessels (RV) "Peleng" of the Sevastopol branch of the State Oceanographic Institute and "Professor Vodyanitsky" of the Federal Research Center InBYuM (115th, 116th, 124th and 126th voyages) in 2018–2023 in accordance with the Plan of Marine Expeditions on Research Vessels of the Ministry of Education and Science of Russia. At the same time, the tasks of depth measurements, continuous seismic profiling (CSAP) and acoustic sounding of sedimentary deposits, as well as panoramic survey of the bottom surface using a side-scan sonar were solved. The objectives of the study included: firstly, obtaining new geological and geomorphological data on the history of the development of the Crimean Peninsula shelf, necessary for restoring poorly studied stages of the paleogeographic history of the formation of the continental margin of Crimea in modern times, which will clarify the existing ideas about the change in the Black Sea level, and secondly, obtaining new geological and geomorphological data on the paleogeomorphology of the Crimean Peninsula shelf, which will clarify the position of the ancient hydrographic network and establish the connections of coastal and subaqueous morphostructures. In the process of interpreting continuous seismoacoustic profiling (CSAP) data, anomalous areas identified with gas accumulations were identified in the bottom part of the section.

**Keywords:** *shelf, Crimea, continuous seismoacoustic profiling (CSAP), sparker, acoustic profiler, echo sounder, gas seep, methane, seismic complex, reflecting horizon*

**DOI**: 10.31857/S26867397250107e6

## INTRODUCTION

The research was carried out by a team from the Institute of Oceanology of the Russian Academy of Sciences during expeditions on research vessels (R/V) "Peleng" of the Sevastopol Branch of GOIN and "Professor Vodyanitsky" of FRC IBSS (cruises 115, 116, 124, and 126) in 2018–2023 in accordance with the Marine Expedition Plan for research vessels of the Ministry of Education and Science of Russia.

The research objectives included obtaining new geological and geomorphological data on the development history of the Crimean peninsula shelf, necessary for reconstructing poorly studied stages of the paleogeographic history of the Crimean continental margin formation in recent times, which will help refine existing concepts about Black Sea level changes, clarify the position of the ancient hydrographic network, and establish connections between coastal and subaqueous morphostructures. The tasks included depth measurements, continuous seismic profiling (CSP) and acoustic sounding of sedimentary deposits, as well as panoramic imaging of the seabed surface using side-scan sonar.

It should be noted that studies with similar goals and objectives in this area were conducted by a number of research organizations. Among them, the works of the Kovalevsky Institute of Biology of Southern Seas RAS, the Institute of Geological Sciences of the NAS of Ukraine, SSC JSC Yuzhmorgeologiya, Lomonosov Moscow State University, and others should be highlighted [1–6].

Technically, the implementation of research tasks included: echo sounding and seismoacoustic profiling of the shelf, performed to measure depths and obtain images of the structure of the upper layer

---

*P.P. Shirshov Institute of Oceanology, Russian Academy of Sciences, Moscow, Russian Federation*
**e-mail: khortov.av@ocean.ru*

of sedimentary deposits in the form of sections along the vessel's route using towed unmanned underwater vehicles (TUUV), in particular, seismoacoustic and acoustic profilers (Fig. 1). During the work, numerous anomalous zones associated with gas accumulations in the upper part of the sedimentary cover were identified. Given that seismoacoustic research using the CSP method in this part of the Crimean shelf was practically not conducted before, and acoustic profiling was carried out very limitedly, it can be stated that almost all near-bottom gas accumulations discovered by the seismoacoustic team of the Shirshov Institute of Oceanology RAS in 2018–2023 were identified for the first time.

## RESEARCH METHODS

For CSAP, the "Geont-shelf" seismoacoustic complex based on an electric spark emitter ("sparker") and a receiving seismic streamer was used. Information obtained using the "Geont-shelf" seismoacoustic complex was supplemented with data from geoacoustic sounding using the AP-5T profiler with a working frequency of 5 kHz, which uses a frequency-modulated pulse.

The seismoacoustic complex "Geont-shelf" includes:

- SPES-600 seismic energy accumulator: discharge control unit and high-voltage capacitor unit,
- PSA-1 seismic signal input device,
- towed overboard part: sparker emitter and receiving antenna (seismic streamer),

The towed overboard part of the equipment consists of:

- multi-electrode sparker emitter (with 64 potential electrodes);
- receiving antenna: 25-meter seismic streamer with 10 piezoelectric receivers placed in a polyurethane hose at 2-meter intervals and filled with liquid paraffin;
- 5-meter towing rod ("Vystrel") with nylon halyard braces;
- towing cable for the sparker emitter and receiving seismic streamer;

The seismic streamer was towed from the starboard side using an extendable "Vystrel" rod, and the profiler gondola was lowered overboard using a U-frame (Fig. 2).

The design and operating principle of this equipment are described in detail in works [7, 8].

## RECORDING PARAMETERS

Before starting operations, the seismic survey equipment was calibrated. Setup recordings of the CSAP were made, based on which the following recording parameters were established:

- emitter power not less than 600 J at $C = 50\ \mu F$;
- frequency range 100–1200 Hz;
- emission period 1.5 sec;
- gain $20 \cdot 100 = 2000$;
- recording time $100\ \mu s \cdot 4000 = 400$ ms;
- vessel speed 8–10 knots.

As depths changed, the recording parameters were adjusted. In addition to the profiler with a "sparker" type source, which was used to study the near-bottom section, a high-frequency acoustic profiler and shipboard echo sounder were used in these cruises. To investigate the structure of the upper sediment deposits, a method of continuous

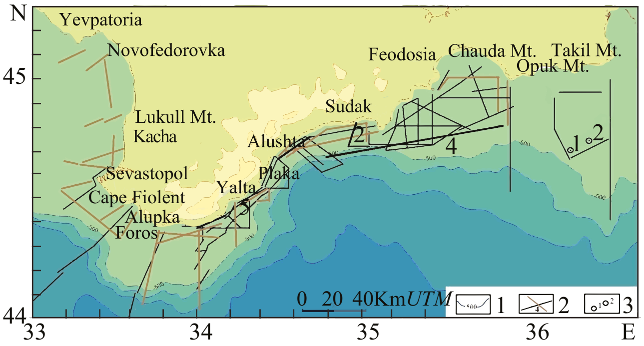

**Fig. 1.** Scheme of R/V "Professor Vodyanitsky" operations in 2018–2023. 1 – isobaths; 2 – seismoacoustic profiles of the "Geont-shelf" CSAP complex (black color) and acoustic profiles of the AP-5T profiler (brown color); 3 – wells from engineering-geological surveys (EGS).

**Fig. 2.** Photo of the R/V "Professor Vodyanitsky", showing the towing devices for seismic equipment. The arrow indicates the "Vystrel" towing rod.

acoustic profiling was applied while the vessel was moving, using acoustic pulses with linear frequency modulation (LFM) of the carrier frequency, which was implemented using the AP-5T acoustic profiler developed at the P.P. Shirshov Institute of Oceanology RAS. The AP-5T includes a towed body (carrier of acoustic antennas), a cable towing line, a storage cable winch, a ship's electronic unit, and a personal computer for data display and recording. When converting time to depth, the wave velocity was considered constant and was assumed to be equal to the velocity in the upper soil layer.

## RESEARCH RESULTS AND DISCUSSION

Taking into account the study of the upper part of the sedimentary cover of the Crimean shelf and the Kerch-Taman shelf, as well as the results of ostracod fauna studies in the engineering-geological wells Glubokaya-1 and Glubokaya-2 (see Fig. 1), it was established that the structure of the seismic complexes identified on seismoacoustic profiles includes Holocene New Black Sea and Old Black Sea deposits (SC-7), New Euxinian deposits of the Upper Neopleistocene (SC-6), Karangatian and Uzunlarian (SC-5, SC-4), and Old Euxinian (SC-3) deposits of the Middle Neopleistocene. Seismic complexes SC-2 and SC-1 are represented, apparently, by older, Early Neopleistocene deposits of the Chaudian rhythm. The lower layers lie on the Triassic-Jurassic rocks of the Taurian series, which form the basement. A more detailed seismostratigraphic division of the Neogene-Quaternary deposits of the southeastern shelf of Crimea, tied to engineering-geological drilling wells on the Glubokaya structure, is provided by us in the paper [9].

When interpreting the obtained results, anomalous sections of the record were identified, stratigraphically confined to the Upper Pleistocene deposits and identified as natural gas accumulations. It was noted that some of the detected anomalies are confined to areas of paleodelta development within the Pleistocene buried hydrographic network. It is known that each river has a two-story structure. In addition to sand accumulations associated with alluvial fans of paleo-rivers, alluvial deposits of their subchannel bed can also serve as an accumulating reservoir on the southeastern shelf. Significant gas-fluid accumulations may be associated with this part of the paleodelta.

Fig. 3 shows a fragment of a seismoacoustic profile, where paleochannel deposits and associated gas accumulations are observed in the interval of 80–120 m.

The marked areas differ from adjacent ones by a number of dynamic and kinematic features characteristic of gas manifestations in the seismic wave field.

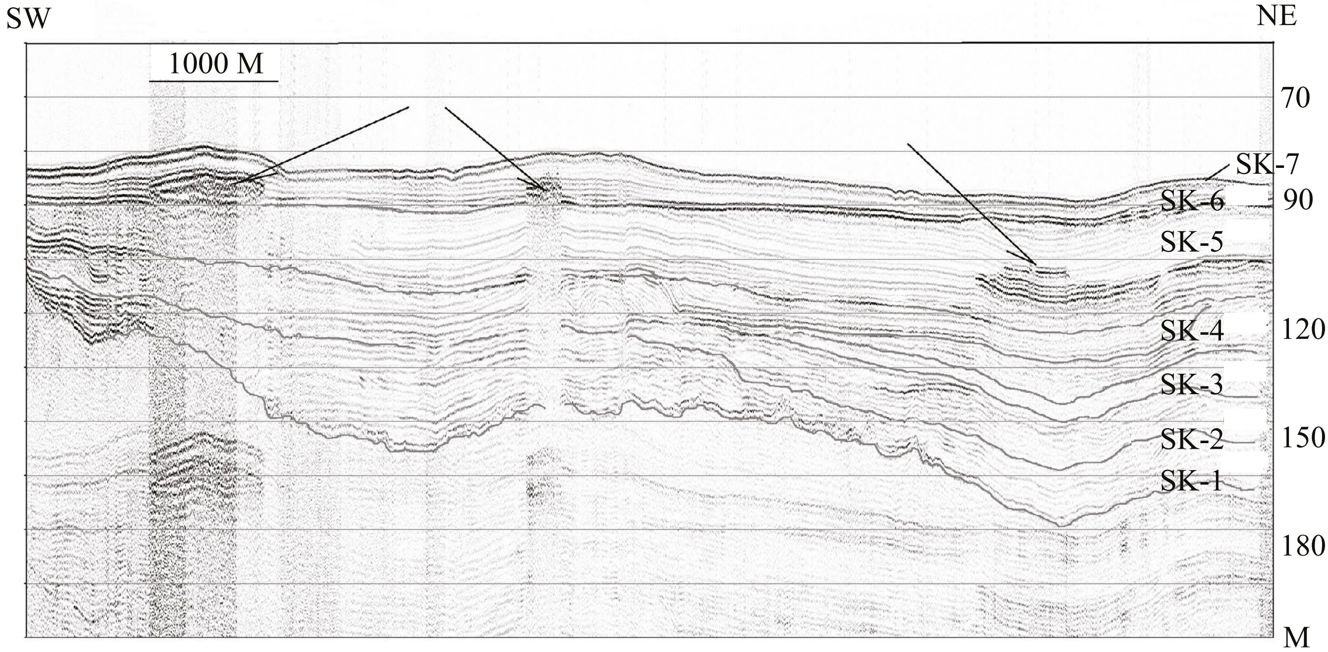

**Fig. 3.** Fragment of seismoacoustic profile 1 NSAP on the traverse of Yalta. Arrows indicate gas accumulations confined to Upper Neopleistocene deposits.

The most characteristic features creating anomalous effects in the reflected wave field are: sharp increase in amplitudes, changes in wave polarity from positive to negative, deflection of the underlying reflecting horizons beneath “bright spots” due to decreased wave velocity in gas-bearing soils.

The methodology for identifying gas anomalies and their interpretation in the seismic wave field of the Black Sea and other water areas is described in detail in several works [10-12].

Fig. 4 shows gas accumulations identified on seismoacoustic profiles in the near-bottom part of the section, confined to the Upper Pleistocene-Holocene deposits.

The anomalous zones identified by seismic features and associated with gas accumulations are divided by us into three types.

The first type of anomalies is associated with near-bottom “rootless” gas accumulations resulting from diagenesis in tertiary deposits. They form characteristic zones of correlation loss caused by the absorption of seismic signals in areas of gas accumulations. Identified by amplitude-frequency characteristics, the lateral dimensions of these accumulations can reach several kilometers. Fig. 5 shows a correlation loss zone associated with a local gas accumulation in the near-bottom part of the southeastern shelf at the meridian of Sudak city. Such accumulations are formed as a result of lateral fluid movement along the rise of layers. Apparently, the gas-fluid mixture migrates through sandy interlayers from the Western Black Sea depression upward along the rising layers toward the shore.

The second type of anomalies is caused by vertical flows of deep gas under the influence of abnormally high formation pressures, with characteristic narrow vertical zones, often referred to in publications as “fluid breakthrough.” They are characterized by a vertical columnar shape and directionality with the formation of small elevations in the bottom relief, up to several meters in height and tens or even hundreds of meters in width. Within them, a complex recording pattern is observed, apparently associated with accumulations of sand carried by fluid flows through vertical faults from deep horizons, forming elevations in the bottom relief. In relation to the general nature of the recording, such areas have a clearly destructive character,

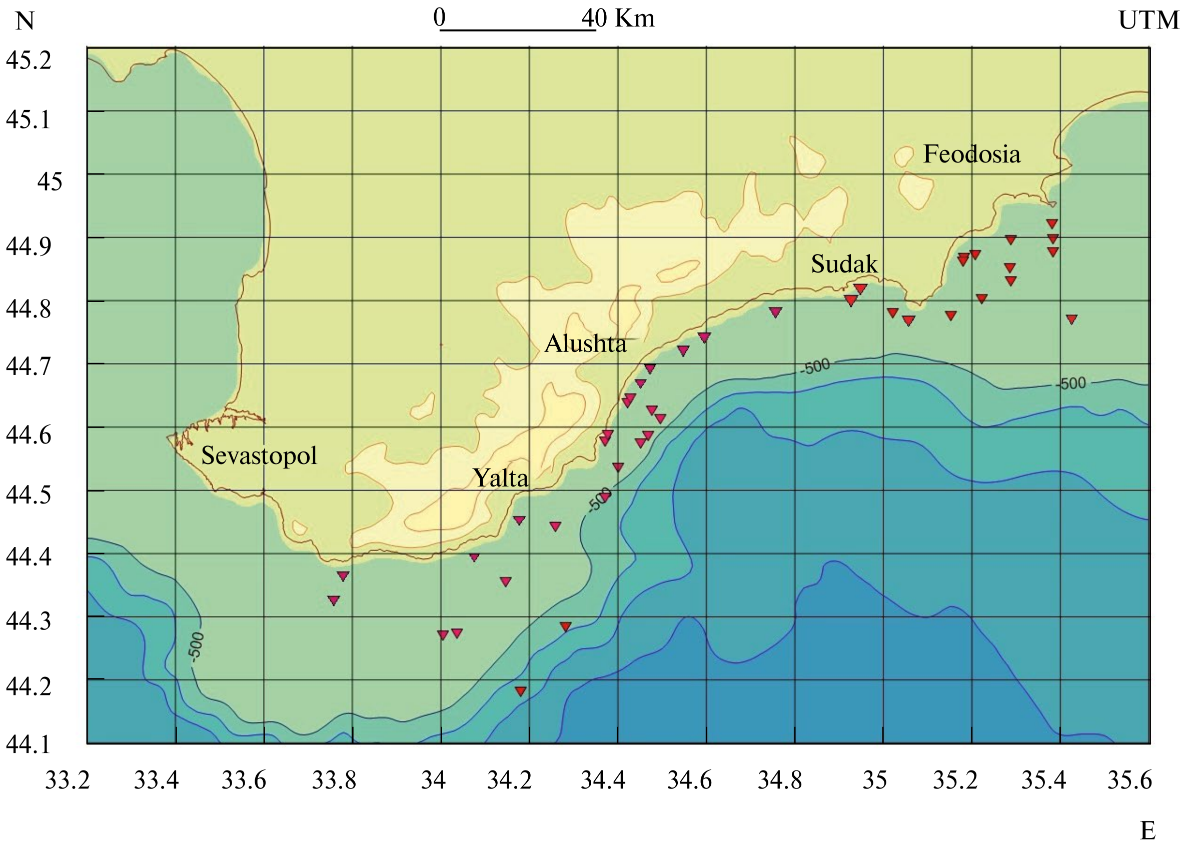

**Fig. 4.** Scheme of gas accumulations in the southeastern part of the Crimean shelf based on seismoacoustic profiling data.

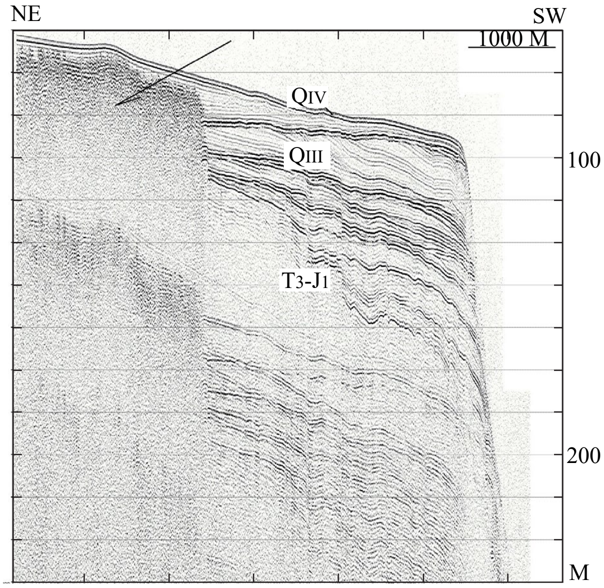

**Fig. 5.** Fragment of seismoacoustic profile 2 of NSAP of the shelf and slope in the area of Sudak Bay. The arrow indicates gas accumulation in Upper Pleistocene deposits.

therefore in specialized literature they are, in certain cases, called zones of destruction. In Fig. 6, arrows indicate elevations in the bottom relief in Quaternary deposits south of Alushta, apparently formed by the discharge of a gas-water mixture, with the removal of sandy material to the bottom surface.

The elevations in the seabed relief noted above are a manifestation form of local gas flows of deep hydrocarbons, usually accompanied, in addition to sand, by emissions of mud breccia, detrital material, water, and forming cone-shaped hills with craters at the tops. The formation of mud volcanoes is characteristic of hydrocarbon seepage sites. There are many examples of such formations, both in the Black Sea and in other water areas [12].

Geodynamic activity in the geological area from Yalta to Alushta manifests itself through fault systems and individual vertical zones of rock destruction. Traces of deep fluid flows are subvertical geological bodies that penetrate to the surface along major discontinuities in the sedimentary cover and are associated with intense localized discharge zones of hydrocarbon fluids. The noted subvertical geological bodies can serve as hydrocarbon migration channels, manifesting on the surface as gas, oil, and water seeps. As a consequence, volcanism, diapirism and vertical structure formation, release and jet vertical migration of hydrogen, lateral migration of mobile fluids, and other geological processes associated with this phenomenon are observed in these zones [13].

The gas composition was studied jointly by researchers from the A.O. Kovalevsky Institute of Marine Biological Research of RAS (Sevastopol) and Lomonosov Moscow State University. Samples of bubble gas were collected by them using special gas traps installed on the seabed in the area of Cape Fiolent, Laspi Bay, the coastal area of Yalta, and others. The conducted studies of the gas seeps composition showed that methane predominates in the component composition of the bubble gas. The polygenic composition of methane fluid flows established by these works is most likely explained by their deep migration [14, 15].

The third type of anomalies is related to the elevated basement rock blocks of the southeastern continental margin of Crimea. Gas accumulations are confined to them, which appear on seismoacoustic profiles as dynamically darkened areas within which there is a loss of correlation of

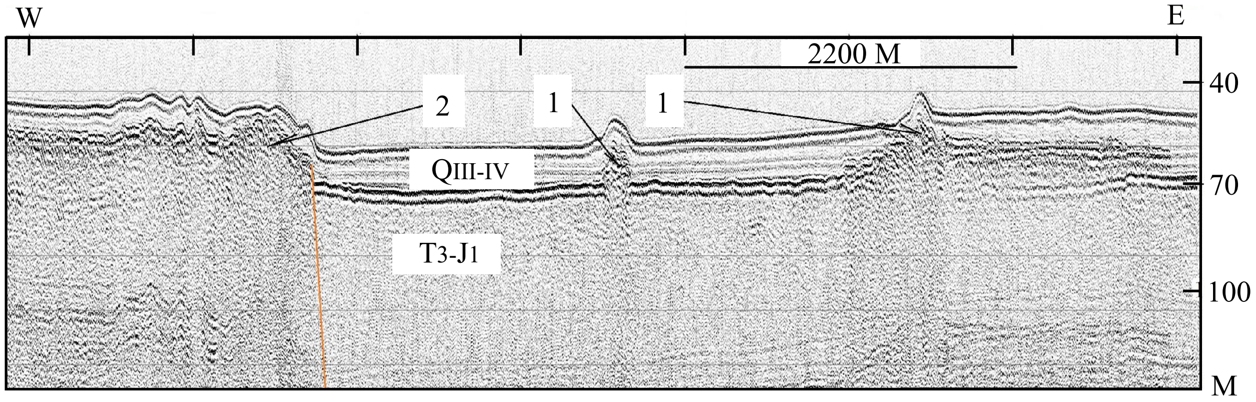

**Fig. 6.** Fragment of seismoacoustic profile 3 of NSAP of the shelf on the traverse of Alushta city. Arrows indicate: 1) gas manifestations, probably associated with mud volcanic activity (with coordinates 44. 36. 38 N, 34. 29. 36 E); 2) confined to modern elevations of the foundation of the southeastern continental margin of Crimea.

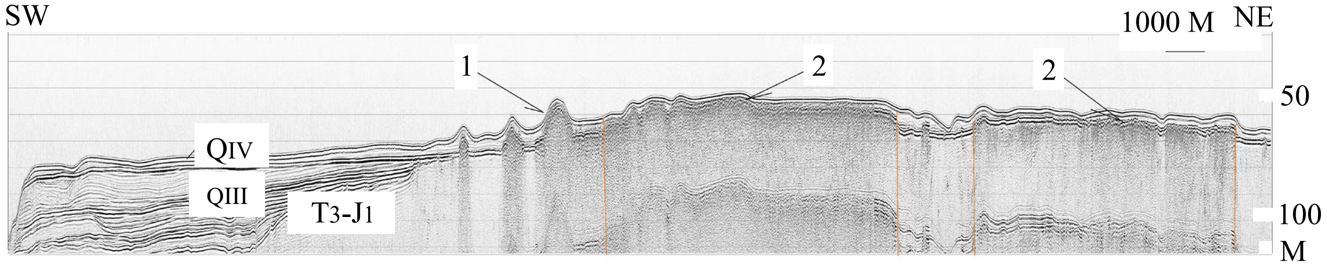

**Fig. 7.** Fragment of the regional latitudinal seismoacoustic profile 4 NSAP along the line Malorechenskoye settlement – Cape Chauda. Arrows indicate: 1) gas manifestations, probably associated with mud volcanic activity (with coordinates 44.42.80 N, 35.00.87 E); 2) confined to modern uplifts of the basement of the southeastern continental margin of Crimea.

reflecting horizons. On the latitudinal profile from the meridian of Malorechenskoye settlement to the meridian of Cape Chauda, elevated and lowered blocks of Taurian series rocks, uplifted along vertical faults and covered with thin Upper Pleistocene-Holocene deposits, are clearly distinguished. Areas of intensive gas occurrence are confined to tectonic blocks that have been uplifted in recent times, and the migration paths of the gas-fluid mixture are the faults that bound them (Fig. 7).

In the study area, the first type of anomalies is stratigraphically confined mainly to the near-surface part of the Upper Pleistocene-Holocene deposits, while the second and third types can cover a more significant recording interval.

The first type of anomalies is associated with strata of paleodelta and paleochannel accumulations. The manifestation of these gases and the formation of their accumulations are due to lateral migration up the uplift of layers.

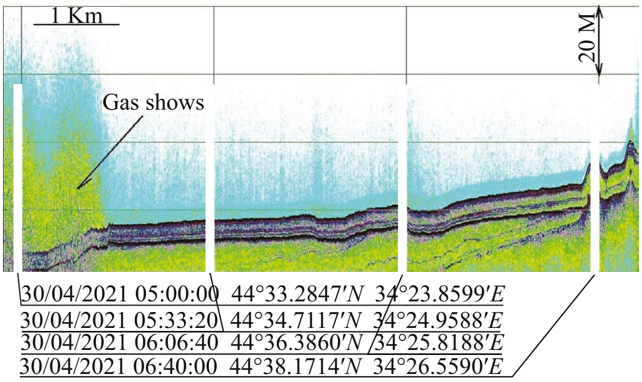

**Fig. 8.** Fragment of acoustic profile 5 near Yalta, in the area of Mount Ayu-Dag, showing gas release to the bottom surface at the point with coordinates 44.33.28 N, 34.23.85 E.

Anomalies of the second and third types are associated with manifestations of deep-migration gases and are confined primarily to active tectonic zones and areas of mud diapirism development. Large tectonic disturbances play a decisive role in creating vertical migration channels for gas-fluid flows and forming gas jets. The staff of JSC "Yuzhmorgeo" published analyses of the chemical and isotopic compositions of gases from sediments (percentage content of methane homologues, concentration of carbon dioxide and nitrogen) collected in soil samples in the northwestern part of the Black Sea in the fault zone on the continental slope and in clays of mud volcanoes. Their identical composition led the authors to conclude that methane gas is predominantly of deep origin. It enters the upper layers of the sedimentary cover by filtration or jet migration [16].

On acoustic profiles, gas seepage from sedimentary rocks into water in discharge zones is clearly distinguished (Fig. 8).

## DISCUSSION OF RESULTS

Seismostratigraphic analysis of the obtained materials showed that the gas manifestations identified on the southeastern shelf of Crimea, totaling 40 anomalies, are stratigraphically confined to Upper Pleistocene-Holocene deposits. The deposits of Pleistocene paleodeltas, traces of which have been discovered by CHIRP data in the study area, can serve as accumulating rocks.

Genetically, the identified anomalies are divided into three types. The first type is associated with near-bottom "rootless" gas accumulations formed by lateral flows. The second type is caused by narrow vertical zones of gas-fluid mixture release under the influence of abnormally high pressures.

The third type of gas accumulations is confined to faults associated with elevated blocks of basement rocks.

The performed seismoacoustic studies have also shown that the continental margin of Crimea is characterized by a block structure. Differentiated vertical neotectonic movements have played and continue to play a decisive role in the structure of the southeastern shelf, in the formation of deep faults as channels for fluid migration from deep horizons to the seabed surface [17, 18]. It is in the zones of active fault tectonics that gas accumulations, mud volcanoes, and gas seeps are formed. Various types of gas-fluid manifestations identified by the research vessel "Professor Vodyanitsky" confirm this. Gas-saturated deposits with zones of abnormally high formation pressure are a feature of the subaquatic engineering-geological environment. Their distribution areas are hazardous for engineering construction. Pressure and gas emissions into the water column are accompanied by deformation of the seabed surface, formation of landslides, reduction of soil bearing capacity, etc. Depressurization of gas accumulations in the upper part of the section during drilling can lead to gas breakthroughs, formation of pits, and gas contamination of the water column [19, 20].

## CONCLUSIONS

1. Near-bottom methane accumulations identified by seismoacoustic profiling are located in the southeastern part of the Crimean shelf and are confined to sandy deposits of Pleistocene-Holocene age, mainly near fault zones.

2. The identified anomalies are located in the area of paleodelta systems development, whose rocks have good accumulation properties.

3. Three types of gas accumulations have been identified, genetically associated with lateral flows, mud volcanic activity, and vertical migration along deep faults.

4. Gas seepages to the seabed surface are caused by seismic activity of the Mountainous Crimea structure and are a consequence of recent tectonic manifestations.

5. Periodic activation of fault blocks underlying the sedimentary cover contributes significantly to the formation of near-surface gas accumulations, which indicates the probability of their deep origin.

6. The identification of gas accumulations in the near-bottom part of the sedimentary cover is important for monitoring potentially dangerous areas for engineering construction and navigation.

7. To clarify the genesis and zoning of gas accumulations identified by seismoacoustics data, it is necessary to conduct an additional full range of studies along all lines of seismoacoustic NSAP profiles, including acoustic profiling, side-scan sonar studies, and echo sounding.

## ACKNOWLEDGEMENTS

The authors express their gratitude to the sailors of the R/V "Professor Vodyanitsky" and *employees of* the Southern Marine Biology Institute for their constant assistance in the work.

## FUNDING

The research was conducted within the framework of the state assignment on topic No. FMWE -2024-0024, as well as with the financial support of the RFBR project No. 20-05 00384_A.

## REFERENCES

1. *Meisner L.B., Tugolesov D.A.* Fluidogenic deformations in the sedimentary fill of the Black Sea basin // Exploration and Protection of Mineral Resources. 1997. No. 7. Pp. 18–22.
2. *Shnyukov E.F., Pasynkov A.A., Kleshchenko S.A. et al.* Gas flares on the bottom of the Black Sea. Kiev, 1999. 133 p.
3. *Glebov A.Yu., Kruglyakova R.P., Shelyping S.L.* Natural emissions of hydrocarbon – gases in the Black Sea // Exploration and Protection of Mineral Resources. 2001. No. 8. Pp. 19–22.
4. *Shnyukov E.F., Starostenko V.I., Rusakov O.M., Kutas R.I.* Deep nature of gas flares in the western part of the Black Sea based on the results of geophysical studies // Geology and Mineral Resources of the World Ocean. 2005. No. 5. Pp. 70–82.
5. *Kruglyakova R.P., Kruglyakova M.V., Shevtsova N.T.* Geological and geochemical characteristics of natural hydrocarbon occurrences in the Black Sea // Geology and Mineral Resources of the World Ocean. 2009. No. 1. Pp. 37–51.
6. *Shnyukov E.F., Kobolev V.P., Pasynkov A.A.* Gas volcanism of the Black Sea. Kyiv: "Logos", 2013. 384 p.
7. *Rimsky-Korsakov N.A., Pronin A.A., Khortov A.V. et al.* Technology and results of seismoacoustic profiling on the Crimean shelf during the 124th cruise of the R/V "Professor Vodyanitsky" // International Journal of

Applied and Fundamental Research. No. 2. 2023. Pp. 37–43.

8. *Rimsky-Korsakov N.A., Pronin A.A., Mutovkin A.D. et al.* Seismostratigraphy of the continental margin of Crimea according to seismoacoustic profiling data / In the collection: “State and prospects of exploration for oil and gas on the continental shelf of the Russian Federation”, June 1-2, 2023. Issue 2. Saint Petersburg: VNIIOkeangeologiya. 2023. 86 p.

9. *Khortov A.V., Rimsky-Korsakov N.A., Pronin A.A., et al.* Seismostratigraphic studies of the Crimean shelf using continuous seismoacoustic profiling // Doklady RAS. Earth Sciences. 2023. Vol. 512. No. 2. Pp. 134–140.

10. *Dimitrov L.L.* Gas-acoustic anomalies of the sedimentary cover of the Bulgarian Black Sea shelf // Geological evolution of the western part of the Black Sea basin in the Neogene-Quaternary period. Sofia. Publishing House of the Bulgarian Academy of Sciences, 1990. Pp. 362–380.

11. *Gainanov V.G.* On the nature of bright spots on time sections of seismoacoustic profiling. // GEOrazrez. Electronic scientific journal of “Dubna” University, 2008. No. 2. Pp. 1–18.

12. *Maraev S.L., Khortov A.V.* Vertical destructive fluid discharge zones of the Caspian Sea as a type of geologically hazardous phenomena // Scientific Journal of the Russian Gas Society. Geoecology Section. 2022. No. 1. Pp. 30–35.

13. *Shnyukov E.F., Pasynkov A.A., Lyubitsky A.A., et al.* Black Sea bottom relief forms as possible manifestations of modern geodynamic activity // Geology and Mineral Resources of the World Ocean. 2012. No. 2. Pp. 99–103.

14. *Malakhova T.V., Kanapatsky T.A., Egorov V.N., et al.* Microbial processes and genesis of jet methane gas emissions in the coastal areas of the Crimean Peninsula // Microbiology. 2015. Vol. 84. No. 6. Pp. 743–752.

15. *Malakhova T.V., Malakhova L.V., Murashova A.I., et al.* Monitoring of shallow-water seeps near Cape Fiolent (Black Sea) // Oceanology. 2023. Vol. 63. No. 1. Pp. 135–148.

16. *Kruglyakova R.P., Byakov Y.A., Kruglyakova M.V., et al.* Natural oil and gas seeps of the Black Sea floor // Geo-marine Letters. 2004. No. 23. Pp. 193–201.

17. *Evsyukov Yu.B., Rudnev V.I.* Geomorphology and neotectonic transformation of the continental shelf in the western part of the Black Sea // Geology, Geography and Global Energy. 2013. No. 3 (50 ) . Pp. 46–55.

18. *Esin N.I., Khortov A.V.* Dynamics of vertical movements of the Earth’s crust in the Holocene // Ecology of the Hydrosphere. 2022. No. 2 (8). Pp. 47–68.

19. *Mironyuk S.G., Kleshchin S.M.* Experience in using geophysical methods to identify marine geological hazards // GeoEngineering. 2010. No. 1. Pp. 48–54.

20. *Mironyuk S.G., Markaryan V.V., Shelting S.K.* Experience of Comprehensive Assessment and Large-Scale Engineering-Geological Zoning of the Northeastern Black Sea Shelf by Geological Hazards for Linear Infrastructure Construction // Engineering Survey. 2013. № 13. Pp. 48–59.

*DOKLADY EARTH SCIENCES, 2025, Vol. 520, No. 1, pp. 76–82*

## PETROLOGY

# THE JURASSIC THROUGH EARLY CRETACEOUS MAGMATIC BELT OF THE SOUTHERN MARGIN OF CHUKOTKA TERRANE (NORTHEASTERN RUSSIA): NEW ZIRCON U–Pb AGE DATA

**© 2025 P. L. Tikhomirov**[a, b, *], **M. S. Gulpa**[c]

Presented by Academician of the Russian Academy of Sciences K. E. Degtyarev on April 27, 2024

Received May 20, 2024
Revised June 26, 2024
Accepted July 03, 2024

**Abstract.** The U-Pb dating of zircons from igneous rocks of the Central Chukotka area (left bank of the Amguema River) indicated that two granitic batholiths (Telekai and Chanuan massifs) and the series of smaller plutons have been formed during 143–127 Ma time span. This age is substantially greater than that determined for the greater part of the North Chukotka's granites (109–100 Ma). Both new and published isotopic age data infer that there was a large subduction related magmatic belt at the margin of the Chukotka continental block, at least during the Late Jurassic and Neocomian time. Then, the newly discovered Early Jurassic U–Pb ages of Chukotka's igneous complexes (ca. 196 Ma) imply much longer duration of magmatic activity at the margin of the Chukotka microcontinent. The Albian granitic plutons of the observed area (106–100 Ma) were controlled by a different fault system, and they are probably related to a separate magmatic event.

**Keywords:** *shelf, Chukotka terrane, Jurassic and Cretaceous periods, Andean type magmatic belt, U-Pb geochronology, magmatic pulses*

**DOI**: 10.31857/S26867397250108e4

## INTRODUCTION

Almost all modern paleotectonic reconstructions of the Arctic assume that during the Jurassic-Early Cretaceous period, the Chukotka continental terrane was separated from the Eurasian continent by a basin with oceanic-type crust: the South Anyui (Anyui-Angayucham, Proto-Arctic) Ocean. The final closure of this basin at the end of the Early Cretaceous led to the formation of the South Anyui Suture Zone [1, 2]. There is much less consensus regarding the width of the South Anyui Basin and the kinematics of tectonic block movements during its closure ([3, 4] and references cited in these works). The nature of the southern boundary (in modern coordinates) of the Chukotka block also continues to be debated: whether it was passive or active (subduction). According to some models [2], this boundary was passive, and the admixture of pyroclastic material in the rocks of the Late Jurassic-Early Cretaceous basins of the Chukotka terrane is associated with the activity of the intra-oceanic Kulpolney arc [2, 5]. Alternative models suggest subduction of the South Anyui Ocean lithosphere directly beneath the Chukotka microcontinent [1, 6–8]. Until now, the weakness of the second group of models has been the absence within the Chukotka terrane of geological formations that could confidently be combined into a Late Jurassic-Early Cretaceous subduction magmatic belt. Publications mention only individual granitoid massifs with an age of about 136 Ma [9, 10], small areas of volcanics and comagmatic intrusives aged 147–141 Ma [11], as well as an admixture of pyroclastic material in Tithonian-Berriasian sedimentary rocks, where a significant portion of detrital zircons shows ages in the range of 150–140 Ma [6].

In this publication, we present the results of U–Pb dating of zircons from igneous rocks of Central Chukotka (left bank of the Amguema River, sheet Q-60-V, VI), which may be of decisive importance in the discussion about the nature of the southern boundary of the Chukotka

---

[a] *Schmidt Institute of Physics of the Earth, Russian Academy of Sciences, Moscow, Russia*
[b] *Shilo North-East Interdisciplinary Scientific Research Institute, Far Eastern Branch of the Russian Academy of Sciences, Magadan, Russia*
[c] *North-Eastern Production Geological Association, Magadan, Russia*
**e-mail: petr_tikhomirov@mail.ru*

microcontinent. The territory of this sheet (Fig. 1) is bounded from the west and south by outcrops of the Okhotsk-Chukotka volcanic belt (OCVB) of Albian-Campanian age [11, 12]. The largest igneous bodies in the area under consideration are the Telekai and Chanuan granitoid batholiths with areas of 730 and 780 km$^2$ respectively. The Chanuan intrusion is composed mainly of granites of normal and increased alkalinity. The Telekai pluton is heterogeneous in composition: its larger northern part is composed of leucogranites, the southern part – of granites and granodiorites. Both massifs intrude Triassic terrigenous rocks and are unconformably overlain by OCVB volcanics. Due to the similarity of their position in the regional structure with other plutons of Northern Chukotka, both of these massifs, as well as the smaller bodies accompanying them, were usually associated with the region-wide Early Cretaceous pulse of magmatic activity [13]. At the same time, most of the available U–Pb age determinations for granitoids of Northern Chukotka correspond to the interval of 109–100 Ma [14].

## ANALYTICAL TECHNIQUE

Sampling and analytical work were carried out in 2020–2023 as part of the geological additional study of sheet Q-60-V, VI at a scale of 1:200 000 (Chaantal detachment of the SSU "Chukotka Group of Parties" of JSC "SVPGO") commissioned by FSBI "VSEGEI", responsible executor I.V. Gulpa). This publication presents the results of dating 18 samples representing the main

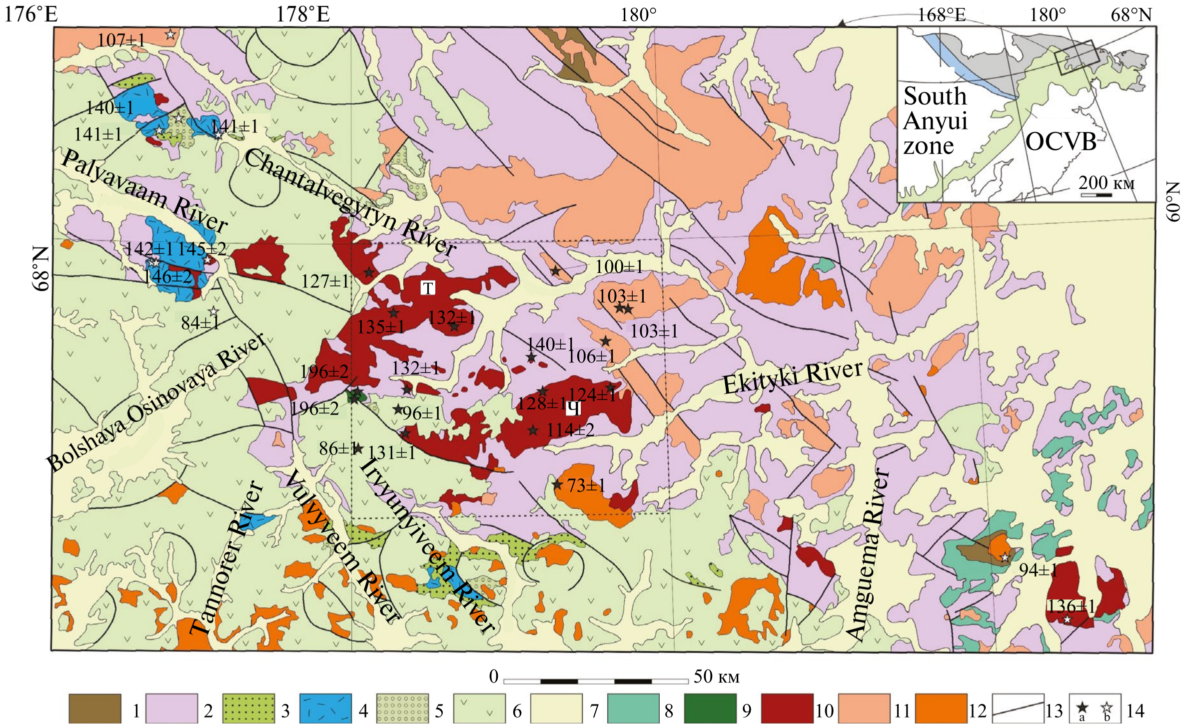

**Fig. 1.** Geological structure scheme of Central Chukotka (left bank of the Amguema River, upper reaches of the Palyavaam, Pegtymel, Ekiatap, Bolshaya Osinovaya Rivers). Compiled based on materials from [2], with modifications. The age of geological complexes has been adjusted taking into account data from this publication, as well as data from works [4, 5, 9, 10, 19]. 1 – crystalline schists, gneisses, marbleized limestones of Devonian – Carboniferous; 2 – sandstones, siltstones and mudstones of the Upper Permian and Triassic; 3 – terrigenous-clastic and volcanomictic sedimentary rocks of the Upper Jurassic – Neocomian; 4 – volcanics of the Upper Jurassic-Neocomian (predominantly tuffs and rhyolite ignimbrites); 5 – terrigenous-clastic and volcanomictic sedimentary rocks of the Albian; 6 – volcanics of the OCVB (from basalts to rhyolites; within the considered area – of Cenomanian-Campanian age), 7 – Quaternary deposits; 8–12 – intrusive formations: 8 – Early-Middle Triassic gabbroids, 9 – Early Jurassic gabbroids, 10 – Late Jurassic(?)-Early Cretaceous (pre-Albian) granitoids, 11 – Albian granitoids, 12 – Late Cretaceous granitoids; 13 – faults; 14 – sampling points for U–Pb dating of zircon grains and obtained age values (±2σ), rounded to whole million years (a – data from this publication, b – data from [5, 10, 12, 19]).

stages of magmatic activity in the territory under consideration. The locations of the sampling points are shown in Fig. 1, and the dating results are presented in Figs. 2 and 3. Brief information about the studied samples is summarized in Table 1.

The boundaries of sheet Q-60-V, VI are shown by dotted lines. Letters in squares – Telekaiskiy (T) and Chanuanskiy (Ch) batholiths. The inset shows outcrops of the Chukotka terrane complexes (gray fill), OCVB and South Anyui zone; the bold line indicates the contours of the area under consideration.

Zircon monofractions were extracted using a standard procedure in heavy liquids followed by

**Table 1.** List of magmatic rock samples taken on the left bank of the Amguema River and in the upper reaches of the Palyavaam, Pegtymeel, and Velmay rivers, used for U–Pb dating of zircon grains

| No. | Sample No. | Rock | U–Pb age, Ma (± 2σ) | Longitude (deg.) | North latitude (deg.) |
|---|---|---|---|---|---|
| 1 | 1026.05 | Granosyenite | 103.5±1.0 | 179.737829 | 67.837954 |
| 2 | 1028.01 | Subalkaline granite | 103.2±1.0 | 179.702033 | 67.839535 |
| 3 | 1034.01 | Granodiorite | 99.9±0.9 | 179.300916 | 67.936851 |
| 4 | 1067.01 | Granite | 126.8±1.2 | 178.110236 | 67.929333 |
| 5 | 1091.01 | Subalkaline leucogranite | 135.2±1.2 | 178.249431 | 67.830949 |
| 6 | 1149.01 | Trachyrhyolite ignimbrite | 85.8±0.8 | 178.041056 | 67.500753 |
| 7 | 1205.01 | Subalkaline granite | 114.3±1.6 | 179.138983 | 67.537193 |
| 8 | 1206.01 | Subalkaline leucogranite | 72.6±1.2 | 179.304503 | 67.439387 |
| 9 | 1218.01 | Diorite | 143.2±2.4 | 178.345262 | 67.647946 |
| 10 | 1240.01 | Rhyolite ignimbrite | 96.0±0.6 | 178.306770 | 67.589596 |
| 11 | 1261.01 | Subalkaline granite | 131.2±1.2 | 178.366745 | 67.549308 |
| 12 | 1318.01 | Gabbro | 195.8±1.9 | 178.031639 | 67.641690 |
| 13 | 1341.01 | Gabbro | 196.2±1.9 | 178.028732 | 67.619201 |
| 14 | 1374.01 | Granite | 128.0±0.7 | 179.207239 | 67.632002 |
| 15 | 1398.01 | Granosyenite | 105.8±1.1 | 179.646833 | 67.748808 |
| 16 | 1401.01 | Subalkaline granite | 124.3±1.0 | 179.663452 | 67.640613 |
| 17 | 1413.01 | Quartz diorite | 140.5±1.0 | 179.155229 | 67.719510 |
| 18 | 1440.01 | Granite | 132.0±1.1 | 178.672907 | 67.795310 |
| 19 | SL1 | Granodiorite | 107.0±1.0 | 176.788278 | 68.509917 |
| 20 | T10-52 | Rhyolite tuff | 140.8±1.2 | 176.744111 | 68.270861 |
| 21 | T10-47e | Rhyolite ignimbrite | 140.4±1.1 | 176.783889 | 68.285750 |
| 22 | T10-82 | Rhyolite ignimbrite | 140.9±1.0 | 177.172250 | 68.267556 |
| 23 | 3873b/90 | Rhyolite tuff | 142.5±1.4 | 176.722036 | 67.949538 |
| 24 | 3876a/90 | Rhyolite tuff | 146.0±2.4 | 176.740976 | 67.949332 |
| 25 | 7938d/91 | Granodiorite-porphyry | 145.5±1.8 | 177.071780 | 67.956874 |
| 26 | 7155a/89 | Dacite tuff | 84.55±0.50 | 177.080683 | 67.815497 |
| 27 | 09-353/1 | Granite-porphyry | 93.74±0.82 | –178.015549 | 67.201816 |
| 28 | 09-341 | Syenite | 135.6±1.0 | –177.682394 | 66.995077 |

Note. Analyses 1–18: new data, 19–28: data published earlier [5, 10, 12, 19]. Negative longitude values are given for samples taken in the western hemisphere.

manual purification under a binocular microscope. Isotopic ratios were measured on a SHRIMP II ion microprobe at the VSEGEI Center for Isotopic Research using the methodology described in [15]. Nearly all samples had 10 zircon grains analyzed, with one sample having 11 grains. For the vast majority of spot analyses, concordant values of isotopic ratios were obtained, and the results for different grains from the same sample show good agreement (Fig. 2). The proportion of non-radiogenic $^{206}$ Pb usually does not exceed 0.5%, and only for 6 spot analyses out of 181 does it exceed 2%.

## RESULTS AND DISCUSSION

With high probability, all obtained U–Pb age values correspond to the age of magma crystallization. In two samples (1218.01 – diorite from a small stock between the Telekai and Chanuan massifs and 1240.01 – rhyolite ignimbrite of the Amgen Formation, the lower straton of the OCVB in this area), xenocrysts of zircon with relatively ancient ages are present (4 and 2 grains, respectively). One of the xenocrysts was determined to have an Early Proterozoic U–Pb age (1864±20 Ma), while the others are 8–30 million years older than the main zircon population (Fig. 2 and, k), which significantly exceeds the error of individual determinations. In sample 1401.01 (subalkaline granite of the main phase of the Chanuan massif), 8 out of 10 grains yielded ages in the range of 126–122 Ma, and 2 grains in the range of 118–117 Ma (Fig. 2c). There are reasons to assume partial loss of radiogenic lead in some zircons from sample 1401.01, since a younger intrusion is located near the sampling point (Fig. 1). Analyses of suspected xenocrysts and grains with disturbed isotopic systems were excluded from the calculation of the overall sample age.

The obtained U-Pb ages generally cover the time interval from 196 Ma (Early Jurassic, Sinemurian) to 73 Ma (Late Cretaceous, Campanian) (Fig. 3). The most numerous group of isotopic dates corresponds to the interval of 143–127 Ma (Early Cretaceous, Berriasian-Barremian), it was during this time that the Telekai pluton, most of the Chanuan massif, and numerous small intrusive bodies located between them were formed (Fig. 1). The intrusives of the territory under consideration turned out to be noticeably older than most of the granitoid massifs of Northern Chukotka, combined in the Chaun province dated at 109–100 Ma [14, 16, 17]. Together with the volcanic and plutonic formations of the Tithonian-Barremian (147–126 Ma) previously identified within Central and Eastern Chukotka [8, 9, 13, 18], the pre-Albian magmatic complexes form a northwest-trending belt over 300 km long (from the upper reaches of the Pegtymel River to the upper reaches of the Velmay River; Fig. 1) with a width of up to 70 km. Separate outcrops of granitoid bodies with U-Pb ages of 136–132 Ma have also been identified further to the southeast, up to Providence Bay [10, 19], suggesting an even greater extent of this magmatic belt, over 600 km. Since, within the accepted geodynamic models, the oceanic basin that separated the Chukotka block from Eurasia finally closed at the end of the Neocomian [1, 2, 7], the Jurassic-Neocomian magmatic formations of Central Chukotka, including granitoid batholiths, small intrusives, and relics of volcanic strata of the calc-alkaline series, are confidently interpreted as traces of a *subduction magmatic province of Andean type*.

For two samples from the gabbroid stock on the right bank of the Pravyi Teleakai River, almost identical U–Pb ages of about 196 Ma were obtained (Fig. 2m, n). This first Early Jurassic date determined for the magmatic rocks of Chukotka gives grounds to assume that the subduction margin of the Chukotka microcontinent maintained activity for at least 70 million years (possibly with interruptions).

The U–Pb age of the subalkaline granite of the additional phase of the Chanuan massif is 114.3±1.6 million years, which is significantly (at least 10 million years) younger than other U–Pb dates for rocks of the proposed continental margin belt. With limited data available, it is still difficult to judge the place of Aptian magmatism in the history of Central Chukotka. We will only note that in the western part of the Chukotka block, Aptian magmatism (123-112 million years) is widely manifested and presumably has a post-collisional nature [14].

In the composition of the pre-Albian magmatic complexes of Central Chukotka, intrusive rocks sharply predominate over volcanic rocks. Very likely, this is a consequence of the deep erosional truncation of the Jurassic-Early Cretaceous magmatic province. This is also indicated by the parageneses of the prehnite-pumpellyite facies of metamorphism, identified in the relics of volcanic strata of the corresponding age [11].

Some granitoid intrusives, formed synchronously with the plutons of the Chaun province (109–100 million years), within sheet Q-60-V, VI have a pronounced linear form and northwestern strike,

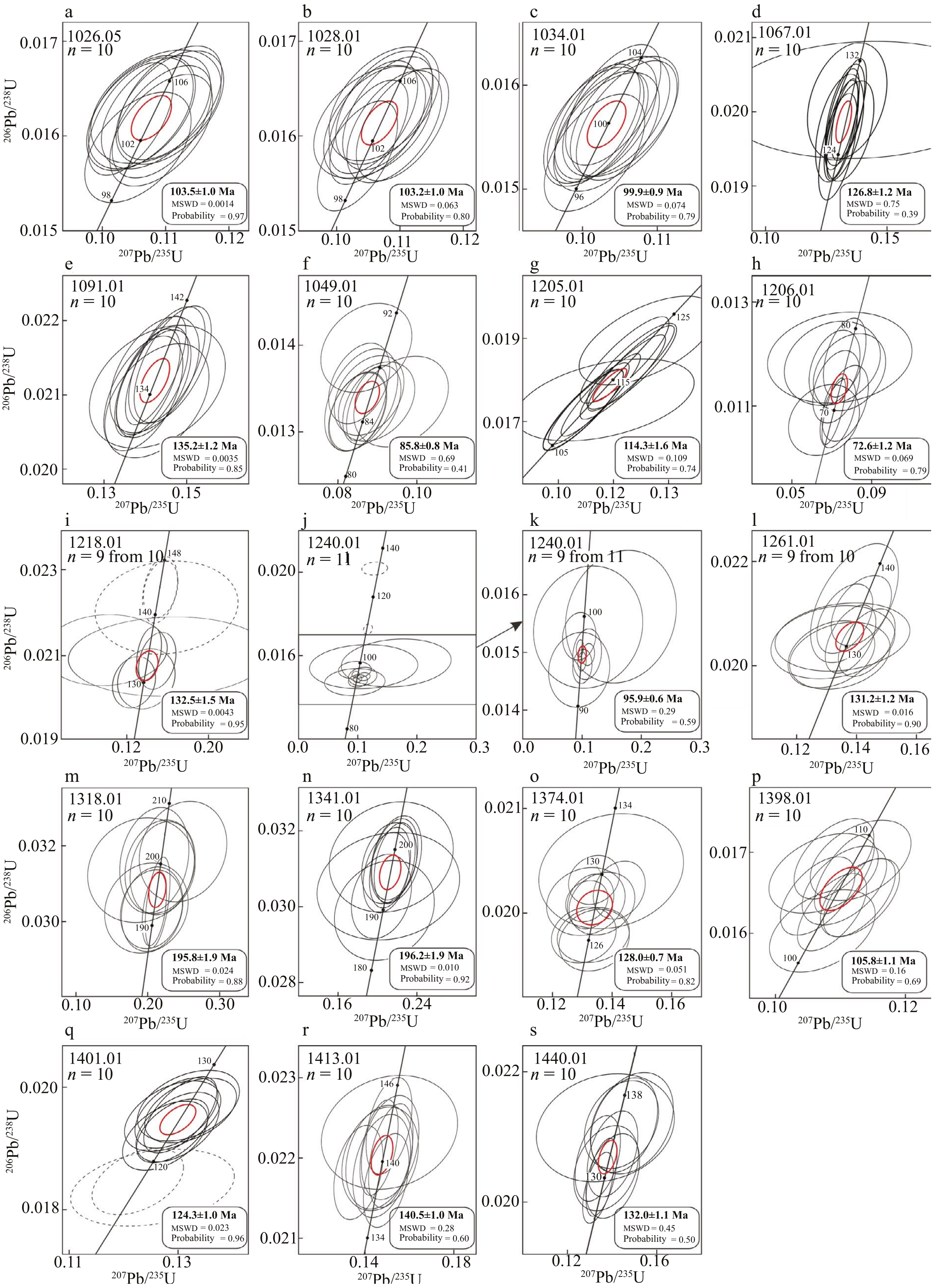

**Fig. 2.** Results of U–Pb dating of magmatic rock samples from the left bank of the Amguema River (sheet Q-60-V, VI). The names of rocks and coordinates of sampling points are given in Table 1. The size of the error ellipses corresponds to 2σ. Dotted lines show ellipses for point analyses excluded from the age calculation of samples.

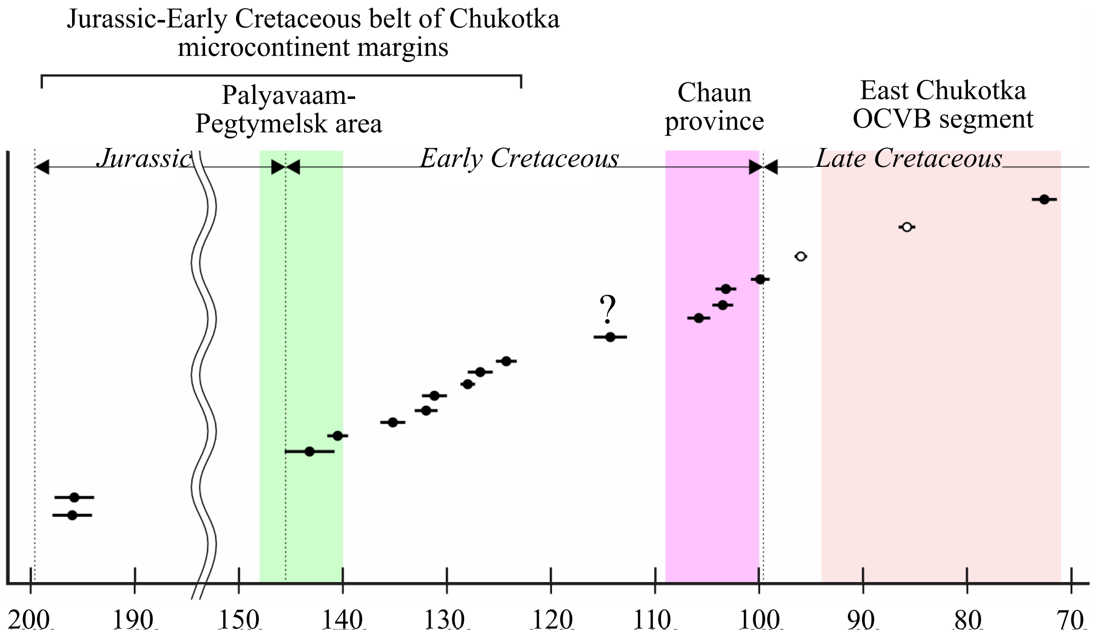

**Fig. 3.** Diagram of U–Pb age of magmatic rocks from the left bank of the Amguema River. Horizontal segments represent error margins (2σ). Black-filled symbols indicate plutonic rocks, unfilled symbols represent volcanic rocks. Colored fills show the time intervals of formation of the Palyavaam-Pegtymelsk magmatic area [10, 19], the Chaun magmatic province [20], and the East Chukotka segment of the OCVB [10, 11].

sharply different from the strike of older intrusive bodies and their groups (Fig. 1). These features agree well with the assumption about the intrusion of Chaun province magmas in the setting of right-lateral strike-slip displacements along faults of northwestern strike [17].

The age of the youngest magmatic rocks of sheet Q-60-V, VI (72.6±1.2 Ma) is quite consistent with data on the age of the upper strata of the East Chukotka segment of the OCVB and confirms the assumption about the relatively late completion of activity in this area of the volcanic belt (72–71 Ma versus 76–74 Ma in other areas [11, 12, 17, 20]).

## CONCLUSIONS

1. The obtained data confirm the assumption [1, 6, 8] about the active nature of the southern (in modern coordinates) boundary of the Chukotka continental terrane, at least during the Tithonian-Barremian time (147–127 Ma).

2. The presence of Early Jurassic (about 196 Ma) gabbroids within Central Chukotka suggests prolonged magmatic activity of the margin of the Chukotka block, possibly spanning the entire Jurassic period.

3. The Albian granitoids of the considered territory (106–100 Ma) are most likely related to the tectono-magmatic system of the Chaun province [11, 14]. The intrusion of magmas during this period was largely controlled by fractures with northwest orientation, which distinguishes the Albian intrusions from older ones.

## FUNDING

Field work and U–Pb dating of zircons were carried out in accordance with State Assignment No. 049-00016-21-00 issued to FSBI VSEGEI. P.L. Tikhomirov's work on the interpretation of results was carried out with the support of the Russian Science Foundation (grant No. 23–17-00112), and on the preparation of the article – within the framework of the State Assignment of Northeastern Complex Research Institute, FEB RAS (topic 121031700312-1).

## REFERENCES

1. *Parfenov L.M., Nokleberg W.J., Monger J.W.H., Norton I.O., Stone D.B., Fujita K., Khanchuk A.I., Scholl D.W.* Formation of collage of terranes in orogenic belts of the northern Pacific rim // Geology and Geophysics. 1999. V. 40. No. 11. Pp. 1563–1574.
2. *Sokolov S.D.* Essays on the tectonics of Northeast Asia // Geotectonics. 2010. No. 6. Pp. 60–78.
3. *Kuzmichev A.B* . Where does the South Anyui suture go in the New Siberian islands and Laptev

Sea?: Implications for the Amerasia basin origin // Tectonophysics. 2009. V. 463. P. 86–108.

4. *Miller E.L., Meisling K.E., Akinin V.V., Brumley K., Coakley B.J., Gottlieb E.S., Hoiland C.W., O'Brien T.M., Soboleva A., Toro J.* Circum-Arctic Lithosphere Evolution (CALE) Transect C: Displacement of the Arctic Alaska–Chukotka microplate towards the Pacific during opening of the Amerasia Basin of the Arctic // Geological Society, London, Special Publications. 2018. V. 460. No. 1. Pp. 57–120.

5. *Moiseev A.V., Maskaev M.V., Ulyanov D.K., Sokolov S.D., Belyatsky B.V.* Kulpolney volcanic complex of the South Anyui suture (Western Chukotka): composition, age and paleotectonic interpretations // Doklady RAS. Earth Sciences. 2021. V. 499. No. 1. Pp. 42–48.

6. *Vatrushkina E.V., Tuchkova M.I., Sokolov S.D.* Late Jurassic–Early Cretaceous suprasubduction volcanism of the Chukotka terrane (Arctic region, Russia) // Geotectonics. 2019. No. 6. P. 78–91.

7. *Amato J. M., Toro J., Akinin V.V., Hampton B.A., Salnikov A.S., Tuchkova, M.I.* Tectonic evolution of the Mesozoic South Anyui suture zone, eastern Russia: A critical component of paleogeographic reconstructions of the Arctic region // Geosphere. 2015. V. 11(5). Pp. 1530–1564.

8. *Tikhomirov P.L., Kalinina E.A., Kobayashi K., Nakamura E.* Late Mesozoic silicic magmatism of the North Chukotka area (NE Russia): age, magma sources, and geodynamic implications // Lithos. 2008. V. 105. Pp. 329–346.

9. *Luchitskaya M.V., Sokolov S.D., Moiseev A.V.* Stages of Late Mesozoic granitoid magmatism in Chukotka (Northeast Russia) // Doklady RAS. Earth Sciences. 2013. V. 450. No. 1. Pp. 1–6.

10. *Pease V., Miller E., Wyld S., Sokolov S., Akinin V., Wright J.* U–Pb zircon geochronology of Cretaceous arc magmatism in eastern Chukotka, NE Russia, with implications for Pacific plate subduction and the opening of the Amerasia Basin // Geological Society, London, Special Publications. 2017. V. 460. Pp. 159–182.

11. *Tikhomirov P.L.* Cretaceous continental-margin magmatism of Northeast Asia and questions of genesis of the largest Phanerozoic provinces of silicic volcanism. Moscow: GEOS, 2020. 376 p.

12. *Akinin V.V., Miller E.L.* Evolution of calc-alkaline magmas of the Okhotsk-Chukotka volcanic belt // Petrology. 2011. V. 19. No. 2. Pp. 1–42.

13. *Varlamova V.A., Malysheva G.M., Vyatkin B.V., Zvizda T.V., Zhukov V.A., Kovalenko A.V., Kazinsky V.A.* Information report on incomplete works on the project "Creation of a digital set of geological maps at a scale of 1 : 500 000 for the territory of the Chukotka Autonomous Okrug" (Monitoring of regional geological studies at a scale of 1:500 000). Anadyr, FGUGP "Georegion", 2004.

14. *Tikhomirov P.L., Luchitskaya M.V., Prokofiev V.Yu., Akinin V.V., Miller E.L., Isaeva E.P., Palechek T.N., Starikova E.V., Boldyreva A.I., Wiegand B.* Evolution of Aptian and Albian magmatism of western and northern Chukotka (northeast Russia) based on zircon U-Pb geochronology and rock geochemistry // International Geology Review. 2024. V. 66. Issue 2. Pp. 607–632.

15. *Schuth S., Gornyy V.I., Berndt J., Shevchenko S.S., Karpuzov A.F., Mansfeldt T.* Early Proterozoic U-Pb Zircon Ages from Basement Gneiss at the Solovetsky Archipelago, White Sea, Russia // International Journal of Geosciences. 2012. V. 3. Pp. 289–296.

16. *Tikhomirov P.L., Luchitskaya M.V., Shats A.L.* Age of granitoid plutons of Northern Chukotka: state of the problem and new SHRIMP U-Pb zircon dating // Doklady RAN. Earth Sciences. 2011. V. 440. No. 4. Pp. 507–510.

17. *Akinin V.V., Miller E.L., Toro J., Prokopiev A.V., Gottlieb E.S., Pearcey S., Polzunenkov G.O., Trunilina V.A.* Episodicity and the dance of late Mesozoic magmatism and deformation along the northern circum-Pacific margin: North-eastern Russia to the Cordillera // Earth-Science Reviews. 2020. V. 208, 103272.

18. *Tarasenko A.A.* State Geological Map of the Russian Federation at a scale of 1: 200 000. Second edition. Pykarvaaam Series. Sheet Q-1-VII, VIII (Amguema). Explanatory note. Saint Petersburg, 2023.

19. *Gulpa I.V.* State Geological Map of the Russian Federation at a scale of 1 : 200 000. Second edition. Pykarvaaam Series. Sheet Q-1-XXI, XXII (mouth of the Chevtakan River). Explanatory note. Saint Petersburg, 2020.

20. *Tikhomirov P.L., Lebedev I.E., Pasenko A.M., Lhuillier F., Alekseev D.V., Pavlov V.E.* "Upper Basalts" of the East Chukotka segment of the Okhotsk-Chukotka belt: longitudinal migration of volcanic activity or superposition of a late magmatic event? // Doklady RAN. Earth Sciences. 2021. V. 501. No. 2. P. 47–52.

*DOKLADY EARTH SCIENCES, 2025, Vol. 520, No. 1, pp. 83–90*

## PETROLOGY

# FORMATION CONDITIONS OF THE POSTCOLLISIONAL GRANITES OF THE KARA OROGEN (NORTHERN TAIMYR, CENTRAL ARCTIC): APPLICATION OF 3D NUMERIC MODELING

© 2025 Academician of RAS **V. A. Vernikovsky**[a, c], **A. N. Semenov**[b, c], **O. P. Polyansky**[b],
**A. V. Babichev**[b, c], **A. E. Vernikovskaya**[a, c], **and N. Yu. Matushkin**[a, c, *]

Received September 26, 2024
Revised September 30, 2024
Accepted September 30, 2024

**Abstract.** Using 3D numerical modeling, we analyze the formation of postcollisional granitoids of the Kara orogen in Northern Taimyr under conditions of elevated heat flow due to the orogen's breakup prior to its mantle plume episode (280–250 Ma). The initial geometry of the model area, the boundary conditions and physical properties for the crust and the mantle have been selected to reflect the structure of the crust in the junction zone of the Kara, Central Taimyr, and Siberian blocks. Comparing 2D and 3D modeling results with identical parameters and medium physical properties defined by the Rayleigh number shows that 3D modeling yields a more realistic and correct description of relevant magmatic processes. At the base of the modeled Earth crust at the depth of ~50 km an area of melting of continental crust appears, possibly with slight input of mantle component, which generates magma uplift and the formation of closely spaced granitoid intrusions. Plutons with diameters 10–20 km were emplaced at depths 14–8 km during 15 million years, which is close to the actual geological position of postcollisional stocks of the Kara orogen.

**Keywords:** *Arctic, Kara orogen, North Taimyr, Siberian craton, collision, mantle plume, granite, thermal model*

**DOI**: 10.31857/S26867397250109e2

## INTRODUCTION

The Kara orogen is one of the key structures in the Arctic, extending along the northern part of the Taimyr Peninsula for almost 1000 km. Its formation occurred as a result of oblique collision of the Kara microcontinent with Siberia during the Carboniferous-Triassic periods (literature review in [1, 2]). The orogenic belt contains a large volume of granitoids and metamorphic rocks of different facies (Fig. 1). Based on geological-structural, petro-geochemical and U-Th-Pb isotopic data for zircons from granites, stages of syn-collisional (315–282 Ma) and post-collisional (264–248 Ma) granitoid magmatism have been identified ([3, 4] and literature review therein). In the structure of the Kara orogen, granitoids are zonally distributed – in the western and central parts of the region, predominantly syn-collisional, and in the eastern part, post-collisional (Fig. 1). Syn-collisional granitoids are localized in migmatization zones among rocks of amphibolite facies metamorphism and are represented mainly by granodiorites and granites, less by diorites. They form irregularly shaped bodies of different sizes: lens-shaped from a few meters among migmatites to large (several hundred km$^2$) massifs, often elongated in shape, conforming to the strike of folded and thrust-strike-slip structures (literature review in [3]).

Post-collisional granitoids cut through rocks of both northern and central domains, including unmetamorphosed Paleozoic deposits of the Central Taimyr accretionary belt cover, forming distinct contact hornfels aureoles [1, 2]. They have oval and rounded pluton shapes, small sizes, usually up to several tens of km$^2$ (Fig. 1). Their material composition is more diverse than that of the above-described syn-collisional varieties. They are represented by porphyritic biotite

---

[a] *Trofimuk Institute of Petroleum Geology and Geophysics, Siberian Branch of the Russian Academy of Sciences, Novosibirsk, Russia*
[b] *Sobolev Institute of Geology and Mineralogy, Siberian Branch of the Russian Academy of Sciences, Novosibirsk, Russia*
[c] *Novosibirsk State University, Novosibirsk, Russia*
**e-mail: MatushkinNY@ipgg.sbras.ru*

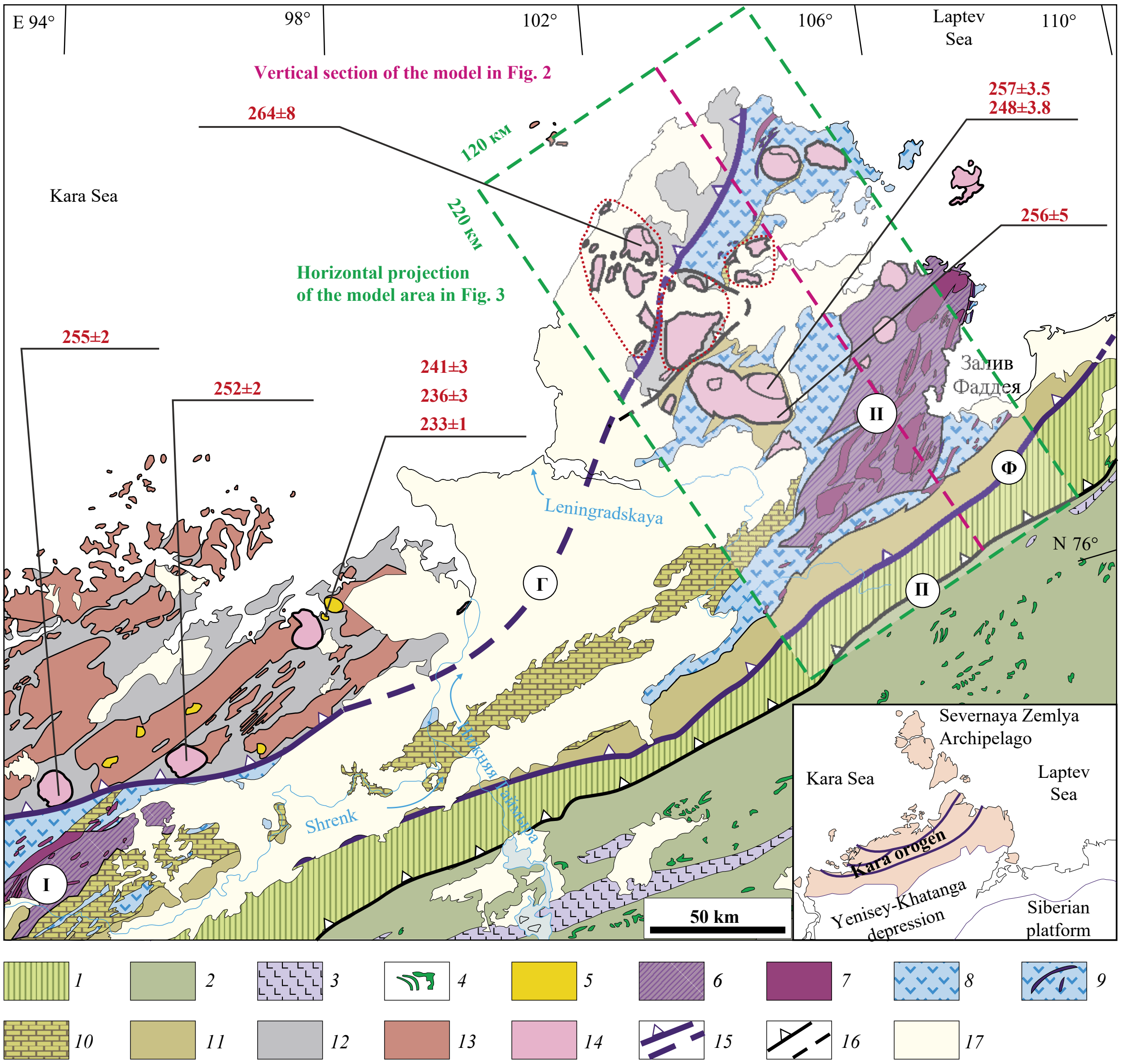

**Fig. 1.** Geological-tectonic scheme of the northeastern part of the Kara orogen according to [2] with modifications. *1–2* – Southern domain (South Taimyr fold belt) – deformed passive margin of the Siberian paleocontinent): *1* – predominantly dolomites and limestones of the North Byrranga zone ($O–C_2$); *2* – predominantly sandstones, mudstones and coal-bearing deposits of the South Byrranga zone ($C_3–P_2$); *3–5* – formations of the Siberian Traps ($P_3–T_1$): *3* – basalts and tuffs; *4* – dolerite sills; *5* – alkaline and subalkaline syenites, granites and monzonites (249–233 Ma); *6–10* – Central domain (Central Taimyr accretionary belt): *6* – Mamonto-Shrenkov (I) and Faddeev (II) granite-metamorphic terranes (PP–MP); *7* – Neoproterozoic granitoids (940–850 Ma); *8* – island-arc complexes ($NP_{1–3}$); *9* – ophiolites, including plagiogranites (750–730 Ma); *10* – carbonate terranes; *11* – deformed cover of the Siberian paleocontinent ($NP_3–C_1$); *12* – Northern domain (North Taimyr (Kara) block) – passive margin of the Kara microcontinent ($NP_3–Є$); *13* – syncollisional granites (315–305 and 287–282 Ma); *14* – postcollisional granites (264–248 Ma) (red dotted line – presumed contours of intrusions); *15* – tectonic sutures – thrusts (G – Main Taimyr, F – Pyasino-Faddeev); *16* – P – Boundary thrust; *17* – overlying deposits (J–Q). U–Pb zircon ages are taken from [1, 2, 5, 6]. [vertical model section in Fig. 3, Laptev Sea, Kara Sea, Horizontal projection of the model area in Fig. 3]

granites, subalkaline granites, biotite-amphibole granodiorites and quartz diorites, amphibole-biotite quartz syenites and monzonites ranging from weakly peraluminous to weakly metaluminous varieties predominantly of alkali-calcic magmatic series. These rocks are enriched in large-ion lithophile elements such as K, Ba, and Sr (literature review in [2]). The intrusion of allochthonous post-collisional granites occurred during the final stage of collision, after the cessation of the main movements of the Kara microcontinent in the formed fold-thrust structure. This is evidenced by the relatively isometric shape of the massifs and the absence of deformations in them.

In previous works considering the formation mechanisms of the Kara orogen at the syncollisional and post-collisional stages [3, 4]. Two-dimensional modeling (2D) was used in the formulation of plane strain problems, examining a cross-section of the orogen perpendicular to the Main Taimyr Suture. The application of a two-dimensional model of the Kara orogen was justified by the great extent of the main faults and the quasi-linear structure of the orogen in the longitudinal direction (northeast-southwest).

Based on modeling, a mechanism for the formation of syncollisional granitoids of the Kara Orogen has been proposed due to heat generation from radioactive elements in the thickened crust of the orogen without significant contribution from mantle heat sources [3]. It is shown that between the beginning of crustal stacking (thickening) and the main pulse of granitoid magmatism in collisional orogens, there is a time interval of about 25 Ma, required for heating the earth's crust to temperatures suitable for granite melt formation. A realistic scenario of uneven plate convergence along the orogen front (oblique collision) is proposed, explaining the sequence of stages of syncollisional magmatism in the Kara Orogen in the intervals of 315–304 and 287–282 Ma ago.

For the post-collisional magmatism stage, a 2D model was developed taking into account the structure of the Kara orogenic belt, which experienced tectonic stacking and crustal thickening with the formation of a thick granite layer with increased content of radioactive heat sources [4]. This model assumes that the Siberian superplume at the initial stage affected the lithosphere as a thermal one, with an excess temperature of about 250°C relative to the surrounding mantle, and its apical part was located in the junction area of the Siberian and Kara plates according to [7]. Such a temperature gradient caused an increased heat flow above the plume, heating and softening the contact zone of the plates. Under the influence of heat flow in the "pre-plume" period of the Kara Orogen development, the temperature at the base of the earth's crust increases by approximately 100°C, which is sufficient for re-melting in the deep parts of the crust. However, the two-dimensional model did not allow solving the problem of the formation of post-collisional granitoid intrusions observed in the upper, non-metamorphosed sedimentary complexes.

The problem of magma intrusion into cold, poorly consolidated sediments remains poorly studied, therefore, for this purpose, we have constructed a three-dimensional thermomechanical numerical model based on solving a closed system of Navier-Stokes equations with an experimentally established rheological law of medium behavior. The problem statement and modeling results are presented below.

## MODEL PARAMETERS

The formulation of the thermomechanical numerical modeling problem was determined by the following constraints, based on available geological data.

1. The absence of mantle basitic magmas is assumed, as the granitoids of the post-collisional stage of magmatism have an age preceding the Permian-Triassic boundary of the main phase of trap eruption (251–250 Ma ago).

2. Due to the long duration of the tectonic stage of orogen collapse (first tens of millions of years) compared to the short, pulse-like impact of a magmatic event (no more than hundreds of thousands to a million years), it was assumed that an increased mantle heat flow was acting for a long time as the cause of melting and formation of granitoids.

3. This paper examines local manifestations of post-collisional granitoid magmatism in separate areas of the orogen. Magmatic formations are represented by groups of small granitoid bodies with oval or rounded shape in plan view, not exceeding 10–30 km in diameter, and therefore an essential point for reconstructing the formation of intrusions is the choice of model dimensionality.

Two-dimensional modeling allows adequately describing the behavior of systems that change little in one of the directions in rectangular or cylindrical coordinates. Geological objects for the application of two-dimensional models are, for example, magmatic tabular bodies of dikes and sills. Post-collisional granitoid bodies of the Kara orogenic belt cannot be described within the framework of a plane- or axisymmetric structure due to the irregular shape of the bodies and random mutual arrangement of massifs (Fig. 1). Therefore, the only possible approach is the use of three-dimensional modeling.

Modeling was carried out for the post-collisional stage (Permian-Early Triassic) with a duration of ~30 Ma (280–250 Ma). It is assumed that during the preceding stage of collision, crustal thickening occurred due to folding and tectonic stacking of the sedimentary-metamorphic cover of the Kara microcontinent and the Siberian craton. In the interval of 264–248 Ma, the intrusion of allochthonous post-collisional granites occurred in the formed fold-thrust zone [2]. This magmatic episode is the subject of modeling in this work.

The initial geometry of the model area, boundary conditions, and physical properties for the crust and mantle are selected to correspond to the structure of the Earth's crust in the junction zone of the Kara, Central Taimyr, and Siberian blocks. We considered a section of the Earth's crust in the eastern part of the Central Taimyr block with dimensions of 270*120*65 km (length – width – depth) in the area of the Main Taimyr Suture (Fig. 1). According to geophysical data, the crust thickens from 40 km in the Kara block (Northern domain) to 46 km under the Central one. In the frontal zone of the Main Taimyr thrust, we assume the presence of a thickened crustal "keel" up to 50 km with a width of 100 km based on seismic data and by analogy with the structure of Alpine-type orogens [8].

The thermophysical, rheological properties, and the amount of radiogenic heat of the crustal tectonic blocks were set similar to those in works [3, 4]. The boundary temperature conditions are: mantle heat flow outside the orogenic belt 18 mW/m$^2$ , thermally insulated lateral boundaries, and constant temperature at the surface. Under the Kara orogen, in a 90 km wide strip, an increased mantle heat flow was set, which varied in the models from 36 to 72 mW/m$^2$ [9].

The increased heat flow is assumed due to two factors: (1) due to the presence of a thickened heat-generating crustal layer under the orogen and (2) the effect of thermal impact on the lithosphere from the mantle superplume that approached the base of the lithosphere thinned to 160 km [10]. The temperature distribution in the Earth's crust and mantle at the initial moment is set linearly from 0 at the surface to 850°C at the lower boundary of the model at a depth of 65 km. The initial moment (model time $t = 0$) in the calculations is taken as the age of 280 million years, i.e., the moment of completion of the collision stage, marked by the age of the emplacement of the latest syn-collisional granites (282 million years ago).

The modeling was carried out using the ANSYS Fluent software package; the system of equations and description of the numerical method are presented in [11].

## MODELING RESULTS

The modeling results are presented as evolutionary patterns showing the shape of the solidus surface and temperature distribution in the host rocks and in the partial melting region. Fig. 2 shows the isothermal surface with a solidus temperature of 730°C, which is the boundary of the melting region in the Earth's crust, as well as the temperature in the vertical cross-section and at the crust-mantle interface. In all models, melting occurs in the most submerged and heated area of the crust. Vertical magma ascent takes place in the thickened crust area under the influence of increased heat flow. Almost simultaneously with the onset of increased heat flow, melts formed in the lower crust during its thickening at the syn-collisional stage (315–282 Ma) become mobile due to re-melting (post-collisional) of the crust. The process of magmatic material ascent begins when the melt fraction reaches approximately 6–7%. These values of granite melting degree correspond to the rheological threshold at a melt volume fraction of 6–8%. Melt formation occurs at the transition from thickened crust with increased heat generation to normal crust. The maximum temperature near the base of the crust reaches 780°C. This location is the area of melt formation. The average ascent time for magma reaching depths of 8–10 km is approximately 15 million years, after which repeated ascents of magma portions occur, forming smaller bodies with a periodicity of 1–2 Ma.

Plutons (stocks) of granitoids form in practically unmetamorphosed upper crust. The process has a periodic character: the molten magma cools and partially crystallizes during ascent, while at the base of the crust, melting continues due to the continuous action of increased mantle heat flow, and new portions of melt form, which rise along the heated path of magma ascent.

The horizontal sections in Fig. 3 show the evolution of temperature at depths of 10 and 15 km at moments from 27 to 36 Ma from the beginning of the increased heat flow. It is important to note that in the model, intrusion occurs in the form of a "cluster" of several bodies about 30–35 km in diameter, which does not shift over time. The distance between the bodies can reach 10–15 km. Subsequently, the following portions of magma rise along the most heated path, and in such places, magma reaches the maximum level of uplift up to 8–10 km.

A comparison of modeling results in two- and three-dimensional settings was conducted with completely identical model parameters and physical properties of substances, characterized by the Rayleigh number $Ra = g\alpha\Delta Td^3\rho/\mu\varkappa$, where the symbols denote (sequentially): gravitational acceleration, thermal expansion, temperature difference, crust thickness, density, viscosity, and thermal diffusivity.

Currently, the development of numerical methods and computing technology allows researchers to model Rayleigh-Bénard convective flows not only in a plane (2D), where two spatial coordinates are present, but also in a three-dimensional (3D) setting. In this regard, a number of problems arise in interpreting the results obtained in 2D settings and results obtained with the introduction of the third coordinate (3D), which are discussed in [12-15].

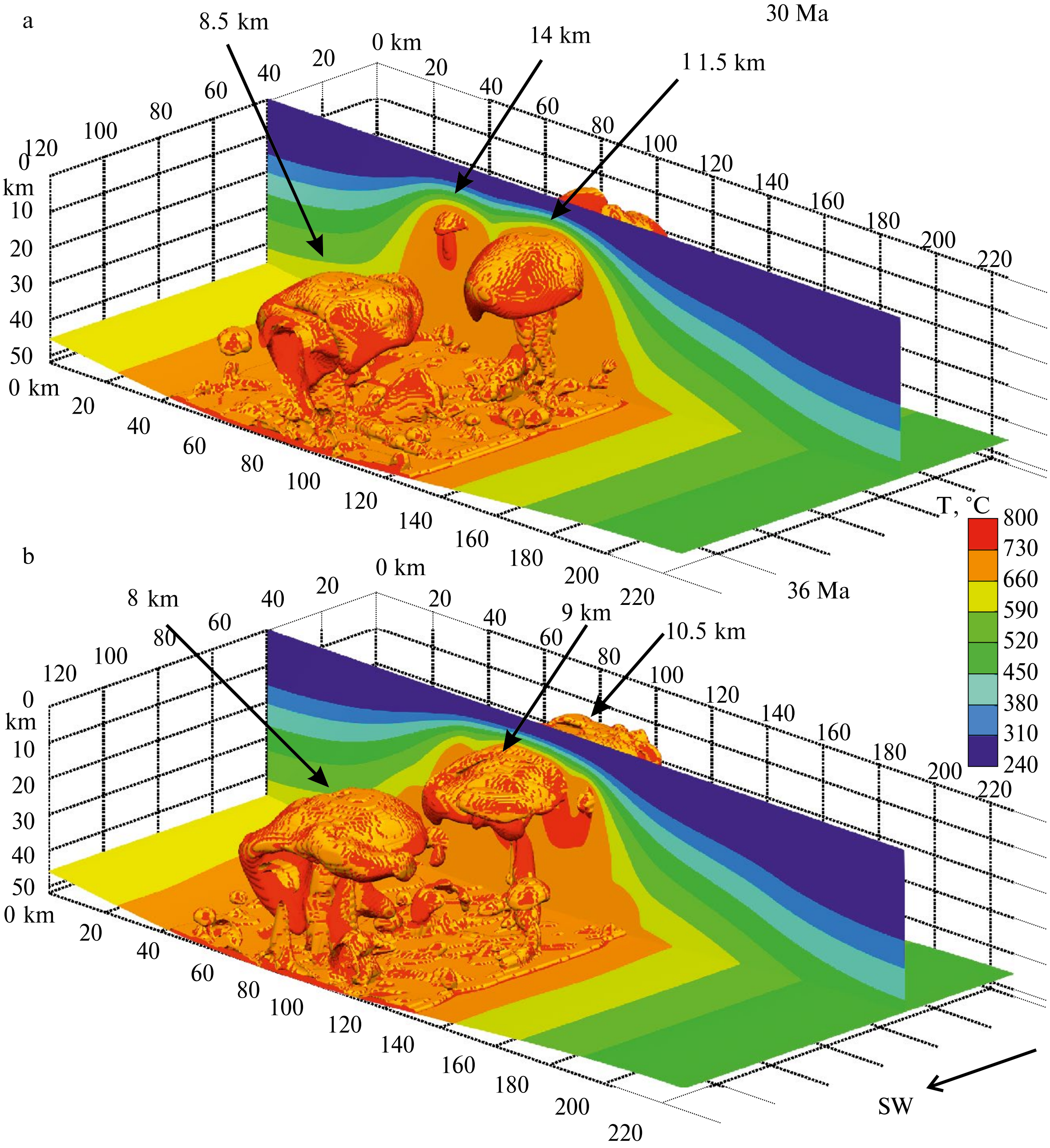

**Fig. 2.** Results of 3D modeling. The area corresponds to the rectangle in Fig. 1, where the left far edge of the model relates to the Kara block, the right near edge to the Central Taimyr, and the lower surface to the base of the Earth's crust. The isothermal solidus surface is shown at moments 30 (a) and 36 (b) Ma from the beginning of the increased heat flow, with maximum uplift marked. The color scale is given in the range of 240–730°C for detailing the structure of massifs.

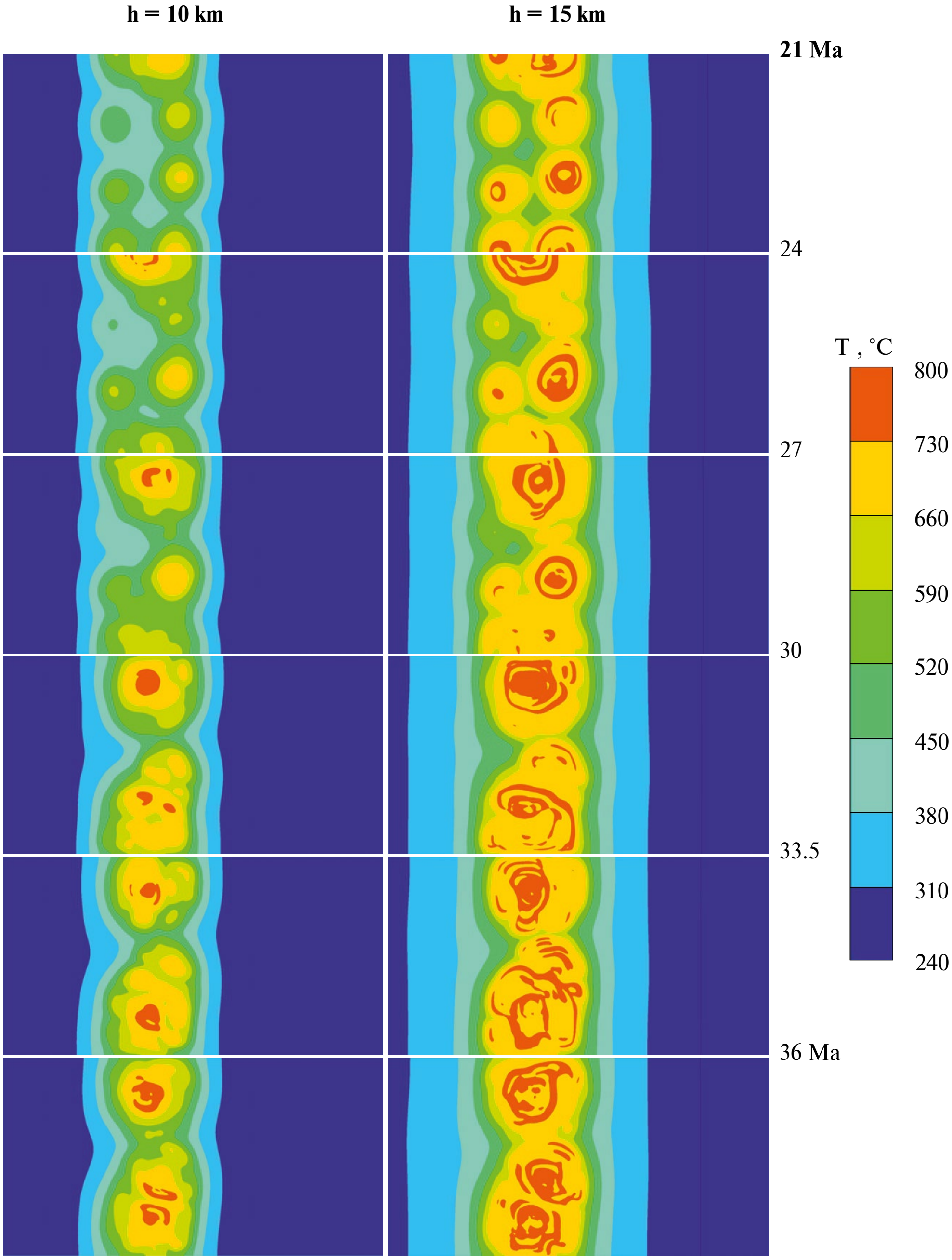

**Fig. 3.** Horizontal sections of the model (Fig. 2) at depths of 10 and 15 km for time points 21, 24, 27, 30, 33.5, and 36 million years, corresponding to geological time 260–245 Ma ago. Red areas with temperatures > 730°C show the shape and position of the massifs at the given moment in time.

When solving the convection problem in a 3D formulation at certain Rayleigh numbers, a stationary solution (established convection) is obtained in the form of a longitudinal temperature shaft, the axis of which coincides with the direction of the third coordinate. That is, the solutions of the 2D problem, where the third coordinate is fixed, and the solutions in 3D differ slightly [12]. However, the transition from the heat conduction mode to the convection mode is delayed in 3D calculations compared to 2D calculations, but the solutions still coincide. Also in [12], a significant influence of the spatial discretization method (division of the computational domain) of the Navier-Stokes equations on the solution is indicated. The further transition from the temperature shaft (shaft convection) to plumes (cellular convection) [16] loses meaning in a two-dimensional formulation, since we will always obtain a solution that will be invariant with respect to the third coordinate.

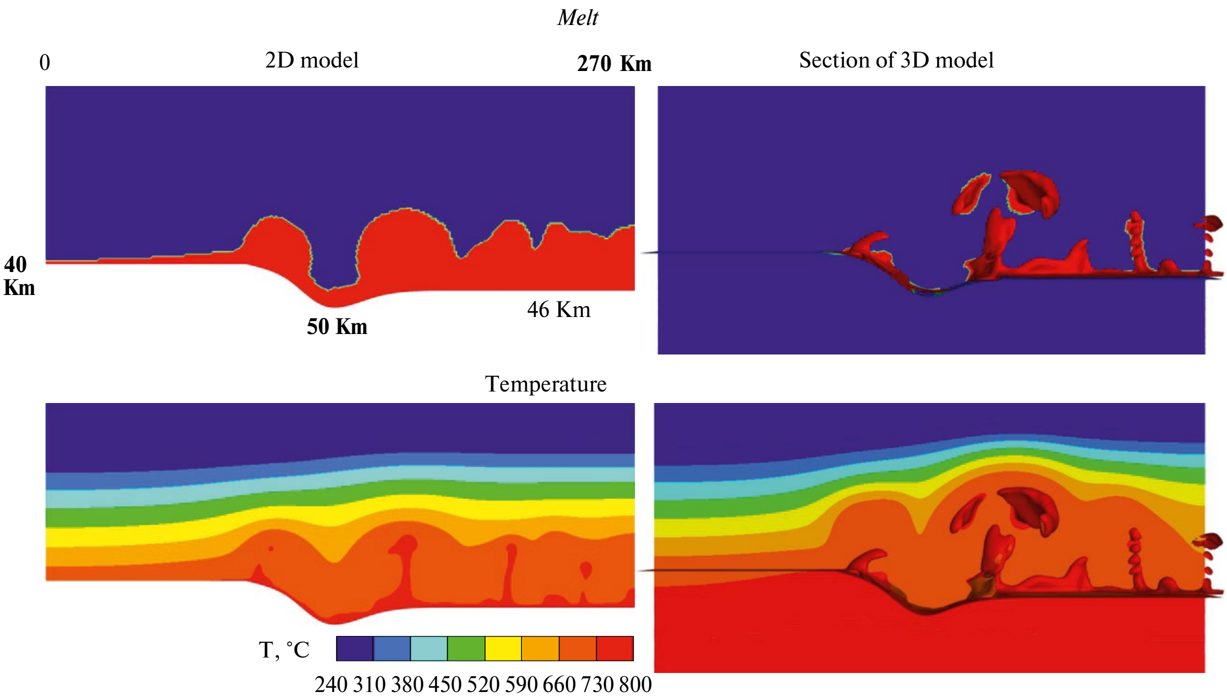

**Fig. 4.** Comparison of simulation results in two-dimensional (left) and three-dimensional (right) settings is given for a similar geometry of the model area. The vertical cross-section in the 3D model variant is shown in the middle of the model area, where portions of partial melt rise to different depth levels. The area of partial melt (top row) and temperature (bottom row) is shown. [3D model section]

Solutions in a two-dimensional formulation in [4] allow us to talk about melting and convective movement of magma in the form of shafts in the lower crust, but cannot explain the mechanism of formation of stock-like bodies. In this regard, the choice of a 3D formulation becomes relevant, taking into account that the geological objects considered in the work are not elongated structures, but irregularly located bodies in space.

The results of modeling in 2D and 3D problems differ significantly in the nature of the convective movement of the melt, the temperature field, and the shape of bodies containing partial melt (Fig. 4). In the 3D model, a rise to a greater height is observed (8–10 km compared to 20–25 km). In the 3D model, the formation of feeding channels and a head is observed, and the main body separates from the melt formation area. Melts due to convection are more intensively localized with the formation of separate massifs. The configuration of the temperature field also changes significantly, reflecting small-scale convective movements of partial melt masses. Thus, 3D models carry more information about the formation process and the volumetric structure of magmatic bodies.

## CONCLUSIONS

Interpretation of the obtained numerical modeling results allows us to draw some petrological conclusions about the formation mechanism of post-collisional granitoids of the Kara orogen.

1. The formation mechanism of post-collisional granitoids of the Kara orogen is well described within the framework of three-dimensional models of crustal heating under conditions of increased heat flow due to the orogen collapse at the pre-trap stage of the Earth's crust evolution of the northern margin of the Siberian platform. The impact of mantle heat influences the composition, conditions of melting, and intrusion of magmas into the upper crust before the main phase of trap magmatism (251–250 Ma ago).

2. It is shown that the regime of three-dimensional cellular convection is realized when using a complete three-dimensional formulation, in contrast to the regime of two-dimensional roll convection characteristic of the 2D problem of plane deformations. Thus, 3D modeling is a more realistic and correct way to describe the corresponding magmatic processes.

3. At the base of the Earth's crust, at a depth of about 50 km, a melting zone of continental

crustal material is established, possibly with a small contribution of the mantle component, generating magma ascent and the formation of a group of spatially close granitoid massifs. The formation of massifs with a diameter of 10–20 km occurred at depths from 14 to 8 km over 15 million years, which is close to the real geological position of post-collisional stocks of the Kara orogen.

## FUNDING

This work was supported by the Russian Science Foundation (project 24-17-00057).

## REFERENCES

1. *Vernikovsky V.A.* Geodynamic evolution of the Taimyr fold area // Proceedings of OIGGM; Issue 831. Novosibirsk: Publishing House of SB RAS, SRC IGM, 1996. 202 p.
2. *Vernikovsky V.A., Vernikovskaya A., Proskurnin V., Matushkin N., Proskurnina M., Kadilnikov P., Larionov A., Travin A.* Late Paleozoic – Early Mesozoic Granite Magmatism on the Arctic Margin of the Siberian Craton during the Kara-Siberia Oblique Collision and Plume Events // Minerals, 2020. V. 10(6). 571. http://dx.doi.org/10.3390/min10060571
3. *Vernikovsky V.A., Polyansky O.P., Babichev A.V., Vernikovskaya A.E., Proskurnin V.F., Matushkin N. Yu.* Tectonothermal model for the Late Paleozoic syncollisional stage of the Kara Orogen formation (Northern Taimyr, Central Arctic) // Geology and Geophysics. 2022. V. 63. No. 4. Pp. 440–457. http://dx.doi.org/10.15372/GiG2021178
4. *Vernikovsky V.A., Semenov A.N., Polyansky O.P., Babichev A.V., Vernikovskaya A.E., Matushkin N.Yu.* Tectonothermal model and magmatism evolution at the postcollisional (pre-plume) stage of the Kara Orogen development (Northern Taimyr, Central Arctic) // RAS Reports. Earth Sciences. 2024. V. 514. No. 1. Pp. 56–64. https://doi.org/10.31857/S2686739724010077
5. *Proskurnina M.A., Proskurnin V.F., Remizov D.N., Larionov A.N.* Ring intrusions of the Bespamyatninsky areal: manifestations of shoshonite-latite magmatism in Northern Taimyr // Regional Geology and Metallogeny. 2019. No. 79. Pp. 5–22.
6. *Khudoley A.K., Verzhbitsky V.E., Zastrozhnov D.A., O'Sullivan P., Ershova V.B., Proskurnin V.F., Tuchkova M.I., Rogov M.A., Kyser T.K., Malyshev S.V., Schneider G.V.* Late Paleozoic—Mesozoic tectonic evolution of the Eastern Taimyr-Severnaya Zemlya Fold and Thrust Belt and adjoining Yenisey-Khatanga Depression // J. Geodyn. 2018. V. 119. Pp. 221–241. https://doi.org/10.1016/j.jog.2018.02.002
7. *Sobolev S.V., Sobolev A.V., Kuzmin D.V., Krivolutskaya N.A., Petrunin A.G., Arndt N.T., Radko V.A., Vasiliev Y.R.* Linking mantle plumes, large igneous provinces and environmental catastrophes // Nature. 2011. V. 477. Pp. 312–316. https://doi.org/10.1038/nature10385
8. *Jamieson R.A., Beaumont C.* On the origin of orogens. GSA Bull. 2013. V. 125(11–12). Pp. 1671–1702. https://doi.org/10.1130/B30855.1
9. *Polyansky O.P., Filippov Yu.F., Fomin A.N., Fedorovich M.O., Reverdatto V.V.* Reconstruction of subsidence dynamics and paleotemperature regime of the northern margin of the Siberian platform // Geology and Geophysics. 2024. in press. https://doi.org/10.15372/GiG2024145
10. *Priestley K., McKenzie D* . The relationship between shear wave velocity, temperature, attenuation and viscosity in the shallow part of the mantle // Earth Planet. Sci. Lett. 2013. V. 381. Pp. 78–91. https://doi.org/10.1016/j.epsl.2013.08.022
11. *Semenov A.N., Polyansky O.P.* Numerical modeling of magma mingling and mixing mechanisms on the example of complex intrusive formation // Geology and Geophysics. 2017. V. 58. No. 11. Pp. 1665–1683. https://doi.org/10.15372/GiG20171104
12. *Lee J.R.* On the three-dimensional effect for natural convection in horizontal enclosure with an adiabatic body: Review from the 2D results and visualization of 3D flow structure // Int. Comm. Heat and Mass Transfer. 2018. V. 92. Pp. 31-38. https://doi.org/10.1016/j.icheatmasstransfer.2018.02.010
13. *Janssen R.J.A., Henkes R.A.W.M.* Instabilities in three – dimensional differentially heated cavities with adiabatic horizontal walls // Physics of Fluids. 1996. V. 8(1). Pp. 62–74. https://doi.org/10.1063/1.868814
14. *Astanina M.S., Buonomo B., Manca O., Sheremet M.A.* Three-dimensional natural convection of fluid with temperature-dependent viscosity within a porous cube having local heater // Int. Comm. Heat and Mass Transfer. 2022. V. 139. 106510. https://doi.org/10.1016/j.icheatmasstransfer.2022.106510
15. *Zhu W., Wang M., Chen H.* 2D and 3D lattice Boltzmann simulation for natural convection melting // Int. J. Thermal Sci. 2017. V. 117. Pp. 239–250. https://doi.org/10.1016/j.ijthermalsci.2017.03.025
16. *Dobretsov N.L., Kirdyashkin A.G., Kirdyashkin A.A.* Deep Geodynamics. Novosibirsk: Geo Publishing, 2001. 409 p.

*DOKLADY EARTH SCIENCES, 2025, Vol. 520, No. 1, pp. 91–96*

# SYMMETRY AND STRUCTURAL COMPLEXITY OF MINERALS OF THE EARTH DEEP GEOSPHERES (PYROLITE MODEL)

**© 2025 Academician of RAS S. V. Krivovichev**[a, b, *]

Received August 12, 2024
Revised August 29, 2024
Accepted September 02, 2024

**Abstract.** Using the Dolivo-Dobrovol'sky index and information-based parameters on the basis of new experimental data, the problem of symmetry and structural complexity of the mineral matter of the deep geospheres is considered in the framework of the pyrolite model of the Earth's mantle. It is shown that, in contrast to the previously made conclusions about the increase of the symmetry of minerals with depth, the behavior of the quantitative parameters of symmetry and structural complexity is nonlinear. The symmetry increases (and the structural complexity decreases) to the boundary of the decomposition of ringwoodite into bridgmanite and "magnesiowustite" (660 km), after which there is a decrease of the Dolivo-Dobrovol'sky index to 18.40 and an increase of the atomic parameter of structural complexity to 2.786 bit/atom. This behavior is due to the uneven and opposite effect of temperature and pressure on the symmetry and complexity of the crystalline substance, which is caused by the nonlinear nature of the averaged geotherm of the Earth's crust and mantle. Information parameters of structural complexity are a more sensitive indicator of symmetry than the Dolivo-Dobrovol'sky index, which is due to the former taking into account the features of the crystal structure of specific minerals.

**Keywords:** *symmetry, structural complexity, information, mineralogy, deep Earth geospheres, mantle geotherm, temperature, pressure*

**DOI**: 10.31857/S26867397250110e7

## INTRODUCTION

Symmetry is one of the most fundamental properties of mineral matter [1]. The large amount of accumulated data on the symmetry of crystal structures of minerals allows analyzing the frequency of occurrence of various types of symmetry and space groups [2] and drawing conclusions about the evolution of symmetry and complexity of crystalline matter in the geological history of Earth [3-5]. More than forty years ago, V.V. Dolivo-Dobrovol'sky studied – based on the data available at that time – the evolution of the symmetry of Earth's shells and concluded that there is a "regular increase in the symmetry of Earth's matter with depth" [6]. As a measure of symmetry, V.V. Dolivo-Dobrovol'sky used an averaged symmetry value $\sigma$ , later called the Dolivo-Dobrovolsky index (see below) [4, 5]. Relatively recently, the conclusion about the increase in the average symmetry of minerals with depth was repeated by S.K. Filatov [7] based on calculations made in a 1984 paper [6]. However, a large number of experimental studies conducted over the past 20 years using modern methods for studying matter at high temperatures and pressures (see reviews [8, 9]) have significantly expanded and deepened our understanding of the mineral composition and structure of Earth's geospheres. The purpose of this work is to analyze the depth evolution of symmetry and structural complexity of Earth's crystalline matter using the latest experimental data and theoretical methods. As will be shown below, V.V. Dolivo-Dobrovol'sky conclusion about the increase in mineral symmetry with depth needs significant clarification.

## METHODOLOGY

To study the structure of the Earth's mantle, T. Ringwood [10] proposed the so-called pyrolite (pyroxene + olivine) model, according to which the average composition of the mantle is expressed in molar percentages as follows: 44.71 $SiO_2$, 38.73

---

[a] *Federal Research Center "Kola Science Center of the Russian Academy of Sciences", Apatity, Russian Federation*
[b] *St. Petersburg State University, St. Petersburg, Russian Federation*
**e-mail: s.krivovichev@ksc.ru*

MgO, 8.18 FeO, 3.98 $Al_2O_3$, 3.17 CaO, 0.13 $Na_2O$. Despite the fact that the pyrolite model is not the only one, in this work it is used as one of the generally accepted models of the composition and structure of the Earth's mantle. A generalized diagram of the mineral structure of the Earth's shells, compiled on the basis of geophysical data and experimental studies, is presented in Fig. 1 (works [11] and [12] were used). Based on this diagram, percentage ratios (in atomic quantities) of mineral species comprising the Earth's shell were calculated for different depths with a step of 50 km. Despite all the conventionality and approximation of such estimates, they fully meet the task of studying the evolution of symmetry of mineral matter with depth.

To assess the average symmetry of the mineral aggregate, the Dolivo-Dobrovol'sky index σ (characterizing the average order of the holohedry group of the corresponding mineral system) and the mean atomic complexity parameter introduced for the first time in this work $\overline{I_G}$ (reflecting the average amount of structural information per atom in bits) were used.

Dolivo-Dobrovolsky Index σ was calculated using the formula:

$$\sigma = \sum_{i=1}^{n} x_i s_i \qquad (1)$$

where $x_i$is the normalized atomic amount of phase $i$ in the aggregate; $s_i$ numerical characteristic of the mineral phase crystal system, equal to the order of the holohedry group in the given crystal system (= maximum order of the point group in the crystal system); $n$ is the number of phases in the aggregate. Note that

$$\sum_{i=1}^{n} x_i = 1 \qquad (2)$$

and the parameter $s_i$ equals 2, 4, 8, 12, 16, 24, and 48 for triclinic, monoclinic, orthorhombic, trigonal, tetragonal, hexagonal, and cubic crystal systems, respectively. V.V. Dolivo-Dobrovol'sky [6] used the fraction of the total mass of the aggregate attributed to phase i as the $x_i$ parameter, which does not seem entirely correct due to differences in molecular masses of various mineral components of the Earth shells.

To calculate the informational parameters of symmetry and complexity of crystalline matter, the methodology previously developed in [13, 14] was used. According to this approach, the complexity of a crystal structure is evaluated as the amount of information per atom in the reduced unit cell, using the following formula:

$$I_G = -\sum_{i=1}^{k} p_i \log_2 p_i \quad \text{(bit/atom)} \qquad (3)$$

where $k$ is the number of crystallographic orbits (Wyckoff positions or number of sites) and $p_i$ is the

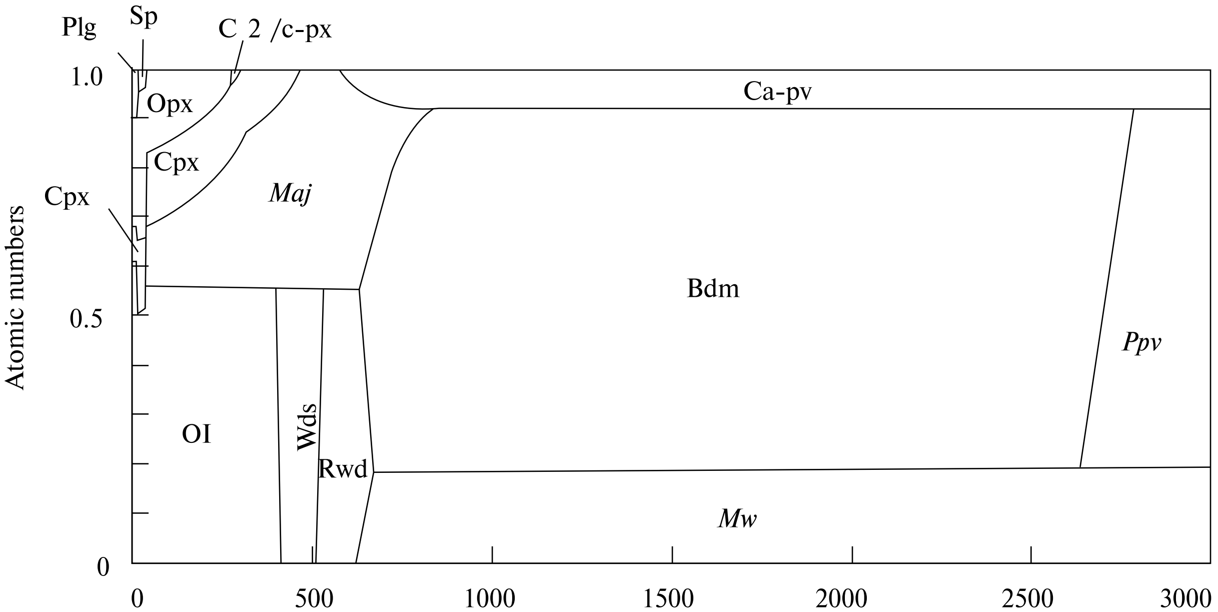

**Fig. 1.** Diagram of the structure of the Earth's deep geospheres to the "mantle-core" boundary (according to [11, 12]). The interpretation of mineral phase symbols is given in Table 1.

probability of randomly selecting an atom from the $i$-th Wyckoff position, i.e.:

$$p_i = m_i / v \,, \tag{4}$$

where $m_i$ is the multiplicity of the orbit in the reduced cell, and $v$ the number of atoms in the reduced unit cell.

Knowing the values of parameters $I_G^i$ for each mineral phase in the aggregate, the average atomic complexity parameter $\overline{I_G}$ can be calculated as

$$\overline{I_G} = \sum_{i=1}^{n} x_i I_G^i \,. \tag{5}$$

Table 1 shows the values of parameters $s_i$ and $I_G^i$ for all mineral phases appearing in the diagram in Fig. 1. As already mentioned, the values of parameter were estimated directly from the diagram with a depth increment of 50 km.

## RESULTS

Fig. 2a shows a graph of the change in the Dolivo-Dobrovol'sky index σ with depth. It is clearly visible that, contrary to the conclusions of work [6], repeated in work [7], the average symmetry of mineral matter does not increase with depth, but behaves nonlinearly. Up to a depth of approximately 600 km, the index σ increases sharply (the substance on average becomes more symmetrical, with the maximum index value of 48 being reached, at which all matter has cubic symmetry), whereas after 600 km there is a sharp decline, and from ~880 km to the "mantle-core" boundary, the index σ has a constant value of 18.40.

The behavior of parameter $\overline{I_G}$ (Fig. 2b) with depth turned out to be even more uneven. Up to a depth of 600 km, its value generally decreases (which corresponds to an increase in symmetry and a decrease in structural complexity), after which there is an increase, a plateau (2.786 bits/atom; from approximately 850 to 2650 km), and a decrease to a value of 1.712, which is maintained to the "mantle-core" boundary are observed. Thus, the behavior of parameter $\overline{I_G}$, which describes structural complexity (or the symmetry of the crystal structure taking into account the space group and the size of the unit cell), is more

**Table 1.** Symmetry characteristics of the main minerals of the Earth's crust and mantle within the pyrolite model

| Mineral | Symbol* | Crystal system | Space gr.** | $s_i$ | $I_G^i$ [bit/atom] |
|---|---|---|---|---|---|
| "Plagioclase"*** | Plg | triclinic | $P\bar{1}$ | 2 | 4.700**** |
| "Spinel" | Sp | cubic | $Fd\bar{3}m$ | 48 | 1.379 |
| "Orthopyroxene" | Opx | orthorhombic | *Pbca* | 8 | 3.322 |
| "Clinopyroxene" | Cpx | monoclinic | $P\,2_1/c$ | 4 | 3.322 |
| "High-temperature clinopyroxene"***** | $C\,2/c$-px | monoclinic | $C\,2/c$ | 4 | 2.522 |
| "Olivine" | Ol | orthorhombic | *Pnma* | 8 | 2.522 |
| Majorite | Maj | cubic | $Ia\bar{3}d$ | 48 | 1.595 |
| Wadsleyite | Wds | orthorhombic | *Imma* | 8 | 2.807 |
| Ringwoodite | Rwd | cubic | $Fd\bar{3}m$ | 48 | 1.379 |
| Bridgmanite | Bdm | orthorhombic | *Pnma* | 8 | 3.374 |
| "Magnesiowüstite" | Mw | cubic | $Fm\bar{3}m$ | 48 | 1.000 |
| "Calcium perovskite" | Ca-pv | cubic | $Pm\bar{3}m$ | 48 | 1.371 |
| "Post-perovskite" | Ppv | orthorhombic | *Cmcm* | 8 | 1.922 |

Note. * Mineral symbols in Table 1 correspond to those in Fig. 1.
** Sp. gr. = space group
*** Terms in quotes correspond to mineral names not approved by the International Mineralogical Association but widely used in geological literature
**** The parameter value $I_G^i$ for "plagioclase" is chosen as the average of the values for albite (3.700 bits/atom) and anorthite (5.700 bits/atom)
***** High-temperature modification of pyroxene with space group $C2/c$

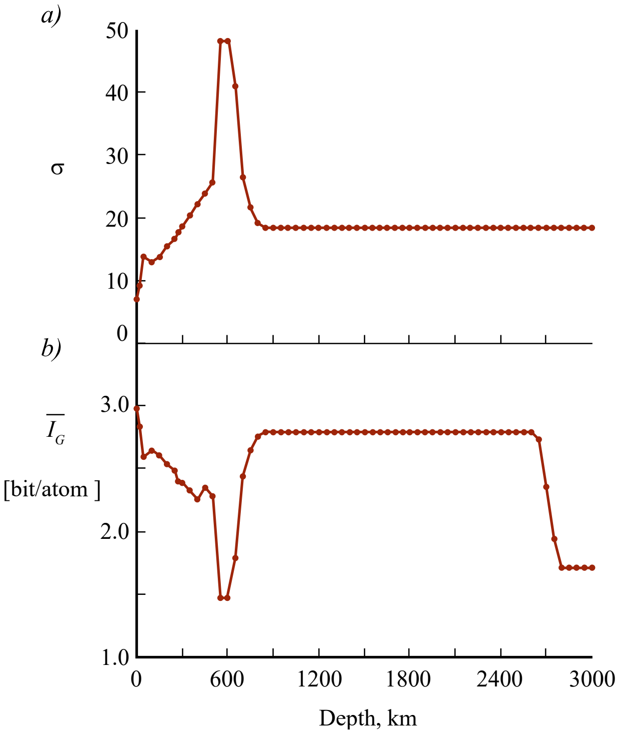

**Fig. 2.** Dependence of the Dolivo-Dobrovolsky index σ (a) and information parameter $I_G^i$ (b) on depth.

nuanced, i.e., this parameter appears to be more sensitive to changes in symmetry than the Dolivo-Dobrovol'sky index.

There is no doubt that the discrepancy between our results and the conclusion made in works [6, 7] is associated with the emergence of new data on the structure of the Earth's mantle and the symmetry of its constituent minerals. Thus, the symmetry of bridgmanite – perovskite-like $MgSiO_3$ – presumably the main mineral by mass of the Earth as a planet [15, 16] is not cubic, as V.V. Dolivo-Dobrovol'sky assumed, but orthorhombic (space group *Pnma*), and the orthorhombic symmetry is preserved throughout the entire range of temperatures and pressures of the lower mantle [17]. It should be noted that in his work, V.V. Dolivo-Dobrovol'sky noted that "for pure $MgSiO_3$, the perovskite-type phase has a distorted structure with orthorhombic symmetry" [6], however, he did not use this information in his further conclusions.

## DISCUSSION

The nonlinear change in parameters σ and $\overline{I_G}$ requires an explanation, which, in our opinion, should be sought in the relationship between the influence of temperature and pressure on the symmetry and structural complexity of matter. It is known that there is a statistically significant tendency for increasing symmetry [18] and decreasing structural complexity [14] of crystalline matter with increasing temperature. Despite the fact that increased pressure ambiguously affects structural complexity, the influence of pressure and temperature on matter has the opposite direction. There are known cases when, with increasing pressure, crystalline matter undergoes phase transitions in the same order that is observed when the temperature decreases. While increasing temperature leads to disordering of the crystal structure, increasing pressure is usually accompanied by processes of atomic ordering.

It is well known that the deep temperature and pressure gradients in the Earth's geospheres have different characteristics [19]. While pressure increases almost linearly with depth (up to the boundary of the mantle and core) with an intensity of about 30–35 MPa/km [20], deep geotherms have a more complex nature. Fig. 3 shows averaged geotherms for whole mantle convection (a) and layered mantle convection (b) models (for hybrid convection models, geotherms are between these extreme variants) [19]. The diagram shows that the dependence of temperature on depth has two (a) or three (b) inflection points (or rather, intervals) where the intensity of temperature increase changes. The temperature rises quite sharply to a depth of about 200 km (for both oceanic and continental geotherms), after which the temperature increase slows down. At the same time, the symmetry of matter increases, and structural complexity decreases (Fig. 2). According to generally accepted concepts [8], at a depth of about 410 km, olivine $Mg_2SiO_4$ transitions to wadsleyite (orthorhombic spinel-like structure), and this reaction is exothermic and accompanied by heat release in the amount of 90 kJ/kg [19]. This leads to additional heating of the substance and a sharp increase in the index σ and a decrease in the value of $\overline{I_G}$ to a depth of approximately 600–650 km. At a depth of 660 km, ringwoodite ($Mg_2SiO_4$ with cubic spinel structure) decomposes into cubic "magnesiowüstite" (isomorphic mixture of periclase MgO and wüstite FeO) and orthorhombic bridgmanite $MgSiO_3$. This reaction is endothermic with heat absorption in the amount of 70 kJ/kg, which causes a temperature decrease of 70 K [19]. This cooling of the substance against the background of constant pressure increase leads to a decrease in average symmetry and an increase in structural complexity. Further to a depth of approximately 2650 km (to the so-called *D*''-layer) the temperature increases monotonically

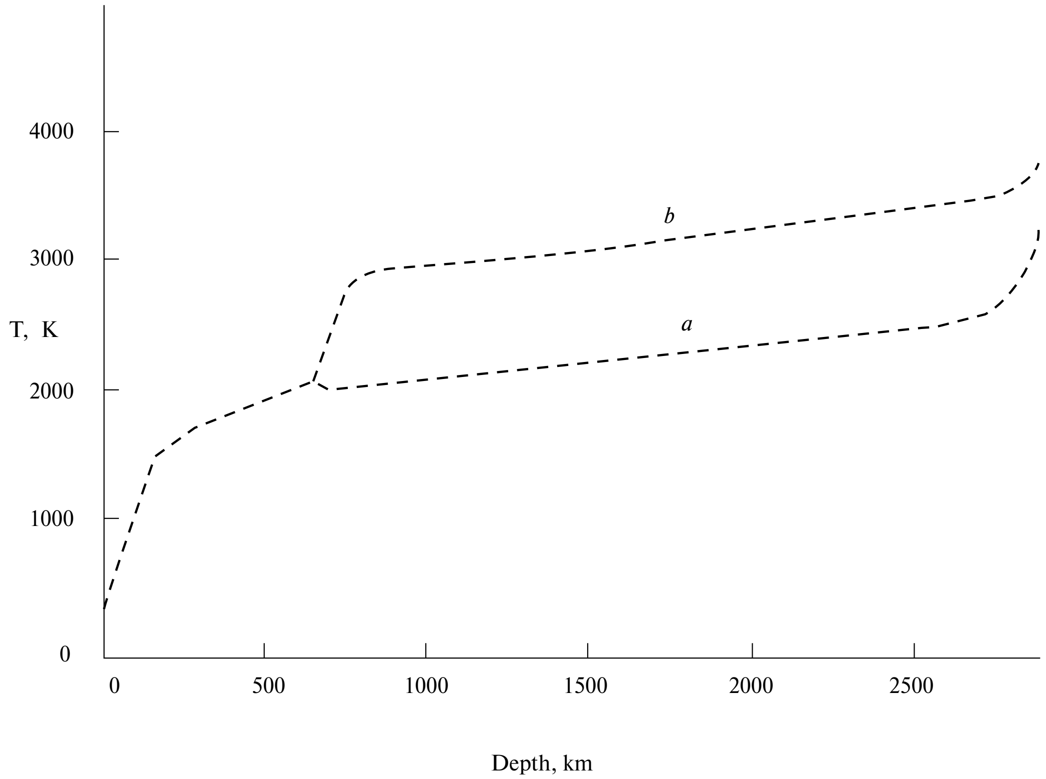

**Fig. 3.** Averaged geotherms of the Earth for models of whole-mantle (a) and layered (b) mantle convection (based on data from [19] with modifications).

and (according to currently accepted models) the phase composition of the mantle does not change. As it approaches the Earth's core, the temperature increases and bridgmanite transitions to "post-perovskite" with a $CaIrO_3$ structure, which also has orthorhombic symmetry [9]. This does not affect the value of the Dolivo-Dobrovol'sky index, but directly influences the information parameter of structural complexity $I_G$, which in "post-perovskite" is lower (1.922 bits/atom) than in bridgmanite (3.374 bits/atom), which corresponds to the general principle of decreasing structural complexity with increasing temperature [14].

Thus, the nonlinear behavior of the index σ and parameter $\overline{I_G}$ with increasing depth can be explained by the uneven influence of temperature and pressure on the crystalline matter of the Earth's mantle. While pressure monotonically increases with depth, the intensity of temperature change varies, which leads to a change in the predominant role of one or another thermodynamic parameter in determining the symmetry and structural complexity of matter.

## CONCLUSIONS

Based on the pyrolite model of the Earth's mantle, using quantitative parameters (the Dolivo-Dobrovol'sky index and information parameters of complexity), it is shown that the symmetry and structural complexity of mineral matter behave nonlinearly with increasing depth, which contradicts the previously made conclusions about the monotonic increase in the symmetry of minerals in the deep geospheres of the Earth [6, 7]. Such behavior may be associated with the uneven and opposite effects of temperature and pressure on the symmetry and complexity of crystalline matter, which is caused by the nonlinear nature of the averaged geotherm of the Earth's crust and mantle. It is also important that the information parameters of structural complexity are a more sensitive indicator of symmetry than the Dolivo-Dobrovol'sky index, which is due to the former's consideration of fine details of the structural organization of specific minerals. While the Dolivo-Dobrovol'sky index only takes into account the crystal system of a mineral, the information parameters characterize its space group and the distribution of atoms among crystallographic orbits.

When evaluating the conclusions of this work, one should take into account the conditionality of the pyrolite model of the Earth's mantle and the existence of other models, which will be considered in subsequent works.

The author dedicates this article to the memory of Professor V.V. Dolivo-Dobrovol'sky from St. Petersburg Mining University, an outstanding scientist and remarkable person.

## FUNDING

The research was carried out with support from the Russian Science Foundation grant No. 24-17-00083, https://rscf.ru/project/24-17-00083/.

## REFERENCES

1. *Urusov V.S.* Symmetry statistics of mineral species and evolutionary dissymmetrization of mineral matter // Zap. RMO. 2006. Vol. 135. No. 6. Pp. 1–12.
2. *Krivovichev S.V., Krivovichev V.G., Hazen R.M., Aksenov S.M., Avdontceva M.S., Banaru A.M., Gorelova L.A., Ismagilova R.M., Kornyakov I.V., Kuporev I.V., Morrison S.M., Panikorovskii T.L., Starova G.L.* Structural and chemical complexity of minerals: an update // Mineral. Mag. 2022. V. 86. Pp. 183–204.
3. *Krivovichev S.V. , Krivovichev V.G. , Hazen R.M .* Structural and chemical complexity of minerals: correlations and time evolution // Eur. J. Mineral. 2018. V. 30. Pp. 231–236.
4. *Bermanec M., Vidović N., Ma X., Hazen R.M.* The average symmetry index of minerals co-varies with their hydrogen content, rarity, and paragenetic mode // Minerals. 2024 . V. 14 . P. 387.
5. *Bermanec M., Vidović N., Gavryliv L., Morrison S.M., Hazen R.M.* Evolution of symmetry index in minerals // Geosci. Data J. 2024. V. 11 . Pp. 69–85.
6. *Dolivo-Dobrovolsky V.V.* On the crystallography of Earth's shells // Zap. VMO. 1984. Vol. 113. No. 5. Pp. 586–590.
7. *Filatov S.K* . Symmetry statistics of mineral species in various thermodynamic environments // Zap. RMO. 2019 . Vol. 148. No. 3. Pp. 1–13.
8. *Pushcharovsky D.Yu., Pushcharovsky Yu.M.* The mineralogy and the origin of deep geospheres: A review // Earth-Sci. Rev. 2012. V. 113. Pp. 94–109.
9. *Krivovichev S.V.* High-pressure silicates: crystal chemistry and systematics // Zap. RMO. 2021. Vol. 150. No. 5. Pp. 1–78.
10. *Ringwood A.E* . Composition and Petrology of the Earth's Mantle. New York: McGraw Hill, 1975.
11. *Stixrude L., Lithgow-Bertelloni C.* Mineralogy and elasticity of the oceanic upper mantle: Origin of the low-velocity zone // J. Geophys. Res . 2005. V. 110. P. B03204.
12. *Irifune T., Tsuchiya T.* Mineralogy of the Earth – phase transitions and mineralogy of the lower mantle // Treatise on Geophysics. V. 2. Mineral Physics. Ed. by D. Price. Amsterdam: Elsevier, 2007. Pp. 33–62.
13. *Krivovichev S.V.* Topological complexity of crystal structures: quantitative approach // Acta Crystallogr. 2012. V. A68. Pp. 393–398.
14. *Krivovichev S.V.* Structural complexity of minerals: information storage and processing in the mineral world // Miner. Mag . 2013. V. 77. No. 3. Pp. 275–326.
15. *Tschauner O., Ma C., Beckett J.R., Prescher C., Prakapenka V.B., Rossman G.R* . Discovery of bridgmanite, the most abundant mineral in Earth, in a shocked meteorite // Science. 2014. V. 346. Pp. 1100–1102.
16. *Liu L.G.* Silicate perovskite from phase transformations of pyrope-garnet at high pressure and temperature // Geophys. Res. Lett. 1974. V. 1. No. 6. Pp. 277–280
17. *Ismailova L., Bykova E., Bykov M., Cerantola V., McCammon C., Boffa Ballaran T., Bobrov A., Sinmyo R., Dubrovinskaia N., Glazyrin K., Liermann H.-P., Kupenko I., Hanfland M., Prescher C., Prakapenka V., Svitlyk V., Dubrovinsky L.* Stability of Fe,Al-bearing bridgmanite in the lower mantle and synthesis of pure Fe-bridgmanite // Science Advances. 2016. V. 2. P. e1600427.
18. *Filatov S.K* . Generalized concept of increasing crystal symmetry with temperature rise // Crystallography. 2011 . V. 56. Pp. 1019–1028.
19. *Turcotte D. L., Schubert G.* Geodynamics. Cambridge University Press, 2014.
20. *Winter J.D* . Principles of Igneous and Metamorphic Petrology. Essex: Pearson Eduction Limited, 2014.

*DOKLADY EARTH SCIENCES, 2025, Vol. 520, No. 1, pp. 97–105*

**PALEOGEOGRAPHY**

# THE ENVIRONMENT OF THE UPPER KAMA REGION DURING THE LATE GLACIAL AND EARLY HOLOCENE AS REVEALED BY THE STUDY OF BOTTOM SEDIMENTS FROM LAKE NOVOZHILOVO

**© 2025 S. V. Kopytov[a, e, *], N. E. Zaretskaya[b, c], E. A. Konstantinov[b], E. G. Lapteva[d, e], P. Yu. Sannikov[a], N. V. Sychev[b], and E. A. Mekhonoshina[a]**

Presented by Academician of the Russian Academy of Sciences S. A. Dobrolyubov on July 02, 2024

Received July 02, 2024
Revised August 28, 2024
Accepted September 02, 2024

**Abstract.** For the first time, a high-resolution record of natural events covering the Late Glacial and Early Holocene (14,150–9,730 cal BP) was obtained for the southern part of the Kama-Vychegda watershed based on drilling sediments in lake Novozhilovo (Kama-Keltma lowland, Upper Kama basin). The article presents the results of the study on the reconstruction of sedimentation conditions, based on paleobotanical, sedimentological and radiocarbon dating analyses. The beginning of the lake's formation was apparently preceded by a period of predominantly alluvial morpholithogenesis, which is thought to correspond to the LGM. There were four stages in the evolution of the lake basin, with the first three characterized by lacustrine-alluvial sedimentation that was predominantly mineralogenic in nature, and the fourth stage marked by typical lacustrine organic-rich sedimentation. The first stage covered the Bølling-Allerød interstadial period from 14,150 to 13,500 cal BP, and it was characterized by the accumulation of sand under conditions of high water flow. At the boundary between the Allerød and Younger Dryas periods, bioproductivity increased significantly. During the second stage, which lasted from 13,500 to 12,420 cal BP, water exchange slowed down and organic-mineral lake sediment formed. The third stage, known as the transitional sedimentation period, refers to the Younger Dryas and Early Holocene periods (12,420–10,700 cal BP). During this time, alluvial inputs predominated, with a decrease in organic matter content. Finally, the fourth stage, the eutrophic lake stage (10,700–9,730 cal BP), was characterized by a high organic matter content in sediment, and an increase in the size of silty particles.

**Keywords:** *Late Neopleistocene, Holocene, Late Glacial, alluvial morpholithogenesis, bottom sediments, geochronology, lithostratigraphy, palynological analysis, diatom analysis*

**DOI**: 10.31857/S26867397250111e1

## INTRODUCTION

The relief of the northeastern Russian Plain (the southern part of the Komi Republic and the north of the Perm Territory) (Fig. 1a) is characterized by the presence of a large number of swampy depressions, which in the Neo Pleistocene and Holocene became the arenas of river basin rearrangements [1-4]. One of these depressions is the Kama–Keltma lowland (Fig. 1b), which cuts through the Northern Hills and the Nemskaya Upland. The rivers Kama, Yuzhnaya Keltma, Timsher, Bortom, and Chepets flow within the lowlands. The depression is 60 km long and 25 km wide.

The Kama here is pressed against the high right bank and forms a relatively straight channel with a narrow left-side floodplain and fragments of floodplain terraces. The surface of the lowland in its southern extension is occupied by lakes (Bolshoy and Maly Kumikush, Novozhilovo, Chelvinskoye, etc.) and oligotrophic ridge-hollow raised bogs.

Similar in shape lakes Kadam and Sher-Kadam are located in the valley of the upper Vychegda, in the so-called Kadam expansion (Fig. 1b). The expansion is limited by the Vychegda River itself and its abandoned paleochannel, which now contains

---

[a] *Perm State University, Perm, Russia*
[b] *Institute of Geography, Russian Academy of Sciences, Moscow, Russia*
*c Geological Institute, Russian Academy of Sciences, Moscow, Russia*
[d] *Institute of Plant and Animal Ecology, Ural Branch, Russian Academy of Sciences, Yekaterinburg, Russia*
[e] *Perm State Humanitarian Pedagogical University, Perm, Russia*
**e-mail: sergkopytov@gmail.com*

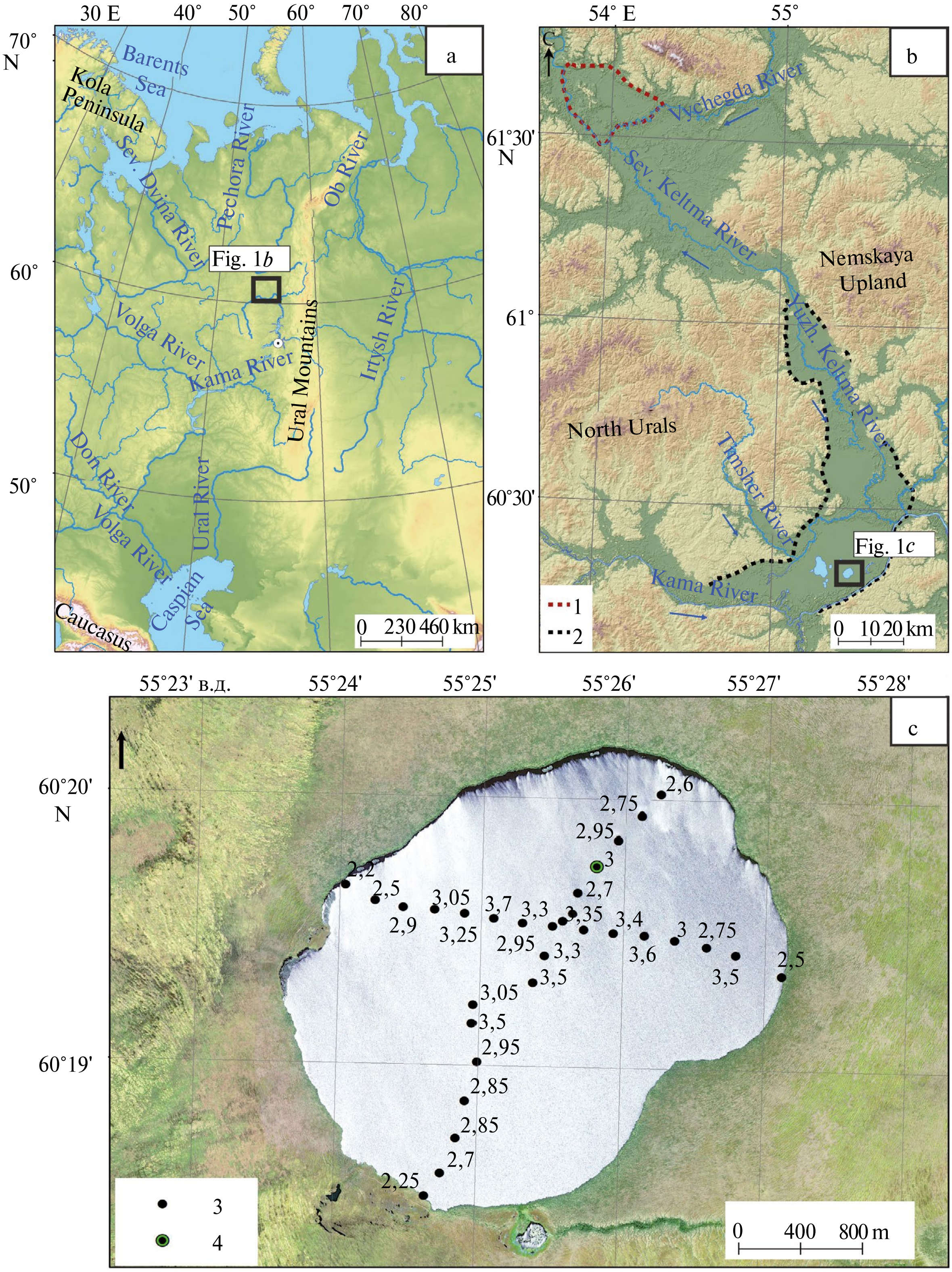

**Fig. 1.** Work area and location of drilled wells
a – location of the study area on the map of the East European Plain; b – Kama-Vychegodsk watershed; c – location of drilled wells on Lake Novozhilovo.
Legend:
1 – boundaries of the Kadam expansion in the Vychegda valley; 2 – contour of the Kama-Keltma lowland; 3 – measured depths of the lake, m; 4 – location of the NZH-1 well.

Lake Don-ty. It has been established that the age of the paleochannel and terrace in the Kadam expansion is Late Glacial, and the terrace itself was formed as a result of the Vychegda River activity in extraglacial environments [5]. Within the adjacent basins of Vychegda and Kama at this time, alluvial and aeolian morpholithogenesis prevailed [6] – a sublatitudinal macrodune with drainage channels cutting through it was formed [2].

All results of paleogeographic studies of previous years in this region, starting from the time of designing the Upper Kama Reservoir, were predominantly based on the study of paleoarchives of river valleys draining the Kama-Keltma lowland (floodplains and terraces of Kama, Timsher, Southern Keltma) [2, 7, 8]. Lakes have not received due attention in the studies. To date, there is no information about the structure, composition, sedimentological characteristics, and age of their bottom sediments. In addition, the landscape and climatic conditions of the Late Glacial in the region are almost unexplored, although there are many potential paleoarchives for this.

The absence of geochronometric and micropaleontological data on bottom sediments of water bodies within the southern part of the Kama-Keltma lowland motivated our research aimed at studying the sediments of Lake Novozhilovo (Fig. 1c).

## MATERIALS AND METHODS

*Field research.* Depth measurements in Lake Novozhilovo were conducted in February 2023 using a lead weight from the ice (Fig. 1c). The recorded maximum depth was 3.7 m. The absolute water level mark in the lake was 131 m, in the Kama River – 117.6 m. Using a hand auger with an Eijkelkamp semi-cylindrical sampler, 18 exploratory wells were drilled along two transverse profiles with lengths of 2940 m and 3435 m, respectively. A core from the reference well NZH-1 was obtained using a Livingstone piston corer (Fig. 1c).

*Determination of sediment age.* Radiocarbon age of six samples of organomineral and mineral sapropel from the lower part of the NZH-1 core (depths 6.5–8.2 m) was determined by liquid scintillation counting (LSC) and accelerator mass spectrometry (AMS) methods on bulk organic carbon, as well as on wood (Table 1). The LSC dating and sample preparation for AMS analysis were performed at the Center for Collective Use “Laboratory of Radiocarbon Dating and Electron Microscopy” of the Institute of Geography RAS, while measurements were conducted at the Center for Applied Isotope Studies, University of Georgia (USA). Calibration of radiocarbon dates was performed using the Calib 8.10 program with the IntCal20 calibration curve [9].

Age models were constructed based on radiocarbon dates using the Bayesian method in the Bacon package of R 4.3.2 environment. In addition to the “depth-age” model, sedimentation rate graphs (cm/thousand years) were plotted as a function of depth and calendar age (Fig. 2).

*Studies of the lithological composition of sediments.* Sample analysis was performed with a step of 5–10 cm in the laboratory of facies-genetic research of geosystems at Perm University (loss on ignition) and in the laboratory of natural environment paleoarchives at the Institute of Geography RAS (granulometric analysis, magnetic susceptibility).

Grain size analysis of deposits was conducted for 18 samples using a Malvern Mastersizer 3000 laser particle analyzer. Sample preparation included dissolution of carbonates with 10% HCl solution and oxidation of organic matter with 30% $H_2O_2$. After washing off the reagents, the samples were mixed with 4% sodium pyrophosphate $Na_4P_2O_7$ solution for additional dispersion and suspension

**Table 1.** Results of radiocarbon dating of samples from core NZH-1

| Lab. number IGAN | Depth, m | Material | Method | $^{14}$C date, yr BP | Calibrated age, yr BP | | |
|---|---|---|---|---|---|---|---|
| | | | | | 1σ | 2σ | Median |
| 10417 | 6.6–6.7 | Sapropel | LSC | 8950±190 | 9730–10250 | 9545–10440 | 10110 |
| 10418 | 6.7–6.8 | | | 9220±130 | 10240–10510 | 10150–10770 | 10320 |
| 10419 | 7.15–7.25 | | | 9580±120 | 11180–11410 | 10640–11210 | 11130 |
| 10420 | 7.25–7.35 | | | 9870±110 | 10750–11110 | 11080–11750 | 11390 |
| 10421 | 7.6–7.7 | | | 10440±130 | 12100–12410 | 11930–12710 | 12420 |
| 10517 | 8.17 | Wood | AMS | 12240±40 | 14080–14190 | 14050–14320 | 14150 |

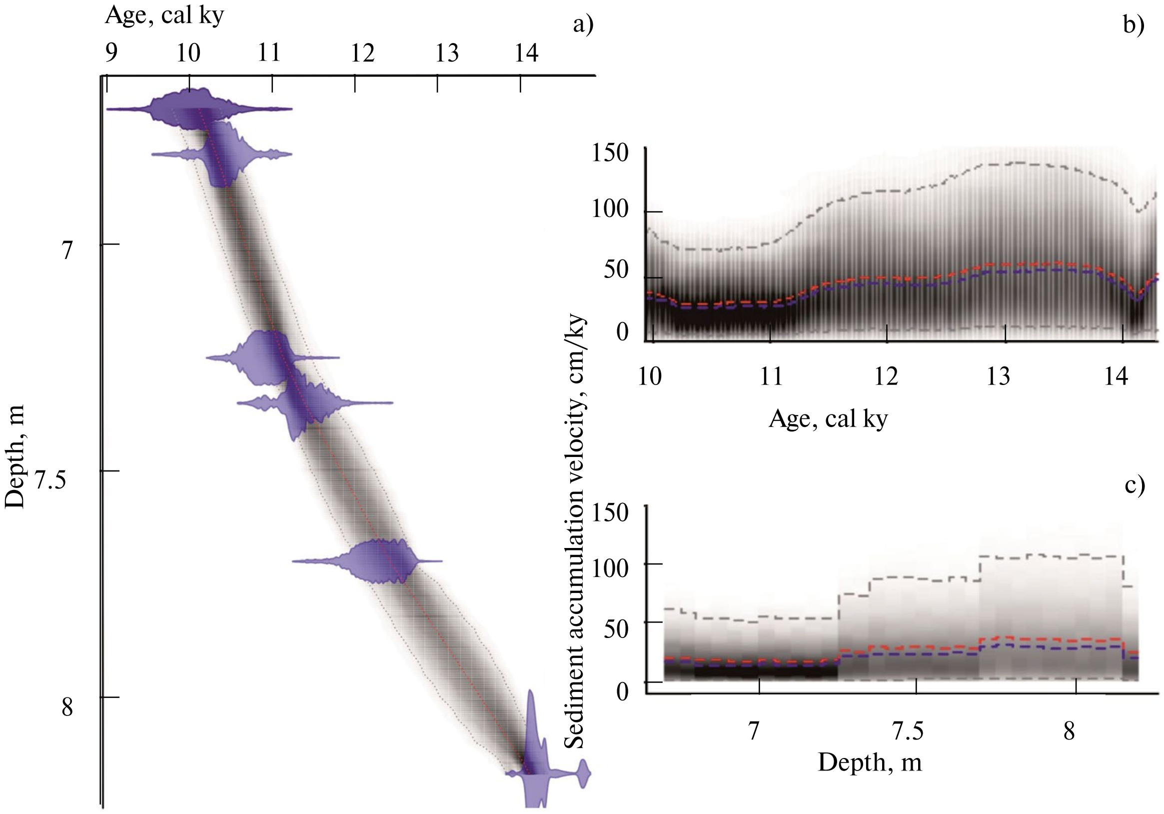

**Fig. 2.** Age-depth model and sediment accumulation rate of core NZH-1. a – age-depth model plot; sedimentation rate dependencies: b – on calendar age; c – on depth

stabilization. Before measurement, the material was dispersed in an ultrasonic bath for 30 minutes. The analyzer performed 7 repeated measurements, which were averaged in the Mastersizer v.3.62 application. Particle size distribution was calculated based on Mie optical theory, with dispersion medium refractive index $n_w = 1.33$, particle refractive index $n_p = 1.55$, and absorption coefficient $k_p = 0.1$.

Loss on ignition (LOI) was determined according to the methodology [10]. Samples of 5 ml volume, placed in porcelain crucibles, were dried at 105°C for 4 hours. Then, sequential ignition at 550°C was performed for 2 hours. After each stage, weighing was performed on electronic scales with 0.01 g precision. The resulting values were calculated using the formula LOI 550 = ((DW105-DW550)/DW105) · 100, where DW is dry weight. According to [10], LOI at 550°C allows estimation of organic matter (OM) content in the sediment.

Specific (mass) magnetic susceptibility (MS) measurement was performed using a ZH Instruments 150L kappameter following the methodology [11]. Samples of 8–12 ml volume were preliminarily dried to air-dry condition in a drying oven for 24 hours at 40°C. Then the mass of samples was determined with 0.01 g precision. MS measurement was performed at field strength 320 A/m and frequency 500 Hz.

*Diatom analysis*. Laboratory preparation of 20 samples was carried out according to the methodology [12] in several stages: removal of carbonates and organic matter, elutriation (removal of clay fraction), centrifugation with the addition of lycopodium. Identification of diatom taxa was performed under an optical microscope at 1000x magnification using the identification guide [13].

*Palynological analysis***.** Sample preparation was carried out according to the standard methodology [14]. Within the depth interval of 6.5–8.2 m, 35 samples were studied. For each sample, at least 300 pollen grains were counted with parallel registration of spores of higher cryptogamous plants and non-pollen palynomorphs (conifer stomata, algae, fungal spores, etc.). The percentage calculation of palynomorph taxa was conducted based on the sum of arboreal and herbaceous pollen. Vegetation types were determined both by the ratio of dominant taxa and groups pollen [14] and using the biomization method [15].

## RESULTS

*Lithological structure of deposits.* In the lower part of the column, the following layers were successively exposed (from top to bottom) (Fig. 3b): 6.5–7 m – brown sapropel, weakly consolidated (layer 1); 7–7.65 m – dense sapropel, greenish-yellowish, mineralized (layer 2); 7.65–8.1 m – gray (brownish-gray) sapropel, mineralized, with isolated plant remains, mineralization and density increase towards the bottom; at a depth of 7.85 m – strongly peaty interlayer (3 cm thick) (layer 3); 8.1–8.2 m – fine-grained sand with peat and sapropel interlayers (up to 2–3 cm), with wood fragments in peat (layer 4).

In the sediment texture of the lower core part at the level of 7.8–8.2 m, rhythmic stratification is observed, manifested in the alternation of dense mineral brownish-gray and dark peaty sapropel, peat, and light sandy layers. Above (6.5–7.8 m), the material gradually becomes enriched with organic matter, becoming increasingly peaty, viscous, and uniform.

*Age of deposits.* The accumulation of deposits exposed in the lower part of core NZH-1 occurred during the Late Glacial and Early Holocene (Fig. 3a). Based on the age model, it can be stated that the highest rates of deposit accumulation are characteristic for depths of 7.7–8.2 m, corresponding to 14150–12420 cal. BP: 120–130 cm/thousand years (Fig. 2).

According to *grain size composition,* three intervals can be distinguished (6.5–7 m, 7.1–7.9 m, 8–8.2 m), characterized by different sedimentation regimes (Fig. 3c). In the interval of 6.5–7 m, fine and medium silt fractions predominate, accounting for 42–45%. Fine sand fraction accounts for about 1% on average, while very fine sand accounts for about 2–3%. In the interval of 7.1–7.9 m, the proportion of clay and very fine silt fractions slightly decreases. The content of very fine (up to 17%) and fine sand (up to 16%) fractions significantly increases. At a depth of 8–8.2 m, the proportion of clay and silt fractions decreases to almost zero. The fine sand fraction at a depth of 8.2 m is 57%, very fine – 15.4%, medium – 26%.

The range of median particle diameter (MD) changes from 5–10 μm at a depth of 6.5–7.9 m to 200 μm at a depth of 8–8.2 m (Fig. 3d). A small jump is noted at a depth of 7.6 m, where MD is 18.2 μm.

*Loss on ignition.* The LOI curve (Fig. 3e) revealed maximum organic matter content at depths of 6.7–6.95 and 7.7–7.85 m. The first interval of LOI increase (6.7–6.95 m) corresponds to the transition from layer 1 to layer 2. The maximum organic matter content was recorded at a depth of 6.7 m – 94.4%. At a depth of 7–7.65 m, a sharp decrease in LOI was noted – the average value is 30%, with a maximum of 42.5% (at a depth of 7.1 m). In the underlying layer (7.7–7.85 m), LOI increases 2.5 times to an average value of 74.8%, with the maximum value characteristic for a depth of 7.7 m – 87.4%.

*Magnetic susceptibility.* Characteristic sections of MS curve variations provide additional grounds for stratigraphic division. Based on the indicator values, two intervals with relatively uniform values are distinguished (Fig. 3f): 6.5–6.85 m; 6.9–8.2 m. In the first interval (6.5–6.85 m), the MS indicator varies from –0.100 to –0.011 with an average of 0.063 $*10^{-6}$ m$^3$ /kg. The first interval practically completely corresponds to organic sediment, as MS indicators have stable negative values. At a depth of 6.9–8.2 m, MS varies from 0.012 to 0.0762 with an average of 0.053 $*10^{-6}$ m$^3$ /kg. The interval corresponds to mixed sediment with high mineral matter content.

In bottom sediments, 71 taxa of *diatom algae* belonging to 35 genera were identified. The highest number of diatom algae is present in samples from depths of 7–8 m. Overall, representatives of genera *Staurosira, Staurosirella and Pseudostaurosira dominate.* Algae are pioneers colonizing forming water bodies and can be resistant to unstable and changing environmental conditions [13]. At a depth of 6.5–6.6 m, there are isolated findings of diatom algae. Dominant species (>10%) at depths of 6.7–6.8 m are *Pinnularia spp.*, 6.9–7 m – *Crenotia thermalis, Tabellaria flocculosa,* 7.1 m – *Pseudostaurosira brevistriata, Punctastriata lancettula, Staurosira cf. tabellaria,* 7.2–7.6 m, – *Ps. brevistriata, Pseudostaurosira polonica, St. cf. tabellaria, Staurosirella cf. ovata,* 7.7 m – *Achnanthidium anastasia, C. thermalis, Ps. brevistriata* , *St. cf. tabellaria,* 7.8 m – *Nitzschia fonticola* , *Staurosirella cf. pinnata, St. cf. tabellaria,* 7.9 m – *St. cf. pinnata,* 8–8.2 m – *P. lancettula* , *St. cf. pinnata, St. cf. tabellaria*, *Staurosira cf. venter, Ps. brevistriata.*

The results of *palynological analysis* are presented in the spore-pollen diagram (Fig. 4), where three groups of palynospectra can be distinguished based on changes in the content of dominant pollen.

The first group in the interval of 7.7–8.2 m is characterized by high content of green algae colonies with maximum species concentration of *Pediastrum* (119–465 thousand specimens/g) and *Botryococcus* (up to 20 thousand specimens/g) in the depth interval of 7.8–8 m. This indicates favorable conditions for phytoplankton development in the formed freshwater reservoir with high organic matter content. At a depth of 7.7 m, pondweed

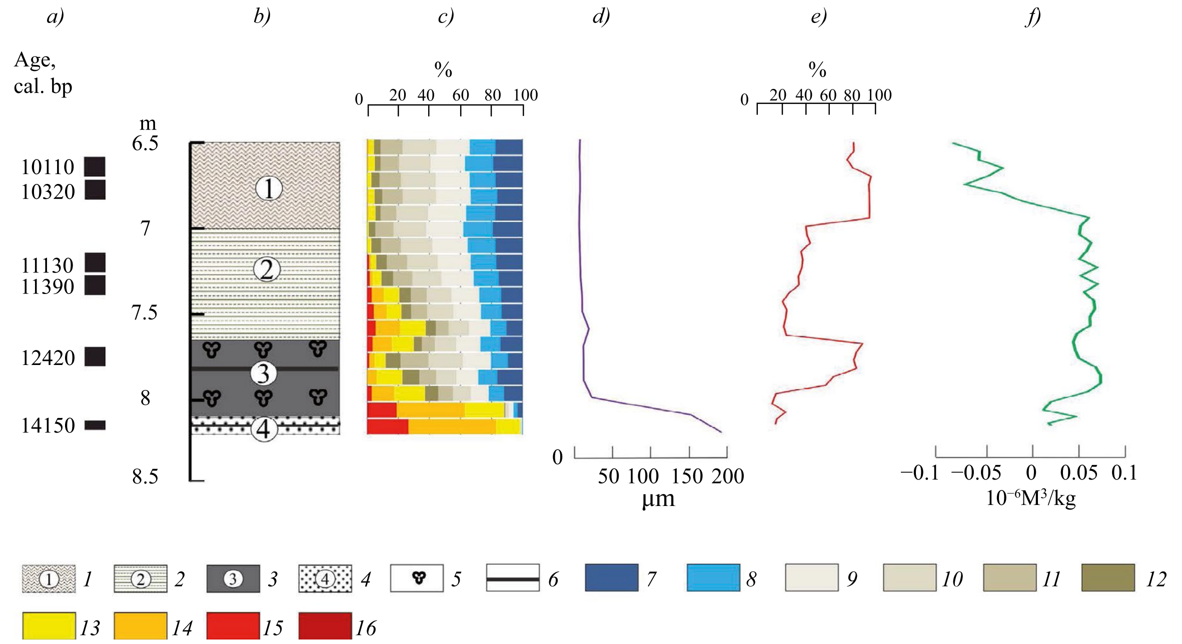

**Fig. 3.** Structure, composition, and age of bottom sediments in Lake Novozhilovo: a – calibrated radiocarbon dates; b – lithological column of NZH-1; c – granulometric composition; d – median particle diameter; e – losses on ignition at 550°C; f – specific magnetic susceptibility measured at low frequency (500 Hz).
Legend: 1 – brown, slightly consolidated sapropel (layer 1); 2 – sapropel dense, greenish-yellowish (layer 2); 3 – gray sapropel (brownish-gray), mineralized (layer 3); 4 – sand (layer 4); 5 – plant remains; 6 – layers of peat. Granulometric fractions (µm): 7 – <2 (clay); 8 – 2–4 (very fine silt); 9 – 4–8 (fine silt); 10 – 8–16 (medium silt); 11 – 16–31 (coarse silt); 12 – 31–63 (very coarse silt); 13 – 63–125 (very fine sand); 14 – 125–250 (fine sand); 15 – 250–500 (medium sand); 16 – 500–1000 (coarse sand).

seeds (*Potamogeton natans* and *P. filiformis*) were found – perennial aquatic plants that grow in shallow waters, characteristic of slow-flowing or standing waters and mark the initial stage of lake development. The overall high pollen concentration (100–500 thousand pollen grains/g) indicates good biological productivity of existing landscapes in the relatively warm climate of the Bölling-Alleröd interstadial. The combination of tundra (*Betula* sect. *Apterocaryon=B. sect. Nanae, Salix*), steppe (*Ephedra*, *Artemisia*, Chenopodiaceae, Poaceae) and forest ( *Betula* sect. *Betula=B.* sect . *Albae*, *Larix*) components in palynological spectra indicates the spread of periglacial landscapes around the water body with shrub thickets of dwarf birch and willow, as well as open woodlands of tree birch and larch.

In the second group of palynological spectra at depths of 7.35–7.7 m, the concentration of pollen and algae sharply decreases, reflecting deteriorating conditions and, consequently, reduced bioproductivity of landscapes and the water body itself. The predominance of wormwood pollen (30–45%), presence of pollen grains of *Ephedra*, Plumbaginaceae, Caryophyllaceae, *Polygonum, Valeriana* and reduction of tree birch proportion to minimum (less than 10%) indicates climate aridization.

The third group of palynospectra in the depth interval of 6.5–7.35 m is characterized by the predominance of tree pollen (70–82%), with the taiga biome (forest vegetation type) becoming most prevalent. The maximum of spruce (*Picea* – up to 55%) and larch, with a slight increase in the abundance of other conifers against the background of decreasing pollen content of shrub birches (less than 15%) and wormwood (5–10%), is recorded in the interval from 7 to 6.7 m, the upper boundary of which dates to 10513–10244 cal. BP. The increase in spruce and larch abundance is accompanied by findings of conifer stomata. In palynospectra from a depth of 6.7 m (10246–9730 cal. BP), against the background of spruce reduction, the abundance of tree birch (*Betula* sect. *Betula* = *B* .sect. *Albae*) increases to 40% and pine (*Pinus*) increases.

## DISCUSSION

Based on the obtained data, the history of Lake Novozhilovo was reconstructed in the context of the Upper Kama valley development during the Late Glacial – Early Holocene.

The lake formation was apparently preceded by *a stage of predominantly alluvial morpholithogenesis*, presumably during the Late Pleniglacial. This is indicated not only by the significant content of sand fraction but also by the median particle diameter of up to 200 μm at a depth of 8.2 m. We assume that the formation of Lake Novozhilovo is the result of erosion-accumulative processes that prevailed within the ancient alluvial plain of the Kama River during the Late Glacial period. The lake morphology and geomorphological position in relation to the modern channel indicate similarity with West Siberian sors – large shallow water bodies that form on the Ob River floodplain during long and high floods [16]. It should be noted that during the drilling of the raised bog by the Kama expedition of the VSEGEI (1938-1939), fine-grained gray sands, exposed by a borehole on the southwestern shore of Lake Novozhilovo at a depth of 8 m, were interpreted by geologists as "ancient alluvial" [7].

*The first stage of lacustrine-alluvial (transitional) sedimentation* occurred in 14150–13500 cal. BP (depths 8–8.2 m) and covered the Bølling-Allerød interstadial. This period was characterized by rhythmic environments: alternation of sapropel, peat, and sand layers in the basal part of the core. The rate of sediment accumulation was most intensive during this time.

The average LOI values were 14%, which corresponds to organomineral sediment and lacustrine-alluvial conditions. The boundary between the first and second stages is erosional, with a sharp increase in OM content values, which corresponds to the end of the period of active sediment erosion.

The alternation in depth of diatom findings *Staurosirella cf. pinnata* and *Pseudostaurosira brevistriata* indirectly confirms the rapid change of conditions from flowing water body to a lake with calm hydrodynamic regime and vice versa. Sedges and grasses with the participation of forbs formed coastal-aquatic and meadow communities. Ephedra and Chenopodiaceae-Artemisia groups occupied unvegetated areas and dry habitats with poor sandy soils. Tree birches grew in small numbers in the vicinity of the water body. Conifers (probably larch) were also present, as indicated by the presence of single pollen grains of *Larix* and the finding of Pinaceae stomata. Although the Bølling-Allerød stage is characterized by the northward advancement of forest ecosystems up to 60°N and the spread of sparse coniferous and small-leaved forests combined with tundra and steppe communities [17], our data do not indicate the predominance of forest vegetation type.

*The second stage of lacustrine-alluvial sedimentation.* The increase in OM content at a depth of 7.7–8 m (13,500–12,420 cal. BP) indicated increased bioproductivity of the formed water body. The content of sand fraction decreased compared to the underlying layers, while the silt fraction, conversely, increased. The conditions of a non-flowing water body with slightly alkaline environment and high productivity are identified by diatom findings of *Staurosirella cf. pinnata* at a depth of 7.8–7.9 m.

MS indicators show the predominance of alluvial (mineragenic) sedimentation conditions. A possible explanation for this could be the increase in high floods on the Kama River [8], during which mineral particles could enter the lake. When compared

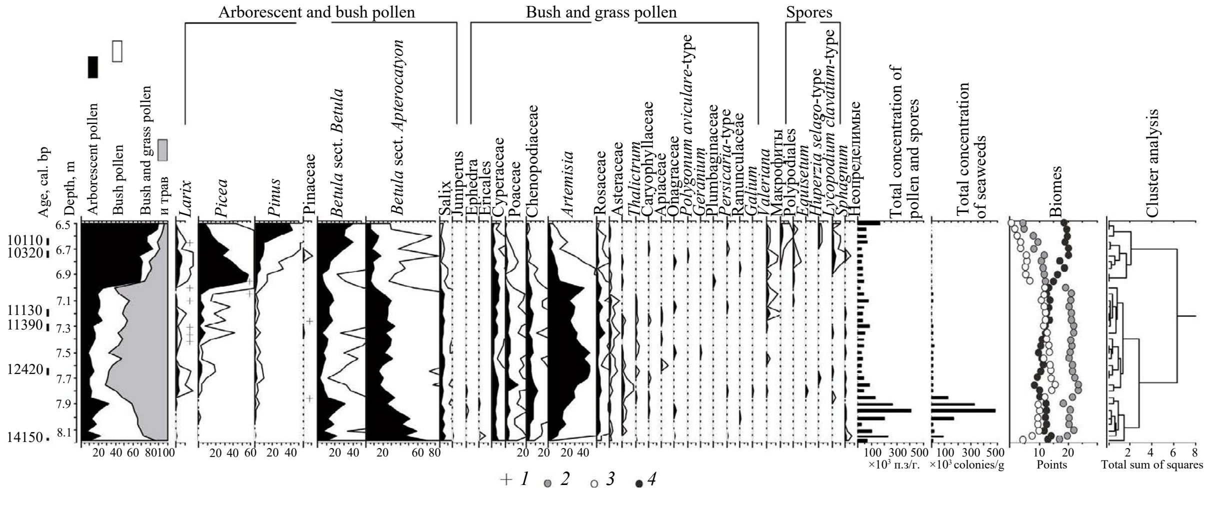

**Fig. 4.** Spore-pollen diagram of sediments from core NZH-1.
Legend: 1 – finds of stomata from coniferous plants; Biomes: 2 – taiga; 3 – steppe; 4 – tundra.

with the curve of fluvial epoch activity [18], this time corresponds to the intensification of erosion-accumulation processes on the East European Plain during 13,700–11,800 cal. BP.

*The third stage of lacustrine-alluvial (transitional) sedimentation* refers to the Late Dryas – Early Holocene (12,420–10,700 cal. BP, depths 7–7.7 m). This period was characterized by a decrease in organic matter content. The granulometric composition shows an increase in clay fraction content, while at depths of 7.3–7.7 m, the proportion of sand increases. MS values, a short-term increase in sand fraction, and a small jump in GS at a depth of 7.6 m generally indicate the predominance of alluvial material input. This is indirectly confirmed by findings of diatom algae *Staurosirella cf. ovata* at depths of 7.5–7.6 m. They typically identify flowing conditions with possible lowering of water level and activation of erosion processes in the catchment [13].

The combination of tundra, steppe, and forest components in the Late Dryas palynological spectra indicates the dominance of open periglacial landscapes with prevailing Chenopodiaceae-Artemisia groups, sedge and grass-forb communities, shrub thickets of willow and dwarf birch, and isolated larches. Colder conditions during the transition from Late Dryas to Holocene are also identified by findings of Arctic-Alpine type diatoms *Tabellaria flocculosa* at a depth of 6.9 m .

*The fourth stage of predominantly lacustrine sedimentation* (10,700–9,730 cal. BP, depths 6.5–7 m) was characterized by the predominance of organic sediment according to MS measurements. Sedimentation rates stabilized at 50 cm/thousand years – the lowest accumulation rate of lake bottom sediments. According to LOI analysis results, organic matter content increased almost 3 times compared to the previous stage (averaging 87%). The granulometric composition of sediments was dominated by silt fraction with minor presence of very fine sand, which may indicate aeolian input or high water levels in the Kama River during floods. For comparison, in the Mologa-Sheksna lowland during this time, there was a sharp and stable transition to organogenic sedimentation regime, with almost complete cessation of minerogenic accumulation [19].

The transition to active waterlogging in the lake catchment area is identified by findings of diatoms of the genus *Pinnularia* at a depth of 6.7–6.8 m. The increase in the proportion of tree pollen in the early Holocene palynological spectra is characteristic of forest vegetation type and reflects the spread of larch-spruce open woodlands with shrub birches during the Preboreal period (10,510–10,240 cal. BP) and birch forests with spruce and pine during the Boreal period (10,250–9,730 cal. BP). From a depth of 6.65 m, the total pollen concentration began to increase in the palynological spectra corresponding to the Boreal period. Such replacement of periglacial plant communities with forest vegetation was characteristic of the East European Plain during the transition from the Late Neopleistocene to the Early Holocene [20].

## CONCLUSION

Based on chrono-, bio- and lithostratigraphic data, it was possible to obtain a high-resolution record of the transition from the Late Glacial to Early Holocene within the southern part of the Kama-Keltma lowland. It can be stated that Lake Novozhilovo sediments are represented by a two-member sequence of lacustrine-alluvial and lacustrine deposits. The age of sediments in the basal core sequence is 14,150–13,500 cal. BP, which chronologically correlates with Bølling and Allerød.

The alternation of organic-mineral lake silt, peat and sand with diatom algae, identifying changes in limnological conditions under periglacial conditions, changes in bioproductivity and sedimentation rates, made it possible to distinguish a stage of predominantly alluvial morpholithogenesis, three stages of lacustrine-alluvial sedimentation, and a stage of lacustrine accumulation. Features of the granulometric composition of deposits revealed periodic connection of the lake with erosion-accumulation processes in the catchment area, mainly with the activity of the Kama River, similar to the formation of sors in Western Siberia.

## FUNDING

The study was carried out with the support of the Russian Science Foundation, grant No. 22-77-00086, https://rscf.ru/project/22-77-00086/

## REFERENCES

1. *Kvasov D.D.* Late Quaternary History of Large Lakes and Inland Seas of Eastern Europe. Leningrad: Nauka, 1975. 280 p.

2. *Nazarov N.N., Kopytov S.V., Zhuykova I.A., Chernov A.V.* Pleistocene drainage channels in the southern part of the Keltma Depression (Kama-Vychegda interfluve) // Geomorphology. 2020. No. 4. Pp. 74–88. https://doi.org/10.31857/S0435428120040070

3. *Panin A.V., Astakhov V.I., Lotsari E., Komatsu G., Lang J., Winsemann J.* Middle and Late Quaternary glacial lake-outburst floods, drainage diversions and reorganization of fluvial systems in northwestern Eurasia // Earth-Science Reviews. 2020. Vol. 201. 103069. https://doi.org/10.1016/j.earscirev.2019.103069

4. *Lysa A., Larsen E., Buylaert J.-P., Fredin O., Jensen M., Kuznetsov D.* Late Pleistocene stratigraphy and sedimentary environments of the Severnaya Dvina-Vychegda region in northwestern Russia // Boreas. 2014. Vol. 43. Pp. 759–779. https://doi.org/10.1111/bor.12080

5. *Zaretskaya N.E., Panin A.V., Golubeva Yu.V., Chernov A.V.* Sedimentation environments and geochronology of the Late Pleistocene to Holocene transition in the Vychegda River valley // ras reports. Earth Sciences. 2014. Vol. 455. No. 1. Pp. 52–57. https://doi.org/10.7868/S0869565214070238

6. *Zaretskaya N.E., Panin A.V., Utkina A.O., Baranov D.V.* Aeolian sedimentation in the Vychegda river valley, north-eastern Europe, during MIS 2-1 // Quaternary International. 2024. Pp. 83–89. https://doi.org/10.1016/j.quaint.2023.05.022

7. *Ziling D.G., Kapitanova K.V., Kulagin S.I., Galushkin Yu.A., Simonov A.N., Korganova L.S.* Report on the results of engineering-geological studies conducted by the Kama Party in the zone of the projected Upper Kama reservoir (in the section from Bondyug village to Gainy village) in 1958-59. Moscow: Ministry of Geology USSR, 1960. 830 p.

8. *Lapteva E.G., Zaretskaya N.E., Lychagina E.L., Trofimova S.S., Demakov D.A., Kopytov S.V., Chernov A.V.* Holocene vegetation dynamics, river valley evolution and human settlement of the upper Kama valley, Ural region, Russia // Vegetation History and Archaeobotany. 2023. Vol. 32. Pp. 361–385. https://doi.org/10.1007/s00334-023-00913-5

9. *Reimer P., Austin W.E.N., Bard E. et al.* The IntCal20 Northern Hemisphere radiocarbon age calibrationcurve (0–55 cal kBP) // Radiocarbon. 2020. Vol. 62. No. 4. Pp. 725–757. https://doi.org/10.1017/RDC.2020.41

10. *Heiri O., Lotter A.F., Lemcke G* . Loss on ignition as a method for estimating organic and carbonate content in sediments: reproducibility and comparability of results // J. Paleolimnol. 2001. No. 25. Pp. 101–110. https://doi.org/10.1023/A:1008119611481

11. *Maher B.A.* Magnetic properties of modern soils and Quaternary loessic paleosols: paleoclimatic implications // Palaeogeography, Palaeoclimatology, Palaeoecology. 1998. Vol. 137 (1–2). Pp. 25–54. https://doi.org/10.1016/S0031-0182(97)00103-X

12. *Battarbee R.W., Jones V.J., Flower R.J.* Diatoms // Tracking Environmental Change Using Lake Sediments. Terrestrial, Algal and Siliceous Indicators. 2001. Vol. 3. Pp. 155–202.

13. *Kulikovsky M.S., Glushchenko A.M., Genkal S.I., Kuznetsova I.V.* Guide to Diatoms of Russia. Yaroslavl: Filigran, 2016. 804 p.

14. *Chernova G.M.* Spore-pollen analysis of Pleistocene-Holocene deposits. St. Petersburg: SPbSU Publishing House, 2004. 128 p.

15. *Prentice C., Guiot J., Huntley B. et al.* Reconstructing biomes from palaeoecological data: a general method and its application to European pollen data at 0 and 6 ka // Climate Dynamics. 1996. Vol. 12. Pp. 185–194. https://doi.org/10.1007/BF00211617

16. *Beletskaya N.P.* Genetic classification of lake basins of the West Siberian Plain // Geomorphology. 1987. No. 1. Pp. 50-58.

17. *Markova A.K., Kolfschoten T., Simakova A.N., Puzachenko A.Yu., Belonovskaya E.A.* Ecosystems of Europe during the Late Glacial Bølling-Allerød warming (10.9–12.4 thousand years ago) based on palynological and theriological data // Proceedings of the Russian Academy of Sciences. Geographical Series. 2006. No. 1. Pp. 15–25.

18. *Panin A.V., Matlakhova E.Yu.* Fluvial chronology in the East European Plain over the last 20ka and its palaeohydrological implications // Catena. 2015. Vol. 130. Pp. 46–61. https://doi.org/10.1016/j.catena.2014.08.016

19. *Sadokov D.O., Sapelko T.V., Bobrov N.Yu., Melles M., Fedorov G.B.* Late Glacial and Early Holocene History of Lake Sedimentation in the North of Mologa-Sheksna Lowland: Case Study of Lake Beloe (Northwest Russia) // Bulletin of Saint Petersburg University. Earth Sciences. 2022. Vol. 67. Issue 2. P. 266–298. https://doi.org/10.21638/spbu07.2022.204

20. *Paleoclimates* and Paleolandscapes of the Extratropical Northern Hemisphere. Late Pleistocene – Holocene. Atlas-monograph / A.A. Velichko, O.K. Borisova, V.P. Grichuk et al.; ed. A.A. Velichko. Moscow: GEOS, 2009. 119 p.

DOKLADY EARTH SCIENCES, 2025, Vol. 520, No. 1, pp. 106–113

PALEOGEOGRAPHY

# DIGITALIZATION OF ISOLATED BASINS PALEOGEOGRAPHIC RECONSTRUCTIONS: A CASE STUDY OF THE EARLY OLIGOCENE SOLENOVIAN CRISIS IN THE EASTERN PARATHETIS

© 2025 **I. S. Patina*, V. V. Fomina**, A. A. Tkacheva***, and** Corresponding Member of RAS **N. B. Kuznetsov******

Received July 15, 2024
Revised September 26, 2024
Accepted September 30, 2024

**Abstract.** A new methodology for paleogeographic reconstructions of regressive stages of sedimentary basins, which experienced isolation from the World Ocean, has been tested using the example of the Eastern Paratethys. The application of this methodology makes it possible to fill the gaps in understanding the development history of the Paratethys and other similar sedimentary basins (such as Pricaspian and South Atlantic), which experienced isolation at various stages of their existence. Digital modeling of the results and consequences of the Early Oligocene Solenovian regression manifested in the Eastern Paratethys has been carried out. Based on the synthesis of paleogeographic reconstructions and data on changes in the geodynamic setting of the Black Sea-Caspian region, a digital model has been created depicting the depth changes of the Paratethys during its initial (transgressive), transitional, and final (regressive) stages in the Solenovian time of the Early Oligocene. This model takes into account relative sea level fluctuations, as well as the influence of later tectonic deformations superimposed on the structure of the Oligocene infill of the Eastern Paratethys sedimentary basin.

**Keywords:** *Paratethys, Maykopian series, seismic stratigraphy, regression, paleogeography*

**DOI**: 10.31857/S26867397250112e8

## INTRODUCTION

The basis of paleogeographic reconstructions is the study of the distribution of sediments of ancient basins. In most cases, data on sedimentation conditions are obtained by analyzing geological and paleontological data. These approaches work well for open-type marine basins, where the water level is determined by the level of the World Ocean. However, when studying closed “Mediterranean” basins, standard methods of paleontological and lithological analysis are uninformative and do not provide complete data on their depth, erosion basis, and development mode.

Such basins periodically became isolated not only from the World Ocean but also lost connection with neighboring basins. The history of water level variations in such closed basins is difficult to directly correlate not only with the global eustatic curve of the World Ocean level fluctuations but also with data from other intracontinental basins with which connections were interrupted. During isolation periods, each basin with its watershed area transformed into a separate tectono-sedimentary system with a unique development history and its own erosion base determined by the water level within it. Examples include the Atlantic and Arctic basins in the early stages of their formation, Neoproterozoic aulacogens of the East European Platform, Paleozoic basins of the Caspian region, the Mediterranean Sea, as well as the Paratethys sea system located along the southern margin of Western Eurasia during the second half of the Cenozoic.

One of the most significant, but still poorly studied isolation episodes is the Solenovian event at the end of the Rupelian age of the Early Oligocene. According to geological data, clear signs of regression have been identified in the Solenovian layers [5, 13, 14, 16]. However, the scale of this event and the expression of its consequences in the closed parts of the basin have practically not been discussed earlier.

---

*Geological Institute, Russian Academy of Sciences, Moscow, Russian Federation*
**e-mail: irina.patina@gmail.com*
***e-mail: valery.fomina17@gmail.com*
****e-mail: a.a.tkacheva1@yandex.ru*
*****e-mail: kouznikbor@mail.ru*

The task of tracing and evaluating events similar to the Solenovian event can be solved using seismostratigraphic interpretation methods of CDPM seismic data. Seismostratigraphic analysis allows tracking over considerable distances both lateral variations in the structural plan of geological bodies and the profile of erosional-sedimentary equilibrium, as well as seismofacial parameters of elements in the sedimentary section.

In this work, based on the results of seismostratigraphic analysis, an attempt has been made to reconstruct the events of the Solenovian crisis in the Eastern Paratethys.

## SOLENOVIAN CRISIS

The deposits of the Solenovian horizon are represented by clays with interlayers of sands and

|  | Seismic facies (vertical section) | The nature of the wave field | Estimated composition and conditions of sedimentation | Distribution areas |
|---|---|---|---|---|
| a) | 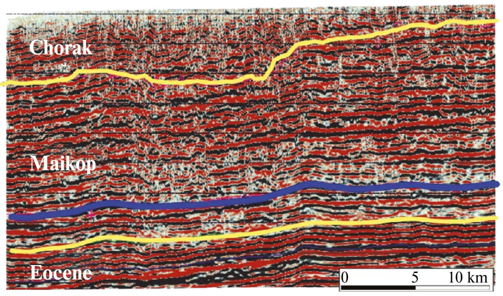 | Alternation of bright, extended, and intermittent reflections, as well as consonantal and erosive boundaries | Facies of shallow Shelf sedimentation conditions. The alternation of transgressino-regressive phases is expressed in a change in the nature of seismic activity. | Western Pre-Caucasus, North East and Central Pre-Caucasus, Northern Caspian, periphery Mangyshlak depression |
| b) | 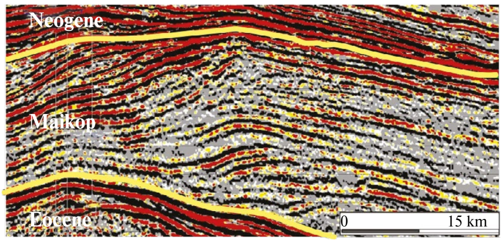 | Wedge-shaped oblique reflections detected within the Maikop seismic complex areas of transition from the shallow shelf to the deeper parts of the basin | Areas of transition from the shallow shelf to the deeper parts of the basin | West Kuban Trough, East Pre-Caucasus, Middle Caspian, Mangyshlak, Ustyurt |
| c) | 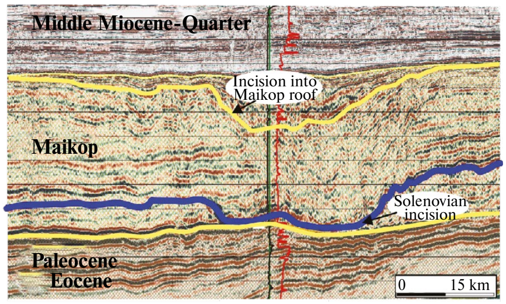 | The erosive surface is a milling cutter with a deep cut into the underlying strata and chaotic filling | Buried river cutters in the offshore part of the Maikop seismic complex. The first incision was formed during the Solenovian regression and has an inherited character: subsequent regressions formed milling cutters in the same place. | Kanevskoy-Berezansky val, South of Timashevskaya step, Kumo-Manych trough, Prikum lifting system, Nogai step |
| d) | 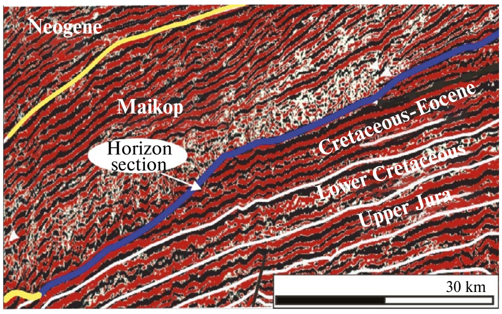 | Abrupt interruption of horizons as a result of erosion | The erosion board. The depth of the erosion corresponds to the amplitude of the sea level drop | The Azov, West Kuban and Tersko-Caspian troughs |

╱ 1 ╱ 2 ╱ 3

**Fig. 1.** Characteristic seismofacies of the Maykop seismic complex. a – parallel seismofacies of the shallow shelf (fragment of regional profile No. 10 in the Eastern Ciscaucasia, b – clinoform seismofacies of the shelf (fragment of regional profile FR050916 in the Western Ciscaucasia), c – erosional incisions of river systems (fragment of regional profile FR060722a in the Western Ciscaucasia), d – abrasion scarp (fragment of regional profile No. V in the Eastern Ciscaucasia). 1 – boundaries of the Maykop seismic complex; 2 – surface of Solenovian age; 3 – other seismostratigraphic boundaries.

sandstones, as well as a characteristic layer of light marl at the base (named the “ostracod layer”). The horizon is distinguished in the lower (Khadum) part of the Maikop series and is of Early Oligocene age.

The Maikop seismic complex is distributed over almost the entire territory of the Black Sea-Caspian region (except for areas of its post-sedimentation erosion). It is characterized by variability in thickness (from tens to 2500 m) and internal structure with an almost monotonous lithological composition (dark clayey rocks with sandy interlayers). The structure of the seismic complex is examined in detail in our previous publications [11, 21] and in the works of predecessors [6, 7, 8]. The main results of the conducted research can be summarized as follows. In the shallowest shelf areas, parallel reflecting horizons of varying degrees of expression were formed (Fig. 1a). The deeper part of the Maikop seismic complex consists of large clinoform sedimentary bodies (Fig. 1b), which sequentially filled the basin from the platform towards the open sea.

Inside the shelf part of the Maikop seismic complex, we traced an erosional surface corresponding to the regression of the Late Solenovian time (Fig. 2). It is characterized by regional distribution and is expressed throughout almost the entire territory of Ciscaucasia and the Middle Caspian. The surface is complicated by a system of incised valleys, which were inheritedly formed by river channels during the Oligocene-Miocene regressions, starting from the Solenovian time (Fig. 1c). The degree of erosion expression and erosion of complexes underlying the identified surface increases from north to south towards the northern flanks of the Ciscaucasian and Caspian troughs. Along them, a steep abrasion escarpment about 500 m high is distinguished (Fig. 1d). Here, the underlying complexes are eroded down to the Cretaceous. Further in the direction of the open basin, the reflecting horizons lie conformably, and the erosional surface is absent [21].

Geological data on the Solenovian crisis (incisions, rewashing, areas of zero sedimentation and traces of planar erosion, wavy surface, bioturbation of sediments, coal accumulation, coarse terrigenous facies, sedimentary brecciation, olistostromes, etc.) have been established practically throughout the northern shelf of the Eastern Paratethys – in the territory of Ciscaucasia, Northern Yergeni, Northern Caspian and Kazakhstan 2, 5, 15, 16]. Its traces are also present on the Black Sea coast. For example, in the Karburun outcrop (Istanbul, Turkey), an eroded Eocene surface filled with coarse terrigenous facies and debris flow deposits was mapped. Paleontological studies confirm the Solenovian age of the deposits [23]. Similar incisions are described in the Getian depression (Romania) [22] and mapped on the Odessa and Romanian shelf of the Black Sea [18], where Early Oligocene and even Eocene strata were eroded, however, data on the age of the incisions themselves are absent here.

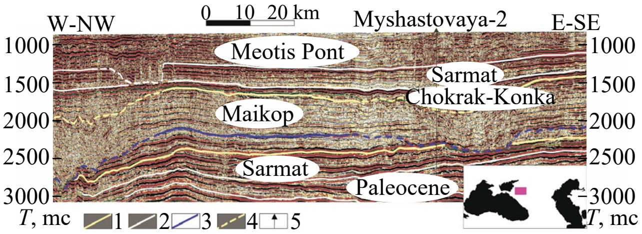

**Fig. 2.** Seismostratigraphic profile 040823ab [4], showing the erosional surface of Solenovian age within the Maykop seismic complex and the inherited system of river incisions. 1 – boundaries of the Maykop seismic complex; 2 – boundaries of other seismic complexes; 3 – surface of Solenovian age, 4 – boundaries of incisions, color corresponds to the legend; 6 – wells. The inset shows the position of the profile.

## METHODOLOGY FOR RECONSTRUCTING PALEOBATHYMETRY

During paleogeographic reconstructions of basins similar to the Eastern Paratethys, a regional seismostratigraphic analysis of their closed parts (not currently exposed on the surface) is first conducted with the identification and mapping of shallow and deep-water areas of the shelf, slopes, and deep-water depressions. Based on this zoning, indicators of water level fluctuations in the basin characteristic of its various areas are identified.

For the Eastern Paratethys, the most effective approach for determining paleobathymetry and the amplitude of relative sea level fluctuations has been measuring the heights of clinoform complex edges (defining the depth difference between shallow and deep shelf), as well as the heights of abrasion escarpments and incisions (defining the amplitude of relative sea level fall during regression). It is the sum of such markers and the characteristics of their distribution, supported by geological data, that can be interpreted as the result of water level drops and changes in erosion base level, whereas singular observations of one of the features described above do not always mark transgressive-regressive events specifically.

Based on the synthesis of paleogeographic data on the transgressive stages of the Oligocene in the Eastern Paratethys, we have developed a structural-palinspastic scheme (model) of the seafloor relief of the Solenovian basin (Fig. 3). The depths of the paleosurface were determined based on the results of our own research [21] and previous reconstructions [13]. The base map for creating the relief was the map of the Eastern Paratethys during the Pshekhian time [14] and palinpastic data for the Early Oligocene [1]. The base maps were updated with refined depth values obtained from seismostratigraphic analysis. The relative sea level marks at the transgression maximum at the beginning of the Solenovian time were accepted as the zero surface. Then, by interpolating the data array, depth values were extended to areas where paleosurface depth data were absent. This process involved controlling and correcting the interpolated values according to the tectonic position and known facies environments.

The model takes into account changes in the geodynamic structure of the region. To accomplish this, the consequences of shear along the Crimean-Kopetdag zone of concentrated deformations of pre-Pliocene age were removed. Detailed description and palinspastic reconstruction of movements along this zone were presented earlier [9, 12]. The zone represents a transregional post-collisional right-lateral strike-slip fault that extends from southeast to northwest from the Kopetdag through the Apsheron Sill and the Greater Caucasus to the Crimean Mountains. The active phase of the strike-slip zone formation coincides with the end of the Alpine stage and the collision stages of the Eurasian and Arabian plates. The main movements along the strike-slip zone occurred in the Late Miocene or even in the Pliocene-Quaternary time. During this same period, the Caucasian source of clastic material first actively manifested itself [19]. The amplitude of the strike-slip during this period was about 150-200 km, which was determined based on geological and seismostratigraphic data on the distance between marker paleogeographic elements located on different sides of the strike-slip zone [9, 11]. Currently, movements in the northeastern direction continue, as recorded by

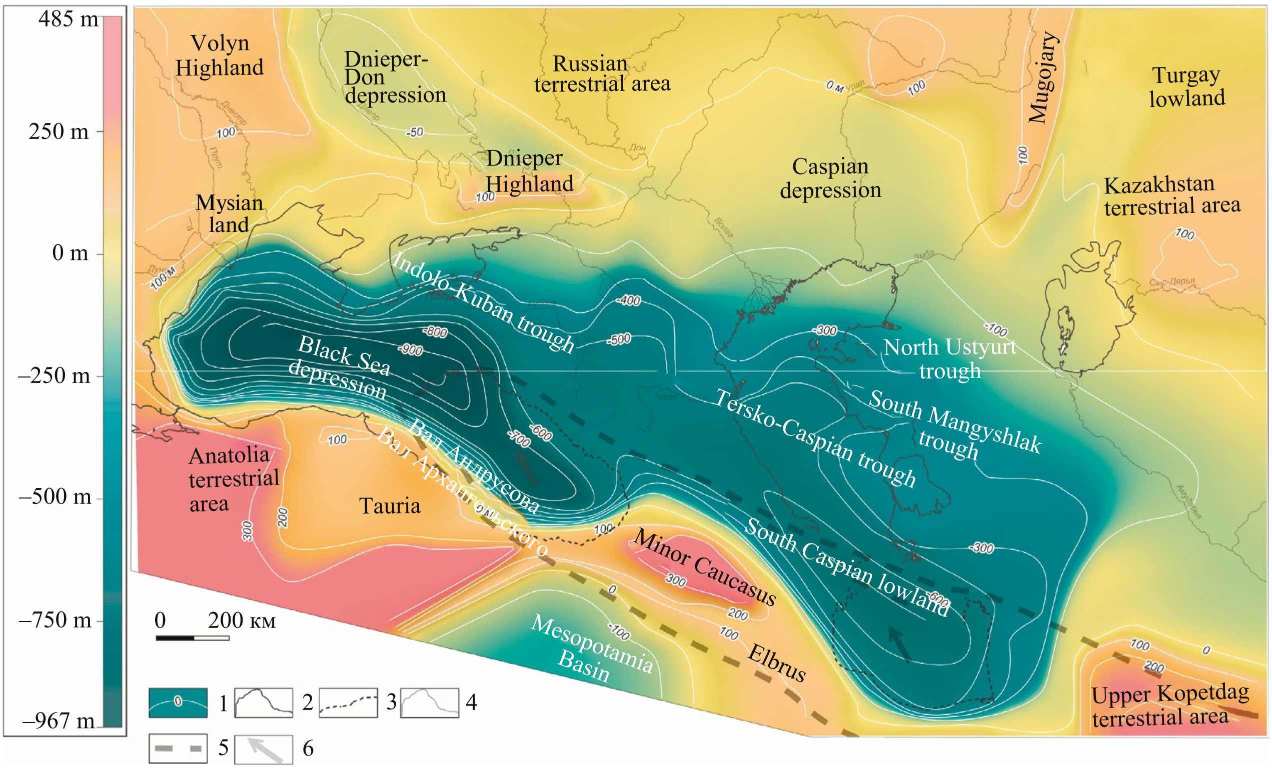

**Fig. 3.** Structural-palinspastic scheme of the Eastern Paratethys relief during the Solenovian time of the Early Oligocene based on digital modeling results. 1 – isolines of the Solenovian paleosurface, calculated from the relative sea level mark at the beginning of the Solenovian time, taken as zero; 2 – modern coastlines of seas; 3 – coastlines of seas, relocated taking into account movements along the Crimean-Kopetdag deformation zone; 4 – rivers; 5 – boundaries of the Crimean-Kopetdag strike-slip deformation zone; 6 – direction of movement of the hanging wall of the strike-slip fault (during Pliocene-Quaternary time).

GPS observations. Modern velocities are 26–28 mm per year [10]. At similar rates of movement, since the end of the Pliocene, the Eastern Black Sea block would have covered a distance of about 140 km, which practically corresponds to the amplitude of the strike-slip. The total amplitude of the strike-slip was determined using paleogeographic analysis. The reconstruction made it possible to restore the original contours of sedimentary basins that were disrupted and separated by the strike-slip zone. Thus, the Andrusov and Arkhangelsky ridges in the Black Sea, when reconstructing the strike-slip movement, connect into a single structure representing an elevated part of a relatively deep-water shelf; a single deep-water basin was located in the western and eastern parts of the Black Sea.

It is also important to note that detailed study of the material composition of the Solenovian horizon did not reveal any influence from the Caucasian source area [15, 16]. The results of our seismostratigraphic analysis indicate that sediment transport from the Caucasus during the Oligocene time is also not evident. Recent studies on the distribution pattern of detrital zircon grain ages extracted from Cenozoic strata in the Caucasus region [19] have shown that the Greater Caucasus mountain range did not exist as a major source of clastic material until the end of the Miocene. Sedimentary flows into the Western Kuban Trough from the Greater Caucasus are not recorded earlier than the Pliocene-Quaternary boundary. Thus, based on seismostratigraphic data, tectonic and lithological analysis, we assume the existence of open basin conditions in the area of the modern Greater Caucasus mountain range during the Solenovian time. During major regressions, this area became significantly shallower, which may explain the presence of shallow-water and deltaic sand facies, as well as remnants of terrestrial vegetation [17] that grew on the dried shelf surface and was brought in by rivers flowing into the basin.

Thus, the obtained relief model combines the structural-paleogeographic scheme of the Early Oligocene Eastern Paratethys with palinspastic reconstructions. This reconstruction allows for the most adequate assessment of changes in the area and relationship between sedimentation and erosion zones during water level fluctuations in the basin.

## RECONSTRUCTION OF THE SOLENOVIAN TRANSGRESSION AND REGRESSION

For the compiled terrain model, changes in the coastline and contours of the sedimentary basin were reconstructed with changes in water level during the Solenovian Age of the second half of the Early Oligocene (Fig. 4).

During the transgressive stage (beginning of the Solenovian time), the main part of the shelf (North Ciscaucasia, Yergeni, Northern Caspian, and Kazakhstan) represented areas of shallow-marine sedimentation (Fig. 4a). In deeper shelf areas (southern and central regions of Ciscaucasia, Middle Caspian, Kara-Bogaz-Gol, Mangyshlak depression), clinoform bodies were formed. Based on the heights of the clinoform complex edges, it was determined that the depths of the northern shelf of the Eastern Paratethys were about 150–300 m, increasing in the southern direction. Here, the relatively shallow shelf transitioned into a system of depressions (Indolo-Kuban, East Kuban, Terek-Mangyshlak, and North Ustyurt troughs and the Kura depression), where depths reached 500 meters or more. Towards the basin, these troughs opened into the deep-water basins of the Black Sea and Southern Caspian.

When the water level fell with the amplitude of 100–150 m, the basin boundaries changed insignificantly in spatial terms, without forming any marker elements that clearly define their contours (Fig. 4b). The coastline of southern outskirts adjacent to orogenic areas retreated by a few kilometers. On the northern platform shelves, the changes were more extensive, but nevertheless, the main part of the shelf remained covered with water. The water retreated gradually here, forming shallow bays. Deposits characterizing such facies environments occurred in the northern parts of Ciscaucasia, Yergeni, on the flank parts of the South Mangyshlak depression and southern regions of the Transcaspian mainly during the Early Solenov time. In deeper areas, conditions of uncompensated sedimentation persisted.

With further fall of the relative sea level at the end of the Solenovian age, the basin underwent more large-scale changes (Fig. 4c). Almost the entire territory of the northern shelves dried up, and the coastline boundary shifted southward by 100 kilometers or more. Water remained only in the most deeply submerged areas: the Kuban and Terek-Mangyshlak depressions, the Black Sea and Caspian basins. The amplitude of sea level fall during the regression in the Late Solenovian time was estimated based on measurements of the abrasion scarp height and incision depth. It was about 450–500 m [21].

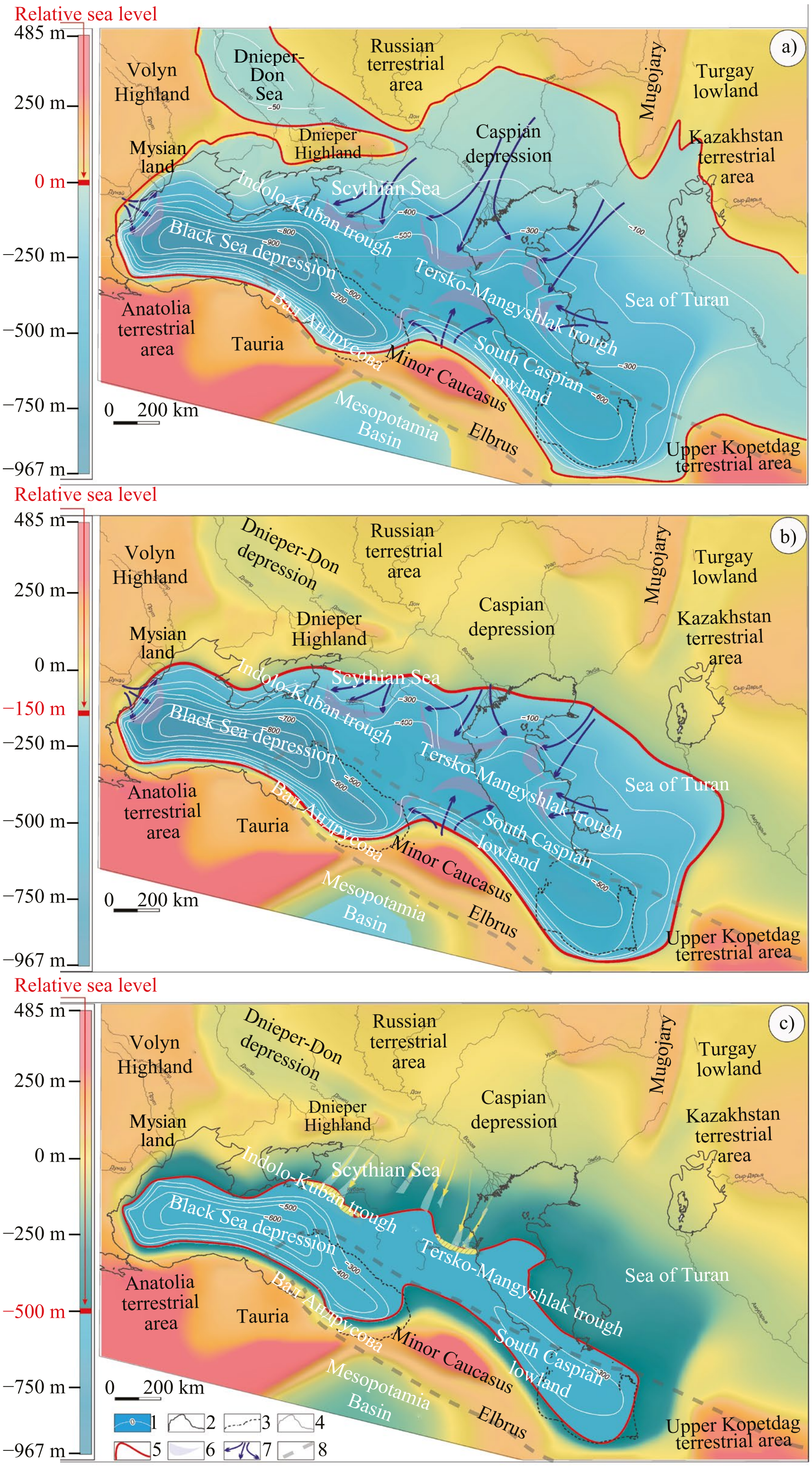

**Fig. 4.** Migration of the Eastern Paratethys coastline during relative sea level fluctuations: a – maximum of the transgressive stage at the beginning of the Solenovian Age. Relative sea level taken as 0 m; b – beginning of regression in the second half of the Early Solenovian time. Relative sea level – 150 m; c – maximum regression. Late Solenovian time. Relative sea level – 500 m. 1 – presumed paleodepth contours; 2 – modern sea coastlines; 3 – sea coastlines displaced considering movements along the Crimean-Kopetdag deformation zone; 4 – rivers; 5 – Eastern Paratethys coastline; 6 – areas of clinoform formation; 7 – direction of terrigenous material transport; 8 – abrasion scarps; 9 – incised paleoriversvalleys and direction of terrigenous material transport within them; 10 – boundaries of the Crimean-Kopetdag shear deformation zone.

## CONCLUSION

The conducted research allowed testing a number of methodological approaches to seismostratigraphic analysis applicable for reconstructing the paleogeography of regressive episodes in closed-type basins using the Eastern Paratethys as an example.

Analysis of the distribution of seismic facies (parallel seismic facies of shallow shelf, clinoform seismic facies of slopes, depression deposits in basins, etc.) made it possible to identify various facies zones and trace paleotopography elements across the area (erosional surfaces, incisions and abrasion scarps) and amplitudes of water level fluctuations characteristic for different stages of basin development. Accounting for geodynamic changes allowed for an adequate assessment of changes in the area and the relationship between sedimentation and erosion zones during transgressive and regressive regimes.

This seismostratigraphic analysis helps solve the problem of identifying developmental patterns of isolated sedimentary basins with unique evolutionary histories. The applications of this approach are quite broad and diverse. Identification and mapping of the described structural features and erosion-sedimentation regimes of closed basins, as well as considering the depths of paleobasins, can be used in modeling sedimentary basins and hydrocarbon systems, when instead of an eustatic curve, it is necessary to set specific values for water level fluctuations. Also, determining the relationship between areas and types of sedimentation with areas of erosional processes is important when compiling local and regional stratigraphic schemes and assessing potential mineral resources.

## CONFLICT OF INTEREST

The authors of this paper declare that they have no conflict of interest.

## FUNDING

The research was conducted and carried out with the financial support of the Russian Science Foundation (grant 22-27-00827, https://rscf.ru/project/22-27-00827/ ).

## REFERENCES

1. Atlas of lithologic-paleogeographic, structural, palinspastic and geoecological maps of Central Eurasia (ed. Yu.G. Leonov, V.A. Bykadorov, Yu.A. Volozh, T.N. Kheraskova et al.). Alma-Ata: Research Institute of Natural Resources YUGGEO, 2002.
2. *Voronina A.A., Popov S.V.* The Solenovsky Horizon of the Eastern Paratethys // Izvestiya AN SSSR. Seriya geol. 1984. No. 9. Pp. 41–53.
3. *Egorova T.P., Baranova E.P., Gobarenko V.S., Murovskaya A.V.* The structure of the Earth's crust of the Mountainous Crimea along the "Sevastopol-Kerch" profile based on the results of DSS and local seismic tomography // Geotectonics. 2018. No. 4. P. 77–95.
4. *Efimov V.I.* Geological study and evaluation of the hydrocarbon potential of the platform cover complexes of the Western Ciscaucasia based on regional seismic exploration work to ensure stable development and expansion of the resource base of the Fuel and Energy Complex of the Southern Federal District (Krasnodar Territory and the Republic of Adygea). Krasnodarneftegeofizika. Krasnodar. 2007.
5. *Zastrozhnov A.S., Popov S.V., Benyamovsky V.N., Musatov V.A., Akhmetyev M.A., Zaporozhets N.I., Bogachkin A.B., Stolyarov A.S.* Reference section of the Oligocene in the south of the East European platform (Northern Ergeni) // Stratigraphy. Geol. correlation. 2019. Vol. 27. No. 4. Pp. 59–92
6. *Ismagilov D.F., Kozlov V.N., Martirosyan V.N., Terekhov A.A* . Structure and formation features of the platform cover within the Middle Caspian (based on seismic research) // Geotectonics. 2003. No. 4. Pp. 51–60.
7. *Kozmodemyansky V.V., Popkov V.I., Titov B.I.* Lateral accretion bodies in the Oligocene of Mangyshlak // Bull. MOIP. Geol. section. 1987. Vol. 62. No. 1. P. 37–40.
8. *Kunin N.Ya., Kosova S.S., Medvedev E.N., Pustovoyt O.Yu.* Seismostratigraphic analysis of the Maikop deposits in the North-Eastern Ciscaucasia // Soviet Geology. 1990. No. 4. Pp. 79–84.
9. *Leonov Yu.G., Volozh Yu.A., Antipov M.P., Bykadorov V.A., Kheraskova T.N.* Consolidated crust of the Caspian region: zoning experience. Moscow: GEOS, 2010. 64 p.
10. *Milyukov V.K., Mironov A.P., Rogozhin E.A., et al.* Estimates of the rates of modern movements of the North Caucasus based on GPS observations // Geotectonics. 2015. No. 3. Pp. 56–65.
11. *Patina I.S.* Structure of the Maikop complex of the Caspian region based on the results of seismostratigraphic studies // Stratigraphy. Geol. correlation. 2017. Vol. 25. No. 3. Pp. 1–10.
12. *Patina I.S., Leonov Yu.G., Volozh Yu.A., Kopp M.L., Antipov M.P.* Crimean-Kopetdag zone of concentrated orogenic deformations as a transregional late-collisional right-lateral strike-slip fault // Geotectonics. 2017. No. 4. Pp. 17–30

13. *Popov S.V., Antipov M.P., Zastrozhnov A.S., Kurina E.E., Pinchuk T.N.* Sea level fluctuations on the northern shelf of the Eastern Paratethys in the Oligocene-Neogene // Stratigraphy. Geol. correlation. 2010. Vol. 18. No. 2. Pp. 3–26.

14. *Popov S.V., Akhmetyev M.A., Lopatin A.V., Bugrova E.M., Sychevskaya E.K., Shcherba I.G., Andreeva-Grigorovich A.S., Zaporozhets N.I., Nikolaeva I.A., Kopp M.L.* Paleogeography and biogeography of the Paratethys basins. Part 1. Late Eocene – Early Miocene // Proc. PIN RAS. Vol. 292. Moscow: Scientific World. 2009. 178 p.

15. *Stolyarov A.S.* Paleogeography of Ciscaucasia, Volga-Don and Southern Mangyshlak in the Late Eocene and Early Oligocene // Bull. MOIP. Geol. section. 1991. Vol. 66. Issue 4. Pp. 64–80.

16. *Stolyarov A.S., Ivleva E.I.* Solenovsky deposits of the Lower Oligocene of Ciscaucasia, Volga-Don and Mangyshlak (central part of the Eastern Paratethys). Report 1. Main features of composition and structure // Lithology and Mineral Resources. 1999. No. 3. Pp. 298–317.

17. *Akhmetiev M.A.* Palaeobotanical data on Geological Age of the Grater Caucasus // Paleontological Journal. 1995. V. 29. № 1. Pp. 172–181.

18. *Dinu C., Wong H.K., Tambrea D., Matenco L* . Stratigraphic and structural characteristics of the Romanian Black Sea Shelf // Tectonophysics. 2005. 410(1):417-435. DOI: 10.1016/j.tecto.2005.04.012

19. *Kuznetsov N.B., Romanyuk T.V., Shatsillo A.V., Latysheva I.V., Fedyukin I.V., Strashko A.V., Novikova A.S., Shcherbinina E.A., Drazdova A.V., Makhinya E.I., Marinin A.V., Dubenskiy A.S., Erofeeva K.G., Sheshukov V.S.* Cretaceous–Eocene Flysch of the Sochi Synclinorium (Western Caucasus): Sources of Clastic Material Based on the Results of U–Th–Pb Isotope Dating of Detrital Zircons // Lithology and Mineral Resources. 2024. V. 59. No. 1. Pp. 47–69.

20. *Palcu D.V., Patina I.S., Sandric I., Lazarev S., Vasiliev I., Stoica M., Krijgsman W.* Late Miocene megalake regressions in Eurasia // Scienific Reports. 2021. V. 11. No. 11471.

21. *Patina I.S., Gorkin G.M., Postnikova I.S* . Manifestations of the Early Oligocene Solenovian Crisis on the Northern Shelf of the Eastern Paratethys // Lithology and Mineral Resources. 2024. V. 59. No. 4. Pp. 381–389.

22. *Roban R.-D., Melinte M.C* . Paleogene litho- and biostratigraphy of the NE Getic Depression (Romania) // Acta Palaeontologica Romaniae. 2005. V. 5. Pp. 423–439.

23. *Simmons M.D., Bidgood M.D., Connel P.G., et al.* Biostratigraphy and paleoenvironments of the Oligocene succession (Ihsaniye Formation) at Karaburun (NW Turkey) // Turkish Journal of Earth Sciences. 2020. 29. Pp. 28–63. https://doi.org/10.3906/yer-1907-7

DOKLADY EARTH SCIENCES, 2025, Vol. 520, No. 1, pp. 114–117

GEOPHYSICS

# VERTICAL GRADIENT OF THE GEOMAGNETIC FIELD BY MULTIPLE ALTITUDE AEROMAGNETIC SURVEY

© 2025 **I. M. Aleshin**[a, b, *], Corresponding Member of RAS **A. A. Soloviev**[a, b],
**K. I. Kholodkov**[a, b], **F. V. Perederin**[a, b], and **Y. V. Taran**[a]

Received July 09, 2024
Revised September 05, 2024
Accepted September 09, 2024

**Abstract.** Modern geophysical survey technologies are progressing fast. One notable milestone of this progress is substantial increase of georeferencing performance with benefits of advanced satellite radionavigation. This article delves into the advantages of employing multiple altitude (also referred to as multilevel) aeromagnetic measurements conducted using unmanned aerial vehicles for deriving vertical gradient. This approach contrasts with conventional methods that rely on the calculation of the corresponding transform of the anomalous magnetic field. A comparative analysis was conducted on two study areas, characterized by distinct magnetic anomalies. One region exhibited strong anthropogenic disturbances against a background of a relatively calm regional magnetic field, while the other demonstrated weaker anthropogenic anomalies. The comparison between the maps of the anomalous field gradient calculated directly and derived from multilevel survey in both regions underscores the potential benefits of straightforward gradient measurement methods.

**Keywords:** *low altitude survey, multiple altitude survey, UAV, drone, airborne magnetic survey, magnetic field transform*

**DOI**: 10.31857/S26867397250113e1

The benefits of using transforms to analyze anomalies in potential fields have long been recognized. In fact, each transformation acts as a filter, highlighting specific features in the spatial distribution of an anomalous field, such as the boundaries of anomalies. This includes the vertical gradient of the magnetic field module herein referred to as the “vertical gradient”. The vertical gradient is the focus of our interest. The theory and practice of vertical gradientometry were extensively discussed in the mid-20th century.

While most transformations of the measured distribution of an anomalous field are purely mathematical, the vertical gradient of the field can be measured directly. During the early development of magnetic surveying equipment in the 1950s and 1960s, this technique was the one of choice. However, with the advancement of computing power, numerical techniques for transforming potential fields have become widely used, e.g. [3]. Nevertheless, this approach has several limitations, primarily due to instrument and environmental noise in real measurements. In aerial magnetic surveys with unmanned aerial vehicles (UAVs), interferences are associated with motion irregularities during the measurement process, leading to instability in the calculation of the vertical gradient and significant high-frequency interferences, which is common among other transforms. Therefore, the use of specialized computational techniques is required to enhance stability, but in turn, this increases the risk of the factual information loss. Challenges also arise during the analysis of calculated data, often when identifying near-surface abnormalities.

With the advancement of measurement equipment, the direct measurement of vertical gradients has become increasingly relevant. Many modern instruments, primarily designed for on-foot magnetic survey, feature two instruments in single assembly and can function as field gradiometers. [4] Since the field measurements are taken simultaneously on two sensors, there is no need to

---

[a] *Schmidt Institute of Physics of the Earth of the Russian Academy of Sciences, Moscow, Russia*
[b] *Geophysical Center of the Russian Academy of Sciences, Moscow, Russia*
**e-mail: ima@ifz.ru*

account for geomagnetic variations. Additionally, in this scenario, there is also no requirement for geological correction of regional structures. To conduct gradient surveys, it is essential to ensure that the straight line connecting the instruments is positioned vertically. Conducting aerial magnetic gradient measurements, however, poses additional technical challenges. Primarily, it is the positioning of the sensors at a considerable distance apart from one another and from the UAV carrier. Despite these challenges, aerial magnetic gradiometer systems are currently undergoing intensive development and application [5].

Currently, aeromagnetic survey with UAVs is widely used and grows rapidly. This technique allows for the determination of the vertical gradient through the use of multiple altitude aeromagnetic survey. The measurements are taken above the same area on the ground surface at multiple levels at various altitudes above ground level (AGL). If the altitude spacing between the levels is sufficiently small, this technique enables the estimation of the surface distribution of vertical gradients. An example of practical application of vertical gradient measurements is described here [7]. Unlike on-foot gradientometry, aerial survey requires the use of a base magnetic variation station since measurements at different altitudes are taken at different time. The technique for field gradient measurements does not differ significantly from aeromagnetic surveys in general. The main challenge is maintaining the spacing between survey levels and ensuring maximum repeatability of the flight path at different altitudes. In practice, accurately recording the altitude difference between survey levels is not feasible, and this limitation is compensated for by precise determination of the position of the magnetometer with post-processing of raw recordings of onboard Global Navigational Satellite Systems. The method called Post-Processing Kinematic also requires raw GNSS recordings from a fixed ground station in the vicinity of the survey site.

The following is a comparison of vertical gradient maps obtained using multilevel survey and ones computed with GravMagInv software [8]. The analysis was conducted based on measurements at two locations. The first location is the suburban research site of Vladimir State University (hereinafter referred to as “VLGU”) with a calm regional magnetic field. There are several notable anthropogenic anomalies, including power transmission towers, office buildings, utility structures, and parking lots for vehicles. The second set of measurements was conducted in the vicinity of the mid-latitude geophysical observation complex “Mikhnevo”, operated by the Sadovsky Institute for Geospheric Dynamics of the Russian Academy of Sciences. This location is chosen due to the fact that anthropogenic disturbances caused by the complex’s construction have a significantly lower impact on the regional magnetic field compared to other areas. In order to increase the accuracy of the survey, the measurements were taken while flying at minimum safe altitudes following the terrain. Prior to the survey, aerial photographs were taken and a digital elevation model was created based on these images. To validate the calculated values against the actual measurements, the vertical gradient of the anomalous field was determined in both sets of data. The anomalous field was obtained at each level of the survey using standard processing: accounting for corrections for variations in the geomagnetic field, data selection, alignment, interpolation onto a regular grid, etc.

At both sites, aeromagnetic surveying was conducted using an unmanned aerial vehicle (UAV) equipped with a quantum scalar magnetometer. Measurements were taken around the perimeter of the terrain on two levels, $z_+(x, y)$, $z_-(x, y)$, which differ in altitude by 15–25 meters. Note that the vertical axis points towards the center of the Earth i.e. downwards. At the VLGU site, UAV flights were conducted along the $x$-axis at both levels. In contrast, at Mikhnevo, flight paths at the lower level were perpendicular to those on the upper level. The position of the survey equipment mid-air was determined using measurements from the onboard GNSS (Global Navigation Satellite System) receiver, processed with data from a GNSS reference station located near the surveyed area to get centimeter-level special accuracy. With measurements from a magnetic variation station the variations were removed from the survey data and maps of the anomalous magnetic field were generated: $B_A(x, y, z_+(x, y))$ and $B_A(x, y, z_-(x, y))$ at corresponding altitude levels.

Then, we used equation:

$$B'_A\left(x,y,z_0\left(x,y\right)\right)=\frac{\mathrm{d}B_A\left(x,y,z_0\left(x,y\right)\right)}{dz}\approx$$

$$\approx\frac{B_A\left(x,y,z_+\left(x,y\right)\right)-B_A\left(x,y,z_-\left(x,y\right)\right)}{z_+\left(x,y\right)-z_-\left(x,y\right)}\quad(1)$$

to compute the distribution of vertical gradient.

The surface

$$z_0(x,y) = \left(z_+(x,y) + z_-(x,y)\right)/2 \qquad (2)$$

for which the gradient is computed lies between the survey levels.

Fig. 1. panels $A_1$ and $A_2$, shows the distribution of the anomalous magnetic field $B_A(x,y,z_+)$ at the lower level of the survey $z_+(x,y)$ obtained at the VLGU and Mikhnevo sites, respectively. In both cases, the anomalous field correlates with topography, i.e., it is largely due to regional magnetic field. The maps from the VLGU site clearly show local anomalies associated with anthropogenic structures: a tower and power line in the north, and office buildings and access road in the south. At Mikhnevo, anomalies are linked to geomagnetic observatory structures and are therefore less pronounced in the anomalous field. Their amplitude is significantly smaller than at VLGU. However, they stand out more clearly on maps of vertical gradients of both measured and computed magnetic fields.

Panels $B_1$ and $B_2$ of Fig. 1 present maps of the vertical derivative, $B'_A(x,y,z_+)$, calculated for two polygonal areas using the GravMagInv [8]. Panels $C_1$ and $C_2$ show the vertical gradient $B'_A(x,y,z_0)$, computed for the two polygons according to Equation (1). Overall, the calculated and measured values of the vertical derivatives appear to be in agreement. After the transformation the anomalies become much more prominent, and the structure of the anomalous field becomes more clearly visible compared to the initial maps (panels $A_1$ and $A_2$). This observation holds true for both polygonal regions, regardless of how the vertical gradients were derived, calculated or measured. It should be noted that the amplitudes of the measured vertical gradients are lower than those calculated, which can be attributed to the fact that measurements were

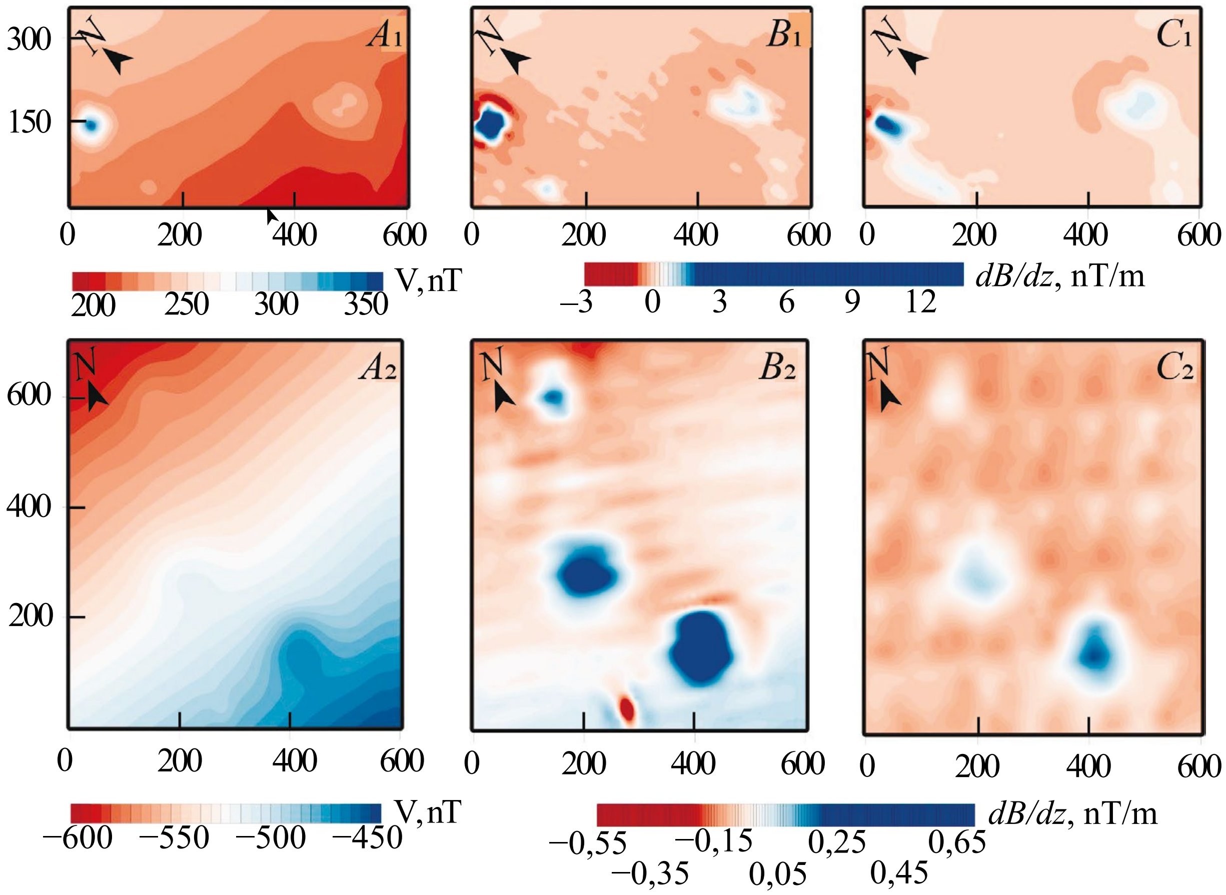

**Fig. 1.** Comparison of the results of processing and transformation of the anomalous field of high-altitude aeromagnetic survey. For the VLGU site, panels $A_1$, $B_1$, and $C_1$ show maps of the anomalous magnetic field (panel $A_1$), the numerical vertical derivative of the field (panel $B_1$), and the calculated field survey (panel $C_1$), respectively. For the Mikhnevo site, similar maps are shown on panels $A_2$, $B_2$ and $C_2$.

taken at different survey levels. Thus, the calculated vertical derivatives were obtained for the lower level $z_+(x,y)$, and the measured vertical gradient was set at the level $z_0(x,y)$, which is on average 10–20 meters further from the sources of anomalies.

The vertical derivative in both cases is influenced by the regional background. However, on the measured vertical gradient this effect is suppressed without the use of additional reductions. In the maps of the vertical gradient for the Mikhnevo (site $C_2$, Fig. 1) there are noticeable rudiments of profiles, which arose due to imprecisions of flight missions at different levels. Conversely, at the VLGU (site $C_1$, Fig. 1), where missions were conducted on a much more coincident profile system at two levels with an altitude gap of about 10 m, this effect was not present. However, the defect might have been be suppressed by replacing the interpolation algorithm when calculating the grid.

The experiment demonstrated that the vertical gradient derived from the results of the multiple altitude aeromagnetic survey provides a qualitative interpretation of the separation of magnetic anomalies that is at least as accurate as traditional computational methods.

The initial data used to calculate the vertical derivative is inevitably tarnished with errors of the Standard field model and assumptions made when calculating the regional component. The method of determining the vertical gradient from multi-level survey data reduces both of these factors and may be more advantageous for quantitative interpretation. However, its implementation will require significant improvement of the methodology for planning and conducting the fieldwork. Specifically, additional work is required to refine the methodology for determining the optimal mission altitude and number of levels for calculating the gradient, etc. Nevertheless, even at this stage, the described method has the potential to contribute to solving modern geological and geophysical problems.

## ACKNOWLEDGEMENTS

We thank the staff of Vladimir State University and Sadovsky Institute for Geospheric Dynamics of the Russian Academy of Sciences for helping with fieldwork organization. We also thank «Lolgeo» Ltd. for computation assistance.

## FUNDING

The research was conducted under the Russian Science Fund grant No. 24-17-00346. This work utilized the Analytical Center for Geomagnetic Data (the RAS Geophysics Center) services and data (https://ckp.gcras.ru/). We used the equipment of IPE RAS and GC RAS that was made available with State Programme of Scientific Equipment Upgrade under the «Nauka i universitety» umbrella.

## REFERENCES

1. *Prasad, K.N.D., Pham, L.T. & Singh, A.P.* A Novel Filter “ImpTAHG” for Edge Detection and a Case Study from Cambay Rift Basin, India. // Pure Appl. Geophys. 2022. No.179. Pp. 2351–2364.
2. *Hood P.* Gradient measurements in aeromagnetic surveying // Geophysics. 1965. No.30 (5). Pp. 891–902.
3. *Blokh Yu.I.* Detection and separation of gravitational and magnetic anomalies. Moscow: izdatelstvo MGGA, 2009. 80 p.
4. *Soloviev A.A., Sidorov R.V., Krasnoperov R.I. et al. Klimovskaya:* A new geomagnetic observatory // Geomagnetism and Astronomy. 2016. Vol. 56. No. 3. Pp. 342–354. DOI 10.1134/S0016793216030154.
5. *Kulüke, C., Virgil, C., Stoll, J., Hördt, A.* A new system to measure the gradient vector of the magnetic field on unmanned aerial vehicles — data processing and field experiment // RAS Techniques and Instruments. April 2022. Vol. 1. No. 1. Pp. 65–80.
6. *Aleshin I.M., Solovyov A.A., Aleshin M.I., Sidorov R.V., Solovyova E.N., Kholodkov K.I.* Applications of Light Unmanned Air Vehicle in Geological and Geophysical Research // Nauka i Tekhnologicheskie Razrabotki (Science and Technological Developments), 2019. Vol. 98. No. 3. Pp. 32–48. https://doi.org/10.21455/std2019.3-3
7. *Walter, C., Braun, A., Fotopoulos, G.* High-resolution unmanned aerial vehicle aeromagnetic surveys for mineral exploration targets // Geophysical Prospecting. 2020. No.68. Pp. 334–349.
8. *Chepigo L.S.* GravMagInv. Software Patent RU 2022610137, 10.01.2022

*DOKLADY EARTH SCIENCES, 2025, Vol. 520, No. 1, pp. 118–124*

## GEOPHYSICS

# THICKNESS AND THERMAL STATE OF THE LITHOSPHERIC MANTLE BENEATH THE YUBILEYNAYA PIPE (ALAKIT-MARKHA KIMBERLITE FIELD, SIBERIAN CRATON)

**© 2025 M. V. Milaushkin[a, b, *], V. G. Malkovets[a, b], A. A. Gibsher[a, b], A. M. Dymshits[c, d], I. V. Yakovlev[b], and Academician of RAS N. P. Pokhilenko[a]**

Received June 17, 2024
Revised September 05, 2024
Accepted September 09, 2024

**Abstract.** The paper presents the results of a study on the chemical composition of chromdiopside xenocrystals from the concentrate of the heavy fraction of kimberlites from the Yubileinaya pipe. A reconstruction of the mantle paleogeotherm was achieved through the application of monomineral clinopyroxene geothermobarometry and the FITPLOT program. The palaeogeotherm was found to correspond to a surface heat flux of 34.8 mW/m². The estimated thickness of the lithosphere beneath the Yubileinaya pipe is 230 km, with a diamond window interval of approximately 105 km (from 125 to 230 km). In order to facilitate a comparison of the palaeogeotherm, lithosphere and diamond window thicknesses beneath the Yubileinaya and Udachnaya pipes, the mantle palaeogeotherm beneath the Udachnaya pipe was reconstructed. The resulting values for the heat flux, lithosphere thickness, and diamond window beneath the Udachnaya pipe are 34.7 mW/m², 233 km, and 108 km, respectively. However, the diamondiferous content of the Yubileinaya pipe is approximately two times lower than that of the Udachnaya pipe kimberlites. Consequently, the observed difference in diamondiferousness may be related not only to the thickness of the sampled lithosphere and the diamond window, but also to other petrological parameters, such as the degree of manifestation of diamond-generating and diamond-destructive metasomatism.

**Keywords:** *kimberlite pipe, lithospheric mantle, chromdiopside, paleogeotherm*

**DOI**: 10.31857/S26867397250114e6

## INTRODUCTION

Within the Alakit-Markha Middle Paleozoic kimberlite field (AMKF, Siberian craton) (Fig. 1a) [1], over 100 kimberlite bodies have been discovered, including the diamond-bearing kimberlite pipes Yubileynaya, Komsomolskaya, Sytykanskaya, Aikhal, Zarya and Krasnopresnenskaya (Fig. 1b) [2]. Diamond mining currently takes place at the Yubileynaya, Aikhal and Zarya pipes, the Sytykanskaya and Komsomolskaya pipes have been developed by now, and the Krasnopresnenskaya pipe is classified as a reserve deposit. The Yubileynaya pipe is a unique body in terms of its size; its dimensions are 1293 · 741 m, and its surface area is ~560 000 m². The pipe breaks through a layer of lower Paleozoic subhorizontal rocks of the sedimentary cover, represented by deposits of the Cambrian, lower and middle Ordovician and lower Silurian. The layer overlying the pipe is represented by terrigenous deposits of the upper part of the Carboniferous system and sedimentary deposits of the Lower Permian. The age of the emplacement of the pipe kimberlites was determined by the U–Pb method for perovskite using SHRIMP (356±7 Ma) [3]. The Yubileynaya pipe is a striking example of a typical explosion funnel (central part) and dike-like bodies (on the flanks), forming three isolated "ore bodies" in its structure [4]. The diatreme of the central ore body, as well as the flank bodies, are composed of various proportions of porphyritic kimberlite (PK), autolith kimberlite breccia (AKB) and, less frequently, samples of kimberlite breccia (KB). The central "ore body" is dominated by AKB, and the flanks are composed of PK. The

---

[a] *Sobolev Institute of Geology and Mineralogy, Siberian Branch of the Russian Academy of Sciences, Novosibirsk, Russia*
[b] *PJSC "ALROSA", Novosibirsk, Russia*
[c] *Institute of the Earth's Crust, Siberian Branch of the Russian Academy of Sciences, Irkutsk, Russia*
[d] *Kola Science Centre of the Russian Academy of Sciences, Geological Institute, Apatity, Russia*
**e-mail: milaushkinmv@igm.nsc.ru*

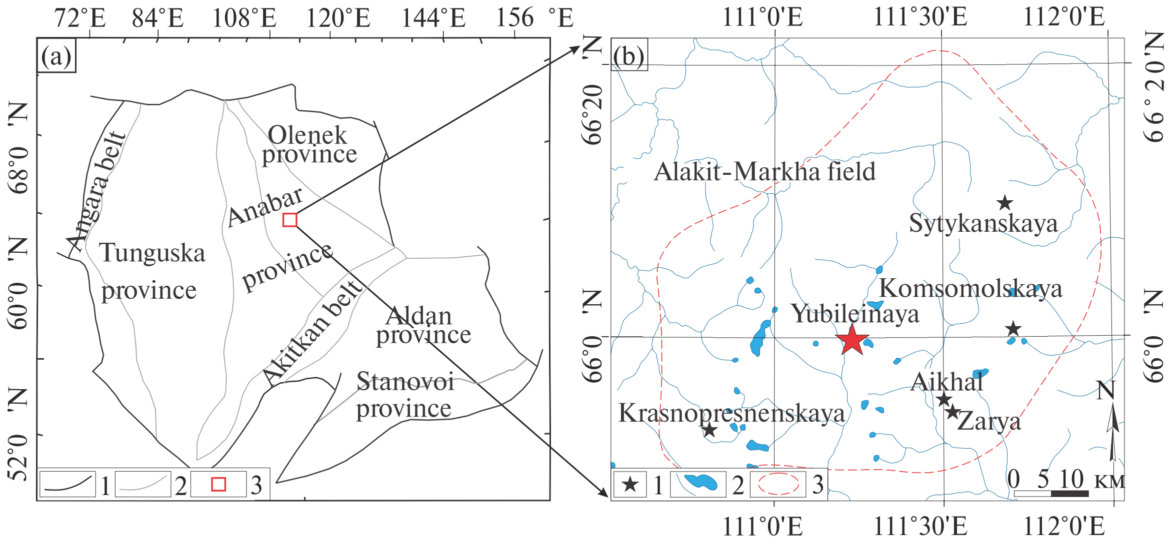

**Fig. 1.** (a) is a schematic map of the Siberian craton [1] with changes; 1 is the boundaries of the craton; 2 is the boundaries of tectonic provinces; 3 is the location of the Alakit–Markha kimberlite field (AMKF) within the craton. (b) is the arrangement of kimberlite bodies in the AMKF [2]; 1 is the primary diamond deposits; 2 is the rivers; 3 is the contour of the AMKF.

diamond content of kimberlites varies; in the rocks that make up the flanks, the diamond content is lower than in the central “ore body”. In general, the diamond content of kimberlites is increased in the three “ore bodies”: 0.89 ct/t [5].

The diamond content of kimberlites depends on many factors, including the thickness of the cratonic lithosphere traversed by kimberlite magma, and the thickness of the sampled “diamond window.” One way to estimate the thickness of the cratonic lithosphere is to determine the depth of intersection of the calculated conductive geotherm with the adiabat of the convecting mantle. The thickness of the “diamond window” is determined by the intersection of the paleogeotherm line with the graphite-diamond line [6] and the line of intersection of the lithosphere-asthenosphere boundary. To determine the thickness of the lithosphere, as well as the thickness of the ‘diamond window,’ the method of the paleogeotherm reconstruction is tradinionally used in combination with mineral geothermobarometry methods using peridotite xenoliths and discrete mineral samples, including clinopyroxenes, garnets, etc. The kimberlites of the Yubileynaya pipe are intensely serpentinized; fresh unaltered xenoliths are absent in the pipe. As a result, calculating the paleogeotherm using traditional techniques of mineral thermobarometry for xenoliths is not possible. However, the heavy mineral concentrate of kimberlites from the Yubileynaya pipe contains garnets and clinopyroxenes of mantle parageneses suitable for calculating *PT*-parameters using single-crystal thermobarometry methods.

In this paper, we present the results of paleotherm reconstruction using single-crystal geothermobarometry for clinopyroxenes [7, 8] from the heavy mineral concentrate of the Yubileinaya pipe. This method allows us to reconstruct mantle paleogeotherms and evaluate the thermal state of the mantle during the period of kimberlite magmatism, as well as the thickness of the subcontinental lithospheric mantle (SCLM) in specific areas of the craton. Estimation of SCLM thickness and the “diamond window” is extremely important both at the early stages of prospecting work for preliminary assessment of the potential diamond content of a particular kimberlite body/field, and for individual blocks/terranes within ancient cratons. The first and only reliable paleotherm estimates for kimberlite bodies of the Alakit-Markha kimberlite field (AMKF) were given in [9] using the method of single-crystal garnet geothermobarometry. To evaluate *PT parameters* in garnets in [9], the Ni-in-Gar geothermometer and Cr-in-Gar geobarometer [10] were used. The reconstructed paleotherm corresponds to typical “cold” cratonic conductive geotherms with a heat flux value of $\sim$35 mW/m$^2$. The lithosphere thickness within the AMKF was 230 km [9]. Single-crystal garnet thermobarometry reliably works only for garnet xenocrysts that were in chemical equilibrium with chromite in the mantle.

In them, the calculated values of *PT parameters* (Ni and Cr in garnet) are suitable for constructing a paleotherm. In turn, single-crystal clinopyroxene thermobarometry works for any garnet-bearing peridotites. The aim of this work is to estimate the paleotherm, lithosphere thickness and "diamond window" beneath the Yubileinaya pipe based on the study of clinopyroxenes from the heavy mineral concentrate of kimberlites.

## MATERIALS AND METHODS

The paper presents the results of a study of 199 chromdiopside grains from the heavy mineral concentrate (HMC) extracted from autolithic kimberlite breccias (AKB) that compose the central ore body and from porphyritic kimberlites (PK) of the western ore body of the Yubileinaya pipe. A total of 150 chromdiopside grains from AKB and 49 grains from PK were studied.

The analysis of the chemical composition of clinopyroxenes was performed by X-ray spectral microanalysis using a JEOL JXA-8100 electron probe microanalyzer at the Center for Collective Use "Multi-element and Isotope Research" of the IGM, SB RAS (Novosibirsk). Samples for analysis were prepared as epoxy resin mounts with embedded mineral grains. The surface of the mounts, polished with diamond pastes, was covered with a conductive carbon coating approximately 25 nm thick. Analytical conditions: accelerating voltage 20 kV, probe current 30–100 nA, probe beam diameter 1–3 µm, spectrum acquisition time at the peak was 10 s for Mg, Ti, Ca, Si, Fe, Mn and 20 s for Na, Cr, K, Al. To avoid Na volatilization during analysis, the probe current for Na analysis was 30 nA. Matrix corrections were calculated using the ZAF method. Certified mineral standards were used as reference materials.

*PT-parameters* of clinopyroxene equilibrium were calculated using the NT00 thermobarometer [7], and the mantle paleogeotherm at the time of kimberlite emplacement ~356 Ma was reconstructed using the FITPLOT program [11]. The following input parameters were used: heat generation value in the mantle – 0 mW/$m^3$ [11], and the temperature of the mantle adiabat at the surface 1315°C [11]. The values used for the thickness of the upper (UC) and lower crust (LC) were adopted from [12] – 12 km and 29 km, respectively. Heat generation in the UC is 0.76 µW/$m^3$, and in the LC – 0.36 µW/$m^3$ according to [13].

## RESULTS

NT00 *PT*-calculation [7] is applicable only to clinopyroxenes from garnet peridotites. To identify clinopyroxenes from garnet peridotites, a classification diagram [14] based on $Cr_2O_3$ and $Al_2O_3$ content in chromdiopsides was used. Based on this diagram, 174 grains (87.4%) were identified as clinopyroxenes from cratonic garnet peridotites, and thus are suitable for *PT* calculations using this method (Fig. 2). Thirteen grains (6.5%) contain less than 0.5 wt. % $Cr_2O_3$ and belong to eclogites, megacrysts and cognate clinopyroxenes; twelve grains (6%) fall into the field of spinel peridotites and off-craton garnet peridotites (Fig. 2).

To reject clinopyroxenes that are not in equilibrium with garnet and orthopyroxene under mantle conditions, as well as grains that have been significantly metasomatized, the filters proposed in [7, 8] were used. After applying the filters, 111 clinopyroxene analyses were excluded from the *PT*-calculation procedure. The remaining 63 filtered grains (Fig. 2) were identified as chromdiopsides with variations in composition: Ca#=100·Ca/(Ca+Mg+Fe)=32–49; Mg#=100·Mg/(Mg+Fe) = 88–96; $Cr_2O_3$ = 0.5–4.4 wt. %, $Na_2O$ = 0.9–4% wt. %.

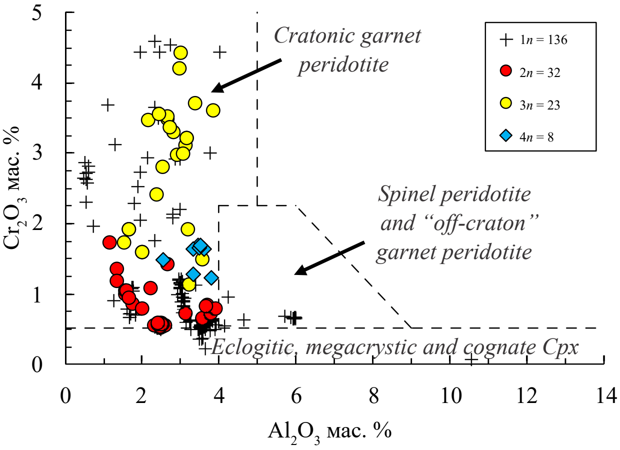

**Fig. 2.** Discriminatory diagram of $Cr_2O_3$-$Al_2O_3$ [14] and composition of studied clinopyroxenes from the Yubileynaya pipe. 1 – chromdiopsides that did not pass the selection filters [7, 8] (111 grains) as well as chromdiopsides from the field of eclogites, megacrysts and cognate clinopyroxenes (13 grains) and chromdiopsides from the field of spinel peridotites and "off-craton" garnet peridotites (12 grains). 2 – high-temperature chromdiopsides with values T > 1200°C (32 grains) (see Fig. 3a). 3 – chromdiopsides with T values from 700 to 1200°C (23 grains). 4 – low-temperature chromdiopsides with P values < 30 kbar (8 grains).

Using the NT00 thermobarometer for 63 chromdiopsides, the calculated temperatures range from 725 to 1369 °C, and the pressure values range from 20 to 69 kbar. Using the obtained *PT*-parameters, the paleogeotherm beneath the Yubileynaya pipe was reconstructed using the FITPLOT program. The resulting surface heat flux was 35.5 mW/m$^2$, with a lithospheric thickness of 218 km and a diamond window thickness of 93 km. The thickness of the "diamond window", determined by the "Y-edge" in garnets according to [9], is 65 km (from 125 to ~190 km) (Fig. 3a).

At the depths from 167 to 213 km beneath the Yubileinaya pipe (Fig. 3a), a group of high-temperature points (red circles) with calculated temperatures > 1200°C is identified. This phenomenon is related either to the specifics of the

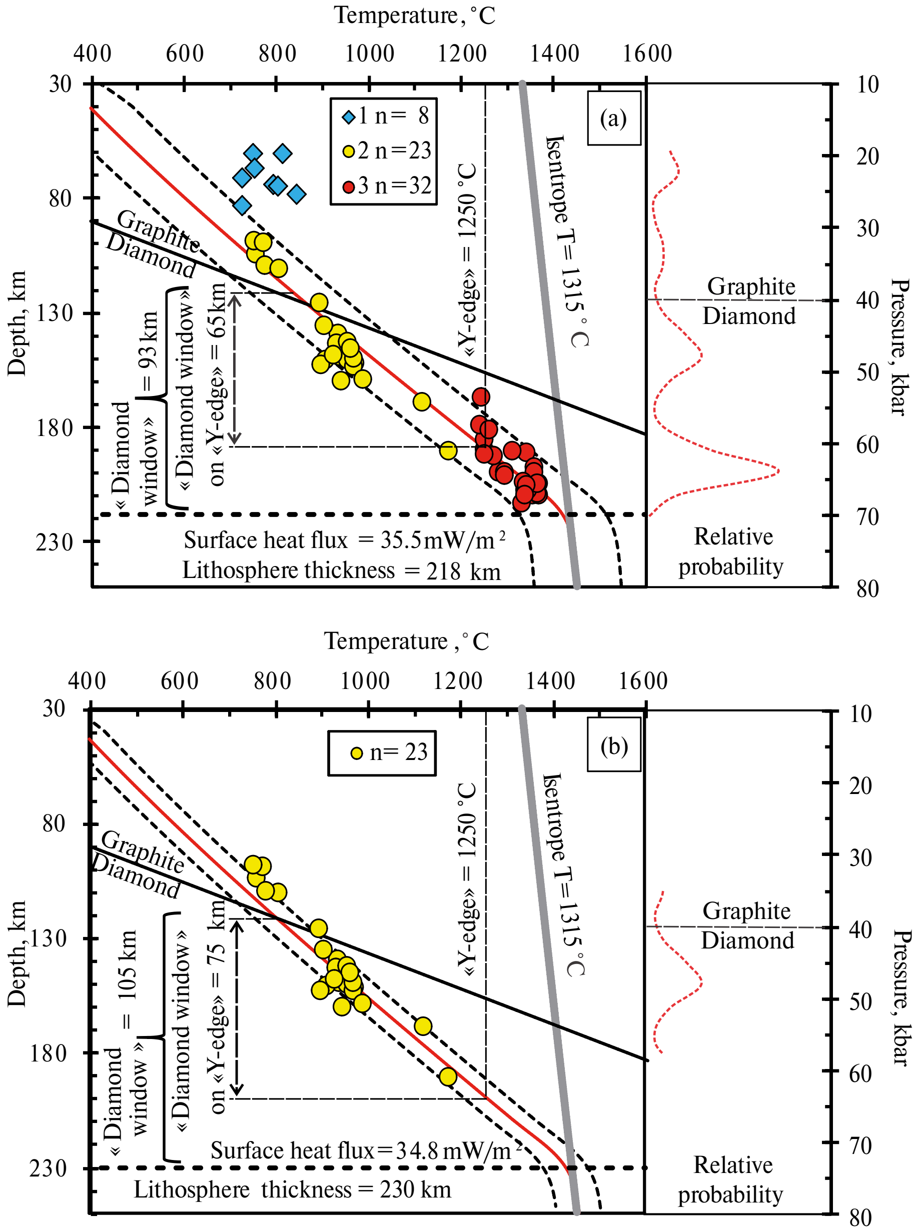

**Fig. 3.** Reconstructed paleogeotherm beneath the Yubileynaya pipe. a) – paleogeotherm reconstructed from 63 chromdiopsides, heat flux 35.5 mW/m$^2$, lithosphere thickness 218 km, "diamond window" thickness 93 km; b) – paleogeotherm reconstructed from 23 chromdiopsides, heat flux 34.8 mW/m$^2$, lithosphere thickness 230 km, "diamond window" thickness 105 km. "Diamond window" thickness by "Y-edge" [9] – 65 km (a) and 75 km (b). Dotted lines – error of geotherm reconstruction. 1 – low-temperature chromdiopsides with P values < 30 kbar (8 grains), 2 – chromdiopsides with T values from 700 to 1200°C (23 grains), 3 – high-temperature chromdiopsides with T values >1200°C (32 grains). Red dotted line – distribution of chromdiopsides by depth.

NT00 thermobarometer, as experimental data used for barometer calibration [7] were obtained only up to 60 kbar [7,8], or to the local thermal impact of the asthenosphere on the deep part of the lithospheric mantle [15, 16]. It is believed that high-temperature chromdiopsides may represent secondarily enriched rocks that have been affected by asthenospheric melts [15]. The presence of such clinopyroxenes may be associated with rock deformation and formation of so-called sheared peridotites. We tend toward the second option, therefore high-temperature chromdiopsides were excluded from further constructions, as their *PT-parameters* overestimate the heat flux value, underestimate the lithospheric thickness, and do not relate to the position of the conductive paleogeotherm at the time of kimberlite magmatism.

Among 63 chromdiopsides, there are eight grains with low pressure parameters (20–27 kbar) and temperatures from 725 to 846°C. (Fig. 3a, diamonds). It is possible that these shallow chromdiopsides do not characterize the original properties of the lithospheric mantle [15]. Apparently, these chromediopsides originate from a horizon where upwelling melts stop for a sufficiently long time and react with the colder lithosphere, forming texturally equilibrated coarse-grained hybrid rocks before the eruption of their host kimberlite [16]. Therefore, these chromdiopsides were also excluded from the paleogeotherm construction procedure.

Equilibrium temperature values of the remaining 23 chromdiopsides grains vary from 752 to 1175°C, and pressure values from 32 kbar to 62 kbar, which corresponds to depths of ~100–194 km. The resulting heat flux was 34.8 mW/m$^2$ , and the thicknesses of the lithosphere and the “diamond window” were 230 km and 105 km, respectively (Fig. 3b), the thickness of the “diamond window” determined by the “Y-edge” in garnets according to [9] is 75 km (from 125 to 200 km). Thus, the paleogeotherm reconstructed from the *PT-parameters* of 23 chromdiopsides represents the middle part of the section, with the coldest heat flux [16, 15], which most likely reflects a stable conductive geotherm not subjected to heating by mantle melts [16, 17].

## DISCUSSION

The reconstructed paleogeotherm beneath the Yubileynaya pipe is characterized by a cold heat flux of 34.8 mW/m$^2$ , which correlates with the previously calculated paleogeotherm for the Yubileynaya pipe based on chrome-rich peridotitic garnets [9]. The obtained data indicate the existence of a thick cold lithosphere beneath the Yubileynaya pipe at the time of kimberlite magma emplacement.

For the AMKP field, there is little data because mantle xenoliths found on the surface of kimberlite pipes are highly altered; however, in the neighboring Daldyn field, there is the Udachnaya pipe, which contains many fresh unaltered xenoliths and for which a large number of studies have been conducted. For the Udachnaya pipe, papers [16–18] present the results of mantle xenolith studies, as well as *PT-parameters* calculated for these xenoliths using various thermobarometers. In [16], *PT- estimates* of chromdiopsides from Udachnaya pipe xenoliths are presented, including those based on the single-crystal clinopyroxene thermobarometer NT00. We used the *PT- estimates* of clinopyroxenes provided in [16] for reconstructing the paleogeotherm beneath the Udachnaya pipe in order to compare the paleogeotherm, lithosphere and “diamond window” thicknesses beneath the Yubileynaya and Udachnaya pipes. The studied xenoliths from the Udachnaya pipe [16-18] are represented by coarse-grained peridotites (Fig. 4, green circles), as well as transitional and sheared peridotites (Fig. 4, red circles). Transitional and sheared peridotites are characterized by high equilibrium temperatures (> 1200°C), which may be associated with local thermal effects of the asthenosphere on the deep part of the lithospheric mantle. For paleogeotherm reconstruction, only chromdiopsides from xenoliths where clinopyroxene is in equilibrium with orthopyroxene and garnet were used [16]. The same values of heat generation and thickness of the upper and lower crust as for the Yubileynaya pipe were used. The resulting surface heat flux for the Udachnaya pipe was 35.1 mW/m$^2$, with a lithosphere thickness of 224 km, and a “diamond window” thickness of 99 km (Fig. 4). Due to high equilibrium temperatures, we excluded chromdiopsides from transitional and sheared peridotites and used only chromdiopsides from coarse-grained peridotites. As a result, the heat flux was 34.7 mW/m$^2$, lithosphere thickness 233 km, “diamond window” thickness 108 km, and the “diamond window” thickness determined by the “Y-edge” in garnets according to [9] is 70 km (from 125 to 195 km) (Fig. 4).

The obtained results indicate that the paleogeotherms of the Yubileynaya and Udachnaya pipes are characterized by similar values of heat flux, as well as lithosphere thickness and “diamond

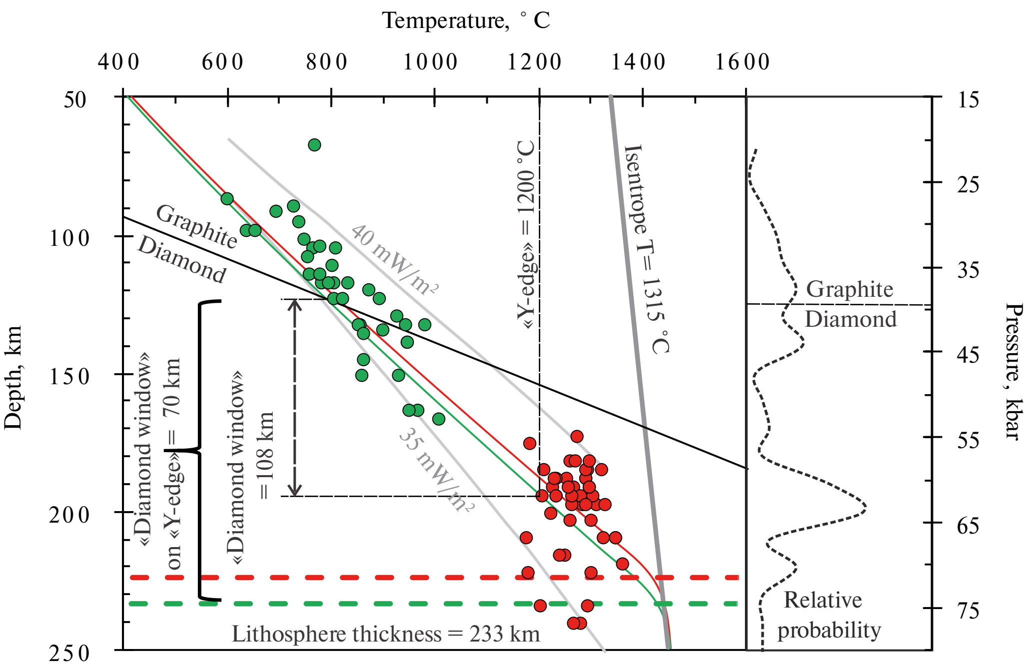

**Fig. 4.** Reconstructed paleogeotherm beneath the Udachnaya pipe (Daldyn field). *PT* -estimates from [16]. Red circles – transitional and cataclased peridotites, green circles — coarse-grained peridotites. Red solid line — paleogeotherm reconstructed from chrome diopsides from transitional, cataclased, and coarse-grained peridotites. Heat flow – 35.1 mW/m$^2$, lithosphere thickness 224 km, "diamond window" thickness 99 km. Green solid line – paleogeotherm reconstructed from chrome diopsides only from coarse-grained peridotites. Heat flow – 34.7 mW/m$^2$ , lithosphere thickness 233 km, "diamond window" thickness 108 km, the thickness of the "diamond window" determined by the "Y-edge" in garnets according to [9] is 70 km. Red and green dashed lines — asthenosphere-lithosphere boundary. Black dashed line — distribution of clinopyroxenes by depth. Model conductive geotherms from [20].

window" thickness. However, the diamond content of kimberlites in the Udachnaya pipe differs significantly from the Yubileynaya pipe – 1.47 c/t and 0.89 c/t [5], respectively. Consequently, the difference in diamond content may be associated not only with the thickness of the sampled lithosphere but also with other petrological parameters, such as the degree of manifestation of diamond-generating and diamond-destructive metasomatism [19]. The work [9] provides data on the abundance of harzburgite garnets under the pipes of the AMKP and Daldyn field. According to [9], within the AMKP in the depth range of 105–205 km, the proportion of harzburgite garnets among peridotite associations exceeds 30%. Within the Daldyn field, the proportion of harzburgite garnets also exceeds 30%, but in the depth interval from 145 km to 210 km. Such differences in garnet distribution indicate that the nature of metasomatic transformations of lithospheric mantle peridotites is unique beneath individual kimberlite pipes. Apparently, the mantle section beneath the Udachnaya pipe contains a higher proportion of harzburgite-dunite garnets than the mantle section beneath the Yubileynaya pipe.

It should be noted that the mantle paleogeotherm beneath the Yubileynaya pipe using the FITPLOT program was reconstructed for the first time. This study provides valuable data on the lithospheric mantle beneath the Yubileynaya pipe, including mantle composition, thermal state, and thickness. Further studies of mineral compositions, such as garnet, chrome spinel, ilmenite, as well as the use of a wider range of geothermobarometers and consideration of additional parameters, for example, seismic data, can expand our understanding of the structure and evolution of the lithosphere in the studied region.

## FUNDING

The research was carried out with the support of RSF grant 22-27-00724.

## ACKNOWLEDGEMENTS

The authors are grateful to ALROSA PJSC for providing clinopyroxene grains from the heavy fraction concentrate of kimberlites from the

Yubileynaya pipe and for kindly permitting the publication of the results of this research.

## CONFLICT OF INTEREST

The authors declare that they have no conflict of interest.

## REFERENCES

1. *Rozen O.M., Manakov A.V., Suvorov V.D.* Collision system of the northeastern Siberian craton and the problem of the diamond-bearing lithospheric keel // Geotectonics. 2005. No. 6. Pp. 42–67.
2. *Kostrovitsky S.I. et al.* Atlas of primary diamond deposits of the Yakutian kimberlite province. 2015.
3. *Lepekhina E., et al.* SHRIMP U-Pb zircon ages of Yakutian kimberlite pipes / International Kimberlite Conference: Extended Abstracts. 2008. V. 9.
4. *Kharkiv A.D., Zinchuk N.N., Kryuchkov A.I.* Primary diamond deposits of the world. 1998. https://www.rudmet.ru/media/docs/3_20_diamond.pdf
5. *Kennedy C.S., Kennedy G.C.* The equilibrium boundary between graphite and diamond // Journal of Geophysical Research. 1976. V. 81. No. 14. Pp. 2467–2470.
6. *Nimis P., Taylor W.* Single Clinopyroxene Thermobarometry for Garnet Peridotites. Part I. Calibration and Testing of a Cr-in-Cpx Barometer and an Enstatite-in-Cpx Thermometer // Contributions to Mineralogy and Petrology. 2000. V. 139. Pp. 541–554.
7. *Ziberna L., et al.* Error sources in single-clinopyroxene thermobarometry and a mantle geotherm for the Novinka kimberlite, Yakutia // American Mineralogist. 2016. V. 101. No. 10. P. 2222–2232.
8. *Griffin W.L., et al.* The Siberian lithosphere traverse: mantle terranes and the assembly of the Siberian Craton //Tectonophysics. 1999. V. 310. No. 1–4. Pp. 1–35.
9. *Ryan C.G., Griffin W.L., Pearson N.J.* Garnet geotherms: Pressure-temperature data from Cr-pyrope garnet xenocrysts in volcanic rocks // Journal of Geophysical Research: Solid Earth. 1996. V. 101. No. B3. Pp. 5611–5625.
10. *Mather K.A., et al.* Constraints on the depth and thermal history of cratonic lithosphere from peridotite xenoliths, xenocrysts and seismology // Lithos. 2011. V. 125. No. 1–2. Pp. 729–742.
11. *Manakov A.V.* Features of the lithosphere structure of the Yakutian kimberlite province. – 1999.
12. *Rozen O.M., Soloviev A.V., Zhuravlev D.Z.* Thermal evolution of the northeastern Siberian platform in light of dating core deep drilling by apatite fission tracks // Izvestiya. Physics of the Solid Earth. 2009. V. 45. Pp. 914–931.
13. *Ramsay R.R., Tompkins L.A.* The geology, heavy mineral concentrate mineralogy, and diamond propectivity of the Boa Esperanca and Cana Verde pipes, Corrego D'anta, Minas Gerais, Brasil / The geology, heavy mineral concentrate mineralogy, and diamond propectivity of the Boa Esperanca and Cana Verde pipes, Corrego D'anta, Minas Gerais, Brasil. – Companhia de Pesquisa de Recursos Minerais, Special Publication, 1994. Pp. 329–345.
14. *Tychkov N.S. et al.* Mesozoic lithospheric shell of the northeastern Siberian craton (based on inclusions in kimberlites) // Geology and Geophysics. 2018. V. 59. No. 10. Pp. 1254–1270.
15. *Liu Z., et al.* Thermal and compositional anomalies in a detailed xenolith-based lithospheric mantle profile of the Siberian craton and the origin of seismic midlithosphere discontinuities // Geology. 2022. V. 50. No. 8. Pp. 891–896.
16. *Ionov D.A., Doucet L.S., Ashchepkov I.V.* Composition of the lithospheric mantle in the Siberian craton: new constraints from fresh peridotites in the Udachnaya-East kimberlite // Journal of petrology. 2010. V. 51. No. 11. Pp. 2177–2210.
17. *Doucet L.S., Ionov D.A., Golovin A.V.* The origin of coarse garnet peridotites in cratonic lithosphere: new data on xenoliths from the Udachnaya kimberlite, central Siberia // Contributions to Mineralogy and Petrology. 2013. V. 165. Pp. 1225–1242.
18. *Malkovets V.G., et al.* Diamond, subcalcic garnet, and mantle metasomatism: Kimberlite sampling patterns define the link // Geology. 2007. V. 35. No. 4. P. 339–342.
19. *Hasterok D., Chapman D.S.* Heat production and geotherms for the continental lithosphere // Earth and Planetary Science Letters. 2011. V. 307. No. 1–2. Pp. 59–70.

*DOKLADY EARTH SCIENCES, 2025, Vol. 520, No. 1, pp. 125–134*

**OCEANOLOGY**

# WATER MASS-STRUCTURE AND VARIABILITY OF THE KANE GAP IN THE EQUATORIAL ATLANTIC OCEAN

**© 2025 A. N. Demidov[a], *, K. V. Artamonova[a], [b], S. B. Krasheninnikova[a], [c], and Academician of RAS S. A. Dobrolubov[a]**

Received June 29, 2024
Revised September 04, 2024
Accepted September 09, 2024

**Abstract.** The results of a study of the water mass structure in a poorly studied area of the eastern basin of the Tropical Atlantic (Kane Gap) according to data from the 63rd cruise of P/V «Akademik Ioffe» in 2022 are presented in the paper. Variability of the average monthly characteristics of these waters using the GLORYS12v1 reanalysis for 1993–2022 is shown. Intermediate waters in the section are represented by a mixture of Antarctic intermediate water (AAIW) and Mediterranean water (the share of the latter reaches 34%). It has been established that the North Atlantic Deep Water (NADW) is represented by two layers: the Upper NADW with a maximum of salinity and the Middle NADW with a maximum of oxygen. The bottom water layer contains a mixture of Antarctic Bottom Water (AABW), the Lower and Middle components of the NADW. This mixture, coming primarily from the Vema Fracture zone region, is properly to call Northeast Atlantic Bottom Water (NEABW). Its upper limit corresponded to the isotherm of 1.95°C and the Si/P ratio equal to 33. In this work, using the conservative PO, the proportion of AABW in NEABW, which is about 20%, was calculated. According to the GLORYS12v1 on a seasonal scale in the bottom layer, a significant negative relationship was established between the variability of potential temperature and the meridional speed of currents. Significant trend for an increase in the average annual potential temperature (by 0.06 °C) and a decrease in salinity (by 0.005 psu) in general for the period 1993–2022 was revealed.

**Keywords:** *water masses, physical and hydrochemical properties, PO, North Atlantic Deep Water, Antarctic Bottom Water, interannual variability, ocean reanalysis*

**DOI**: 10.31857/S26867397250115e3

## INTRODUCTION

The mechanisms of interaction and transformation of water masses spreading through oceanic straits and passages are a poorly understood problem of modern oceanology, which, due to the complex underwater relief and the incompleteness of available field observation data, is inadequately resolved even by ocean reanalysis. There is very little deep-sea expeditionary research in the eastern part of the tropical Atlantic. The proposed paper presents the results of an analysis of the water structure performed on an oceanological section along the deep-sea Kane Gap connecting parts of the Cape Verde and Sierra Leone basins between the Grimaldi Mountains and the continental slope of the African continent (Fig. 1). The study area was located near the research vessel Akademik Ioffe section, 2000 [1], and the A06 WOCE latitudinal section, made along 7.5° n in 1993 and 2000.

The analysis of water masses and water circulation in the equatorial Atlantic is presented in [2-4]. However, there is still a lot of uncertainty about the structure of deep and bottom waters. Thus, the number of isolated components of the North Atlantic Deep Waters (NADW) and their boundaries, as well as the sources of their formation, differ from one author to another [5, 6]. It was shown in [3, 7] that there is no spread of NADW as a whole: each component carries the characteristics of the water masses from which it originates, and all components have different distribution paths, interact with waters of different characteristics, and eventually form their own unique features. This explains the discrepancy in the vertical position of the extremes of various

---

[a] *Lomonosov Moscow State University, Faculty of Geography, Moscow, Russia*
[b] *Russian Federal Research Institute of Fisheries and Oceanography, Moscow, Russia*
[c] *A.O. Kovalevsky Institute of Biology of the Southern Seas, Russian Academy of Sciences, Sevastopol, Russia*
**e-mail: tuda@mail.ru*

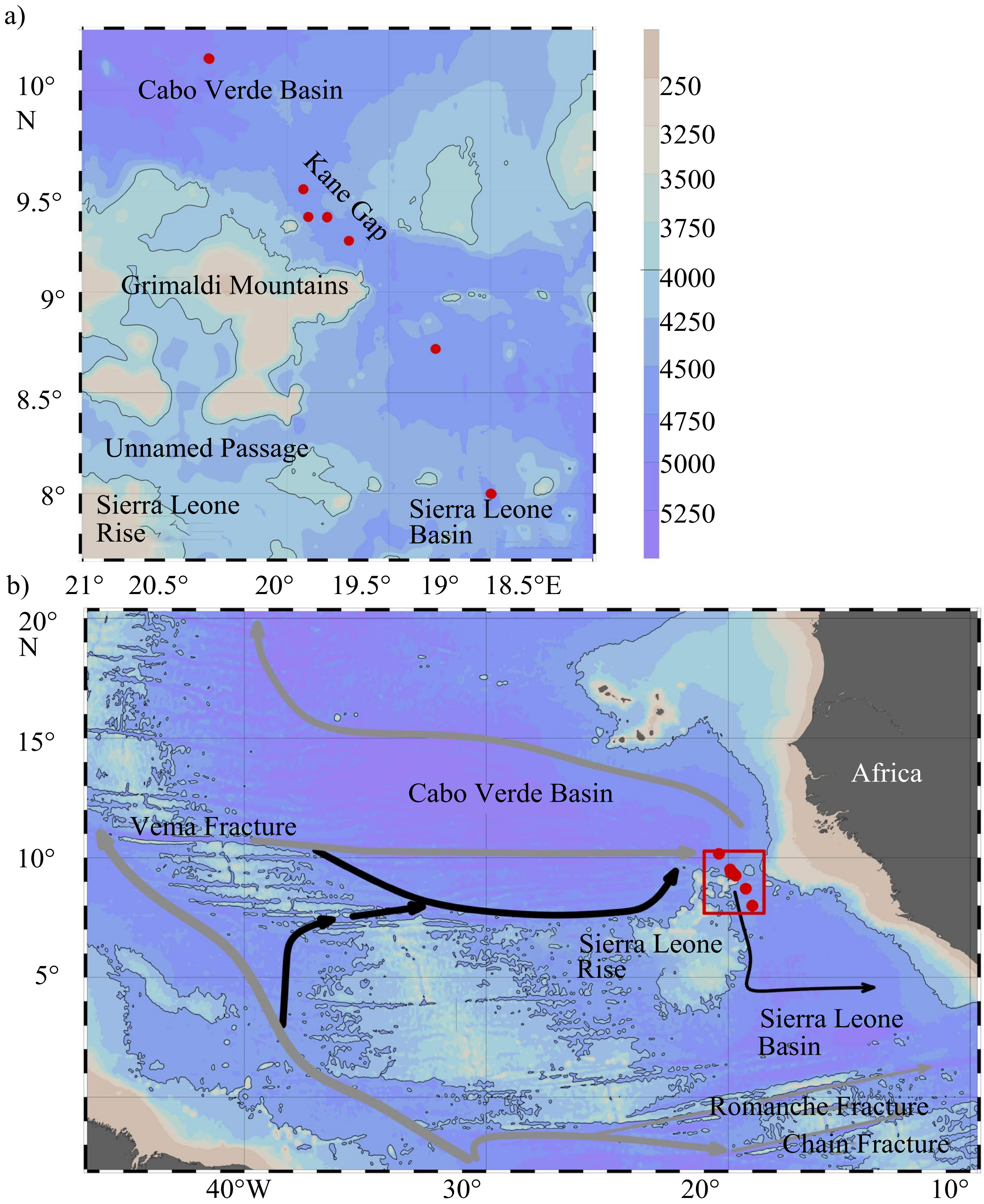

**Fig. 1.** Position of stations in the 63rd cruise of R/V "Akademik Ioffe" (AI-63) in the Kane Gap. a – Schematic map of the Kane Gap, red dots – station positions. b – Schematic map of the research area with bottom water circulation scheme. The red square shows the research area, and dots – station positions, gray arrows show the circulation scheme of Antarctic Bottom Water (AABW) and North East Atlantic Deep Water (NEADW) according to [9, 7] for the Cape Verde Basin. Black arrows – the path of NEADW to the research area, reconstructed using GLORYS12v1 reanalysis.

characteristics inherent in the same water mass, but the differences between the components themselves are not so significant as to distinguish them as independent water masses. In the classic work [5] it is shown that in the North Atlantic deep water layer three layers should be distinguished: the Upper NADW, the source of which is the Mediterranean waters [5, 2], the Middle NADW, which originate from the Labrador Waters (LW) [6], and the Lower NADW, the main source of which is the waters of the Denmark Strait [5, 6]. Sometimes NADW is divided into four components [6], where the middle NADW is divided into two layers with minimum and maximum oxygen, respectively. In this case, the NADW components in later works are already represented as a mixture of Mediterranean, Labrador, Iceland-Shetland waters, Danish Strait waters, and Antarctic Bottom Waters (AABW) in different proportions [6, 2]. And for the bottom waters of the eastern part of the Tropical Atlantic, which come mainly through the Vema Fracture Zone and differ in their characteristics from the waters coming through the Romanche and Chain Fracture Zones [7], there is still no unified name in the literature.

The study of intra-annual variability of current velocities and potential temperature in the Kane Gap was previously conducted using recorders over a year [8]. Harmonics were identified and a connection between positive temperature anomalies and currents of the southeast direction was established. But on a climatic scale, information about changes in characteristics in this passage still does not exist in the literature.

In this regard, the purpose of this work is to analyze the water structure and its variability on interannual scales in the poorly studied area of the Kane Gap based on our own data and reanalysis.

## MATERIALS AND METHODS

*Description of measurement data.* The work used data obtained during the 63rd cruise of the R/V "Akademik Ioffe" from 09.29.2022 to 12.10.2022 along a longitudinal section passing through the Kane Gap (hereinafter AI-63). Measurements in the Kane Gap itself were carried out on October 19-21, 2022.

Hydrological measurements during the cruise were conducted using a high-precision CTD probe from the surface to the bottom. Water samples were collected using 10-liter Niskin bottles mounted on the sounding complex. Hydrochemical analysis included determination of dissolved oxygen content and concentrations of nutrients (phosphates, nitrites, nitrates, silicates). Water samples were processed immediately after collection in the ship's laboratory, according to standard methods [10].

Additionally, the quasi-conservative hydrochemical indicator PO proposed in [11] was calculated:

$$PO = 135[PO_4] + O_2, \tag{1}$$

where $PO_4$ and $O_2$ are the measured concentrations of phosphates and dissolved oxygen in μM/kg.

In this work, the percentage content of water masses, for the case of mixing two water masses, was calculated as:

$$f_{WM1} = |(PO - PO_1)/(PO_2 - PO_1)| * 100\%. \tag{2}$$

For the case of mixing three water masses, a system of linear equations was composed using formulas similar to (2):

$$\begin{cases} f_{WM1} = |(PO - PO_1)/(PO_2 - PO_1)| * 100\%/3 \\ f_{WM2} = |(PO - PO_2)/(PO_3 - PO_2)| * 100\%/3, \\ f_{WM3} = |(PO - PO_3)/(PO_1 - PO_3)| * 100\%/3 \end{cases} \tag{3}$$

where PO is the calculated concentration (using formula 1) based on measured concentrations of phosphates and dissolved oxygen; $PO_1$, $PO_2$, and $PO_3$ are the PO values in the water mass sources, calculated using the original values from [4].

For intermediate and deep waters, the proportion of each water in the mixture was calculated using the PO indicator. In the layer below 500 m, Antarctic Intermediate, Mediterranean Labrador Sea, Iceland-Shetland Overflow, and Antarctic Bottom Waters (AAIW, MW, LSW, ISOW, and AABW, respectively) were considered. Restrictions were placed on the presence of certain waters in the mixture below and above the core of adjacent waters based on structural features, so that the maximum number of waters in the mixture was three. Thus, in the 500–1200 m layer, a mixture of AAIW and MW was considered; in the 1200–2000 m layer, LSW was added to them. In the deep water layer of 2000–3500 m, the proportions of MW, LSW, and ISDW were estimated, and in the bottom layer – a mixture of NADW and AABW.

For the analysis of hydrological characteristics and description of their variability on seasonal and interannual scales in the Kane Gap of the Tropical Atlantic, the GLORYS12v1 reanalysis with a grid step of 1/12° for the period 1993–2022 was used, and temperature, salinity, and current velocity components at the bottom horizon of 4405 m were analyzed in the coordinates of the passage.

From the initial series of monthly mean values of the GLORYS12v1 reanalysis, the linear trend was subtracted and spectral analysis was performed. The resulting detrended series were represented as a set of harmonic functions with different periods and amplitudes using fast Fourier transform. The original series of interannual values of the analyzed parameters were first transformed into series multiple of $2^N$ , with $N = 10$. The resulting series of transformed data were tested for normality using the Kolmogorov-Smirnov criterion (>0.05). Periodograms were then analyzed and periods making the largest contribution to the total variance of the original series were identified. The corresponding periods (0.5–1, 2–4, 10–30 years) were isolated using a Hamming band-pass window filter. Correlation analysis was applied to the original and filtered series. The significance of the obtained results was evaluated using Student's t-test. For monthly characteristics, significant correlations at the 5% confidence interval ranged from –0.3 to 0.3. The significance of long-term trends in the original series of monthly and annual mean current velocities, as well as ~~and~~ potential water temperature for 1993–2022 was evaluated using the Mann-Kendall test.

## RESULTS

*Water structure in the Kane Gap.* The Kane Gap area is characterized by a water structure typical for the eastern part of the Tropical Atlantic. On the AI-63 section in the Kane Gap, we identified the following water masses (Fig. 2).

Surface waters were represented by the upper quasi-homogeneous layer (up to a depth of 30 m), in which temperature varied from 28 to 29°C, dissolved oxygen content ranged within 200–203 μM/kg , and its percentage saturation throughout the entire layer was more than 100%. This layer was also characterized by low concentrations of nutrients.

Below the upper mixed layer were the Central Waters (CW), in which accumulation of nutrients occurred with active consumption of dissolved oxygen. At a depth of 350-450 m, the content of dissolved oxygen sharply decreased, reaching its minimum (40–60 μM/kg ), while the concentrations of nutrients, on the contrary, sharply increased and in the core – oxygen minimum varied within the following ranges: phosphates – 1.8–2.0 μM /kg ; silicates – 14–26 μM /kg ; nitrates – 31–34 μM /kg. The lower boundary of these waters can be considered the position of the oxygen minimum at a depth of 400–460 m.

Below the CW, in the layer of 500-1050 m, there were intermediate waters, mainly represented by the Antarctic Intermediate Water mass (AAIW), with a core: salinity minimum (about 34.7 psu) at a depth of 800–900 m. The lower boundary of AAIW is close to the isotherm $\theta = 5°C$ and was located at a depth of 1050 m. AAIW was characterized by a low content of dissolved oxygen (110–120 μM/kg), as well as a maximum of nutrients, reaching very high concentrations in the core: phosphates up to 2.24 μM /kg , nitrates up to 34 μM /kg ; silicates up to 30 μM /kg (Fig. 2). In the lower layer of AAIW, according to our calculations, there is a significant proportion of Mediterranean waters from 17 to 26%.

Below the intermediate layer was the complex of North Atlantic Deep Waters (NADW), represented in the Kane Gap by the upper and middle components. The Upper North Atlantic Deep Water mass (UNADW) was distinguished on the section by a maximum salinity (more than 34.97 psu) and by a minimum of silicates (21–35 μM/kg) in the layer of 1050–2700 m. For UNADW, minimums were observed in the distribution of phosphates (1.33–1.40 μM/kg) and nitrates (19–21 μM/kg). The lower boundary of these waters, calculated by the maximum vertical gradients of hydrological and hydrochemical characteristics [12], was close to the isotherm $\theta = 2.7°C$. In addition, UNADW was characterized by an increase with depth in the concentration of dissolved oxygen, its content increased from the upper boundary of UNADW (230 μM/kg) to the lower (248 μM/kg), respectively. We suggest that in the area of the Kane Gap, UNADW is represented by a mixture of Labrador, Antarctic Intermediate, and Mediterranean waters. According to our calculations using formula (2), the proportion of Labrador waters was about 30% (with a maximum in the 2500–2700 m layer), Antarctic waters 24–50% (near the upper boundary), and Mediterranean waters – 10–34%. Due to the Mediterranean waters, this layer was characterized by a salinity maximum, with their main portion concentrated in the 1000-2000 m layer.

As noted above, for the underlying NADW, there is still no clear understanding in the global literature about the number of components and their origin, as the positions of extremes of various characteristics do not coincide in depth. In Table 1, we provide previously available information about the sources

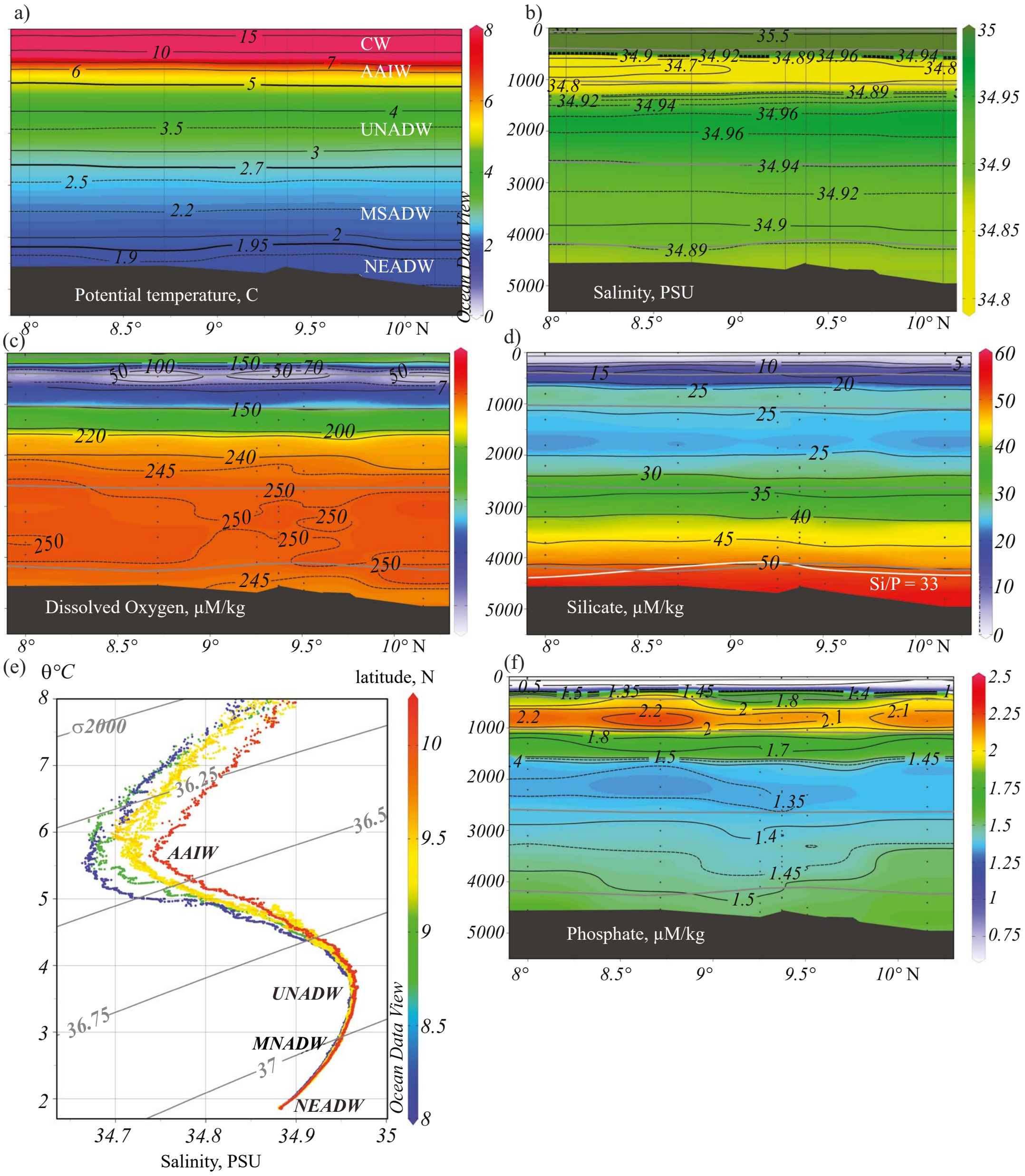

**Fig. 2.** Distributions of potential temperature, ˚C (a), salinity, psu (b), dissolved oxygen content, µM /kg (c), silicates, µM /kg (d), θ,S-diagram (e), and phosphate content, µM /kg (f) at the AI63 section in the Kane Gap and gray lines show the boundaries of water masses, white line on (d) – position of Si/P=33.

of deep water components in this area compared with the results obtained in this work.

In the section at the 2700–4100 m layer, middle NADW (MNADW) were identified by the maximum of dissolved oxygen (245–249 µM/kg). These waters with elevated oxygen values possibly come to the study area from the west. We assume that in the Kane Gap area, there is a transformation of waters, mainly represented by a mixture of Iceland-Scotland and Labrador waters (proportions 40–70% and 30–40% respectively), to which, after passing through fractures in the Mid-Atlantic Ridge (MAR) at 5–11°N in the Cape Verde Basin, strongly transformed deep waters with low oxygen content are added. This minimum is formed in the area of the African continental slope as a result of mineralization of large amounts of organic matter in the Canary upwelling zone [14].

The bottom layer in the study area was occupied by the North-East Atlantic Deep Water (NEADW). Variants of the name and boundary of NEADW in comparison with previous works are presented

**Table 1.** Components of deep water in the tropical part of the Atlantic according to different authors.

| | Wust 1935 [5] | Tsuchiya et al., 1992* | Rhein et al, 1995 [6] | Schmitz, 1996* | Andrie et al. 1998 [2] | Liu, Tanhua, 2019 [4] | de Carvalho Ferreira, Kerr, 2017 [13] | Present work |
|---|---|---|---|---|---|---|---|---|
| UNADW | MW | MW + LSW | upper LSW | LSW + MW | LSW | ISOW + LSW | | LSW, AAIW, MW |
| MNADW | LSW | ISOW + EBW + DSOW | LSW<br>CGFZW | ISOW + AABW | CW + LSW + ISOW | ISOW + DSOW + (LSW) | LSW + DSOW + ISOW + (MW) | ISOW, LSW, NEADW |
| LNADW (western part) | DSOW | AABW + DSOW | DSOW | DSOW + AABW | DSOW | | DSOW+ WSDW | CGFZW, AABW, DSOW |

Note. AAIW – Antarctic Intermediate Water, MW – Mediterranean Water, LSW – Labrador Sea Water, ISOW – Iceland-Scotland Overflow Water, lCGFZW – Charlie-Gibbs Fracture Zone, DSOW – Denmark Strait Overflow Water, WSDW – Weddell Sea Deep Water, AABW – Antarctic Bottom Water, EBW – Eastern Basin Water, NEADW – Northeast Atlantic Water. Parentheses indicate a minor amount of water in the mixture. Results marked with an asterisk (*) are taken from reference [7].

in Table 2. These waters on the section were characterized by minimums of potential temperature (1.85–1.95°C) and salinity (less than 34.88 psu), lower dissolved oxygen content (241–245 μM/kg), as well as higher concentrations of silicates (50–56 μM/kg), phosphates (1.5–1.62 μM/kg) and nitrates (20–22 μM/kg) than the overlying NADW. NEADW is likely a mixture of UNADW, LNADW and AABW, interacting as they pass through fractures in the MAR. These waters flow with a deep current from the Vema Fracture Zone into the Cape Verde Basin and differ in their characteristics from the waters flowing through the Romanche and Chain Fracture Zones (see Fig.1). Moreover, according to the reanalysis, the transfer is not directed straight from the Vema Fracture Zone, as was previously thought [9], but zonally along the southern tip of the basin. In the Kane Gap area, NEADW interacts with local deep waters with low dissolved oxygen content and high concentrations of nutrients [14], and then spreads further south through it. However, as shown in [8], according to current meter data and reanalysis (see the inset in Fig. 3), multidirectional currents of both southern and northern directions are recorded in the bottom layer of the Kane Gap, which indicates the non-stationary nature of this transfer. As evidenced by the latest GEBCO 15' relief data, there is an unnamed deep passage south of the Grimaldi Mountains (depths over the saddles exceed 4000 m), through which NEADW can also pass.

The upper boundary of NEADW in the Kane Gap, according to our estimates, corresponded to the maximum vertical gradients of salinity and oxygen, Si/P ratio equal to 33 [15] and silicate concentration of 50 μM/kg. The identified boundary

**Table 2.** Name and characteristics of Bottom Waters in the eastern Atlantic

| Name | Upper boundary, $\theta$, °C | Authors |
|---|---|---|
| Antarctic Bottom Water (AABW) | 2 | Wust, 1935 [5] |
| | 1.9 (4-11° N)<br>2.0 (36° N) | McCartney et al., 1991 [9] |
| | 1.8 (11° N),<br>1.9 (36° N) | Macdonald, 1998* |
| Eastern Basin (abyssal) Water (EBW) | – | Dobrolyubov et al., 1995* |
| | 1.8-2.0 (0° N) | Morozov et al., 2010 [7] |
| | 1.8 | Stephens, Marshall, 2000* |
| Lower Deep Water (LDW) | 1.8 | Van Aken, 2007 [16] |
| Lower North East Atlantic Deep Water (lNEADW) | 1.98 ± 0.03 | Garcia-Ibanez et al., 2015 [17] |
| North East Atlantic Bottom Water (NEABW) | 1.95 | Liu, Tanhua, 2019 [4],<br>Present work |

Note. Items marked with an asterisk (*) are taken from work [7].

**Table 3.** Potential temperature (θ) and meridional component of current velocity (V) over the Kane Gap sill.

| Authors | Years | Months | Depth, m | θ, °C | V, cm/s | Flow direction |
|---|---|---|---|---|---|---|
| Morozov et al., 2010 [7] | 2009 | 4 | 4552 / 4405 | 1.856 / 1.914 | –10 / –3 | SE / SE |
| Morozov et al., 2013 [18] | 2009 | 10 | 4536–4567 /4405 | 1.846 / 1.983 | 5...10 / 4 | NW / N |
| | 2010 | 10 | 4444–4545 / 4405 | 1.836 / 1.968 | 2 / –15 | NW / SE |
| | 2011 | 10 | 4387–4566 / 4405 | 1.855 / 1.921 | –5...5 / 15 | 0 / NW |
| | 2012 | 10 | 4284–4558 / 4405-4405 | 1.832 / 1.924 | 5 / 10 | NW / NW |
| Our data (2nd cruise of R/V “Ak. Treshnikov”) | 2014 | 5 | 4424 / 4405 | 1.877 / 1.825 | – / –13 | – / SE |
| Our data (63rd cruise of R/V “Ak. Ioffe”) | 2022 | 10 | 4550 / 4405 | 1.858 / 1.878 | – / –12 | – / SE |

Note. Above – based on measurements from different years, below – based on GLORYS12v1 reanalysis for 1993–2022. (Positive current velocity values indicate northward direction).

coincided with the isotherm $\theta = 1.95$°C, proposed by [4], which is slightly below the “classical” boundary of 2°C [5].

The greatest interest is associated with the AABW fraction in NEABW due to the transformation of Antarctic Bottom Water as it passes through the MAR fractures from the western part of the Atlantic Ocean to the eastern part. In the Kane Gap, according to the conservative indicator PO, the calculated share of AABW in NEABW was about 20%. In the area of the passage itself, their share was below 15%, while in the nearby basins, the AABW share was slightly over 20%. Thus, we share the opinion of most researchers (see Table 2) that there is no pure AABW in the eastern Atlantic, their share here is less than 25%. If we take the AABW content at the entrance to the Vema Fracture Zone as 100%, then at the exit to the eastern Atlantic, the AABW share is already about 60% of the waters that approached the fracture from the west.

## INTERANNUAL VARIABILITY. SPECTRAL AND CORRELATION ANALYSIS

The greatest interest in the Kane Gap, due to the absence of oceanological sections for comparison, is the change in temperature and current velocities at the main sill. The paper compared measurements of monthly mean values of potential temperature and the meridional component of current velocity obtained by different authors and using the reanalysis *GLORYS* 12 *v* 1. Values at the point 9.333° N, 19.833° W at a horizon of 4405 m were used, characterizing the bottom layer with a thickness of about 400 m (Table 3, Fig. 4). These characteristics were also compared with data from recorders in the Kane Gap at depths of 4350–4570 m from November 2010 to October 2011 [8].

Comparison of the reanalysis and recorders showed satisfactory correspondence of monthly changes in water temperature and poor reproduction of current velocities (Fig. 3). Coincidences in the direction of the meridional velocity component were detected only episodically (December 2010, January, March, May 2011). In general, it can be noted that periods of temperature increase correspond to southeastern current directions (from the Cape Verde Basin towards the Sierra Leone Basin).

This is confirmed by the maximum values of potential temperature obtained from reanalysis (more than 2°C), which were observed in January-March 1996, April-September 1999, January-March 2003, February-November 2010, December 2011, January-June 2020 during currents of southeastern direction. Minimum temperatures from reanalysis (~1.8°C) were observed in July-October 1995, December 2004, June 2005 during increased current velocities in the opposite northwestern direction. However, in June-November 1996, January-February 1997, February-March 2013, June-July 2014, periods of lower temperature (~1.85°C) were identified precisely during southeastern currents. Thus, according to reanalysis, periods of temperature increase/decrease do not always correspond to the patterns identified by the recorders.

Analysis of the periodogram in Fig. 4 showed that annual (1 year) and semi-annual (0.5 year) harmonics, as well as a period of 2–4-years, stand out in the variability of meridional current velocity.

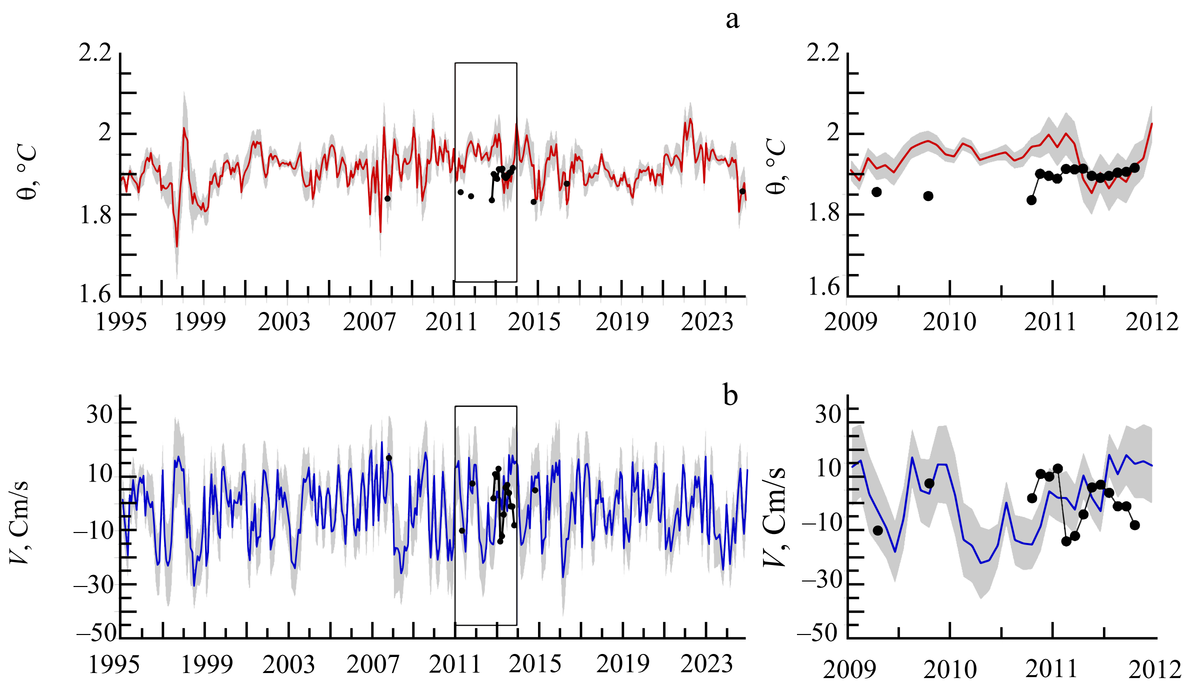

**Fig. 3.** Interannual variability of monthly mean values of potential temperature (θ, °C) (a), meridional current velocity (V, cm/s) (b) in the Kane Gap according to the GLORYS12v1 ocean reanalysis for all months of 1993–2022. The inset (right) shows an enlarged fragment for 2009–2012. Black dots represent estimates by different authors from Table 4. Gray filling shows standard deviations for the series of monthly mean values from the GLORYS12v1 reanalysis, calculated over an 11-month sliding window (+5 and –5 months from the central value).

The amplitude of the annual harmonic of meridional current velocity is 0.045 m/s. In the variability of temperature and salinity, periods of 1, 2–4, 10 years are distinguished. The amplitudes of the temperature harmonic are 0.007, 0.015, 0.027 C, respectively.

Spectral analysis of potential temperature data and bottom current velocity in the Romanche Fracture Zone also showed the important role of semi-annual and annual harmonics [19]. At 26°N for AABW, an annual harmonic of transport with an amplitude of 0.6 Sv and a potential temperature amplitude of 0.01°C was similarly identified [20].

Comparison of Fig. 3 and Fig. 4c, d shows the predominance of south-eastward current velocity in 2006, 2008, 2019, 2022 and north-westward direction in 1996, 2005, 2009, 2018, 2020, 2021.

We also analyzed the correlation between the original series of monthly average values of salinity, potential water temperature, meridional and zonal current velocities for the period 1993–2022 (Table 4). A significant negative relationship between the meridional and zonal components of current velocity ($r = -0.92$) was established for bottom waters, indicating the dominance in the Kane Gap of either northwesterly (43% of cases) or southeasterly currents (50% of cases). The strongest negative correlations between meridional and zonal current velocities are observed on a scale of 2–4 years ($r = -0.94$). At the low-frequency period of 10–30 years, a negative correlation appears between temperature and the meridional velocity component ($r = -0.34$) (Table 4). Thus, with a northwesterly current direction, the potential temperature in the Kane Gap decreases, which confirms the results of [8].

**Table 4.** Correlation matrix of original series, filtered monthly average series (0.5–1, 2–4, 10–30 years) of potential water temperature (θ), zonal ($U$) and meridional current velocity ($V$) at a depth of 4405 m according to the GLORYS12v1 reanalysis in 1993–2022. Significant correlations at 5% confidence interval lie in the range $-0.3 > r > 0.3$.

| Parameters | θ, °C | $V$, m/s | $U$, m/s |
|---|---|---|---|
| θ, °C | **–0.14,** | 0.05, 0.20, **–0.34** | 0.19, 0.05, 0.20, **0.46** |
| $V$, m/s | –0.14, 0.05, 0.20, **–0.34** | – | –0.92,–0.82,–0.94, –0.68 |
| $U$, m/s | 0.19, 0.05, 0.20, **0.46** | –0.92,<br>–0.82,<br>–0.94,<br>–0.68 | – |

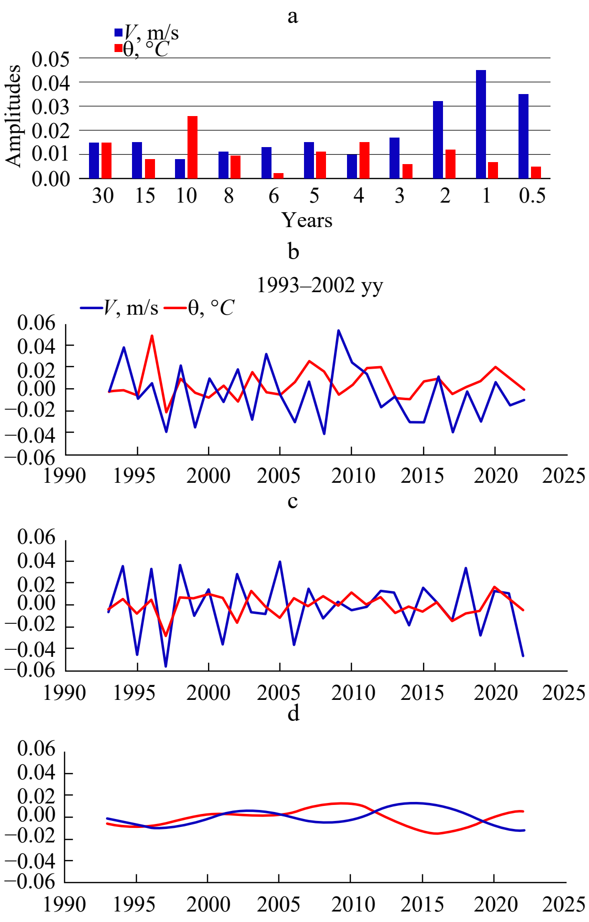

**Fig. 4.** Periodogram of monthly average series (a) and variability of filtered detrended monthly average values of meridional current velocity (V, m/s, blue) and potential temperature (θ, °C, red), at periods of 0.5–1 (b); 2–4 years (c), 10–30 years (d) in the Kane Gap according to the GLORYS12v1 ocean reanalysis

When analyzing long-term trends in hydrological characteristics in the Kane Gap for 1993–2022 using the Mann-Kendall test, a significant trend of decreasing annual mean salinity values (by 0.005 psu) and increasing potential water temperature values (by 0.03°C) was revealed. No significant trends in current velocity changes were detected during this period.

## CONCLUSIONS

Analysis of data from the 63rd cruise of R/V “Akademik Ioffe” in 2022 showed that the Kane Gap region is characterized by a water structure typical for the eastern part of the Tropical Atlantic.

It was found that in the lower layer of intermediate waters, mainly represented by AAIW, our calculations show a presence of 17 to 26% of Mediterranean waters

It was established that in the eastern part of the tropical Atlantic, the NADW complex is represented by two layers: UNADW with a salinity maximum and MNADW with an oxygen maximum. According to our calculations, UNADW is a mixture of waters consisting of Labrador Sea Water (up to 30%), Antarctic Intermediate Water (up to 50% at the upper boundary), and Mediterranean Water (up to 34%).

In the Kane Gap region, MNADW undergoes transformation. It represents a mixture of Iceland-Scotland Overflow Water and Labrador Sea Water, and after passing through fractures at 7–12°N, it is joined by highly transformed deep waters with low oxygen content coming from the African continental slope area.

It was found that AABW in the eastern Atlantic does not exist in pure form (calculated fraction less than 25%). For waters passing through the MAR fractures into the Cape Verde Basin and spreading deeper than NADW, the term Northeast Atlantic Bottom Water (NEABW) has been introduced, with its upper boundary close to the isotherm $\theta = 1.95$°C .

A negative relationship between the meridional velocity of currents and potential temperature (−0.34) was revealed only on a scale of 10–30 years, i.e., with a northwestern flow direction, the temperature in the Kane Gap will decrease, and with a southeastern direction, it will increase.

A significant trend was found showing a decrease in the annual average values of salinity (by 0.005 psu) and an increase in the values of potential water temperature (by 0.03°C) in the bottom layer of the Kane Gap for 1993–2022.

## ACKNOWLEDGEMENTS

The authors thank F.N. Gippius, S.A. Babich, N.Yu. Rodionova, as well as the entire crew and scientific staff of the R/V “Akademik Ioffe” and R/V “Akademik Tryoshnikov,” who assisted in conducting the expeditionary research.

## FUNDING

The work was carried out within the framework of state assignments on the topics of state assignments of Moscow State University No. 121031900090-6, FRC IBSS No. 124030100137-6. Descriptions of hydrological and hydrochemical characteristics were made with the support of the Russian Science Foundation grant No. 23-17-00032.

## REFERENCES

1. *Sarafanov A., Sokov A., Demidov A.* Water mass characteristics in the equatorial North Atlantic: A section nominally along 6.5°N, July 2000 // Journal of Geophysical Research. 2007. 112(C12). C12023. https://doi.org/10.1029/2007JC004222
2. *Andrié C., Ternon J.F., Messias M.J., Memery L., Bourlès B.* Chlorofluoromethane distributions in the deep equatorial Atlantic during January–March 1993 // Deep Sea Research Part I: Oceanographic Research Papers. 1998. V. 45. No. 6. Pp. 903–930.
3. *Herrford J., Brandt P., Zenk W.* Property changes of deep and bottom waters in the Western Tropical Atlantic // Deep-Sea Research. Part I. 2017. V. 124. Pp. 103–125.
4. *Liu M., Tanhua T.* Water masses in the Atlantic Ocean: characteristics and distributions // Ocean Science. 2021. V. 17. Pp. 463–486.
5. *Wust G* . The stratosphere of the Atlantic Ocean / Wiss. Ergebn. Dtsch. Atlant. Exped. Meteor. 1935. V. 6.
6. *Rhein M., Stramma L., Send U.* The Atlantic Deep Western Boundary Current: Water masses and transports near the equator // Journal of Geophysical Research. 1995. 100(C2). 2441. https://doi.org/10.1029/94JC02355
7. *Morozov E.G., Demidov A.N., Tarakanov R.Yu., Zenk W.* Abyssal Channels in the Atlantic Ocean. Water Structure and Flows // Springer Science + Business Media. 2010. https://doi.org/10.1007/978-90-481-9358-5
8. *Van Haren H., Morozov E., Gostiaux L., Tarakanov R.* Convective and shear-induced turbulence in the deep Kane Gap // Journal of Geophysical Research: Oceans. 2013. V. 118. No. 11. Pp. 5924–5930. https://doi.org/10.1002/2013JC009282 .
9. *McCartney M.S., Bennett S.L., Woodgate-Jones M.E.* Eastward Flow through the Mid-Atlantic Ridge at 11°N and Its Influence on the Abyss of the Eastern Basin // Journal of Physical Oceanography. 1991. 21(8). 1089–1121. https://doi.org/10.1175/1520-0485(1991)021
10. *Sapozhnikov V.V., Agatova A.I., Arzhanova N.V., Mordasova N.V., Lapina N.M., Zubarevich V.L., Lukyanova O.N., Torgunova N.I.* Manual on chemical analysis of marine and fresh waters for environmental monitoring of fishery water bodies and promising fishing areas of the World Ocean. Moscow: VNIRO Publishing. 2003. 202 p.
11. *Broecker W.* “NO” a conservative water-mass tracer // Earth and Planetary Science Letters. 1974. V. 23. Pp. 100–107.
12. *Demidov A.N.* On the identification of intermediate and deep water masses in the South Atlantic // Oceanology. 2003. V. 43. No. 2. Pp. 165–175.
13. *de Carvalho Ferreira M.L., Kerr R.* Source water distribution and quantification of North Atlantic deep water and Antarctic bottom water in the Atlantic Ocean // Progress in Oceanography. 2017. V. 153. Pp. 66–83.
14. *Oudot J., Merlin F.X., Pinvidic P.* Weathering rates of oil components in a bioremediation experiment in estuarine sediments // Marine Environmental Research. 1998. V. 45. No. 2. Pp. 113–125. https://doi.org/10.1016/s0141-1136(97)00024-x
15. *Arzhanova N.V., Artamonova K.V.* Hydrochemical structure of waters in the fishing areas of Antarctic krill Euphausia superba Dana // Proceedings of VNIRO. 2014. V. 152. Pp. 118-132
16. *Van Aken H.M.* The Oceanic Thermohaline Circulation: an introduction. Springer Science & Business Media. 2007. V. 39. Pp. 135–182.
17. *Garcia-Ibanez, et al* . Structure, transports and transformations of the water masses in the Atlantic Subpolar Gyre // Progress in oceanography. 2015. V. 135. Pp. 18–36
18. *Morozov E.G., Tarakanov R.Y., Van Haren H.* Transport of Antarctic bottom water through the Kane Gap, tropical NE Atlantic Ocean // Ocean Science. 2013. V. 9, No. 5. Pp. 825–835. https://doi.org/10.5194/os-9-825-2013
19. *Thierry V., Mercier H., Treguier A.-M.* Seasonal fluctuations in the deep central equatorial Atlantic Ocean: A data-model comparison // Ocean Dynamics. 2006. V. 56. Pp. 5–6.
20. *Krasheninnikova S.B., Demidov A.N., Ivanov A.A.* Variability of the Characteristics of the Antarctic Bottom Water in the Subtropical North Atlantic // Oceanology. 2021. V. 61. Iss. 2. Pp. 151–158. https://doi.org/10.1134/S0001437021020090 .

*DOKLADY EARTH SCIENCES, 2025, Vol. 520, No. 1, pp. 135–139*

# INTERNAL GRAVITY WAVES IN THE OCEAN WITH SHEAR FLOWS EXCITED BY NON-STATIONARY SOURCES

**© 2025 V. V. Bulatov[a], *, I. Yu. Vladimirov[b], **, and E. G. Morozov[b], *****

Presented by Academician of the Russian Academy of Sciences M. V. Flint on August 12, 2024

Received August 12, 2024
Revised September 11, 2024
Accepted September 16, 2024

**Abstract.** The problem of internal gravity wave generation by a localized oscillating disturbance source in the ocean of finite depth with background shear currents is considered. Model representations of the buoyancy frequency and the shear current distribution by depth are used to construct analytical solutions in the linear approximation. Under the Miles-Howard assumption, an integral representation of the solution is constructed as a sum of wave modes. Using the stationary phase method, an asymptotic representation of the solution for an individual mode is obtained. The spatial transformation of the phase structures of wave fields is studied depending on the oscillation frequency of the disturbance source and the main characteristics of the shear currents. Experimentally measured shear flows in abyssal channels are shown and compared with the results of laboratory modeling.

**Keywords:** *internal gravity waves, stratified ocean, shear flows, far fields, asymptotics, non-stationary source*

**DOI**: 10.31857/S26867397250116e3

Due to the progress in the study of large-scale oceanic wave processes, the study of the dynamics and propagation of internal gravitational waves (IGW) in the ocean, taking into account the presence of currents, is an urgent task [2, 5, 10, 16, 20]. In the real ocean, internal gravitational waves propagate against the background of background shear ocean currents, so the vertical and horizontal dynamics of shear currents are largely related to these waves. In the ocean, such currents can manifest themselves, for example, in the area of the seasonal thermocline and have a noticeable effect on the dynamics of IGW [16-18]. Intense natural currents are Antarctic bottom water flows that flow around underwater ridges at abyssal depths. Their velocities near the bottom often reach 40–50 cm/s [16-18]. Bottom water flows around underwater ridges in the straits generate intense internal waves, for example in the Kara Gate Strait or the Strait of Gibraltar [16-18]. The depths in the straits are less than in the abyssal faults and vary from tens to hundreds of meters. Unsteady or oscillating sources of disturbances are one of the mechanisms for generating intense internal gravitational waves in natural (ocean, Earth's atmosphere) and artificial stratified environments. Such sources of IGW excitation can be both natural (collapse of the turbulent mixing region, rapid movement of the ocean floor, spread of intense atmospheric disturbances) and anthropogenic (underwater and above-ground explosions). [2, 5, 6, 7, 19, 20]. To simulate IGW generation, a steep slope of a transverse ridge in straits can be considered as a point source in the real ocean, and, for example, wave generation by periodic currents on the slopes of transverse ridges in straits can be considered as a possible mechanism for IGW excitation [5, 16-18]. To a first approximation, it can be assumed that background currents with a vertical velocity shift are weakly dependent on time and horizontal coordinates, so if the scale of the horizontal flow change is much larger than the lengths of the IGW, and the scale of the temporal variability is much larger than the periods of the IGW, then such currents can be considered stationary and horizontally homogeneous [2, 5, 10]. In the general formulation, describing the dynamics of IGW in the ocean with background fields of shear currents is a very difficult

---

[a] *Ishlinsky Institute for Problems in Mechanics, Russian Academy of Sciences, Moscow, Russia*
[b] *Shirshov Oceanology Institute, Russian Academy of Sciences, Moscow, Russia*
**e-mail: internalwave@mail.ru*
***e-mail: iyuvladimirov@rambler.ru*
****e-mail: egmorozov@mail.ru*

task as early as in a linear approximation. [2, 4, 5, 10, 15, 19, 20].

In the Boussinesq approximation, the vertical component of small perturbations of the IGW velocity $W$ satisfies the equation [2, 3, 5, 9]

$$\frac{D^2}{Dt^2}\left(\Delta+\frac{\partial^2}{\partial z^2}\right)W-\frac{D}{Dt}\left(\frac{d^2U}{dz^2}\frac{\partial W}{\partial x}+\frac{d^2V}{dz^2}\frac{\partial W}{\partial y}\right)+$$

$$+N^2(z)\Delta W=\frac{D}{Dt}\left(\frac{\partial}{\partial z}\left(\frac{Dq}{Dt}\right)\right) \qquad (1)$$

$W = 0$, at $z = 0, -H$

where $\frac{D}{Dt}=\frac{\partial}{\partial t}+U(z)\frac{\partial}{\partial x}+V(z)\frac{\partial}{\partial y}$, $\Delta=\frac{\partial^2}{\partial x^2}+\frac{\partial^2}{\partial y^2}$, $N^2(z)=-\frac{g}{\rho^*}\frac{d\rho_0(z)}{dz}$ are the square of the Brent-Weiss frequency (buoyancy frequency), $(U(z),V(z),0)$ are the components of the velocity of the background shear flow on the horizon $z$, $\rho_0(z)$ is the undisturbed density, $\rho^*$ is the characteristic value of the density [2, 5], $q=q(x,y,z,t)$ is the distribution density of the sources. Problem (1) is considered in a vertically finite $-H < z < 0$ and horizontally unlimited $-\infty < x, y < +\infty$ layer. At the bottom of $z = -H$, the vertical velocity component $W$ is zero; at the surface of $z = 0$, the "hard cap" approximation is used: $W = 0$, which filters out the surface mode and has little effect on the main characteristics of the IGW [2, 5]. Next, the Miles-Howard stability condition for the Richardson number is assumed to be fulfilled: $Ri(z) = N^2(z)\Big/\left(\left(\frac{dV}{dz}\right)^2+\left(\frac{dU}{dz}\right)^2\right) > 1/4$, this means that the corresponding spectral problem does not have complex eigenvalues [4, 11, 14]. The characteristic values of Richardson numbers in the waters of the World Ocean in the absence of dynamic instability of background shear currents can range from 2 to 20 [16-18]. The frequency of buoyancy is assumed to be constant: $N(z) = N = const$. Background shear flow is one—dimensional and linear:

$$V(z)\equiv 0,\ U(z)=U_0+\frac{U_0-U_H}{H}z,$$

$$U_0 = U(0),\ U_H = U(-H).$$

The Miles-Howard stability condition is satisfied for the Richardson number:

$$Ri=N^2/\left(\frac{dU}{dz}\right)^2=\frac{N^2H^2}{\left(U_0-U_H\right)^2}>\frac{1}{4}.$$

A point harmonic mass source located at a depth is considered: $q(x, y, z, t) = Q\exp(i\omega t)\delta(x)\delta(y)\delta(z-z_0)$, $Q = const$, $\omega$ is the oscillation frequency of the source when at large distances from an oscillating source of disturbances at $r=\sqrt{x^2+y^2}\to\infty$ asymptotics of solutions along a certain direction, forming the angle $\alpha$ with the positive direction of the $Ox$ axis is constructed using the stationary phase method [1, 2, 12]

$$W(x,y,z,z_0,t)=\sum_{n=1}^{\infty}W_n(x,y,z,z_0,t)$$

$$W_n(x,y,z,z_0,t)\sim$$

$$\sim\sum_{j=1}^{J(\alpha)}\frac{Q\exp\left(i\left(\omega t-\Theta_n\left(\nu_j^n,\omega\right)+\delta_j\right)\right)F_n\left(\nu_j^n,\omega,z,z_0\right)}{\sqrt{2\pi r\chi_n\left(\nu_j^n,\omega\right)}\frac{\partial B\left(\mu_n\left(\nu_j^n,\omega\right),\nu_j^n,\omega\right)}{\partial S_\alpha}}$$

$$\Theta_n(\nu,\omega)=\mu_n(\nu,\omega)x+\nu y,$$

$$F_n(\nu,\omega,z,z_0)=\frac{\varphi_n(\omega,\nu,z)}{d_n(\omega,\nu)}\left(\frac{df(z_0)}{dz_0}\frac{\varphi_n(\omega,\nu,z_0)}{\omega-f(z_0)}+\right.$$

$$\left.+\frac{\partial\varphi_n(\omega,\nu,z_0)}{\partial z_0}\right)$$

$$d_n(\omega,\nu)=\frac{\partial\varphi_0(\omega,\mu_n(\nu,\omega),\nu,-H)}{\partial\mu}$$

$$\frac{\partial\varphi_H(\omega,\mu_n(\nu,\omega),\nu,-H)}{\partial z}$$

$$B\left(\mu_n(\nu,\omega),\nu,\omega\right)=\varphi_0\left(\omega,\mu_n(\nu,\omega),\nu,-H\right)$$

$$\frac{\partial\varphi_H\left(\omega,\mu_n(\nu,\omega),\nu,-H\right)}{\partial z}$$

$$\chi_n(\nu,\omega)=\left|\frac{\partial^2\mu_n(\nu,\omega)}{\partial\nu^2}\right|\left(1+\left(\frac{\partial\mu_n(\nu,\omega)}{\partial\nu}\right)^2\right)^{-3/2}$$

where $\varphi_n(\omega,\nu,z) = \varphi_0(\omega,\mu_n(\nu,\omega),\nu,z) = \varphi_H(\omega,\mu_n(\nu,\omega),\nu,z)$, $\mu_n(\nu,\omega)$ are eigenfunctions and eigenvalues of the vertical spectral problem, which are expressed in terms of modified Bessel functions of the imaginary index [3, 9], $f(z) = \mu_n(\nu,\omega)U(z)$, $\nu_j^n=\nu_j^n(\alpha), j=1,2,..,J(\alpha)$: all such real roots of the equation are $\frac{\partial\mu_n(\nu,\omega)}{\partial\nu}=-\mathrm{tg}\pm$ for which the corresponding stationary points are $\left(\nu_j^n,\mu_n\left(\nu_j^n,\omega\right)\right.$ of the phase function $\Theta_n\left(\nu_j^n,\omega\right)$ lie on the curve $l_n^+(\alpha)$, $\chi_n(\nu,\omega)$ is the curvature of this curve. Phase shift $\delta_j$ is equal to $-\frac{\pi}{4}$ or $-\frac{3\pi}{4}$ depending on whether the curve is reversed $l_n^+(\alpha)$ at point $v_j^n(\alpha)$ with a convexity and concavity to the chosen direction $S_\alpha$ The asymptotics of the stationary phase becomes inapplicable near the corresponding wave fronts (caustics), since each caustic is generated by some inflection point of the corresponding dispersion curve, that is, a point at which the curvature of this curve vanishes [1, 2, 12].

Two models of linear shear currents characteristic of the conditions of the World Ocean were used for numerical calculations: unidirectional (the shear current does not change the direction of its propagation throughout the ocean depth) and multidirectional (bottom and near-surface currents are multidirectional). The Richardson number for the flow models used is $Ri=25$, the calculations are given for the first wave mode. Fig.1 shows the results of calculations of lines of equal phase (solid lines) and wavefronts (dashed lines) for unidirectional shear flow, Fig. 2 for multidirectional flow.

Numerical calculations show that the variability, ambiguity, and qualitative diversity of the obtained dispersion relations determine the nature of the generation of various types of waves. In particular, at relatively low oscillation frequencies of the source, only annular (transverse) waves are excited, and in some cases more than two wave packets of such waves can be excited simultaneously. The number of simultaneously excited wave packets is determined by the total number of individual branches of the dispersion curves. At high frequency values, only longitudinal (wedge-shaped) waves of two types are generated, and as the oscillation frequency increases, the half-wave angle of the wavefronts decreases. It can also be noted that there are frequency values at which the wavefront half-solution angle is close to 90°. Therefore, at these frequency values, due to the ambiguity of the dispersion relations, the wave pattern of the excited fields is a complex wave system with both longitudinal and transverse wave properties. For certain types of wave packets, an increase in phase leads to an approximation of the corresponding line of equal phase to the origin (the position of the source of disturbances), and for other types of waves, to a distance from it. For a multidirectional type of flow, a wave pattern in the form of a wave cross is obtained. In this case, all wave vibrations propagating from the source of disturbances can be localized inside the wave fronts (caustics).

Strong bottom currents in the ocean are observed in the Vema fault in the Mid-Atlantic Ridge at 11°N [16-18]. At the meridian of about 41° W, the near-bottom flow with velocities of about 15–20 cm/s flows around an underwater ridge located across the fault. Next, a stream of dense Antarctic bottom water rushes down the slope for about 8 km, the stream accelerates as it rolls down and then descends to a height of about 250–300 m. According to the measurement data, the flow accelerates to 39 cm/s at a depth of 4000–4500 m and then slows down, since its kinetic energy is insufficient to overcome stratification (Fig. 3). In [7, 8, 13, 15], the flow around underwater obstacles was modeled in laboratory experiments, numerical calculations were performed and theoretical estimates of the parameters were proposed IGW, which are generated when flowing around.

In [7, 8, 13, 15], examples of laboratory modeling for several flow parameters are given, as well as a numerical calculation of the internal vibrations that occur during such a flow. The flow structure in their formulation of the problem and

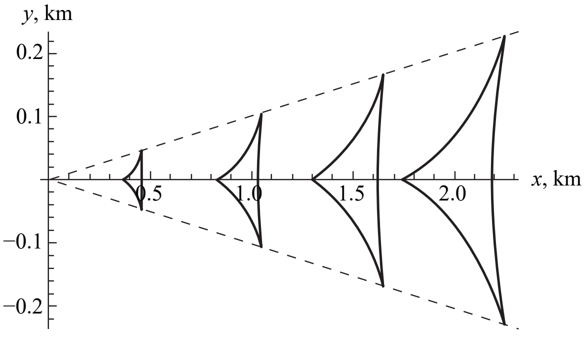

**Fig. 1.** Wave pattern of propagating waves from a source in the positive direction of the Ox axis, two wavefronts at x > 0.

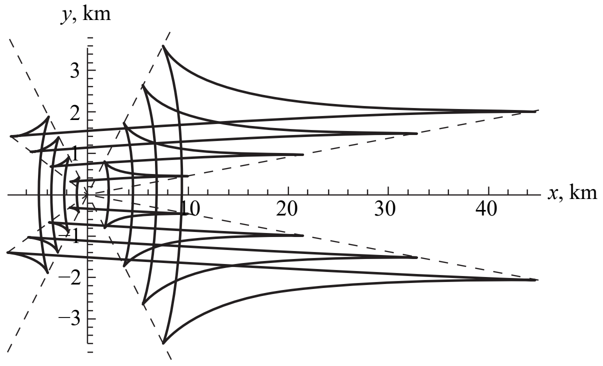

**Fig. 2.** Waves from the source in all directions; two wavefronts at $x > 0$, two wavefronts at $x < 0$.

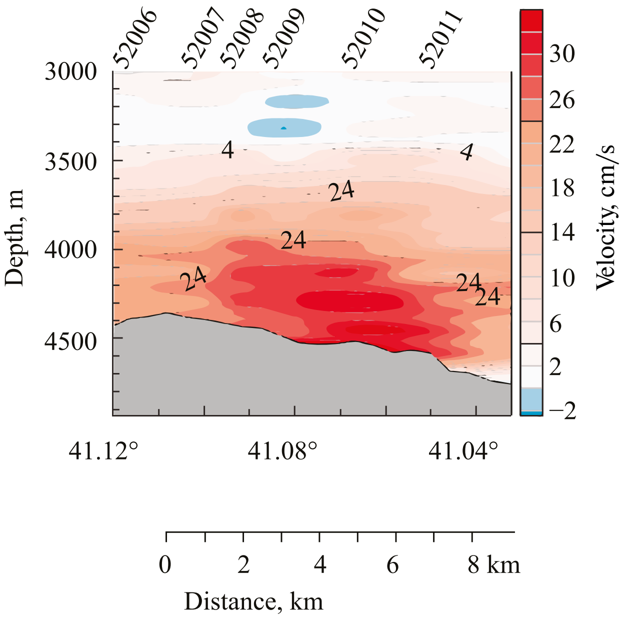

**Fig. 3.** The measured velocity field along the Vema abyssal fault in the tropical Atlantic during the flow of bottom water around a transverse underwater ridge. The numbers on the upper axis show the numbers of current profiling stations with a lowered Doppler current profiler. The maximum eastward flow velocities (from left to right) are observed after the current rolls down the slope.

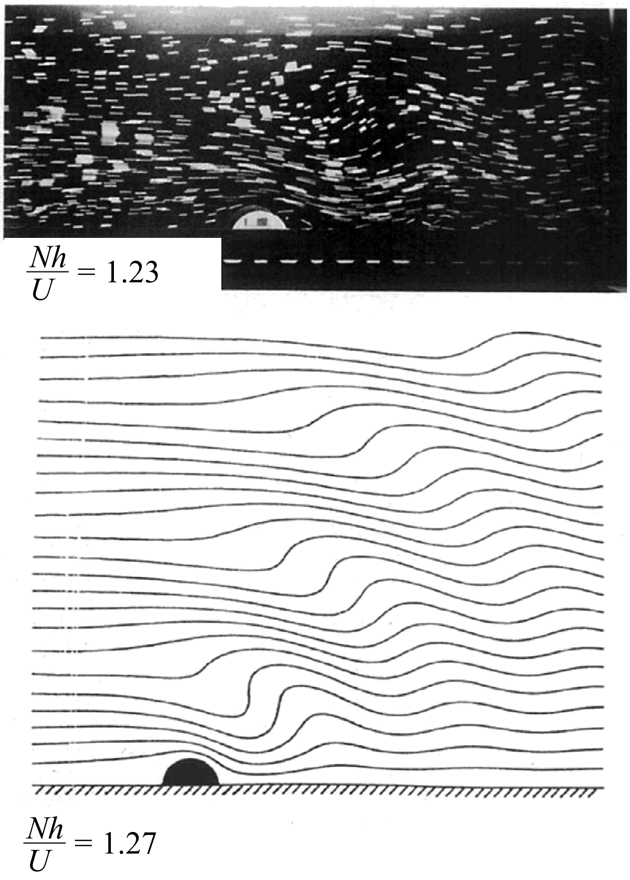

**Fig. 4.** Laboratory modeling (above) and numerical calculation (below) of the flow around an underwater obstacle for values of the $Nh/U$ parameter close to those observed in the ocean.

experiment depends on a dimensionless number $Nh/U$, where $h$ is the height of the obstacle and $U$ is the maximum value of the shear flow velocity. According to the results of the estimates obtained, propagating columnar perturbations occur at $0.5 < Nh/U < 2$. Fig. 4 shows the flow lines in laboratory and numerical simulations for different values of the $Nh/U$ parameter. The available measurements in the ocean correspond to the range of the dimensionless parameter proposed in [7, 8]: the Brunt-Vaisala wave frequency at a depth of 4000-4500 m is $N$=0.002 s$^{-1}$, the maximum shear flow velocity is 0.39 m/s, and a streamlined obstacle with a height of $h$=250–300 m [16-18]. Then the range of values of the dimensionless parameter $Nh/U$ will be 1.28–1.53.

Thus, the obtained asymptotic results with different values of the physical parameters included in them make it possible to evaluate the characteristics of IGW observed in real oceanic conditions with currents, as well as calculate wave fields, including from non-local sources of disturbances of various physical nature. As a result of model multivariate calculations, the simulated wave system can be approximated to the wave patterns observed in field and laboratory conditions, which makes it possible to estimate the physical parameters of real sources of IGW generation in the marine environment and determine the main characteristics of initial disturbances by varying the model values of the initial parameters.

## FUNDING

The work was carried out on the topic of state assignment No. FFGN-2024-0005 (V.V. Bulatov), No. FMWE-2024-0016 (I.Yu. Vladimirov, E.G. Morozov). The measurement data was obtained during voyages of IO RAS vessels with the support of RSF grant No. 21-77-20004

## REFERENCES

1. *Arnold A. I.* Wavefronts and topology of curves. Moscow: Phasis, 2002. 118 p.
2. *Bulatov V. V., Vladimirov Yu. V.* Waves in stratified media. Moscow: Nauka. 2015. 735 p.
3. *Bulatov V.V., Vladimirov I.Yu., Morozov E.G.*. Generation of internal gravitational waves in the ocean when a background shear current strikes an underwater elevation // Reports of the Russian Academy of Sciences. Earth Sciences. 2022. Vol. 505. No.2. Pp. 192–195.
4. *Gavrilyeva A.G., Gubarev Yu.G., Lebedev M.P.* Miles' theorem and new partial solutions of the Taylor-Goldstein equation // Scientific Notes of Kazan University. A series of physical and mathematical sciences. 2016. Vol. 158(2). Pp. 156–171.
5. *Miropolsky Yu.Z.*. Dynamics of internal gravitational waves in the ocean. L.: Hydrometeoizdat, 1981. 302 p.
6. *Slepyshev A.A.*. Vertical momentum transfer by inertial-gravitational internal waves on a two-dimensional shear flow // Marine Hydrophysical Journal. 2021. Vol. 37. No. 4. Pp. 279–287.
7. *Baines P.G.* Mixing in downslope flows in the ocean - plumes versus gravity currents // Atmosphere-Ocean. 2008. V. 46(4). Pp. 405–419.
8. *Baines P.G., Hoinka K.P.* Stratified flow over two-dimensional topography in fluid of infinite depth: a laboratory simulation // J. Atmospheric Sciences. 1985. V. 42 (15). Pp. 1614–160.
9. *Bulatov V.V., Vladimirov Yu.V.* Dynamics of internal gravity waves in the ocean with shear flows // Russian J. Earth Sciences. 2020. V. 20. ES4004
10. *Fabrikant A.L., Stepanyants Yu.A.* Propagation of waves in shear flows. World Scientific Publishing. 1998. 304 p.
11. *Howland C.J., Taylor J.R., Caulfield C.P.* Shear-induces breaking of internal gravity waves // J. Fluid Mechanics. 2021. V. 921. A24.
12. *Kravtsov Yu., Orlov Yu.* Caustics, catastrophes and wave fields. Berlin: Springer. 1999. 210 p.
13. *Long R.R.* Some aspects of the flow of stratified fluids III. Continuous density gradients. // Tellus. 1955. V. 7. Pp. 341–357.
14. *Miles J.W.* On the stability of heterogeneous shear flow // J. Fluid Mech. 1961. V. 10 (4). Pp. 495–509.
15. *Meunier P., Dizus S., Redekopp L., Spedding G.* Internal waves generated by a stratified wake: experiment and theory // J. Fluid Mech. 2018. V. 846. Pp. 752–788
16. *Morozov E.G.* Oceanic internal tides. Observations, analysis and modeling. Berlin: Springer, 2018. 317 p.
17. *Morozov E.G., Frey D.I., Zuev O.A., Makarenko N.I., Seliverstova A.M., Mekhova O.S., Krechik V.A.* Antarctic Bottom Water in the Vema Fracture Zone // J. Geophys. Res. 2023. V. 128. e2023JC019967.
18. *Morozov E.G., Kozlov I.E., Shchuka S.A., Frey D.I.* Internal tide in the Kara Gates Strait // Oceanology. 2017. V. 57 (1). Pp. 8–18.
19. *Shugan I., Chen Y.-Y.* Kinematics of the ship's wake in the presence of a shear flow // J. Mar. Sci. Eng.2021. V. 9. P. 7.
20. *Vallis G.K.* Atmospheric and oceanic fluid dynamics. Cambridge University Press. 2006. 758 p.

*DOKLADY EARTH SCIENCES, 2025, Vol. 520, No. 1, pp. 140–145*

# GERMANIUM-RICH CRUSTS OF THE SEA OF JAPAN

**© 2025 O. N. Kolesnik[a], *, A. N. Kolesnik[a], V. T. S"edin[a], N. V. Zarubina[b], and A. A. Karabtsov[b]**

Presented by Academician of the Russian Academy of Sciences G. I. Dolgikh on March 28, 2024

Received March 28, 2024
Revised September 19, 2024
Accepted September 23, 2024

**Abstract.** Ore crusts with a germanium content of up to 96 ppm were discovered in the Sea of Japan. This is tens of times higher than the Clarke of the Earth's crust. Germanium-rich crusts are dredged together with intermediate and acid volcanic rocks, are composed predominantly of iron oxyhydroxides (goethite) and contain germanium in a dispersed state.

**Keywords:** *germanium, ferromanganese crusts and concretions, Sea of Japan*

**DOI**: 10.31857/S26867397250117e4

## INTRODUCTION

The Russian Academy of Sciences, together with other departments, in order to ensure the technological sovereignty of the country, has been tasked with determining the priorities for the long-term development of the mineral resource base of solid minerals. Germanium is included in the list of the main types of strategic mineral raw materials and, therefore, is in the area of priority attention [1]. At the current stage of study, the main sources of germanium are considered to be stratiform polymetallic and brown coal deposits (the germanium content in sphalerite exceeds 100 g/t, in coal – 200 g/t) [2, 3].

Ferromanganese nodules and crusts (ferromanganese formations, FMF) on the ocean and sea floor are solid minerals and promising for industrial extraction of nickel, copper, cobalt, manganese, and a number of other strategically important metals. Very little is known about the distribution of germanium in FMF. The few publications concern diagenetic, sedimentary (sedimentary, hydrogenic), sedimentary-diagenetic FMF and indicate a generally low germanium content at the level of 1–2 g/t [4-6], which approximately corresponds to the clarke for the upper part of the continental earth's crust. The clarke, according to various estimates, ranges from 1.3 to 1.6 g/t [7]. There are reasons to assume germanium enrichment in hydrothermal FMF. The element content in postmagmatic high-temperature aqueous fluids and mineral-forming solutions that formed hydrothermal mineralization of various deposits averages 17 g/t with a maximum value of 930 g/t [8]. The germanium dispersion halo in water is a reliable indicator of hydrothermal solution discharge onto the seabed [9].

The purpose of our study is to investigate the distribution characteristics of germanium in FMF formed with the participation of a hydrothermal source of matter.

## MATERIALS AND METHODS

The material for the study consisted of 29 samples of FMF from the summit parts of volcanic edifices in the Sea of Japan and 9 samples of volcanic rocks that compose these structures (Fig. 1, 2; Table 1). The material was dredged during the cruises of the R/V "Pervenets" in 1975–1980 and partially studied [10-12]. The Sea of Japan is located in the continent-ocean transition zone and is known for intense volcanic and post-volcanic hydrothermal activity. FMFs developed on volcanic edifices of the Sea of Japan have a hydrothermal-sedimentary origin [13] and are associated with volcanic rocks of two formation-geochemical types: post-rift

---

[a] *V.I. Il'ichev Pacific Oceanological Institute, Far Eastern Branch of the Russian Academy of Sciences, Vladivostok, Russia*
[b] *Far East Geological Institute, Far Eastern Branch of the Russian Academy of Sciences, Vladivostok, Russia*
**e-mail: kolesnik_o@poi.dvo.ru*

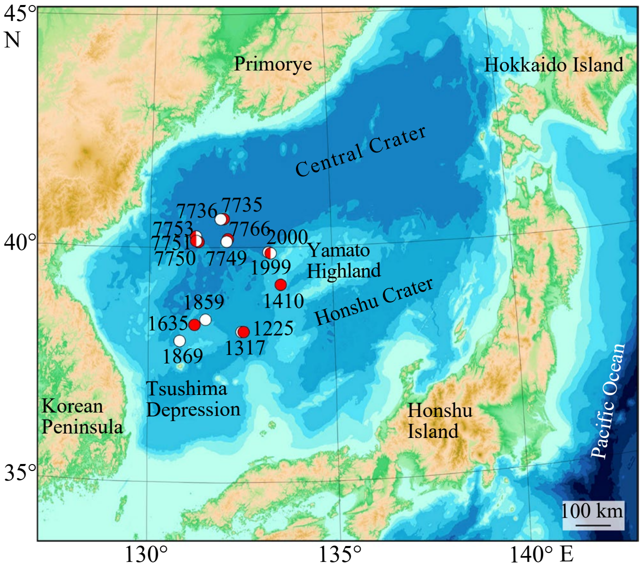

**Fig. 1.** Map of the Sea of Japan showing the largest morphological elements of the seafloor and dredging stations for FMFs (red circles) and volcanic rocks (white circles). Stations 1635, 1859, 1869 – Krishtofovich elevation. Stations 1410, 1999, 2000 – Northern Yamato Ridge. Stations 1225, 1317 – Galagan elevation. Stations 7735, 7736 – Gebass elevation. Stations 7750, 7751, 7753 – Evlanov elevation. Stations 7749, 7766 – Koltso mountain. The cartographic base is compiled according to GEBCO 2022 data.

(the absolute majority of FMFs) and marginal-continental [14]. Volcanic rocks of the post-rift type are mainly basalts. They form volcanic structures in deep-water basins with newly formed (sub)oceanic crust of Cenozoic age (mantle mafic volcanism). In our study, this type of volcanic rocks is represented by samples from the Galagan, Evlanov, Gebass, and Koltso elevations (Fig. 1; Table 1). Volcanic rocks of the marginal-continental type are mainly andesites, dacites, rhyolites, as well as trachydacites and trachyrhyolites. They form superimposed volcanic structures within large elevations with ancient Proterozoic-Mesozoic (sub)continental crust (crustal andesite-rhyolite volcanism). In our study, this type of volcanic rocks is represented by samples from the Krishtofovich elevation and the Northern Yamato Ridge (Fig. 1; Table 1).

Analytical studies were carried out at the Primorsky Center for Local Element and Isotope Analysis of the Far East Geological Institute, Far Eastern Branch of the Russian Academy of Sciences (Vladivostok). For elemental analysis, FMF samples and volcanic rocks were preliminary ground, dried at a temperature of 105–110°C to constant weight and subjected to open acid decomposition ($HF + HNO_3 + HClO_4$). The weight of the FMF samples was 30 mg, for volcanic rocks 50 mg. Loss on ignition (LOI) and silicon content in samples were determined by gravimetry, other macroelements by inductively coupled plasma atomic emission spectrometry using a Thermo iCAP 7600 Duo spectrometer (USA). The content of microelements, including germanium, was analyzed by inductively coupled plasma mass spectrometry on an Agilent 8800x quadrupole spectrometer (Japan) according to the previously proposed method [15], optimized for germanium. Germanium was determined by the isotope $^{74}$Ge. Polyatomic interferences from nickel, iron, potassium, and doubly charged rare earth elements were eliminated by background correction using the collision cell of the spectrometer filled with

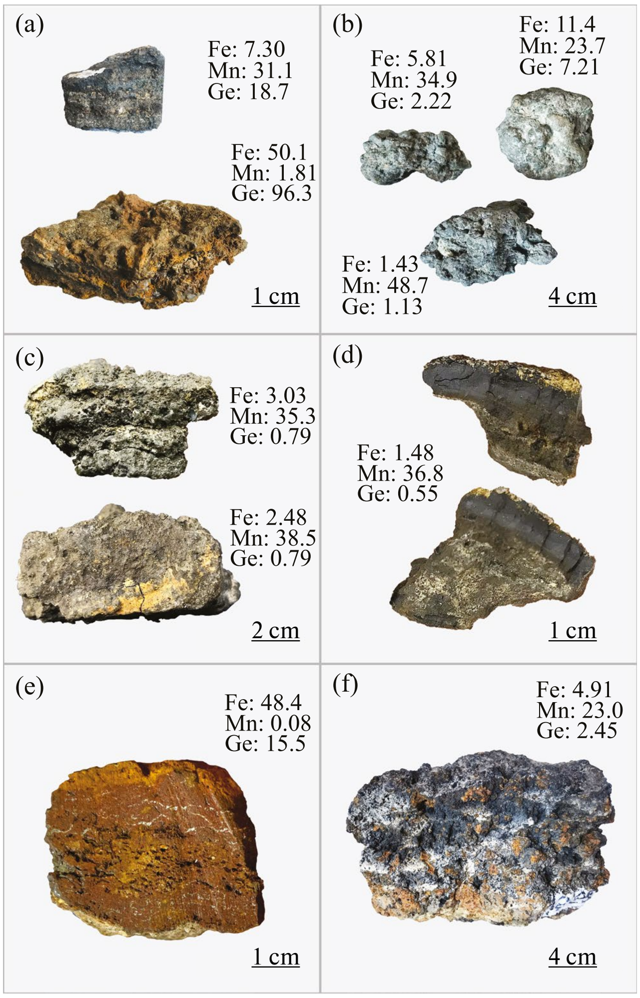

**Fig. 2.** General view of FMFs from the Sea of Japan with indication of average content of iron (wt. %), manganese (wt. %) and germanium (g/t). *a* – station 1635; *b* – station 1999; *c* – station 7753; *d* – station 7766 (view of the sample in chip); *e* – station 1410 (view of the sample in section); *f* – station 1225. For station locations, see Fig. 1.

**Table 1.** Content of iron, manganese, silicon and germanium in FMF and volcanic rocks of the Sea of Japan

| Station No. | Material type | Samples, *n* | Analyses, *n* | Fe, wt. % | Mn, wt. % | Si, wt. % | Ge, g/t |
|---|---|---|---|---|---|---|---|
| Krishtofovich Rise | | | | | | | |
| 1635 | Ferromanganese and ferruginous crusts and nodules | 5 | 7 | (6.63, 50.1)<br>24.7 | (1.81, 31.4)<br>19.8 | (4.4, 9.48)<br>7.01 | (15.9, 96.3)<br>41.5 |
| 1859 | Rhyolite | 1 | 1 | 0.86 | 0.01 | 35.0 | 1.30 |
| 1869 | Rhyolite | 1 | 1 | 1.33 | 0.01 | 31.7 | 1.34 |
| North Yamato Ridge | | | | | | | |
| 1410 | Ferruginous crusts | 10 | 10 | (46.0, 54.4)<br>50.3 | (0.06, 0.15)<br>0.09 | (2.52, 9.13)<br>5.71 | (15.0, 17.1)<br>16.0 |
| 1999 | Ferromanganese and manganese crusts and nodules | 3 | 7 | (0.68, 16.2)<br>6.97 | (11.3, 50.7)<br>34.0 | (1.74, 18.2)<br>8.64 | (0.97, 7.85)<br>4.05 |
| | Andesite | 1 | 1 | 5.59 | 0.10 | 25.1 | 1.07 |
| 2000 | Andesite | 1 | 1 | 4.86 | 0.09 | 27.1 | 1.04 |
| Evlanov Rise | | | | | | | |
| 7750 | Ferromanganese crust | 1 | 2 | (13.1, 17.5)<br>15.3 | (1.76, 13.9)<br>7.83 | (21.4, 27.0)<br>24.2 | (8.31, 10.4)<br>9.38 |
| 7751 | Ferromanganese crust | 1 | 1 | 12.6 | 19.5 | 15.5 | 1.41 |
| | Basalt | 1 | 1 | 5.91 | 0.06 | 22.5 | 1.11 |
| 7753 | Predominantly manganese crusts | 4 | 8 | (0.14, 7.09)<br>2.21 | (28.0, 43.8)<br>38.0 | (0.51, 12.0)<br>4.70 | (0.55, 1.25)<br>0.82 |
| | Basalt | 1 | 1 | 7.82 | 0.08 | 21.8 | 1.12 |
| Galagan Rise | | | | | | | |
| 1225 | Ferromanganese crust | 1 | 3 | (1.64, 9.02)<br>4.91 | (7.65, 35.5)<br>23.0 | (4.42, 16.9)<br>10.2 | (2.33, 2.58)<br>2.45 |
| 1317 | Basalt | 1 | 1 | 6.88 | 0.06 | 21.8 | 1.18 |
| Gebass Rise | | | | | | | |
| 7735 | Manganese crust | 1 | 1 | 0.10 | 42.5 | 0.70 | 1.66 |
| 7736 | Basalt | 1 | 1 | 6.77 | 0.13 | 22.8 | 0.83 |
| Koltso Rise | | | | | | | |
| 7766 | Manganese crusts | 3 | 4 | (0.20, 1.77)<br>0.85 | (35.7, 42.2)<br>39.4 | (0.40-5.90)<br>2.89 | (0.45, 1.02)<br>0.70 |
| 7749 | Basalt | 1 | 1 | 6.45 | 0.07 | 22.1 | 0.80 |

Note. When more than one analysis is available for a station, the minimum and maximum values are indicated in parentheses separated by a comma, with the mean value below the parentheses. The complete chemical composition of FMF and volcanic rocks is provided in the appendix.

helium. Foreign and domestic standard samples of FMFs and rocks were used to control the quality of chemical element determination results (Table 2). The accuracy of element determination results was assessed by the values of the relative standard deviation (RSD). For macroelements, the error did not exceed 2–5%, for most microelements the RSD was 15–20% or less, for germanium less than 18% (Table 2), which meets the quality criteria for quantitative elemental analysis in geochemical studies [17]. Databases compiled for FMFs and volcanic rocks were processed using multivariate statistical methods (appendix). The correlation analysis established the relationships between germanium and other chemical elements. Taking into account the strongest positive relationships in the space of the main factors, geochemical groups were identified, and the position of germanium was noted. The search for germanium-containing mineral phases was carried out in polished sections of FMFs and volcanic rocks using a JXA-8100 microprobe (“JEOL”, Japan) with an

**Table 2.** Results of germanium determination in standard samples of ferromanganese formations and rocks, g/t

| No. | Standard sample | Certified (a), compiled* (c) | Found X ( $n = 5$) | RSD, % |
|---|---|---|---|---|
| 1 | NOD-A-1 (manganese nodule), USA | < 0.5 (c) | 0.63 ± 0.04 | 2.87 |
| 2 | NOD-P-1 (manganese nodule), USA | 0.54–1.09 (c) | 1.06 ± 0.29 | 17.87 |
| 3 | JB-3 (basalt), Japan | 1.19–1.23 (c) | 1.27 ± 0.29 | 11.65 |
| 4 | GSO 8670-2005 (SGD-2a, essexite gabbro), Russia | 1.3 ± 0.2 (a) | 1.37 ± 0.13 | 4.86 |
| 5 | GSO 3333-85 (SG-3, granite), Russia | 2.2 ± 0.4 (a) | 2.23 ± 0.26 | 6.10 |

Note. * – Compiled values are taken from the GeoReM internet resource [16].

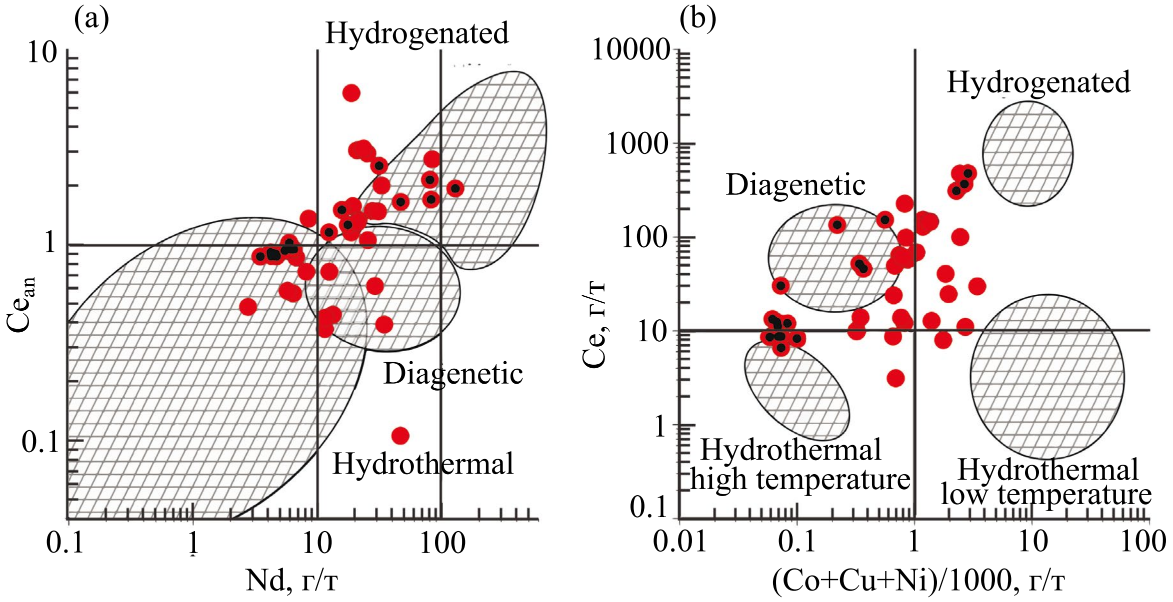

**Fig. 3.** Position of ferromanganese formations from the Sea of Japan (red circles) on genetic diagrams [18] *(a)* and [19] *(b)*. Black dots mark samples with germanium content ⩾ 15 g/t. The complete chemical composition of ferromanganese nodules is provided in the appendix.

energy-dispersive spectrometer according to an established scheme [12]. The detection limit of elements by the microprobe ranged from 0.04 to 0.1 wt. %. A non-built-in set of standards from natural and synthetic materials was used to control the quality of the analysis. The determination error did not exceed ± 10 rel.% with an element content of 1 wt. % and decreased with higher content. Genetic constructions for FMFs were performed based on geochemical data using previously developed diagrams [18, 19].

## RESULTS AND DISCUSSION

The conducted research confirmed the presence of hydrothermal material in ferromanganese nodules of the Sea of Japan (Fig. 3). The average content of germanium in FMF is high (12 g/t), distribution is uneven (standard deviation $S$ – 18.2 g/t) (Table 1). Among samples with near-clarke content (predominantly manganese crusts on basalts), high-germanium samples with content up to 96 g/t (predominantly ferruginous crusts on andesites and rhyolites) were identified. The germanium content in high-germanium samples is several times higher than the maximum values known to us for FMF (15 and 19 g/t) [6, 20] and tens of times higher than the clarke (from 1.3 to 1.6 g/t) [7]. It was previously shown that manganese crusts are composed mainly of todorokite and birnessite, while ferruginous crusts are composed of goethite [10-12]. In the studied samples of volcanic rocks from the Sea of Japan, the average germanium content is 1.09 g/t; the distribution shows little variation despite the presence of rocks with different silicon content in the sample – basalts, andesites, and rhyolites

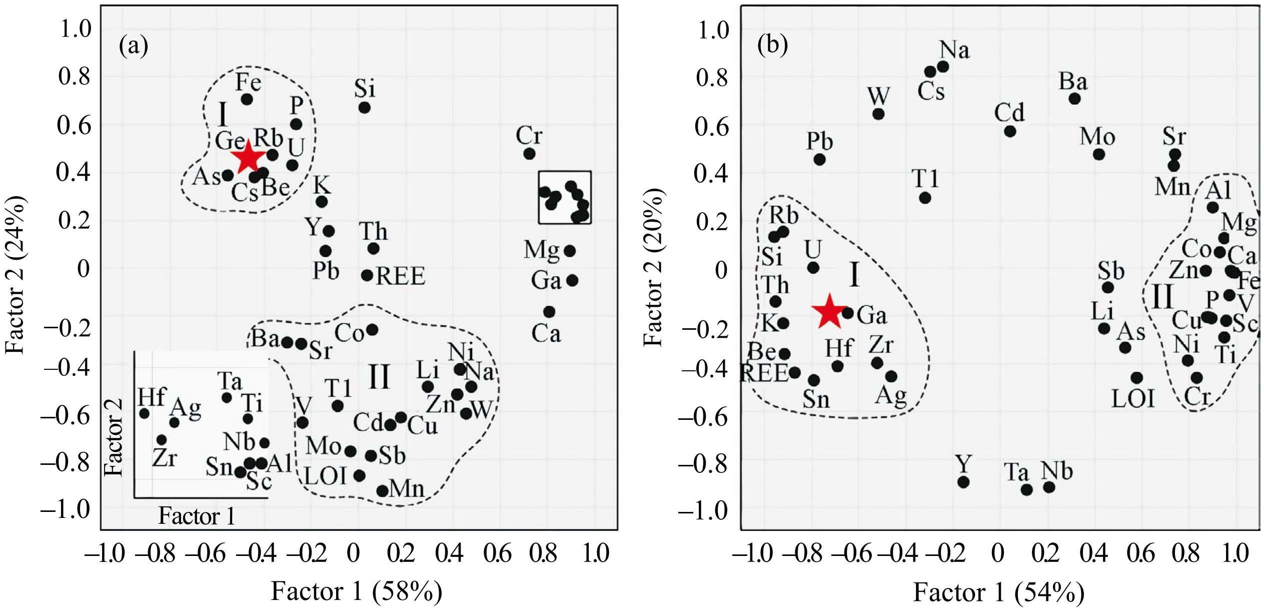

**Fig. 4.** Factor loading plots for germanium, other chemical elements, and loss on ignition (LOI) in FMF *(a)* and volcanic rocks *(b)* of the Sea of Japan. The main groups of elements are highlighted by a dotted line, their numbers are indicated by Roman numerals (I – iron group, II – manganese group). Germanium position is marked with an asterisk. The complete chemical composition and correlation matrices for FMF and volcanic rocks are provided in the appendix.

(standard deviation $S$ – 0.18 g/t). The low variability is consistent with existing ideas about the fairly uniform distribution of germanium in various types of igneous rocks [2].

Statistical analysis results indicate that the main factor controlling the microelement content in FMF of the Sea of Japan is preferential/selective co-precipitation or sorption on iron and manganese oxyhydroxides of different genesis (Fig. 4a, groups I and II respectively). Germanium has positive correlation with iron ($r_{\text{Ge-Fe}}$ : 0.61) and negative correlation with manganese ($r_{\text{Ge-Mn}}$ : –0.52), which indicates the accumulation of germanium on iron oxyhydroxides. The main factor controlling the germanium content in the volcanic rocks underlying the FMF is probably the silicon content in these rocks (Fig. 4b, groups I and II). Germanium belongs to the silicon group ($r_{\text{Ge-Si}}$ : 0.66) and potassium ($r_{\text{Ge-K}}$ : 0.70). Rubidium ($r_{\text{Ge-Rb}}$ : 0.64), uranium ($r_{\text{Ge-U}}$ : 0.67), thorium ($r_{\text{Ge-Th}}$ : 0.72), and light rare earth elements ($r_{\text{Ge-(La-Nd)}}$ : 0.68–0.77) are in the same group. Germanium has a negative correlation with all elements of the magnesium and iron group.

During microprobe analysis in FMF and volcanic rocks of the Sea of Japan, no mineral phase containing germanium was recorded. Obviously, germanium is present in a dispersed state in an amount that does not reach the detection limit of the instrument. The latter is consistent with generally accepted scientific concepts, according to which germanium belongs to rare dispersed elements and is found in nature mainly as impurities in rocks and minerals [2].

## CONCLUSION

Summarizing the results of the conducted research, it can be concluded that the discovery of high-germanium ferruginous crusts among the FMF of the Sea of Japan, formed with the participation of a hydrothermal source of matter, increases interest in further studying the behavior of germanium in metalliferous deposits and, in particular, in hydrothermal ferruginous crusts. Currently, in the general group of oceanic and marine FMF, hydrothermal ore crusts are significantly inferior in mineral resource potential to non-hydrothermal deep-sea ferromanganese nodules and cobalt-bearing manganese crusts.

## FUNDING

The study was carried out at the expense of the RSF grant No. 23-27-00004, https://rscf.ru/project/23-27-00004/.

## REFERENCES

1. *Bortnikov N.S., Volkov A.V., Galyamov A.L., Vikentyev I.V., Aristov V.V., Lalomov A.V., Murashov K.Yu.* Mineral resources of high-tech metals in Russia:

status and development prospects // Geology of Ore Deposits. 2016. Vol. 58. No. 2. Pp. 97–119.

2. *Ivanov V.V., Kats A.Ya., Kostin Yu.P., Meytov E.S., Solovyev E.B.* Industrial types of natural germanium concentrations. Moscow: Nedra, 1984. 246 p.
3. *Frenzel M., Ketris M.P., Gutzmer J.* On the geological availability of germanium // Mineralium Deposita. 2014. V. 49. Pp. 471–486.
4. *Volkov I.I., Sokolov V.S.* Germanium in iron-manganese nodules of modern sediments // Lithology and Mineral Resources. 1970. No. 6. Pp. 24–29.
5. *Volkov I.I., Shterenberg L.E.* Basic types of iron-manganese ores in modern water bodies // Lithology and Mineral Resources. 1981. No. 5. Pp. 4–26.
6. *Hein J.R., Mizell K., Koschinsky A., Conrad T.A.* Deep ocean mineral deposits as a source of critical metals for high- and green-technology applications: Comparison with land-based resources // Ore Geology Reviews. 2013. V. 51. Pp. 1–14.
7. *Kasimov N.S., Vlasov D.V.* Clarkes of chemical elements as a comparison standard in ecogeochemistry // Moscow University Bulletin. Series 5: Geography. 2015. No. 2. Pp. 7–17.
8. *Prokofiev V.Yu., Naumov V.B., Dorofeeva V.A., Akinfiev N.N.* Concentration of germanium and gallium in natural melts and fluids according to the study of inclusions in minerals // Geochemistry. 2021. V. 66. No. 3. Pp. 231–250.
9. *Mortlock R.A., Froelich P.N.* Hydrothermal germanium over the southern East Pacific Rise // Science. New Series. 1986. V. 231. No. 4733. P. 43–45.
10. *Mozherovsky A.V., Gramm-Osipov L.M., Volkova T.I., Mozherovskaya L.V.* Mineralogical features of iron-manganese formations in the Sea of Japan // New data on the geology of the western Pacific Ocean. Vladivostok: Far Eastern Scientific Center of the USSR Academy of Sciences, 1989. Pp. 135–139.
11. *Kolesnik O.N., Karabtsov A.A., Syedin V.T., Kolesnik A.N.* First discovery of goethite crusts in the Sea of Japan // RAS Reports. Earth Sciences. 2022. V. 505. No. 2. Pp. 59–164.
12. *Kolesnik O.N., Karabtsov A.A., Syedin V.T., Kolesnik A.N., Terekhov E.P.* A new atypical case of iron-manganese mineralization in the Sea of Japan // RAS Reports. Earth Sciences. 2024. V. 515. No. 2. Pp. 245–251.
13. *Astakhova N.V.* Hydrothermal ore genesis of the Sea of Japan // Geology and Geophysics. 2021. V. 62. No. 9. Pp. 1191–1203.
14. *Bersenev I.I., Lelikov E.P., Bezverkhny V.L., Vashchenkova N.G., Syedin V.T., Terekhov E.P., Tsoy I.B.* Geology of the Japan Sea Bottom. Vladivostok: Far East Scientific Center of the USSR Academy of Sciences, 1987. 140 p.
15. *Zarubina N.V., Blokhin M.G., Mikhaylik P.E., Segrenev A.S.* Determination of elemental composition of standard samples of ferromanganese formations by inductively coupled plasma mass spectrometry // Standard Samples. 2014. No. 3. Pp. 33–44.
16. GeoReM: Database on geochemical, environmental and biological reference materials. http://georem.mpch-mainz.gwdg.de. Access date: 10.07.2024.
17. *Dvorkin V.I.* Metrology and quality assurance of chemical analysis. M.: Tekhnosfera, 2019. 317 p.
18. *Bau M., Schmidt K., Koschinsky A., Hein J., Kuhn T., Usui A.* Discriminating between Different Genetic Types of Marine Ferro-manganese Crusts and Nodules Based on Rare Earth Elements and Yttrium // Chemical Geology. 2014. V. 381. Pp. 1–9.
19. *Vereshchagin O.S., Perova E.N., Brusnitsyn A.I., Ershova V.B., Khudoley A.K., Shilovskikh V.V., Molchanova E.V.* Ferro-manganese nodules from the Kara Sea: Mineralogy, geochemistry and genesis // Ore Geology Reviews. 2019. V. 106. Pp. 192–204.
20. Cobalt-rich ores of the World Ocean. St. Petersburg: VNIIOkeangeologiya, 2002. 167 p.

*DOKLADY EARTH SCIENCES, 2025, Vol. 520, No. 1, pp. 146–150*

# CHARACTERISTICS OF SHEAR STRATIFIES FLOWS IN THE CONDITIONS OF THE SEA OF JAPAN SHELF BASED ON IN-SITU MEASUREMENTS IN 2022

**© 2025 O. E. Kurkina[a], I. O. Yaroshchuk[b], A. V. Kosheleva[b], Academician of RAS G. I. Dolgikh[b], E. N. Pelinovsky[b, c], and A. A. Kurkin[a, b, *]**

Received August 12, 2024
Revised September 18, 2024
Accepted September 23, 2024

**Abstract.** The article presents some analysis results of in situ data of shear stratified flow measurements on the shelf of the Sea of Japan. The study of critical zones and layers is performed in terms of dimensionless Froude and Richardson parameters. It is shown that during the passage of high-intensity internal bores, sufficiently long (up to several hours) time intervals exist, which are characterized by a supercritical Froude regime, when active generation of short-period internal waves of large amplitude is predicted and occurs. The statistics of the Richardson number shows that with the lower probability estimate in the near-bottom layers during the observation period, the occurrence of shear instability is possible in 15% of cases, and its preservation is possible in 44% of cases.

**Keywords:** *internal waves, Froude number, Richardson number, resonant wave generation, shear instability*

**DOI**: 10.31857/S26867397250118e1

## INTRODUCTION

Monitoring and forecasting of currents, especially in the shelf zone, plays a very important role in planning human economic activities, engineering surveys, and predicting potential impacts on the coastal ecosystem. Estimates of parameters of sheared stratified flows are necessary not only at the initial stages of designing various hydraulic engineering systems (from oil and gas production platforms to wave energy converters) but also for the further operation of marine infrastructure facilities, as these parameters are input data for models that allow predicting loads on structures, potential soil erosion, and the spread of impurities and pollutants.

Tasks related to the description of energy cascades, hydrodynamic instability, laminar-turbulent transitions, and the bottom turbulent boundary layer in natural sheared stratified flows constitute fundamental problems of fluid mechanics and ocean hydrophysics, which are of great applied interest. Shear flows on the shelf are formed under the influence of a complex of physical environmental factors, such as atmospheric impacts, topographic effects, local buoyancy forces, and tidal flows. The temporal variability and spatial features of the velocity field distribution, as well as the dynamic mechanisms supporting them, are of great importance in the study of such currents. The first stage of a qualitative understanding of the dynamics of ongoing processes is the use of simple well-known physical criteria of (in)stability, which are based on models and methods of the theory of linear and nonlinear oscillations and waves. These criteria are built on the dimensionless parameters of Froude and Richardson. Here we use them for a preliminary analysis of the dynamic processes observed in the autumn of 2022 on the shelf of the Sea of Japan.

## MEASUREMENT DATA

Studies of sheared stratified flows applied to the conditions of the Sea of Japan (Peter the Great Bay) were carried out at the hydrophysical test site of the Pacific Oceanological Institute of the FEB RAS, the

---

[a] *Nizhny Novgorod State Technical University, Nizhny Novgorod, Russia*
[b] *Oceanological Institute, Far Eastern Branch of the Russian Academy of Sciences, Vladivostok, Russia*
[c] *Institute of Applied Physics of the Russian Academy of Sciences, Nizhny Novgorod, Russia*
**e-mail: aakurkin@nntu.ru*

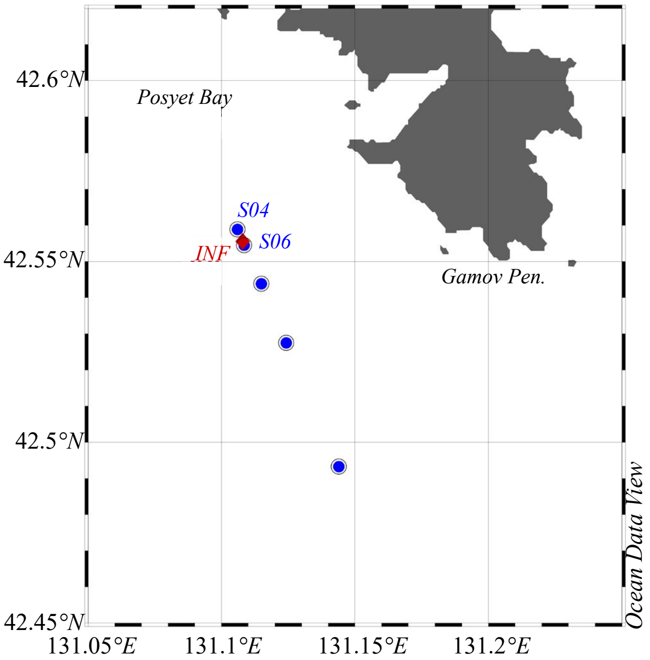

**Fig. 1.** Map of the measurement area indicating the stations of the hydrophysical testing site of POI.

scheme of which is presented in Fig. 1. A detailed description of the field experiments carried out at the test site is presented in papers [1-3].

For the calculations, 1-minute averaged data from the Infinity horizontal current recorder from three horizons and data from thermal chains with a frequency of 10 seconds and CTD sounding during the period from 12:53 on October 8 to 14:16 on October 12, 2022, obtained by POI FEB RAS, were used. The current was measured at point INF (see Fig. 1, 124 m from station S06), the bottom depth was 41.5 m. Velocities (meridional and zonal components) were measured at three levels: 2, 8, 14 m from the bottom (corresponding to depths of 39.5 m, 33.5 m, 27.5 m). The thermal chain at station S06 consisted of 35 sensors, with the last sensor located 2 m from the bottom. Density was reconstructed using the TEOS-10 seawater equation of state with a salinity profile measured by a CTD probe at station S04.

The results of current velocity measurements in the lower sea layer at station INF are shown in Fig. 2 (zonal, $U$, and meridional, $V$, components). It can be seen that the current velocity is quite

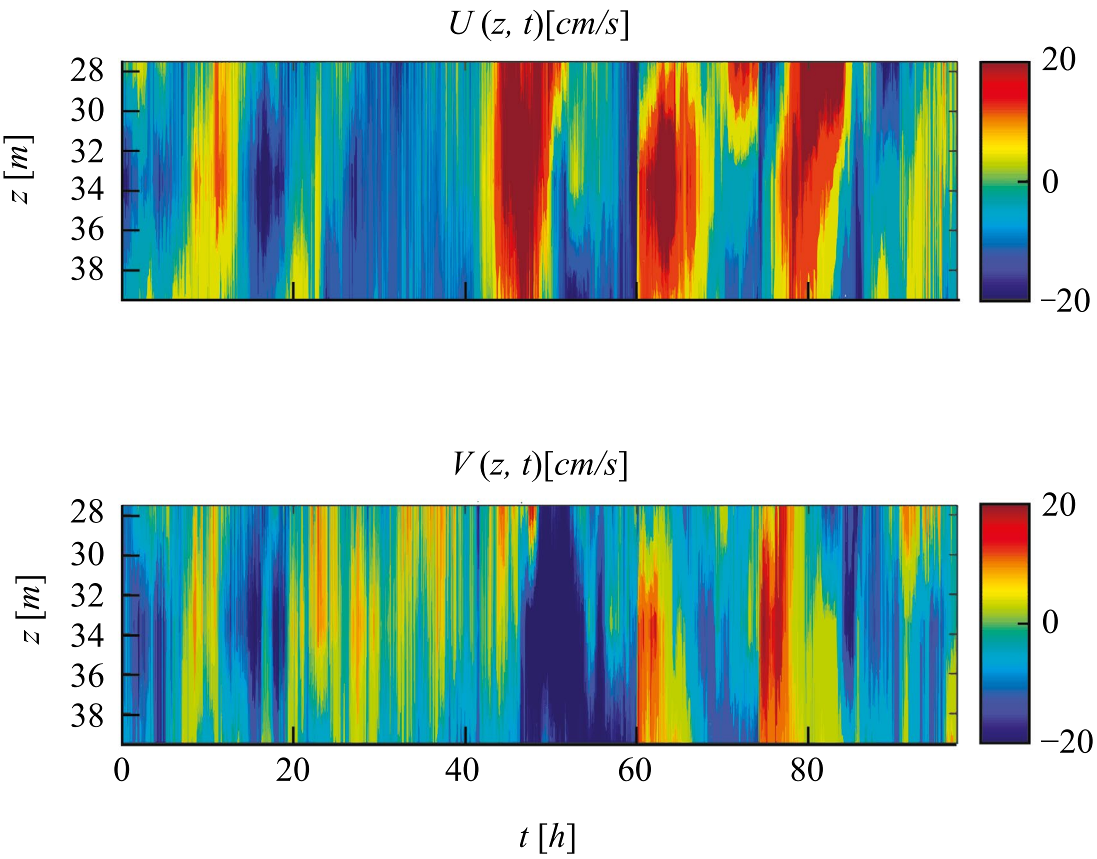

**Fig. 2.** Zonal and meridional velocity components measured at station INF.

significant (exceeding 0.4 m/s at certain times), has a pronounced vertical structure, and is also characterized by strong variability over time, both in magnitude and direction. The recording fragment during the period from 40 to 90 hours from the beginning of the recording is characterized by noticeable quasi-periodicity with predominance of long-wave components with a period close to the inertial period for the latitude of the observation site (16–18 hours). In the temperature and density field during the same period, three pronounced internal wave fronts with the same spectral properties were identified.

## ANALYSIS OF MEASUREMENT RESULTS

Identification of critical zones and layers in the measured flow fields was performed using the classical approach based on Froude and Richardson number calculations [4–6]. In the most common understanding, the Froude number *Fr* represents the ratio of velocities with which two processes, namely, advective and wave, transfer information about disturbance in the medium. Locally, the Froude number also represents the ratio of kinetic and potential energy of the flow and defines the flow as subcritical or supercritical. For stratified fluids, there are many formulations of this criterion, including depending on the type of wave process (see, in more detail in [7]). The Froude number for a stratified flow measured at a point in the presence of internal waves can be calculated as:

$$Fr(t) = \frac{\max\limits_{z} \left|\vec{u}(z,t)\right|}{c(t)},$$

where *c* is the phase velocity of long linear internal waves of the first mode, the algorithm for calculating this value is given, for example, in works [8, 9]. The criterion for linear stability in terms of Froude numbers here is values $Fr < 1$. The $Fr > 1$ regime corresponds to active generation of intense internal waves [10, 11].

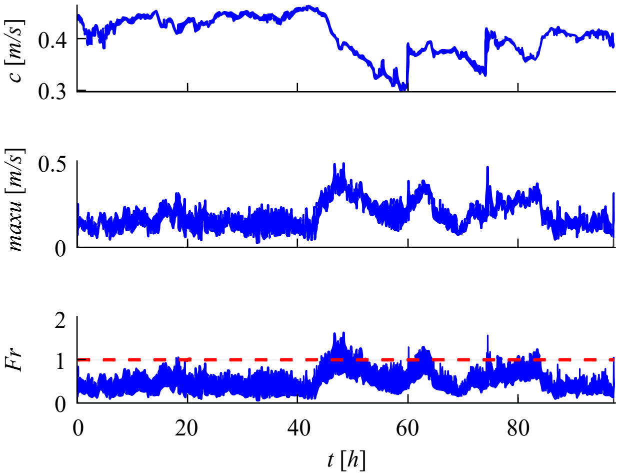

**Fig. 3.** From top to bottom: phase velocity of long linear internal waves of the first mode, maximum velocity of stratified flow, and Froude number for observational data at stations S06 and INF. On the lower panel, the critical value of the Froude number $Fr = 1$ is shown by the red dotted line.

The Froude number and the values necessary for calculating this parameter, according to measurements at stations S06 and INF, are shown in Fig. 3. From this figure, it can be seen that there are quite extended time intervals for which the supercritical regime is characteristic. These time intervals correspond exactly to the passage of high-intensity internal bores, on which short-period internal waves of large amplitude are generated.

The gradient Richardson number (*Ri*) for our problem is defined by the relation:

$$Ri(z,t) = \frac{N^2(z,t)}{Sh^2(z,t)},$$

where

$$N^2(z) = \frac{g}{\rho(z)}\frac{d\rho(z)}{dz},\ Sh^2 = \left(\frac{\partial U}{\partial z}\right)^2 + \left(\frac{\partial V}{\partial z}\right)^2,$$

here *N* is the buoyancy frequency, *z* is the depth, *g* is the acceleration of gravity, ñ is the water density, *Sh* is the modulus of the vertical current velocity shear, *V* and *U* are the northern and eastern components of the current velocity, respectively. The parameter *Ri* is often used in solving problems related to vertical turbulent mixing in a stratified marine environment [12-16]. There are two criteria: for linear instability of a shear flow, a necessary (but not sufficient) condition is $Ri < 0.25$ [17, 18], and for nonlinear stability, a necessary and sufficient condition is $Ri > 1$ [19]. According to the glossary data [20], there is an assumption about hysteresis: a laminar flow becomes turbulent at $Ri < 0.25$, but a turbulent flow can exist until $Ri = 1.0$ before becoming laminar.

Calculations of auxiliary quantities for computing the gradient Richardson number *Ri* : the square of buoyancy frequency $N^2(z, t)$ based on observational data at station S06 and values $\frac{\partial U}{\partial z}$ and $\frac{\partial V}{\partial z}$ based on observational data at station INF show that the numerator and denominator of *Ri* have the same order of magnitude – $10^{-4}$ 1/s,

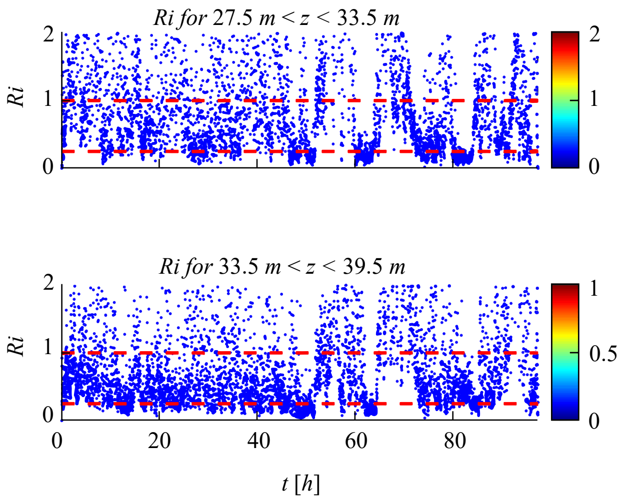

**Fig. 4.** Gradient Richardson number $Ri$ based on observational data at stations S06 and INF. Critical values $Ri = 0.25$ and $Ri = 1$ are shown by red dotted lines.

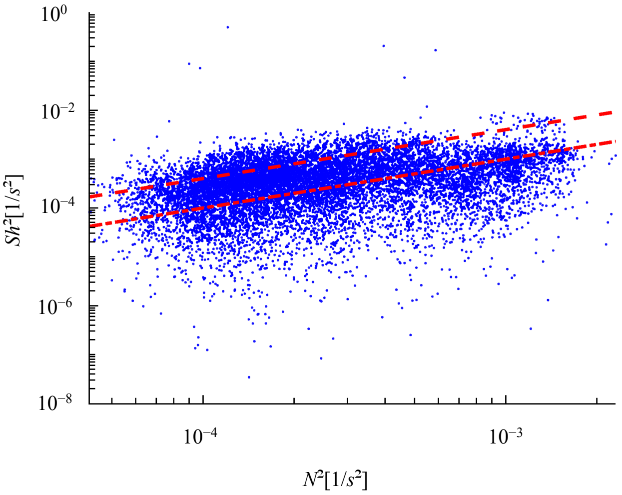

**Fig. 5.** Scatter diagram $N^2 - Sh^2$, calculated from observational data at stations S06 and INF. Critical values $Ri = 0.25$ and $Ri = 1$ are shown by red dotted and dash-dotted lines, respectively.

therefore unstable regimes can occur in the measurement area. This is also confirmed by Fig. 4, which shows the parameter $Ri$ over time (along with critical values $Ri = 0.25$ and $Ri = 1$) for the upper ($27.5$ m $< z <$ $33.5$ m) and lower ($33.5$ m $< z < 39.5$ m) bottom layers, where current measurements were conducted at station INF. The probability of meeting the necessary instability condition $P$ ($Ri < 0.25$) for shear flow in the lower layer is 16%, and in the upper layer, 15%. Fig. 5 shows the scatter diagram $N^2 - Sh^2$ , calculated from observational data at stations S06 and INF. Accounting for two critical values shows that in the current measurement layer, turbulent kinetic energy generation is possible in approximately 15% of cases, and its preservation in 44% of cases.

It should be noted that the canonical instability criterion $Ri < 0.25$ is based on the assumption of a plane-parallel stratified shear flow. Laboratory experiments and numerical modeling have shown that the criterion for curved stratified shear flow during the passage of short-period internal waves can be modified to $Ri < 0.1$ [6]. The probability of meeting this condition in our case $P(Ri < 0.1)$ is only 1.7% in the lower layer and 1.2% in the layer above it. Most likely, such events are associated with waves of high steepness and amplitude.

The main problem of using $Ri$ to estimate vertical turbulent mixing parameters from small-scale measurement data is its strong dependence on the depth increment ( $z$) at which the corresponding derivatives are calculated:

$$\frac{\partial U}{\partial z} = \lim_{\Delta z \to 0} \frac{\Delta U}{\Delta z},$$

or, in other words, on the resolution capability of instruments. In [16], it is shown that according to observational data in the Black Sea, the probability of reaching critical values of the Richardson parameter $Ri < 0.25$ decreases exponentially with increasing $z$, decreasing from 20% at $z = 0.5$ m to 3% at $z = 6$ m. This indicates that in marine conditions, the fulfillment of the instability criterion is more common at small scales. In our case, current measurements were conducted with a vertical resolution of $z = 6$ m, therefore we obtain only a lower estimate of the probability of possible instability zones appearing.

## CONCLUSION

In this paper, we analyzed data from simultaneous measurements of density stratification and bottom stratified currents in the Sea of Japan (Posyet Bay, Peter the Great Bay) at the hydrophysical testing site of POI FEB RAS in October 2022. The results of processing the field experimental data showed that during the observation period of about 25 hours, there are quite extended (up to several hours) time intervals characterized by a supercritical regime, when resonant interaction of long internal waves with shear flow occurs, which is consistent with the observed active generation of short-period internal waves of large amplitude during these time periods. Although the considered criteria for (in)stability emerged from the analysis of linear equations and asymptotic analysis of harmonic wave disturbances of small amplitude, when approaching zones and layers where these criteria are violated, rapid generation of higher vertical modes and wave harmonics occurs, linear description is not applicable here even for waves of small amplitude, and to correctly describe the ongoing processes, it is necessary to solve the complete system of hydrodynamic equations .

## FUNDING

This work was supported by the Laboratory of Nonlinear Hydrophysics and Natural Disasters of the V.I. Il'ichev Pacific Oceanological Institute FEB RAS, grant from the Ministry of Science and Higher Education of the Russian Federation, agreement No. 075-15-2022-1127 dated 01.07.2022.

## REFERENCES

1. *Kosheleva A.V., Yaroshchuk I.O., Shvyrev A.N., Samchenko A.N., Pivovarov A.A., Korotchenko R.A.* Experimental studies of background internal waves in the coastal part of Peter the Great Bay // Physics of Geospheres. 2019. P. 110–113.
2. *Yaroshchuk I., Kosheleva A., Lazaryuk A., Dolgikh G., Pivovarov A., Samchenko A., Shvyrev A., Gulin O., Korotchenko R* . Estimation of Seawater Hydrophysical Characteristics from Thermistor Strings and CTD Data in the Sea of Japan Shelf Zone // Journal of Marine Science and Engineering. 2023. V. 11(6). P. 1204.1–24.
3. *Yaroshchuk I., Liapidevskii V., Kosheleva A., Dolgikh G., Pivovarov A., Samchenko A., Shvyrev A., Gulin O., Korotchenko R., Khrapchenkov F.* Observation and Modeling of Nonlinear Internal Waves on the Sea of Japan Shelf // Journal of Marine Science and Engineering. 2024. V. 12(8). P 1301.1–20.
4. *Stepanyants Yu.A., Fabrikant A.L.* Wave propagation in shear hydrodynamic flows // Success in Physical Science. 1989. V. 159. No. 9. P. 83–123.
5. *Polzin K.* Statistics of the Richardson number: Mixing models and finestructure // Journal of Physical Oceanography. 1996. V. 26(8). P. 1409–1425.
6. *Chang M.H.* Marginal instability within internal solitary waves // Geophysical Research Letters. 2021. V. 48(9). P. e2021GL092616.
7. *Mayer F.T., Fringer O.B.* An unambiguous definition of the Froude number for lee waves in the deep ocean // J. Fluid Mech. 2017. V. 831. P. R3.1–9.
8. *Holloway P., Pelinovsky E., Talipova T., Barnes B.* A nonlinear model of internal tide transformation on the Australian North West Shelf // J. Phys. Oceanogr. 1997. V. 27(6). P. 871–896.
9. *Kurkina O.E., Talipova T.G., Soomere T., Kurkin A.A., Rybin A.V.* The impact of seasonal changes in stratification on the dynamics of internal waves in the sea of Okhotsk // Estonian Journal of Earth Sciences. 2017. V. 66(4). P. 238–255.
10. *Vlasenko V., Stashchuk N., Hutter K* . Baroclinic tides: theoretical modeling and observational evidence. Cambridge University Press. 2005. 350 p.
11. *Kurkina O.E., Talipova T.G* . Huge internal waves in the vicinity of the Spitsbergen Island (Barents Sea) // Nat. Hazards Earth Syst. Sci. 2011. V. 11. P. 981–986.
12. *Munk W., Anderson E.* Notes on a theory of the thermocline // J. Mar. Res. 1948. V. 3. P. 267–295.
13. *Pacanowski R.C., Philander S.G.H.* Parameterization of vertical mixing in numerical models of tropical oceans // J. Phys. Ocean. 1981. V. 11. P. 1443–1451.
14. *Redekopp L.G.* Elements of instability theory for environmental flows //Environmental stratified flows. Boston, MA: Springer US. 2001. P. 223–281.
15. *Galperin B., Sukoriansky S., Anderson P.S.* On the critical Richardson number in stably stratified turbulence // Atmospheric Science Letters. 2007. V. 8. P. 65–69.
16. *Morozov A.N.* Statistics of Richardson numbers based on observational data from an oceanographic platform // Ecological Safety of Coastal and Shelf Zones of the Sea. 2018. No. 2. P. 39–46.
17. *Miles J.W.* On the stability of heterogeneous shear flows // J. Fluid Mech. 1961. V. 10 (4). P. 496–508.
18. *Baines P.G.* Topographic effects in stratified flows. Cambridge university press. 1998. 498 p.
19. *Abarbanel H.D.I., Holm D.D., Marsden J.E., Ratiu T.* Richardson number criterion for nonlinear stability of three-dimensional stratified flow // Physical Review Letters. 1984. V. 52. P. 2352–2355.
20. American Meteorological Society, 2023: critical Richardson number. Glossary of Meteorology, http://glossary.ametsoc.org/wiki/critical_Richarson_number .

*DOKLADY EARTH SCIENCES, 2025, Vol. 520, No. 1, pp. 151–158*

# THERMAL CONVECTION MODELING OF THE EVOLUTION OF THE EARTH CORE

© 2025 Academician of RAS **L. Ya. Aranovich**[a], * **and V. D. Kotelkin**[b], **

Received September 26, 2024
Revised September 27, 2024
Accepted September 30, 2024

**Abstract.** We present a purely thermal convection 2-D model of the Earth's liquid core, occurring on the background of the secular cooling of the planet. The model includes equations of thermal convection in the Boussinesq approximation and the Coriolis force. Metallic iron with 0.9 wt. % H is chosen for the core composition. The results of modeling show that large vortexes, the 2-D analogues of Taylor columns, are formed in the liquid core prior to crystallization, which might be responsible for the early Earth magnetic field. The early stages of the solid core crystallization are characterized by a chaotic and shapeless growth. Continuing growth of the solid core results in rearrangement of the convection structure decreasing its average velocity but increasing heat flow at the core-mantle boundary due to increased amount of heat of crystallization. The solid core reaches its present size in 0.5 Gy. Averaged temperature profile of the modern liquid core differs significantly from the adiabatic.

**Keywords:** *thermal convection, liquid core, 2-D modeling, solid core crystallization*

**DOI**: 10.31857/S26867397250119e8

## INTRODUCTION

The onset of crystallization and growth of the solid core is one of the most important events in the endogenous geological history of our planet. It determined the change in the intensity of Earth's magnetic field [1, 2], the magnitude of heat flow at the boundary between the liquid core and mantle (CMB) [6], as well as the nature of interaction between the liquid core and mantle material [4, 6] due to the fractionation of light elements between the solid and liquid core at their boundary (ICB) [5].

Modern estimates of the age (and, consequently, the growth rate) of the solid inner core vary greatly from > 2.5 Gy [2, 11] to 0.5 Gy [3], depending on the estimation method (paleomagnetic data on the intensity of Earth's magnetic field or thermodynamic calculations), boundary conditions (adiabatic $T$, constant heat flow at the CMB) and values of physical parameters (primarily the thermal conductivity of the core) used in computational models.

Most of the works devoted to processes in the core are related to modeling the generation of the magnetic field [1]. For this purpose, a system of thermal convection equations in the Boussinesq approximation is used, taking into account the Coriolis force due to Earth's rotation, and magnetic induction (for example, [14] and references therein), interacting through the Lorentz force. Modern models in the complete system of equations additionally include the chemical component of convection caused by the fractionation of elements at the CMB and ICB boundaries [6]. Obviously, the processes occurring in the core and at its boundaries are interconnected and interact in a complex nonlinear manner. At the same time, hydrodynamics plays a major role in them. Therefore, for an adequate understanding of the essence of various processes, it is reasonable, as a first approximation, to study convection in its "pure form," limiting ourselves to only the main factors that significantly affect the flow, namely thermal convection and rotation (i.e., without magnetic field and chemical convection). The proposed work is devoted to solving this problem.

---

[a] *Institute of Geology of Ore Deposits, Petrography, Mineralogy and Geochemistry,*
*Russian Academy of Sciences, Moscow, Russia*
[b] *Lomonosov Moscow State University, Moscow, Russia*
**e-mail: lyaranov@igem.ru*
***e-mail: kotelkin55@mail.ru*

## MODEL OF THERMAL CONVECTION WITH CRYSTALLIZATION IN THE BOUSSINESQ APPROXIMATION

Let us choose characteristic scales: $L$, $v_0$, $T_0$, $\rho_0$, $p_0$, $g_0$, $v$, $k$, $\alpha$, $\Omega^E$, $C_V$, H (Table 1).

**Table 1.** Physical values used in model calculations

| Name of value | Designation | Value |
|---|---|---|
| Length — Earth's core radius | $L$ | $3.5 \cdot 10^6$ m |
| Gravitational acceleration | $g_0$ | $10$ m/s$^2$ |
| Density | $\rho_0$ | $12.5 \cdot 10^3$ kg/m$^3$ |
| Density jump | $\delta\rho$ | $0.5 \cdot 10^3$ kg/m$^3$ |
| Pressure | $p_0$ | 360 GPa |
| Temperature<br>Temperature perturbations | $T_0$<br>$\delta T$ | 5000°K<br>1000°K |
| Angular velocity of Earth's rotation | $\Omega^E$ | 0.73 rad/s |
| Thermal expansion coefficient | $\alpha$ | $10^{-5}$ 1/K |
| Heat of phase transition | $H$ | $3 \cdot 10^5$ J/kg |
| Heat capacity at constant volume | $C_V$ | 700 J/(kg · K) |

Let's write the thermal convection model in dimensionless form, using similarity criteria accepted in hydrodynamics. In the Boussinesq approximation [20], the thermal convection model includes:

Navier-Stokes equations

$$dV/dt = -eFr^{-1}T - Eu\nabla p/r_0 + Re^{-1}DV + \\ + \mathbf{Ro}^{-1}\left[\boldsymbol{e}_z \mathrm{x} V\right] + Cfr; \quad (1)$$

heat conduction equation

$$dT/dt = Pe^{-1}\Delta\mathrm{T} - P_0\, div\mathbf{V} + \mathbf{Cr}dQcr/dt \quad (2)$$

and continuity equation

$$V_r dr_0/dr + r_0\, div\mathbf{V} = 0. \quad (3).$$

In these equations $\rho_0(r)$ and $P_0(r)$ are known distributions of density and pressure, the PREM model [8], $V_r$ is the radial velocity component. It is also taken into account that in the Boussinesq approximation, small density perturbations ($\varepsilon <<1$) are linearly expressed through temperature

$$\rho \approx \rho_0(r)(1 - \varepsilon T). \quad (4).$$

The total pressure $P = P_0 + p$, where $P_0 >> p$, consists of hydrostatic $P_0$ and dynamic $p$ parts. The equations of motion (1) are written in a rotating coordinate system ($\boldsymbol{e}_z$ is the unit vector of the $z$ axis, directed along Earth's rotation axis), they account for gravity, characterized by the Froude number $Fr = v_0{}^2/g_0L$, $\varepsilon = \alpha\delta T$; pressure forces, characterized by the Euler number $Eu = p_0/\rho_0 v_0{}^2$; viscous forces, characterized by the Reynolds number $Re = v_0 L/v$ ; Coriolis forces, characterized by the Rossby number $Ro = v_0 / 2\Omega^E L$, and centrifugal forces, characterized by the coefficient $Cf = [\Omega^E]2L^2/v_0{}^2$.

The Peclet number is included in the heat conduction equation $Pe = v_0 L/k$ and the coefficient characterizing the heat of phase transition $Cr = H/(C_V T_0)$. Assuming $p_0 = \rho_0 g_0 L$, we get $Fr{\cdot}Eu = 1$ and exclude the Euler number. Note that in our case $\rho_0$, $g_0$, $L$ are such that $\boldsymbol{p_0} \approx p_{max} = 360$ GPa equals the pressure at the center of the Earth. The Rayleigh number is expressed through the similarity criteria used $Ra = \varepsilon Fr^{-1}RePe$

It should be noted that with a large linear dimension of the problem, despite the uncertainty of viscosity and thermal conductivity coefficients, the Reynolds $Re$ and Peclet $Pe$ numbers are very large, greater than $10^{10}$, so that intense turbulent convection of essentially inviscid and non-heat-conducting fluid occurs in the liquid part of the core. Viscosity and thermal conductivity play a role only in thin boundary layers near solid surfaces. Note that numerical modeling introduces scheme diffusion dependent on the grid step, therefore we will be forced to limit ourselves to Reynolds and Peclet numbers $Re = Pe = 10^6$. The remaining coefficients in our equations are equal to: $Eu = Fr^{-1} = g_0L / v_0{}^2 = 1.4{\cdot}10^6$, $\varepsilon = 0.01$, $Ro^{-1} = 2\Omega^E L / v_0 = 102$.

## INITIAL VALUES AND BOUNDARY CONDITIONS

To complete the problem formulation, it is necessary to set initial values, boundary conditions, and the phase transition condition. The outer radius of the core and the rotation speed of the Earth will be considered constant, i.e., we use simplified model conditions.

Conditions at the boundary with the mantle are the no-slip condition for the velocity vector and the condition for temperature. We will consider the temperature to be the same at all points of the outer boundary and slowly decreasing exponentially with time:

$$T_{\mathrm{CMB}}(t) = T_{\mathrm{CMB}}(0) \cdot \exp(-\lambda_M t). \quad (10)$$

Then the cooling rate will be regulated by the exponent $\lambda_M$. It is clear that the mantle, justifying its name, shields the heat output from the core and slows down the cooling of the planet, so the exponent $\lambda_M$ must be a small value.

To bypass the problem of initial conditions, we first conduct an auxiliary calculation. We set the initial state of rest with small random temperature perturbations, then due to the instability of such a state, movement arises in the system, which will begin to spin up according to the laws of thermal convection. We will continue the calculation until the stabilization of the average flow, i.e., until the state when the initial conditions are forgotten. The velocity distributions $V(r, 0)$ and temperature $T(r, 0)$ obtained in this way will be taken as the initial state for our modeling.

To model the crystallization of the core, it is necessary to specify the dependence of the melting temperature of the core material on hydrostatic pressure. The density deficit and the longitudinal wave velocities of the core, established by seismology [8], indicate the presence of light elements in its composition. One of the most frequently proposed light elements in the Earth's core is hydrogen [10, 12, 19]. The melting temperature of hydrogen-containing iron strongly depends on the composition FeHx, where x is the number of H atoms per formula unit ($0 < x < 1.2$). At $x = 1$ (composition FeH), the melting curve ($T$ – temperature K, $P$ – pressure, GPa) is described by the equation [10]:

$$T1_{\text{melt}} = T_0((P - P_0)/a + 1)^{1/c}, \qquad (11)$$

where $a = 24.6$, $c = 3.8$, $T_0 = 1473$K and $P_0 = 9.5$ GPa. (11)

The equation of melting curves at variable H content was obtained by interpolation between the curve at x=1 (equation 11) and the melting curve of pure Fe according to [13]:

$$T_{\text{melt}} = T1_{\text{melt}} + (d + e \cdot P)\cdot(1 - x), \qquad (12)$$

where $d = 521.7391$, $e = 4.7826$.

According to the estimate [7], the temperature at the present-day CMB boundary with 95% probability lies in the range of 3470–3880°K. Therefore, for modeling the crystallization process, a melting curve with hydrogen content $x = 0.5$ (0.9 wt. % H) was taken, which falls within the specified range of $T_{\text{CMB}}$, and also agrees well with the estimate of density and P-wave velocity in the core [12]. Note that at this stage of modeling, we did not consider the fractionation of the light element between the solid and liquid core.

## ON THE NUMERICAL METHOD AND 2D-MODEL

As a tool for our research, we use a 2D variant of our thermal convection model in a "flat core," the plane of which is orthogonal to Earth's rotation axis. Of course, for realistic modeling, particularly for magnetic field generation, full-scale 3D calculations are necessary. But in this work, to establish the basic properties of thermal convection, a simpler and more understandable 2D model is used, which provides complete visualization, and is also faster and more accurate computationally.

Numerical modeling was carried out using the finite-difference method with second-order approximation of partial differential equations on uniform Cartesian grids. Calculations were performed on grids of 512 · 512 and 1024 · 1024 nodes, which is sufficient for direct numerical simulation of turbulent regimes and accounting for large Reynolds and Peclet numbers.

*Convection in a fully liquid core.* In geophysical literature, it is customary to study and determine the radial distributions of parameters in the Earth in its current state, corresponding to the PREM model. For the core temperature, its adiabatic (or isentropic) distribution is calculated and presented. For example, in the classic monograph by V.N. Zharkov [9], the relation $T_{\text{ad}} = \rho^{\gamma}$ with the Grüneisen parameter $\gamma \approx 1.45$ is used. Since convection in the core is not taken into account in such temperature calculations, the question about its actual distribution remains. The core temperature obtained in our convective 2D model depends on time and coordinates; in polar coordinates, it is a function $T$ (t, $r$, $\phi$). To obtain the temperature distribution in the accepted radial form, it is sufficient to average it over the angular coordinate:

$$T_{av}(t, r) = \langle T(t, r, \phi)\rangle.$$

In Fig. 1, in a natural color scale, deviations of temperature from its average distribution are shown on the left, and the Z-component of vorticity is shown on the right. Shades of red here and further represent positive deviation values, blue color shades represent negative values, and the white color corresponds to near-zero values (when maximum values are exceeded, colors cycle).

It can be seen that thin boundary layers form at the boundary with the mantle: a cold thermal layer and a viscous hydrodynamic layer. The heavy cold layer often detaches and begins to sink in the form of multiple small jets. The thin jets merge and enlarge, and this is repeated in a cascade; ultimately,

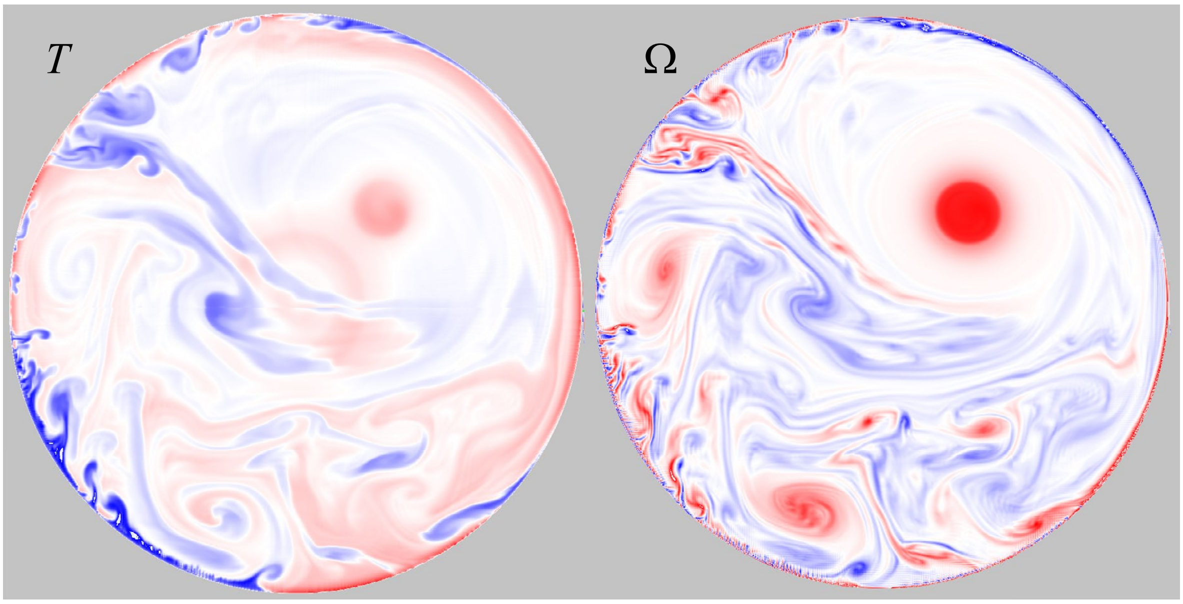

**Fig. 1.** Temperature (*T*) and vorticity (Ω) in the core before the onset of crystallization.

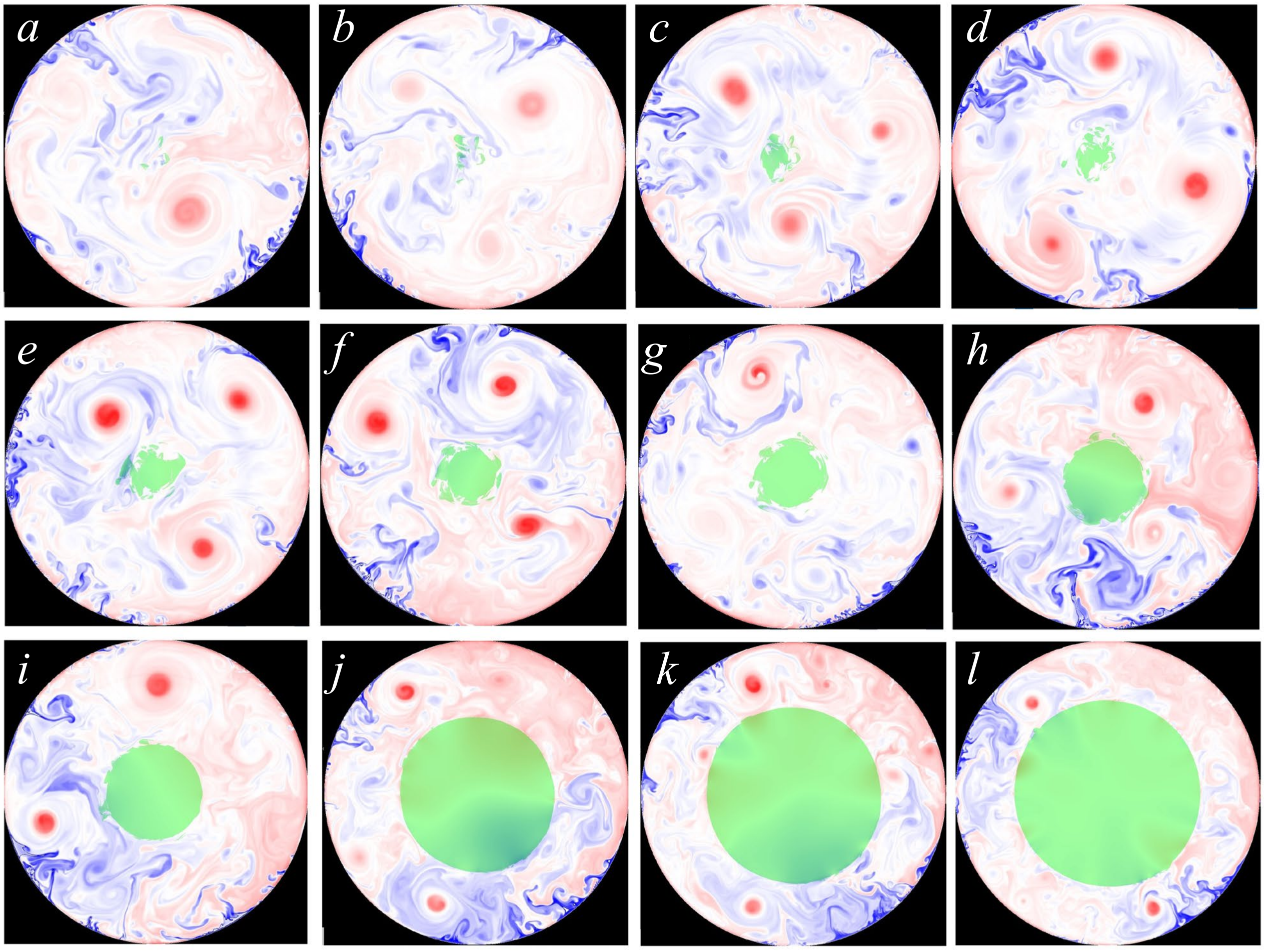

**Fig. 2.** Sequential stages of core crystallization from early (panel *a*) to late (panel *m*). The modern size of the solid core corresponds to panel *i*.

a small number of rapidly sinking jets remain, which by inertia pass through the weightlessness region in the center and move again toward the mantle, with maximum velocities achieved in the central part (video 1 in the Appendix). Both panels show a characteristic feature of convection in a fully liquid core: the substance does not accumulate in the central part but passes through it by inertia and again exits into the peripheral area.

Small vortices, merging together, enlarge to a size comparable to the core radius. In this regard, it should be noted that there are discrepancies in the literature: some researchers (for example, [4]) note predominantly large-scale organized laminar nature of convection, while others [6, 15] observe small-scale turbulent nature. The results of our modeling show that both regimes occur simultaneously. The large rounded vortices that form in this process are analogues of Taylor vortex columns, which are associated with the generation of a dipole magnetic field [15].

*Crystallization modeling*. Modeling of the crystallization process on fine grids was carried out as follows. For each node, the melting temperature is known, which depends on the radius through hydrostatic pressure. The grid nodes were divided into “liquid” and “solid” and a Boolean function was introduced to describe their current state. At the beginning of the simulation, all nodes are “liquid.” Then, at each moment of time, a check is performed at each node and if the temperature in a liquid node drops below the melting temperature (with a small supercooling), then this node transitions to the category of solid nodes. Similarly, if the temperature in a solid node rises above the melting temperature (with a small overheating), then this node returns to the category of liquid nodes. Each transition is accompanied by the release or absorption of phase transition energy and a jump in density. The increase in the density of the solid phase contributes to its movement and concentration in the central part of the core. In addition, the movement of the solid phase should be rotational-translational and connected to the flow of the liquid phase by adhesion conditions.

Fig. 2 shows the stages of core crystallization in green. It can be seen that crystallization begins in the central region with the appearance of individual crystallization centers, around which crystallizing areas grow, then merging with each other, forming a continuous solidified region.

In more detail, the crystallization process corresponding to our numerical model is shown in video 2 of the Appendix. The crystallizing substance becomes not absolutely solid, but only very viscous. Its density, and with it, gravity also increases slightly. Since there is zero gravity in the central region, the crystallizing substance can, by inertia, cross the crystallization zone, exit it into a low-pressure area, and melt again. However, as the core cools further, the radius of the crystallization zone increases, and solidifying fragments begin to rapidly accumulate in the central region. Liquid layers remain between them, so at this initial stage of crystallization, a loose porous structure is observed in the central region [21]. Later, the liquid layers also crystallize, but this occurs under “zero gravity” conditions. As the solid core grows, the convection structure is restructured; large jets cannot pass through the center and they turn around, partly due to the heat released during crystallization, which increases buoyancy force. Vortex structures twisted by jets decrease in size, resulting in a constant increase in the number of jets and vortex structures. Further growth of the inner core occurs unevenly in places where cold jets approach. Since convection is chaotic, jets approach from different places, and the shape of the crystalline part of the core becomes increasingly round. By the time the inner core reaches its modern size $R = 0.35$ (panel *i* in Fig. 2), its shape becomes almost circular (panels *j, k, l* in Fig. 2; video 2 of the Appendix).

*Convection in the core of modern configuration.* Convection in the core of modern configuration (the modern radius of the solid core is 1221.5 km, which is 0.35 of the radius of the entire core) is studied most frequently. In particular, there are similar studies in a purely thermal formulation, without considering the magnetic field [17]. The results of modeling thermal convection in the modern core are shown in Fig. 3. Unlike a completely liquid core (Fig. 1), hot ascending flows are added to the cold descending flows. It can be seen that the maximum size of the vortices decreases.

## INTEGRAL MODELING RESULTS

2D modeling of the thermal evolution of the core, with the condition of exponentially decreasing temperature at the core/mantle boundary, allows finding complete distributions of temperature, velocities, and phase configurations at all points in time. Videos of numerical experiments are provided in the appendix. For the analysis of results obtained at each point in time, the spatially averaged convection velocity $V_{av}$, the Nusselt number averaged along the CMB $Nu$, representing the dimensionless heat flux, and the solid phase area

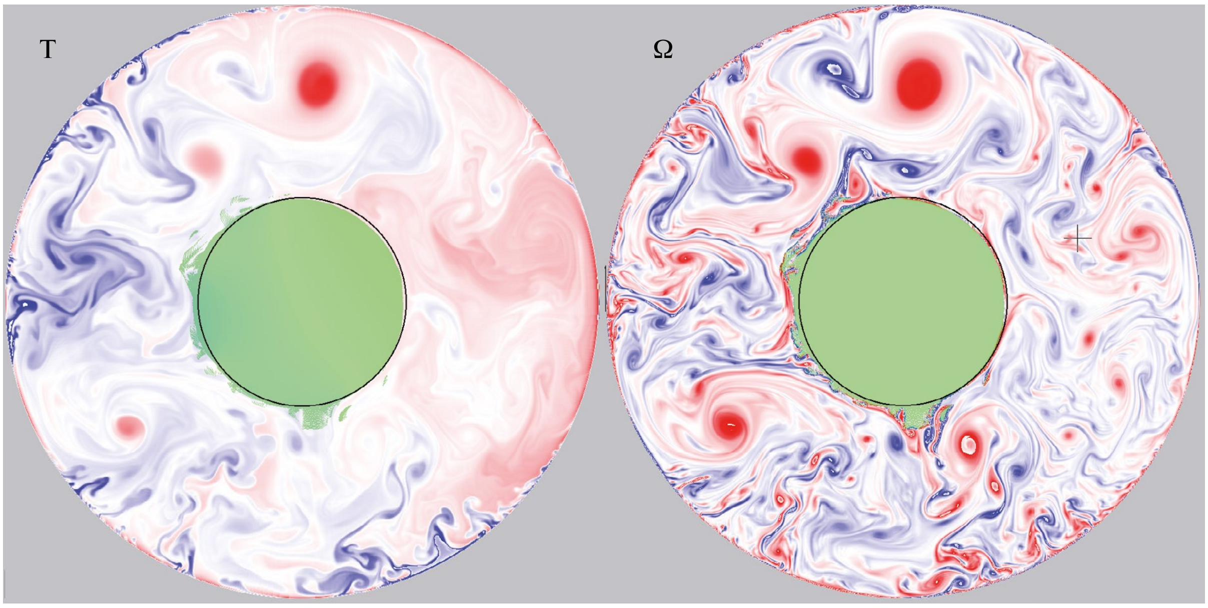

**Fig. 3.** Temperature ($T$) and vorticity ($W$) in the liquid core of the modern configuration.

normalized to the circle radius $R_{ic}$ were additionally calculated (Fig. 4a). The distributions are given in relative variables, with the reference point being the current state t = 0, $R_{ic} = 0.35$.

In our calculations, it is assumed that the CMB temperature decreases exponentially with time (black curve in Fig. 4 on the left). The heat output from the core, i.e., the times of its cooling and crystallization, is controlled by the mantle. To convert the results into dimensional time, additional information about the thermal insulating effect of the mantle, not related to the core, is needed. For example, in [18] it is stated that the gradual cooling of the Earth is about 100° C per billion years. In the work on modeling mantle convection [16], where the first 0.5 billion years are devoted to the crystallization of the mantle itself, it is shown that over the subsequent 4 billion years of geological evolution, the core temperature decreased by 12.5%, which is consistent with the estimate in [18]. This means that 4 billion years ago it was equal to 4434° K. Based on such a cooling rate of $T_{\text{CMB}}$, according to Fig. 4, we find that to reach the current radius of the solid core, its crystallization must have begun approximately 0.5 billion years ago.

The results of the numerical experiment presented in the left part of Fig. 4 show that since the appearance of the solid core, the heat flux from

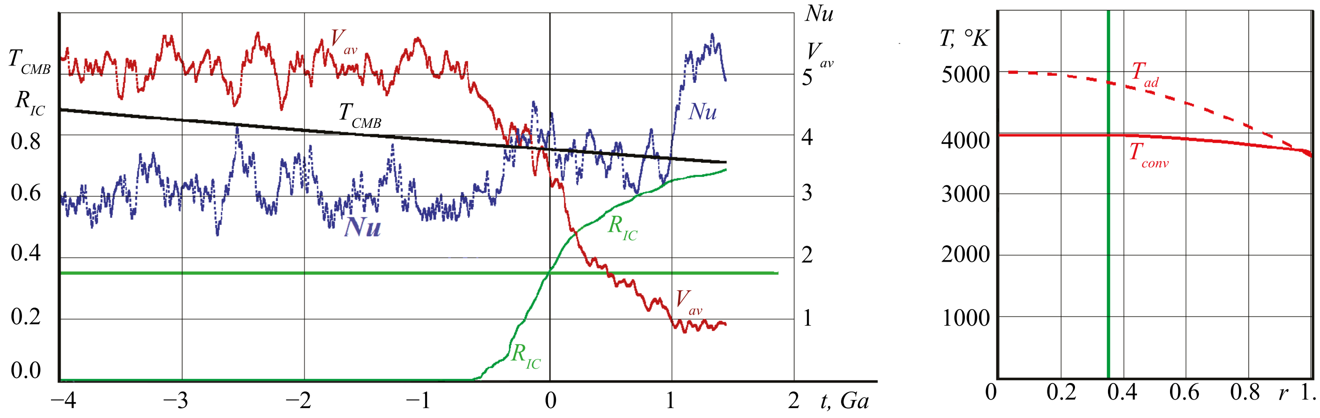

**Fig. 4.** (left) growth of the inner core ($R_{ic}$ , green color), heat flux from the core to the mantle ($Nu$ , blue) and average convection velocity ($V_{av}$ , brown); (right) – averaged temperature profile in the core ($T_{conv}$ , solid red curve) compared to the adiabatic profile according to [9] ($T_{ad}$ , dashed line).

the core to the mantle increases due to the release of crystallization heat, while the convection velocity begins to decrease, but this happens gradually as the solid core grows, which serves as an obstacle to convection. The chaotically oscillating nature of heat and mass transfer processes is also visible.

The modeling of thermal convection in the liquid core shows that developed turbulent convection occurs at very high velocities, approximately $v_0 \sim 5$–7 m/sec and is accompanied by short-wave oscillations of both the core's moment of inertia and its rotational moment. These oscillations should result in compensating oscillations of the mantle's angular velocity, which are registered on the planet's surface [22].

The distribution of the angular-averaged temperature in the modern liquid core is shown in Fig. 4 on the right. It is evident that as a result of intensive convection, the temperature distribution is flatter compared to the adiabatic one, which is most often used in literature [9]! And this temperature decreases over time.

## CONCLUSIONS

The conducted modeling of purely thermal convection has revealed some important features of the evolution of processes that occurred in the Earth's core against the background of planetary cooling.

1. In the liquid outer core, even before the crystallization of the inner core begins, large vortices form, which are two-dimensional analogues of Taylor vortex columns, with which the generation of a dipole magnetic field is associated. That is, the emergence of Earth's magnetic field may not be directly related to the formation of the solid core. This result may resolve contradictions between estimates of the age of existence of Earth's magnetic field.

2. Rapid chaotic growth of the solid core at the initial stage of crystallization.

3. The amorphous configuration of the core at the initial stage of crystallization and its loose structure are naturally explained by the absence of gravity at the center.

4. With the appearance of a solid core that blocks convective flows through the center, the restructuring of the convection pattern begins, and the average convection velocity decreases. However, the heat flux from the core to the mantle increases due to the release of crystallization heat.

5. The averaged temperature profile in the liquid core differs from the adiabatic one.

The model proposed in our work does not include a number of important processes that can significantly affect heat and mass transfer and, consequently, the nature of convection in the core. This is, first of all, the fractionation of the light element (hydrogen) between the solid and liquid core, which generates an important chemical component of convective flows. Secondly, our modeling does not take into account electromagnetic Lorentz forces. In addition, like all previous works known to us, it was conducted under the assumption that the total size of the core corresponds to the modern one, i.e., it did not change over time, and does not take into account the possibility of chemical exchange of metal and light element at the outer core-mantle boundary. Solving these problems is a task for future research.

## FUNDING

The research was carried out within the framework of the state assignment of IGEM RAS.

## REFERENCES

1. *Aubert J.* State and evolution of the geodynamo from numerical models reaching the physical conditions of Earth's core // Geophysical Journal International. 2023. V. 235. Pp. 468–487. https://doi.org/10.1093/gji/ggad229

2. *Biggin, A., Piispa, E., Pesonen, L., et al.* Palaeomagnetic field intensity variations suggest Mesoproterozoic inner-core nucleation // Nature. 2015. V. 526. Pp. 245–248. https://doi.org/10.1038/nature15523

3. *Bono R.K., Tarduno J.A., Nimmo F., Cottrell R.D.* Young inner core inferred from Ediacaran ultra-low geomagnetic field intensity // Nature Geoscience. 2019. V. 12. Pp. 143–147. doi:10.1038/s41561-018-0288-0

4. *Bouffard M., Choblet G., Labrosse S., Wicht J.* Chemical Convection and Stratification in the Earth's Outer Core // Frontiers in Earth Science. 2019. V. 7:99. doi: 10.3389/feart.2019.00099

5. *Braginsky S.* Structure of the F layer and reasons for convection in the Earth's core // Soviet Physics Doklady. 1963. V. 149. Pp. 8–10.

6. *Davies C.J., Greenwood S.* Dynamics in Earth's Core Arising from Thermo-Chemical Interactions with the Mantle. In: Core - Mantle Co - Evolution: An Interdisciplinary Approach (T.Nakagawa, T.Tsuchiya, M.Satish-Kumar, G.Helffrich Eds). 2023. https://doi.org/10.1002/9781119526919.ch12

7. *Deschamps F., Cobden L.* Estimating core-mantle boundary temperature from seismic shear velocity and attenuation // Frontiers in Earth Science. 2022. V. 10:1031507. doi: 10.3389/feart.2022.1031507

8. *Dziewonski A.M., Anderson D.L.* Preliminary reference Earth model // Physics of the Earth and Planetary Interior. 1981. V. 25. Pp. 297–356. https://doi.org/10.17611/DP/9991844

9. *Zharkov V.N.* Physics of the Earth's interior. Moscow: Science and Education. 2012. 383 p.

10. *Hirose K., Tagawa S., Kuwayama Y. et al.* Hydrogen limits carbon in liquid iron // Geophysical Research Letters. 2019. V. 46. Pp. 5190–5197. https://doi.org/10.1029/2019GL082591

11. *Konôpková Z.,McWilliams R.S., Gómez-Pérez N., Goncharov A.F.* Direct measurement of thermal conductivity in solid iron at planetary core conditions // Nature. 2016. V. 534. Pp. 99–101. doi:10.1038/nature18009

12. *Sakamaki K., Takahashi E., Nakajima Y. et al.* Melting phase relation of FeH *x* up to 20 GPa: Implication for the temperature of the Earth's core // Physics of the Earth and Planetary Interior. 2009. V. 174. Pp. 192–201. https://doi.org/10.1016/j.pepi.2008.05.017

13. *Zhang D., Jackson J.M., Zhao J. et al.* Temperature of Earth's core constrained from melting of Fe and Fe0.9Ni0.1 at high pressures // Earth and Planetary Science Letters. 2016. V. 447. Pp. 72–83. https://doi.org/10.1016/j.epsl.2016.04.026

14. *Reshetnyak M.Yu.* Parametric thermal model of Earth's evolution // Astronomy Letters. 2021. V. 47. Pp. 525–534. doi: 10.31857/S032001082107007X

15. *Kirdyashkin A.G., Dobretsov N.L., Kirdyashkin A.A.* Turbulent convection and magnetic field of the Earth's outer core. // Geology and Geophysics. 2000. V. 41. Pp. 601–612.

16. *Kotelkin V.D., Lobkovsky L.I.* Myasnikov's General Theory of Planetary Evolution and Modern Thermochemical Model of Earth's Evolution // Physics of the Earth. 2007. Pp. 26 – 44.

17. *Gorelikov A.V., Ryakhovskiy A.V., Fokin A.S.* Numerical Study of Some Non-Stationary Regimes of Natural Convection in a Rotating Spherical Layer // Computational Continuum Mechanics. 2012. V. 5. Pp. 184–192. doi: 10.7242/1999-6691/2012.5.2.22

18. *Jacobs J.A.* The Earth's inner core // Nature. 1953. V. 172. Pp. 297–298. doi:10.1038/172297a0

19. *Aranovich L.Y., Persikov E.S., Bukhtiyarov P.G., Bondarenko G.S.* Interaction of $Fe_3$ C with Hydrogen: On the Compatibility of Carbon with Hydrogen in Metallic Iron // Petrology. 2021. V. 29. Pp. 695–701. DOI: 10.1134/S0869591121060072

20. *Gershuni G.Z., Zhukhovitskiy E.M.* Convective Stability of Incompressible Fluid. Moscow: Nauka. 1972. 392 p.

21. *Pang G., Koper K.D., Wu S.-M. et al.* Enhanced inner core fine-scale heterogeneity towards Earth's centre // Nature. 2023. V. 620. Pp. 570–575. https://doi.org/10.1038/s41586-023-06213-2

22. *Zotov L., Bizouard Ch., Sidorenkov N. et al.* Multidecadal and 6-year variations of LOD. // Journal of Physics: Conference Series (JPCS). 2020. 1705 012002. IOP Proceedings of FAPM 2019 conference.

*DOKLADY EARTH SCIENCES, 2025, Vol. 520, No. 1, pp. 159–163*

# POINT OF LIMITED AVAILABILITY OF WATER IN SOIL AND ITS DETERMINATION

© 2025 **G. N. Fedotov***, **Corresponding Member of RAS S. A. Shoba, I. V. Gorepekin,**
**A. I. Sukharev, D. A. Tarasenko, A. P. Shvarov, and Z. Tyugai**

Received July 26, 2024
Revised September 05, 2024
Accepted September 09, 2024

**Abstract.** The point of limited availability of water (PLAW) characterizes the lower boundary of the area of the most productive moisture for plants. The analysis of experimental methods for determining PLAW indicates their labor intensity and low productivity. The aim of the study was to develop a high-performance and accurate method for determining PLAW. 18 samples from various soils were used in the work. To determine the PLAW, a method was proposed in which soil samples were placed in a Schott funnel, moistened with excess water, and then the water was pumped out using a water jet pump. As the water was being removed from the sample, the interval between drops falling from the funnel increased. A jump in the intervals between drops was considered an indicator of the end of the experiment. Experiments have shown that the soil moisture content obtained by vacuuming correlates with the values calculated for the lowest soil moisture capacity (according to Dolgov) by 87%. The values of the PLAW obtained by the secant method (according to Voronin) for some of the soil samples do not fall out of the obtained dependence. Using the method, it was shown that soil drying leads to a decrease in the value of the measured PLAW. An explanation of the results from the position of the presence of organomineral gels in soils is proposed.

**Keywords:** *soil hydrological constants, soil drying under vacuum, the lowest soil moisture capacity*

**DOI**: 10.31857/S26867397250120e4

Soil-hydrological constants are moisture values characteristic of each soil, which are used in practical calculations of water reserves and movement in soils [1-3].

Water movement occurs most actively through soil macrocapillaries in the interval between full and field capacity. After water drains from macrocapillaries, its movement rate sharply decreases, and predominant water flows proceed through meso- and microcapillaries. This occurs in the interval between field capacity and point of limited availability of water (PLAW) – the range of moisture most productive for plants. Decrease in moisture below PLAW leads to disruption of hydraulic connection between soil capillaries and their breakdown into separate capillaries [1, 2]. They are partially filled with water and separated by air-filled capillaries in which water exists in the form of films [2].

Approaches to determining PLAW vary. In the high column method by A.F. Lebedev, it is proposed to fill tubes with soil and moisten the soil until saturation [4]. Then soil moisture in the tube is determined layer by layer. In the upper part, where water is retained by molecular forces, moisture is lowest. This is called the capillary break moisture. High labor intensity and low productivity of the method limit the possibility of its widespread laboratory use.

Another approach is proposed in the Dolgov-Matskevich method [5]. When soil moisture is above PLAW, soil solution moves to the surface – the evaporation zone – where salt contained in the soil solution appears as a crust. If moisture is below PLAW, salt does not appear on the soil surface. When selecting a series of samples with different amounts of soil solution with salt, it is possible to determine PLAW – the moisture of the first sample in the series on which salt solution does not appear. The disadvantage of this method is also its labor intensity and low productivity.

In our opinion, the most promising method is determining PLAW by the inflection point that

---

*Lomonosov Moscow State University, Moscow, Russia*
**e-mail: gennadiy.fedotov@gmail.com*

appears on the drying rate curve of soil samples [6]. Moistened soil samples are heated, and water loss is recorded on continuous weighing scales. Researchers obtain a set of points based on which they plot the relationship between sample moisture and drying rate. Analysis of such curves shows that data scatter smooths the inflection point, and increasing the number of points significantly reduces the productivity of the method.

The common feature of these methods is that any soil reaches the PLAW during drying. Therefore, the priority task is to select a signal indicating when the soil sample reaches this moisture level. Such a marker can be a sharp slowdown in the soil drying rate.

The aim of the study was to develop an experimental high-performance and accurate method for determining PLAW.

## RESEARCH OBJECTS

The study used samples collected from various horizons (Table 1):

- soddy-podzolic soil (Moscow region),
- gray forest soil (Tula region),
- leached chernozem (Oryol region),
- ordinary chernozem (Voronezh region),
- chestnut soil (Volgograd region).

The soil samples were divided into two groups: the first was dried to an air-dry state, and the second was maintained at the sampling moisture content (between field capacity and PLAW).

## RESEARCH METHODS

To obtain the calculated PLAW values, the field capacity of the samples was determined using the Dolgov method [7]. The soil sample was poured into an aluminum tube with a diameter of 40 mm[1] and a height of 100 mm. To ensure constant bulk weight, the sample was compacted by vibration, after which it was saturated with water for 24 hours until full water capacity by placing it in a glass with water for 1 day. Then the samples were placed on wet sand for 3 days to drain the gravitational water. The experiments were conducted in triplicate. After that, PLAW was calculated using the formula applied for loamy soils: PLAW = 0.7 FC.

The dependence of the capillary-sorption potential of water on soil moisture – soil water retention curve (SWRC) – was determined by the tensiometric method in the probe version [8]. Based on the SWRC data, PLAW was calculated using the secant method in accordance with the methodology described in [2].

The moisture content of soil samples was determined using an “Ohaus” MB23 device.

## RESEARCH RESULTS

To remove moisture from soils during the determination of PLAW, we used vacuum application. A soil sample weighing 100 g was placed in a glass filter, a Schott funnel #4, which was installed on a Büchner flask connected to a water jet pump. To form a capillary connection between all particles of the soil sample, the soil was moistened with excess water, 50 g. Then the water jet pump was turned on. Water passed through the soil, then through the glass filter and flowed from the lower part of the Schott funnel as a stream, and then in drops. When there was no more water on the surface of the sample, air began to enter the soil. Due to rarefaction, it filtered through the soil layer and pushed water through the capillaries. As water was removed from the sample, the interval between drops falling from the Schott funnel increased (Fig. 1). The indicator of the end of the experiment was considered to be a jump in the intervals between the falling drops (Fig. 1). Upon reaching the jump, the water jet pump was turned off. In a sample from the middle layer of the soil sample, the moisture content was determined, which in physical sense, i.e., the slowdown of water movement through the sample, corresponded to PLAW.

Since air passing through the soil layer additionally dries the sample, this brings distortions in the measurement results (Fig. 2). To eliminate them, the air passing through the soil sample was pre-saturated with water vapor by bubbling the air through water.

At the next stage of the work, we studied the effect of the vacuum level on the determined PLAW value. It was found that in the range from –0.2 to –0.8 atm, the measured PLAW value does not change.

To verify the correctness of the proposed method, we compared the results of PLAW determination by the vacuum method with the calculated method of estimating PLAW through the lowest field capacity value. The experimental results correlate with the calculated values with a correlation coefficient of 87% (Table 1, Fig. 3).

---

[1] For practical convenience, the CGS system, multiple and non-system units of measurement are used in the work.

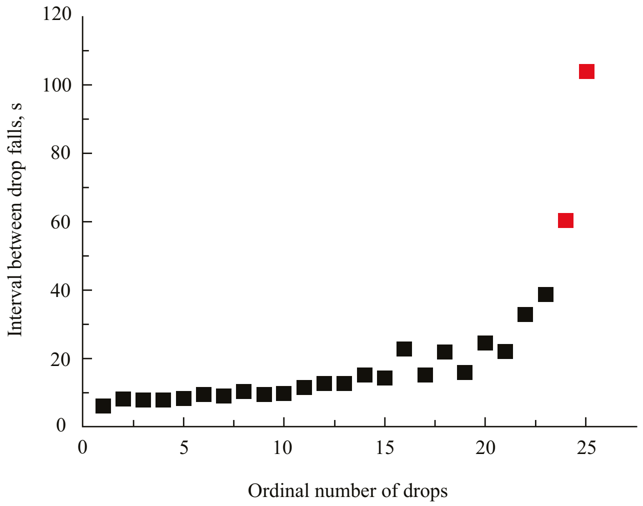

**Fig. 1.** Dependence of the time interval between drops falling from the Schott funnel on the drop sequence number.

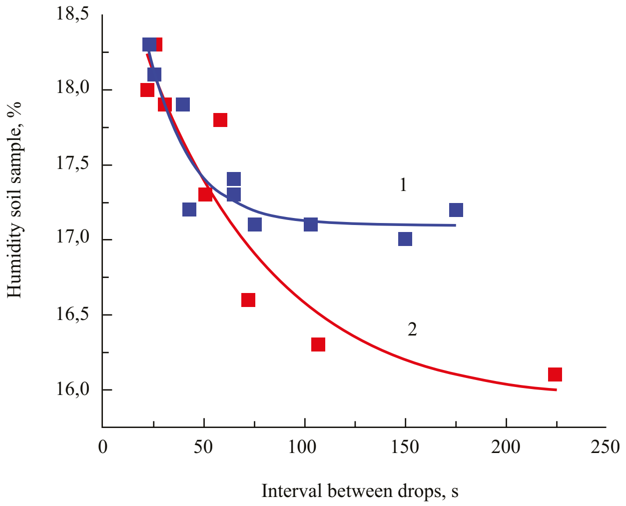

**Fig. 2.** Change in soil sample moisture content (PLAW) depending on the time interval between drops falling from the Schott funnel when passing moist (2) and dry (1) air through a sample of soddy-podzolic soil.

In order to additionally verify the obtained data, for some samples, the PLAW values were calculated using the tangent method after determining the tensiometric part of the main hydrophysical characteristic. The points for samples obtained by the tangent method do not deviate from the obtained relationship (Fig. 3), which confirms the correctness of using the vacuuming method for determining the PLAW of soils.

Using the new method, the influence of gray forest soil moisture on its PLAW values was studied (Fig. 4). The experiments used soil that had not been subjected to drying, which was slowly dried, and samples were taken to determine the PLAW. Uniform water removal throughout the sample was ensured by placing the original soil with a moisture content of 0.7–0.8 field capacity in a 5-liter container covered with cotton fabric. The container itself was placed in conditions of air humidity close to 100%. The soil was mixed daily.

The obtained data indicate that drying leads to a decrease in the PLAW of soils. This calls into

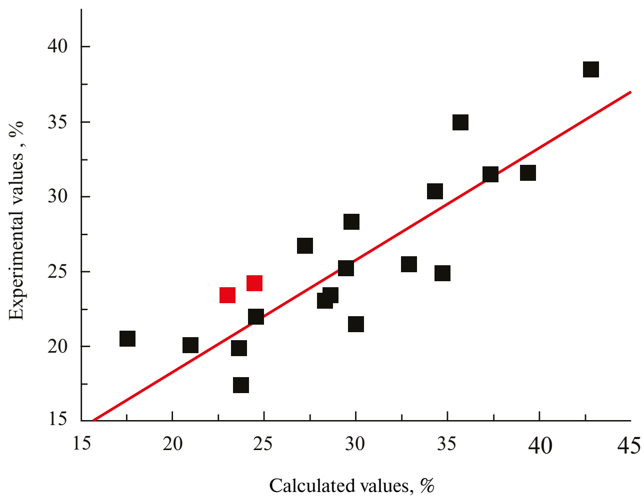

**Fig. 3.** Relationship between experimental values of air-entry value moisture determined by the vacuuming method and calculated values. Points obtained by the tangent method are highlighted in red.

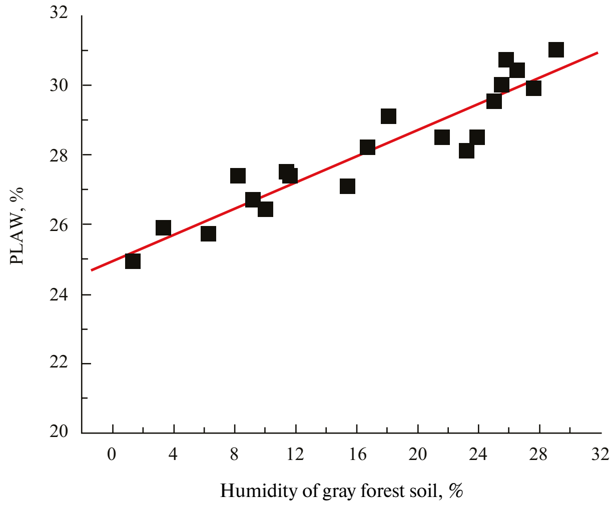

**Fig. 4.** Influence of gray forest soil sample moisture on the determined values of point of limited availability of water (PLAW).

**Table 1.** Soil samples used in the work and their capillary break moisture content values.

| No. | Soil | Sampling horizon | Sample preparation | Calculated PLAW, % | Experimental PLAW, % |
|---|---|---|---|---|---|
| 1 | Sod-podzolic soil (arable land) | A | Dried moistened | 23.7±0.5 | 17.4±0.4 |
| 2 | Sod-podzolic soil (arable land) | A | Initial | 21.0 ±0.8 | 20.1±0.6 |
| 3 | Sod-podzolic soil (arable land) | A | Dried moistened | 23.6 ±0.3 | 19.9±0.2 |
| 4 | Gray forest soil (forest) | A | Dried moistened | 32.9±0.7 | 25.5±0.9 |
| 5 | Gray forest soil (forest) | A | Initial | 37.3 ±1.3 | 31.5±0.12 |
| 6 | Gray forest soil (arable land) | BEL | Dried moistened | 28.6±0.4 | 23.4±0.2 |
| 7 | Gray forest soil (arable land) | BT | Dried moistened | 28.3±0.3 | 23.0±0.7 |
| 8 | Gray forest soil (arable land) | BC | Dried moistened | 29.5±0.8 | 25.2±0.4 |
| 9 | Gray forest soil (forest) | BT | Dried moistened | 27.2±0.5 | 26.7±1.0 |
| 10 | Gray forest soil (forest) | BC | Dried moistened | 17.6±0.4 | 20.5±0.9 |
| 11 | Leached chernozem (fallow) | A | Dried moistened | 39.4±0.8 | 31.6±0.9 |
| 12 | Leached chernozem (fallow) | A | Initial | 35.7±1.3 | 35.0±0.35 |
| 13 | Ordinary chernozem (arable land) | AUB | Dried moistened | 42.8±0.1 | 38.5±0.7 |
| 14 | Ordinary chernozem (forest belt) | BIca | Dried moistened | 29.8±1.3 | 28.3±0.1 |
| 15 | Ordinary chernozem (forest belt) | BC | Dried moistened | 34.3±0.7 | 30.3±0.3 |
| 16 | Chestnut soil (fallow) | A | Dried moistened | 300±0.6 | 21.5±0.4 |
| 17 | Chestnut soil (fallow) | AJ | Dried moistened | 34.7±1.2 | 24.9±0.2 |
| 18 | Chestnut soil (arable land) | BC | Dried moistened | 24.6±0.5 | 22.0±0.2 |

question the currently proposed mechanism of PLAW occurrence in the physical soil model[2] [2], based on the existence of water at PLAW in the form of films on the surface of solid soil particles [2, 5]. In the presence of hydrophilic and hydrophobic areas on the surface of soil particles, it should be expected that films will be located on hydrophilic surfaces. However, how does the proportion of hydrophilic areas on the surface of soil particles change when soil moisture decreases? From the perspective of the three-phase soil model, it is quite difficult to answer this question.

From the standpoint of the gel soil model [9], the basis of soil structure lies in the interactions between supramolecular formations, the basis of which are interconnected fractal clusters of humic substance particles-molecules [11-14] with a mosaic diphilic surface [15].

In soils, the gel structure represents a formation consisting of an openwork framework (fractal clusters connected to each other) and water filling the voids. In moist soils, the branches of fractal clusters interlock with each other through hydrophobic areas, while hydrophilic areas face the water. When soils dry, the clusters contract and their branches penetrate each other more densely. As a result, the thickness of the gel layer consisting of clusters decreases. The gel structure becomes denser, and the volume of water that the gel can hold decreases. This explains the reduction in moisture of point of limited availability of water during soil drying.

## CONCLUSIONS

1. A high-performance method for determining point of limited availability of water based on water removal from a soil sample using vacuum has been proposed. The data obtained using this method correlate with calculated values by 87%.

2. Using the proposed method, it has been shown that the initial moisture content of the sample

---

[2] The physical model of soils is based on the fact that soil is formed by solid, liquid and gaseous phases. This model does not use information about the supramolecular organization of humic substances [9] and the presence of organomineral gels in soils, which are based on humic substances [9, 10], to explain soil processes.

affects the value of the determined point of limited availability of water.

3. A hypothesis for the formation of point of limited availability of water has been proposed from the perspective of the presence of organomineral gels in soils.

## FUNDING

The work was carried out within the framework of the Moscow State University state assignment No. 122011800459-3.

## CONFLICT OF INTEREST

The authors declare that there is no conflict of interest.

## REFERENCES

1. *Eremin D.I., Shakhova O.A.* Dynamics of leached chernozem moisture under different tillage systems for spring wheat in the Northern Trans-Urals conditions //Agrarian Bulletin of the Urals. 2010. No. 1 (67). Pp. 38–40.
2. *Shein E.V.* Soil Physics Course. Moscow: Moscow University Press, 2005. 430 p.
3. *Novák V., Hlaváčiková H.* Applied soil hydrology. Cham, Switzerland: Springer, 2019. 342 p.
4. *Vadyunina A.F., Korchagina Z.A.* Methods for studying physical properties of soils and grounds. 2nd ed. Moscow: 1973, 1969. 399 p.
5. *Voronin A.D.* Structural-functional soil hydrophysics. Moscow: Moscow University Press, 1984. 204 p.
6. *Chestnova V.V.* Rheological properties of typical chernozems in Kursk region: correlation with physical properties and main hydrophysical characteristic. PhD thesis in Biology: 06.01.03. Moscow, 2017. 116 p.
7. Methodological guide for studying soil structure/ Ed. by Revut I.B., Rode A.A. Leningrad: Kolos, 1969. 528 p.
8. *Shein E.V., Arkhangelskaya T.A., Goncharov V.M., Guber A.K., Pochatkova T.N., Sidorova M.A., Smagin A.V., Umarova A.B.* Field and laboratory methods for studying physical properties and soil regimes: Methodological guide. Moscow: Moscow University Press, 2001. 200 p.
9. *Fedotov G.N., Shein E.V., Ushkova D.A., Salimgareeva O.A., Gorepekin I.V., Potapov D.I.* Supramolecular formations of humic substances and rheir fractal organization // Eurasian Soil Science. V.56. No. 8. Pp. 1007–1013.
10. *Tyulin A.F.* Organo-mineral colloids in soil, their genesis and significance for root nutrition of higher plants. Moscow: USSR Academy of Sciences Press, 1958. 52 p.
11. *Angelico R., Colombo C., Di Iorio E., Brtnický M., Fojt J., Conte P.* Humic substances: from supramolecular aggregation to fractal conformation – Is there time for a new paradigm? // Appl. Sci. 2023. V. 13. No. 4. P. 2236.
12. *Osterberg R., Mortensen K.* Fractal dimension of humic acids. A small angle neutron scattering study // Eur. Biophys. J. 1992. V. 21. No. 3. Pp. 163–167.
13. *Senesi N., Rizzi F.R., Dellino P., Acquafredda P.* Fractal humic acids in aqueous suspensions at various concentrations, ionic strengths, and pH values. Colloids and Surfaces A. // Physicochemical and Engineering Aspects. 1997. V. 127. Iss. 1–3. Pp. 57–68.
14. *Senesi N., Rizzi F.R., Dellino P., Acquafredda P.* Fractal dimension of humic acids in aqueous suspension as a function of pH and time // Soil Science Society of Am. J. 1996. V. 60. No. 6. Pp. 1613–1678.
15. *Milanovsky E.Yu.* Soil Humic Substances as Natural Hydrophobic-Hydrophilic Compounds. Moscow: GEOS, 2009. 186 p.
16. *Startsev V.V., Dymov A.A.* Amphiphilic Properties and Water-Soluble Organic Matter of Soils of the Subpolar Urals //Eurasian Soil Science. 2021. V. 54. No. 12. Pp. 1864–1875.